

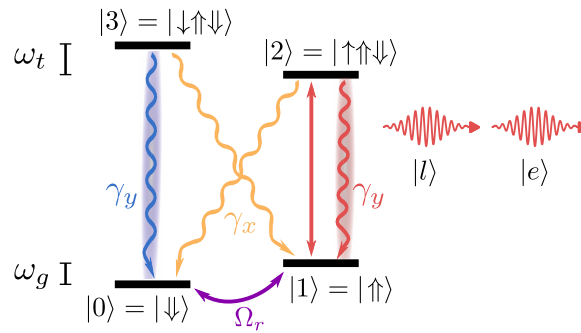
PhD Thesis

# A Quantum Dot Source of Time-Bin Multi-Photon Entanglement

Martin Hayhurst Appel  
July 2021

This thesis is typeset using  $\text{\LaTeX}$ . Figures are produced using Matlab, Python Matplotlib and Inkscape.

The energy level diagram of a positively charged quantum dot in a Voigt geometry magnetic field is frequently referenced throughout this thesis, and is reproduced below for easy reference.



PHD THESIS

---

# A Quantum Dot Source of Time-Bin Multi-Photon Entanglement

---

*Author:*  
Martin Hayhurst Appel

*Supervisors:*  
Prof. Peter Lodahl  
Dr. Alexey Tiranov



---

UNIVERSITY OF  
COPENHAGEN

Quantum Photonics  
Center for Hybrid Quantum Networks  
The Niels Bohr Institute

*This thesis has been submitted to the PhD School of the Faculty of Science  
University of Copenhagen*

July 2021



## Abstract

Quantum states of multiple entangled photons constitute an important resource for measurement-based quantum computing and all-photonic quantum repeaters. However, the generation of such states is challenging, and the probabilistic schemes pursued until now are difficult to scale. Here, we investigate deterministic entanglement generation using a spin-photon interface which, through repeated optical manipulation, can emit long strings of entangled photons. Specifically, we employ a solid-state InAs quantum dot charged with a single hole spin. Additionally, we embed the quantum dot in a photonic crystal waveguide, thereby strongly coupling the emitter to a single optical mode and modifying the light-matter interaction.

A common limitation encountered with quantum dots is the incompatibility of coherent spin control and optical cycling transitions. By applying an in-plane magnetic field and by selectively coupling the linear optical dipoles to the waveguide mode, we measure a broadband increase in optical cyclicity up to  $\times 14.7$  while retaining the ability to drive optical Raman transitions. The waveguide geometry also allows selective pumping of the optical transitions leading to 98% spin initialisation fidelity. We demonstrate a  $T_2^* = 23.2$  ns spin dephasing time, which exceeds most experiments employing comparable nanostructures.

These capabilities allow the realisation of a time-bin entanglement protocol, which we analyse in great detail. By combining resonant optical pulses and Raman pulses, the protocol can generate GHZ states and linear cluster states containing the QD spin and  $N$  photons, where each photon is emitted in a superposition of two temporal modes. This protocol is insensitive to  $T_2^*$ , thanks to a built-in spin-echo process, and is compatible with high magnetic fields and waveguides. We calculate error rates of 2.1% pr. photon while considering realistic parameters and optimal use of the waveguide. The protocol is implemented experimentally, and we realize a spin-photon Bell state with a 66.6% fidelity and 124 Hz detection rate. By using a self-stabilising double-pass interferometer, we are able to construct exact GHZ and Bell state fidelity estimates. Extending to three qubits, we observe clear signatures of coherence which, however, lack the amplitude for certifiable entanglement. By constructing an exhaustive Monte Carlo simulation, we are able to include nearly all relevant errors and identify our modest 88.5% spin rotation fidelity as the leading error mechanism. Other experiments have demonstrated better spin control, and we discuss several possible paths towards achieving higher fidelity and scaling up to more qubits.



## Resume

Kvantemekaniske tilstande bestående af flere entangledede fotoner udgør en vigtig ressource til brug i målingsbaserede kvantecomputere og ved transmission af kvanteinformation. Det er dog særdeles svært at frembringe sådanne tilstande, og hidtidige forsøg har anvendt ikke-deterministiske metoder, som er vanskelige at anvende i stor skala. I denne afhandling belyser vi brugen af et faststof-spin, som på deterministisk vis kan generere store fotontilstande igennem gentagne optisk manipulation. Konkret anvender vi en InAs kvanteprik med et enkelt hul-spin. Kvanteprikken er indlejret i en fotonisk krystal-bølgeleder med en enkel optisk *mode*, hvilket forstærker vekselvirkningen mellem stof og lys.

I kvanteprikker er kohærent spinkontrol normalt uforenelig med lukkede optiske overgange, hvilket er en stor begrænsning. Vi fjerner denne begrænsning ved at anvende et horisontalt magnetfelt og ved selektivt at koble de lineære optiske dipoler til bølgelederen. Dermed måler vi en bredbåndet cyklicitets-forbedring op til  $\times 14,7$  og beholder samtidig muligheden for at drive optiske Raman overgange. Bølgelederens geometri tillader samtidig optisk spin-pumping, som leder til en 98% spin-præparerings fidelitet. Vi demonstrerer desuden en  $T_2^* = 23,2$  ns spin dephasing tid, hvilket overstiger de fleste andre eksperimenter baseret på sammenlignelige nanostrukturer.

Disse færdigheder muliggør en tids-kodet entanglementprotokol, som vi grundigt analyserer. Ved at kombinere resonante optiske pulser og Raman pulser kan protokollen generere GHZ-tilstande og lineære klyngetilstande, som består af kvanteprikkens hul-spin og N fotoner, hvor hver foton er i en superposition af to udsendelsestidspunkter. En indbygget spin-ekko procedure gør protokollen ufølsom overfor  $T_2^*$ . Protokollen er desuden kompatibel med stærke magnetfelter og bølgeledere. Vi beregner en fejlrate på 2,1% pr. foton ud fra realistiske parametre og optimal bølgelederudnyttelse. Protokollen udføres eksperimentelt, og vi måler spin-photon Bell-tilstande med 66,6% fidelity og 124 Hz detektions rate. Ved hjælp af et selvstabiliserende interferometer kan vi foretage eksakte estimater af GHZ- og Bell-tilstandes fidelitet. Når vi udvider til tre kvantebits, observerer vi klare indikationer på kohærens, dog uden at kunne påvise entanglement. Ved at konstruere en dybdegående Monte Carlo simulation kan vi inkludere næsten alle relevante fejlkilder, og vores middelmådige 88,5% spin rotations fidelitet fremstår som den primære fejlkilde. Andre eksperimenter har demonstreret bedre spinkontrol, og vi kan dermed foreslå en række forbedringer, som vil muliggøre tilstande med flere kvantebits af højere fidelitet.



## Preface

This thesis concludes almost 3.5 exciting years spent in the Quantum Photonics group at the Niels Bohr Institute. I spent the majority of this time in the lab, building optical setups, characterising quantum dots and gathering data. Performing experimental work can be often frustrating and feel like "two steps forward, one step back". However, becoming intimately familiar with a complex experiment and using this knowledge to generate quantum entanglement was also very satisfying.

Naturally, this work could never have been performed alone. I am first and foremost thankful towards my supervisor Peter Lodahl, who gave me the opportunity to pursue a PhD in his group and has shown me a high level of trust. I want to thank Tim Schröder, my co-supervisor during my first year, who helped define my research goals. I am also in much debt to Alexey Tiranov, my co-supervisor during the last two years, who has been incredibly resourceful and supportive. Dapeng Ding and fellow PhD student Ming Lai have also been invaluable members of the spin team. Several master students have been involved with the spin project, and I have fond memories of working alongside Maxime Bergamin, Christian Starup, who built the Fabry-Perot cavity, and Simon Pabst, who helped build and characterise the time-bin interferometer.

Having access to high-quality samples is crucial for performing solid-state quantum optics experiments. The third sample investigated during my time in the lab proved to be a fantastic workhorse, yielding 99% of the data in this thesis. This sample was the result of membrane growth in Bochum by Arne Ludwig and Sven Scholz and nanostructure fabrication in Copenhagen by Ying Wang, for which I am very thankful.

Beyond the experimental work, I also spent a substantial amount of time studying and discussing entanglement schemes with the theory group of Anders Søndberg Sørensen at NBI. Many of the theoretical results in this thesis build on the work of Konstantin Tiurev, who played the main role in analysing the time-bin protocol, and Anders' master students Mikkel Bloch Lauritzen and Pol Llopart Mirambell.

2020 was the year of the COVID-19 pandemic, and as a result, I was unable to attend my planned external stay in Vienna. Luckily, in 2019, I managed to visit Mete Atatüre's research group at the University of Cambridge. Although short, this visit was very stimulating and inspired concrete experimental techniques which would be implemented in Copenhagen. I would like to thank Mete Atatüre and Claire Le Gall for facilitating my visit, and Dorian Gangloff and Daniel Jackson for showing me their experiment and sharing their knowledge. I would also like

to thank Richard Warburton, Alisa Javadi and Matthias Löbl at the University of Basel for many constructive discussions. Additionally, Alisa Javadi was kind enough to share his numerical simulations, which have proven very valuable.

The enjoyment of my PhD studies has been greatly elevated by my fantastic friends and colleagues in the Hy-Q research centre. We have had many memorable moments outside the lab including Christmas lunches, karaoke evenings, running clubs and retreats. I especially want to thank Ravitej Uppu, Hanna Le Jeannic, Camille Papon, Henri Thyrestrup, Freja Tilde and Leonardo Midolo for their help in the lab and for fruitful scientific discussions. I also have to thank Ying Wang, Eva M. G. Ruiz, Asli Ugurlu, Vasiliki Angelopoulou, Oliver Sandberg, Patrik Sund, Arianne Brooks, Nils V. Hauf, and Rodrigo A. Thomas for creating an enjoyable atmosphere and helped me stay motivated, especially during writing. Yijian Meng has been a fantastic aid in proofreading most of the thesis.

I am also grateful to my choir and my band for enriching my life my music and making me forget my work once in a while. Finally, I am hugely thankful to my family for their love and support.

## List of Publications

### PUBLISHED

- *Coherent Optical Control of a Quantum-Dot Spin-Qubit in a Waveguide-Based Spin-Photon Interface.* Dapeng Ding, **Martin Hayhurst Appel**, Alisa Javadi, Xiaoyan Zhou, Matthias Christian Löbl, Immo Söllner, Rüdiger Schott, Camille Papon, Tommaso Pregnolato, Leonardo Midolo, Andreas Dirk Wieck, Arne Ludwig, Richard John Warburton, Tim Schröder, and Peter Lodahl. *Physical Review Applied* 11, 031002 (2019).
- *Coherent Spin-Photon Interface with Waveguide Induced Cycling Transitions.* **Martin Hayhurst Appel**, Alexey Tiranov, Alisa Javadi, Matthias C. Löbl, Ying Wang, Sven Scholz, Andreas D. Wieck, Arne Ludwig, Richard J. Warburton, and Peter Lodahl. *Physical Review Letters* 126, 013602 (2021).

### SUBMITTED FOR PUBLICATION

- *Fidelity of time-bin entangled multi-photon states from a quantum emitter.* Konstantin Tiurev, Pol Llopart Mirambell, Mikkel Bloch Lauritzen, **Martin Hayhurst Appel**, Alexey Tiranov, Peter Lodahl, and Anders Søndberg Sørensen. arXiv:2007.09298 (2020).
- *High-fidelity multi-photon-entangled cluster state with solid-state quantum emitters in photonic nanostructures.* Konstantin Tiurev, **Martin Hayhurst Appel**, Pol Llopart Mirambell, Mikkel Bloch Lauritzen, Alexey Tiranov, Peter Lodahl, and Anders Søndberg Sørensen. arXiv:2007.09295 (2020).

### CONFERENCE PROCEEDINGS

- *Towards Spin-Multiphoton Entanglement using Quantum Dots with Asymmetric Waveguide Coupling.* **Martin Hayhurst Appel**, Alexey Tiranov, Konstantin Tiurev, Alisa Javadi, Ying Wang, Leonardo Milodo, Svend Scholz, Andreas D. Wieck, Arne Ludwig, Richard J. Warburton, and Peter Lodahl. Conference on Lasers and Electro-Optics, OSA Technical Digest (Optical Society of America, 2020), paper FW3C.1.



# Contents

<b>Abstract</b>	<b>iii</b>
<b>Resume</b>	<b>v</b>
<b>Preface</b>	<b>vii</b>
<b>List of Publications</b>	<b>ix</b>
<b>Abbreviations</b>	<b>xiii</b>
<b>1 Introduction</b>	<b>1</b>
<b>2 Theory</b>	<b>5</b>
2.1 The Quantum Dot . . . . .	5
2.2 Charge States . . . . .	7
2.3 Selection Rules . . . . .	8
2.4 Resonant Excitation . . . . .	12
2.5 Three Level Spin Pumping . . . . .	14
2.6 Noise Sources . . . . .	17
2.7 Spin Coherence . . . . .	18
2.8 Nuclear Environment . . . . .	19
2.9 Photonic Nanostructure . . . . .	23
<b>3 Experimental Setup</b>	<b>27</b>
3.1 Sample . . . . .	27
3.2 Laser Systems . . . . .	29
3.3 Optical Setup . . . . .	32
3.4 Detection Systems . . . . .	34
<b>4 Spectroscopy</b>	<b>37</b>
4.1 Resonant Transmission . . . . .	37
4.2 Charge State Identification . . . . .	39
4.3 Lifetime Measurements . . . . .	40
4.4 Resonance Fluorescence . . . . .	41
4.5 Hole Spectroscopy . . . . .	42
4.6 Voigt Geometry Resonance Fluorescence . . . . .	46
4.7 Parameter Summary . . . . .	48

<b>5</b>	<b>Cyclicity</b>	<b>51</b>
5.1	PCW Simulation . . . . .	51
5.2	Spin Pumping Measurements . . . . .	54
5.3	Emission Spectrum . . . . .	57
5.4	Resonant Transmission . . . . .	59
5.5	Interpretation of Measured Cyclicity . . . . .	61
5.6	Cyclicity Applications: Single-Shot Readout . . . . .	63
5.7	Discussion . . . . .	64
<b>6</b>	<b>Coherent Spin Control</b>	<b>65</b>
6.1	Ultra-Fast Spin Control . . . . .	65
6.2	Raman Pulses . . . . .	67
6.3	Experimental $\pi$ -Pulse Characterisation . . . . .	74
6.4	Hole Spin Coherence Time . . . . .	80
6.5	Discussion . . . . .	87
6.6	Comparison of Ultra-Fast and Raman Schemes . . . . .	89
6.7	Summary . . . . .	90
<b>7</b>	<b>Theory of Multi-Photon Entanglement</b>	<b>91</b>
7.1	Entangled States of Interest . . . . .	91
7.2	The Lindner-Rudolph Protocol . . . . .	93
7.3	Time-Bin Protocol . . . . .	96
7.4	Intrinsic Infidelities . . . . .	98
7.5	Fidelity Optimisation . . . . .	102
7.6	Fidelity Measures . . . . .	104
7.7	Experimental Approach . . . . .	106
7.8	Summary . . . . .	109
<b>8</b>	<b>Time-Bin Interferometer</b>	<b>111</b>
8.1	Theoretical Analysis . . . . .	112
8.2	Laser Scatter Rejection . . . . .	114
8.3	Timing Considerations . . . . .	115
8.4	Interferometer Characterisation . . . . .	116
8.5	Active Switching . . . . .	117
8.6	Frequency Filtering . . . . .	120
<b>9</b>	<b>Entanglement Measurement</b>	<b>121</b>
9.1	Experimental Pulse Sequence . . . . .	121
9.2	Calibration Measurements . . . . .	123
9.3	Two-Qubit Entanglement Results . . . . .	127
9.4	Three-Qubit Entanglement . . . . .	134
9.5	Discussion of Entanglement Experiment . . . . .	137
9.6	$g_2$ and Hong-Ou-Mandel Visibility . . . . .	139

<b>10 Entanglement Modelling</b>	<b>145</b>
10.1 Additional Errors . . . . .	145
10.2 Explaining Early/Late Asymmetry . . . . .	148
10.3 A Monte Carlo Simulation . . . . .	150
10.4 Monte Carlo Results . . . . .	156
10.5 Discussion . . . . .	162
<b>11 Conclusion and Outlook</b>	<b>163</b>
11.1 Outlook . . . . .	164
<b>A FPGA Architecture</b>	<b>167</b>
<b>B MW Phase Calibration</b>	<b>171</b>
<b>C Single Shot Readout</b>	<b>173</b>
<b>D Adiabatic Elimination</b>	<b>175</b>
<b>E Jones Matrices</b>	<b>179</b>
<b>F EOM Pulse Sequence Alignment</b>	<b>181</b>
<b>G Optical Loss Budget</b>	<b>183</b>



## List of abbreviations

<b>AOM</b> .....	Acousto optical modulator
<b>APD</b> .....	Avalanche photo detector
<b>BS</b> .....	Beamsplitter
<b>CW</b> .....	Continuous wave
<b>DAC</b> .....	Digital to analogue converter
<b>FPGA</b> .....	Field-programmable gate array
<b>FSR</b> .....	Free spectral range
<b>FWHM</b> .....	Full width at half maximum
<b>HWP</b> .....	Half-wave plate
<b>IR</b> .....	Infrared
<b>LED</b> .....	Light-emitting diode
<b>MC</b> .....	Monte Carlo (simulation)
<b>MW</b> .....	Microwave (signal)
<b>PLL</b> .....	Phase-locked loop
<b>PBS</b> .....	Polarising beamsplitter
<b>PCW</b> .....	Photonic crystal waveguide
<b>RF</b> .....	Radio frequency
<b>RT</b> .....	Resonant transmission
<b>SNSPD</b> .....	Superconducting nanowire single photon Detector
<b>TBI</b> .....	Time-bin interferometer
<b>TTL</b> .....	Transistor-transistor logic
<b>QD</b> .....	Quantum dot
<b>QWP</b> .....	Quarter-wave plate
<b>WG</b> .....	Waveguide
<b>WM</b> .....	Wavemeter



# 1 | Introduction

The development of quantum mechanics in the early half of the 20th century was decisive for the evolution of physics and our understanding of reality. Especially two phenomena stood out as being quintessential features of this new theory. First is the notion of superposition, by which a particle such as an electron or photon can occupy two distinct states simultaneously. As an example, the spin of an electron may be described by the wavefunction  $|\psi\rangle = c_1|\uparrow\rangle + c_2|\downarrow\rangle$ , where  $|\uparrow\rangle$  and  $|\downarrow\rangle$  denote the spin projection and  $c_1$  and  $c_2$  are complex probability amplitudes fulfilling  $|c_1|^2 + |c_2|^2 = 1$ . Only upon measurement does the superposition collapse, yielding  $|\uparrow\rangle$  or  $|\downarrow\rangle$ . Second is the concept of entanglement, in which two or more particles may be correlated in such a way that they cannot be described independently. If two spins are prepared in the entangled state  $|\psi\rangle = (|\uparrow\rangle|\uparrow\rangle + |\downarrow\rangle|\downarrow\rangle)/\sqrt{2}$ , measuring the first spin as  $|\uparrow\rangle$  immediately reveals the second spin to be  $|\uparrow\rangle$  as well, regardless of any spatial separation between the particles. Thanks to numerous experiments including experimental violations of Bell's inequalities [1, 2], the predictions of quantum mechanics were confirmed to an impressive degree. Additionally, it was realised that these counter-intuitive phenomena could have real-world applications. Discrete quantum states, such as the aforementioned spin, represent information. As opposed to a classical bit, which is either 0 or 1, a qubit (quantum bit) can be in an arbitrary superposition of  $|0\rangle$  and  $|1\rangle$ . The late 20th century saw the discovery of several quantum algorithms, which leveraged the superposition and entanglement of qubits to achieve speedups over classical algorithms. Notable examples include the Deutsch–Jozsa algorithm [3] and Grover's search algorithm [4]. In 1994, Peter Shor famously published his quantum algorithm for performing integer factorisation in polynomial time [5], thereby potentially breaking current public-key encryption schemes, which rely on classical computers' inability to perform efficient factorisation [6].

We currently live at the possible onset of a quantum revolution, as experimental advances allow a growing number of qubits to be controlled with increasing fidelity. A plethora of qubits currently exist, but this work will focus on the photon. Photons can encode information in their polarisation, frequency, number, spatial or temporal mode and are uniquely qualified for sending quantum information, as they can be transmitted through optical fibre or via satellites. This forms the basis of quantum key distribution protocols such as BB84 [7], whereby distant parties can construct a fundamentally secure cryptographic key by sending quantum information in the form of single photons. Recently, the notion of a quantum internet consisting of many quantum nodes connected by optical channels was put forth [8]. However,

sending photons over long distances is challenging due to optical losses, and the no-cloning theorem forbids simple amplification. This problem can be overcome with quantum repeaters which break down the full distance into smaller, manageable sections. Quantum repeaters either require nodes with long-lived quantum memories [9] or, as more recently proposed, sources of entangled photons. The latter approach, dubbed the all-photonic quantum repeater [10, 11], encodes information in a large entangled photonic cluster state, which acts as an error correction code for photon loss. The main challenge in this approach is deterministically generating large, high-fidelity multi-photon entangled states. Cluster states also form the basis for an alternative approach to quantum computing known as measurement-based quantum computing [12]. Hence, entangled photons serve as a resource for both computation and quantum repeaters.

Creating large, entangled photon states is, however, a formidable challenge. The most widely used approach is based on generating entangled photon pairs through spontaneous parametric down-conversion (SPDC) and subsequent interference of the photon pairs. Using this method, a recent state-of-the-art experiment demonstrated a 12 photon state [13]. SPDC sources are, however, limited in their efficiency due to their probabilistic nature, and scaling up this approach to generate more photons is therefore problematic. An alternative approach is to excite a single quantum emitter to create an on-demand supply of single photons. Addressing a single emitter and coupling its emission to a single mode is a key problem in quantum optics and quantum photonics. Manipulation of single emitters has been achieved with trapped ions [14], as well as solid-state emitters such as Nitrogen vacancy centres in diamond [15] and semiconductor quantum dots [16]. Solid-state emitters provide fast photon emission and can be integrated into photonic nanostructures allowing the light-matter interaction to be greatly enhanced. Especially quantum dots exhibit excellent optical properties including transform-limited linewidth [17] and  $> 96\%$  photon indistinguishability [18]. Furthermore, a single spin in the emitter can serve as an entangler of the emitted photons, thus directly producing an entangled state of one spin and many photons. This requires a highly coherent interface between spins and photons and excellent coherent spin control, which is made challenging by the noisy solid-state environment.

This thesis studies scalable spin-photon entanglement using quantum dot spins. A significant inspiration is Nethanel Lindner and Terry Rudolph's 2009 proposal [19] for a quantum dot source of multi-photon polarisation entanglement, which was experimentally realised in 2016 showing 3-qubit entanglement [20]. However, this work will take an alternative approach, opting to encode information in the photon emission time. This is done in an attempt to better exploit the photon and spin coherence properties and to utilize the power of photonic nanostructures. Crucially, we show that coherent spin control and optical cyclicity can be simultaneously achieved by embedding quantum dots in broadband photonic crystal waveguides. Using this approach, we measure a time-bin encoded spin-photon Bell state with 66% fidelity and observe signatures of entanglement for 3 qubits. By analysing the experimental errors, we deem the generation of far larger states realistic through improvements of the spin qubit, as demonstrated elsewhere.

This thesis is structured as follows:

Chapter 2 introduces the quantum dot, its basic optical and spin properties and the photonic crystal nanostructure.

Chapter 3 presents the experimental setup including details of the studied sample and the optical systems used for optical excitation and fluorescence analysis.

Chapter 4 details the spectroscopic methods used to identify QDs. The chapter also contains characterisation measurements of the main quantum dot including lifetime measurements of the metastable hole spin.

Chapter 5 considers how to induce optical cyclicity using a waveguide. Numerical simulations are analysed to assess the feasibility and a combination of spin pumping measurements and other spectroscopic techniques are used to experimentally estimate the cyclicity.

Chapter 6 describes the method of all-optical spin control and estimates the spin rotation fidelity and spin dephasing times.

Chapter 7 deals with the theory of multi-photon entanglement generation. Existing protocols including the Lindner-Rudolph protocol are analysed, and the time-bin entanglement protocol pursued in this thesis is discussed in great detail.

Chapter 8 describes the time-bin interferometer used for entanglement generation.

Chapter 9 contains the experimental measurements of 2 and 3 qubit entanglement and measurements of the photon purity and indistinguishability.

Finally, chapter 10 attempts to interpret the measured fidelity by simulating the entanglement using a Monte Carlo framework.

A conclusion and outlook is presented in chapter 11

The appendix includes experimental details on the FPGA architecture, microwave setup, pulse sequences and optical loss budget. Additionally, the appendix contains theoretical details on spin control, Jones matrices and single-shot readout.



## 2 | Theory

This chapter contains a basic introduction to quantum dots and spin physics. The phenomenology of a quantum dot is introduced, and methods of optical excitation and quantum dot charging will be discussed. The optical selection rules for trions will be derived with a special focus given to the orientation of the linear Voigt dipoles. The interaction with a classical laser is then introduced to explain the pulsed and continuous excitation schemes used in this work. The effects of phonons, voltage noise and nuclear spins will be discussed with an emphasis on the spin  $T_2^*$  times. Finally, the photonic crystal waveguide will be introduced.

### 2.1 THE QUANTUM DOT

A key experimental ability in quantum optics is exciting a single emitter and coupling the emitter to a single, well-defined optical mode. Achieving this for atoms and ions is difficult, requiring complex schemes for cooling, trapping and photon collection. An alternative approach is using solid-state emitters coupled to nanophotonic structures. The emitters used in this work are InAs/GaAs quantum dots (QDs). QDs are mesoscopic structures consisting of  $10^5$  atoms, yet their optical properties resemble single emitters, hence the nickname "artificial atom". A QD, see figure 2.1a, consists of a dome-shaped indium arsenide (InAs) crystal embedded inside a larger gallium arsenide (GaAs) crystal. The QD is typically  $\sim 20$  nm wide and  $\sim 5$  nm tall [21]. InAs and GaAs are both semiconductor materials. In semiconductors, electronic states are divided into valence bands and conduction bands, which are separated by a bandgap. However, the bandgaps of InAs and GaAs differ, as illustrated in figure 2.1b. This bandgap contrast creates a finite three-dimensional quantum well and the otherwise continuous electronic states give way to quantised states separated by a few meV. Inside the QD, the quantum state of a conduction band electron or a valence band hole (i.e. the absence of a valence band electron) consists of three parts: A large envelope function, giving the spatial extent of wavefunction, an electronic Bloch function, which inherits the symmetries of the atomic orbitals of the host material, and the particle's spin. The Bloch functions and spin component determine the optical selection rules while the envelope function contributes to the transition strength.

The lowest energy conduction band states have Bloch modes with s-like symmetry<sup>1</sup> and zero orbital angular momentum. Hence, the angular momentum is uniquely determined by the electron spin. Following the Pauli exclusion principle,

---

<sup>1</sup>s and p here refer to the orbitals known from atomic physics.

two electrons with spin projections  $S_z = \pm 1/2$  may occupy the same conduction band state.

By contrast, the valence bands contain a p-like Bloch function with  $J = 3/2$  angular momentum. These states are further divided into a heavy-hole (HH) band with  $J_z = \pm 3/2$  and a light hole (LH) band with  $J_z = \pm 1/2$ , which are normally degenerate. However, in a QD this degeneracy is lifted due to the increased quantum confinement along the z-direction [21], see figure 2.1c. As a result, the highest energy valence band states have a predominant heavy hole character and  $J_z = \pm 3/2$  angular momentum projection, where the z-direction is the direction of QD growth.

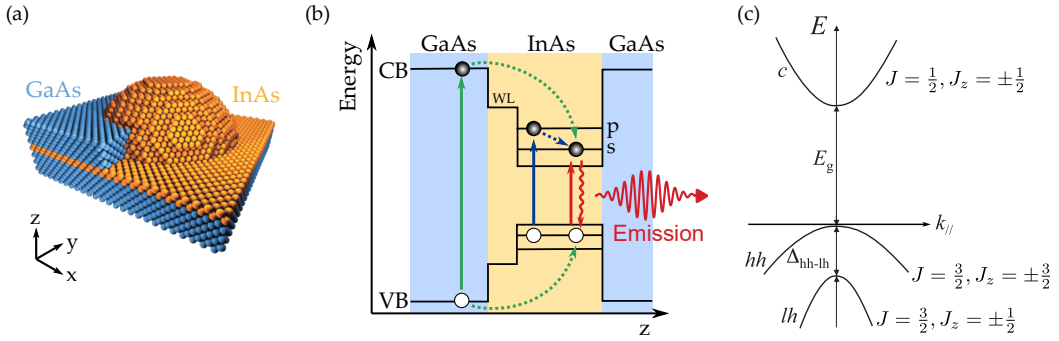


**Figure 2.1:** (a) Illustration of a single quantum dot: A dome-shaped cluster of InAs atoms are encased inside GaAs. In reality, the InAs is infused with some GaAs. (b) Valence band (VB) and conduction bands (CB) energies inside the QD. The reduced InAs bandgap gives rise to quantised electronic states (horizontal lines). Three methods of excitation are illustrated: Above-band (green), P-shell (blue) and resonant (red). All 3 methods result in an electron (black circle) bound to a hole (white circle). The electron-hole pair recombines under the emission of an infrared photon. (c) Band diagram of group  $III-V$  semiconductors. The conduction band (c) is split from the heavy hole (hh) valence band by the bandgap energy  $E_g$ . The light hole (lh) band is lowered by  $\Delta_{ll-hh}$  due to strain.

In a neutral QD, the valence band states are fully occupied and the conduction band states are empty. Exciting an electron to the conduction band creates a bound state between the conduction band electron and the valence band hole known as an exciton. After  $\sim 1$  ns this exciton decays, the hole and electron recombine, and a single photon is emitted. This process is highly efficient as InAs and GaAs both have a direct bandgap. Furthermore, the exciton has a large dipole owing to the QD size. The energy of the emitted photon depends on the bandgap and the confinement potential, leading to emission in the near-infrared ( $\approx 950$  nm in this study). This energy is below the GaAs band gap, allowing the photon to propagate through the surrounding material without absorption.

### 2.1.1 EXCITATION SCHEMES

In this work, three distinct types of optical excitation are applied. Firstly, an above-band (ABB) laser with a photon energy exceeding the GaAs bandgap may create excitons in the surrounding GaAs. An exciton may then "trickle" into the QD and

recombine radiatively. Secondly, a laser may excite an electron from the top valence band to the second conduction band state known as the P-shell. After a few ps [22], this state relaxes to the S-shell followed by a radiative decay. These shells are not to be confused with the s and p Bloch functions introduced earlier.

Finally, a laser may exactly match the energy of the transition. This is known as resonant excitation and is the main method used for quantum information processing as it conserves coherence. However, care must be taken to suppress the excitation laser, which overlaps spectrally with the emitted photon.

### 2.1.2 QUANTUM DOT GROWTH

Quantum dots are grown by depositing single monolayers of InAs on top of a flat GaAs wafer. As InAs has a 7% larger lattice constant than GaAs, it becomes energetically favourable for the InAs to contract into domes after only 1.5 monolayers. It is these islands that constitute the QDs. This growth process is known as the Stranski–Krastanov method and yields QDs with good optical properties. However, as a result of the spontaneous growth process, QDs are randomly scattered across the wafer and their optical wavelengths span a  $\approx 50$  nm range. The single InAs layer at the base of the QDs constitutes a continuum of electron states known as wetting layer states. However, the sample used in this work is grown by a modified method [23] in which coupling to this continuum is strongly suppressed. Despite not requiring optical trapping, QDs are operated at low temperatures, typically 4 K, to reduce phonon occupation and remove the thermal occupation of unwanted electronic states.

## 2.2 CHARGE STATES

A QD can be charged by adding electrons to the conduction band or removing valence band electrons resulting in holes. This is referred to as adding a charge carrier. By doing so one realises a stable matter qubit, as the charge carrier spin can be coherently manipulated. These spins can couple to the emitted photons, thus forming the basis for spin-photon entanglement and quantum information processing.

Control of the charge state can be achieved by embedding the QD in a thin diode structure known as a heterostructure. The heterostructure used in this work constitutes a p-i-n diode (figure 2.2) containing negatively (n) doped and positive (p) doped regions with the QD residing in the intrinsic (i) undoped region. This has the effect of fixing the Fermi level  $E_f$  to the n-doped back contact. By applying a bias voltage  $V_{\text{bias}}$  across the diode, the energy of the QD electronic states may be shifted. Reducing the energy of a single conduction band electron below  $E_f$  allows an electron to tunnel in from the back contact. The state with two electrons occurs at a higher  $V_{\text{bias}}$  because of the coulomb blockade [21]. Hence, a stable region exists where a single electron resides inside the QD. At the transitions between charge states, the electron is rapidly exchanged with the back contact (a process known as co-tunnelling) which has the effect of randomising the spin state. Charging the QD with a single hole is also possible using p-doped diodes such as the one in Ref. [24].

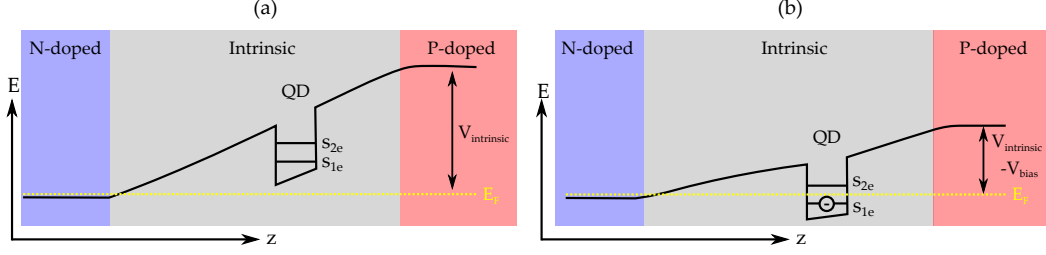


**Figure 2.2:** QD charging using a heterostructure. The conduction and valence band energies vary along the  $z$ -direction owing to the built in field and the applied bias. **(a)** The fermi energy  $E_f$  is below the conduction band, resulting in a neutral QD. **(b)** The conduction band is lowered below  $E_f$ , leading to a negatively charged QD.

However, the heterostructure in this work allows the creation of a metastable hole through optical induction as described in section 4.5.

Beyond controlling the QD charge, the applied  $V_{bias}$  has the effect of tuning the exciton and trion energies through the quantum-confined DC Stark shift [25]

$$\Delta E_{stark} = -pV_{bias} + \beta^2 V_{bias}^2, \quad (2.1)$$

where  $p$  is the permanent dipole and  $\beta$  is the polarisability. However, we only observe linear tunings with  $p$  in the range 0.5 GHz/mV to 0.75 GHz/mV. Stark tuning allows shifting the optical frequency, which may be useful for achieving resonance with a cavity or a second emitter [25].

## 2.3 SELECTION RULES

The selection rules of neutral and charged quantum dots under resonant excitation will now be described with a focus on spin systems in magnetic fields.

### 2.3.1 NEUTRAL QUANTUM DOT

The neutral QD may be excited to the neutral exciton  $X^0$  consisting of an electron and a hole with opposite spin orientations,  $|\uparrow\downarrow\rangle$  or  $|\downarrow\uparrow\rangle$  where  $|\uparrow\rangle$  ( $|\downarrow\rangle$ ) denotes an up(down) electron spin and  $|\uparrow\rangle$  ( $|\downarrow\rangle$ ) denotes an up(down) heavy hole spin. The exciton states with  $J_z = \pm 1$  can be excited with a circular laser polarisation according to angular momentum conservation, e.g.  $|0\rangle \xrightarrow{\sigma^+} |\downarrow\uparrow\rangle$ . However, reduced QD symmetry leads to an exchange interaction between the electron and hole spins [26] and the energy eigenstates are superpositions of the form  $|\downarrow\uparrow\rangle \pm |\uparrow\downarrow\rangle$  leading to two linear dipoles as illustrated in figure 2.3. The two excitons are split by a fine structure splitting (FSS) of a few GHz. Minimizing the FSS is hugely important for exploiting the biexciton cascade as a source of entangled photon pairs [27]. However, in this work, the FSS is mainly prevalent in QD spectroscopy.

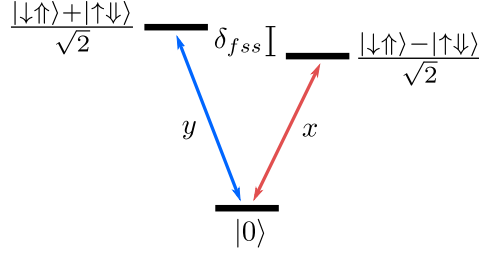


**Figure 2.3:** Energy level diagram of the neutral exciton. The neutral QD  $|0\rangle$  may be excited via orthogonal linear dipoles to two excitonic states split by the fine structure splitting  $\delta_{fss}$ .

### 2.3.2 CHARGED QDs

We will now consider the level structure and selection rules of a negatively charged QD. The ground state containing one electron can be optically excited to a negative trion state  $X^-$  consisting of a hole spin and two electrons in a singlet configuration. The optical dipole coupling a conduction band state to a valence band state can be compactly expressed as [28]

$$\mathbf{d} \propto (\mathbf{e}_x - i\mathbf{e}_y) (|+3/2\rangle\langle+1/2| - \kappa |+1/2\rangle\langle-1/2|) + (\mathbf{e}_x + i\mathbf{e}_y) |-3/2\rangle\langle-1/2| - \kappa |-1/2\rangle\langle+1/2|, \quad (2.2)$$

where  $\mathbf{e}_x, \mathbf{e}_y$  are the x,y unit vectors and  $|J_z\rangle\langle S_z|$  is the projection operator between the electron state with spin projection  $S_z$  and the trion state with total angular momentum projection  $J_z$ . Equation (2.2) also contains transition dipoles for the light hole components, which are weighted by  $\kappa$  to reflect a different dipole strength. In the absence of hole mixing (i.e. no light hole component), (2.2) allows the circularly polarised transitions  $|1/2\rangle \rightarrow |3/2\rangle$  and  $|-1/2\rangle \rightarrow |-3/2\rangle$  with opposite helicities.

In the absence of a magnetic field, the ground states and trions are both degenerate. The trion's singlet electrons have zero angular momentum and don't couple to a magnetic field. Applying a magnetic field thus only affects the electron (e) ground state and the trion hole (h) through the Hamiltonians [28]

$$\hat{H}_B^e = \frac{\mu_B g_e}{2} \mathbf{B} \cdot \vec{\sigma}, \quad (2.3)$$

$$\hat{H}_B^h = \mu_B g_0 \left[ \underbrace{\kappa \mathbf{B} \cdot \hat{\mathbf{J}}}_{\text{Zeeman term}} + \underbrace{q \hat{J}_x^3 B_x + \hat{J}_y^3 B_y + \hat{J}_z^3 B_z}_{\text{Non-zeeman term}} \right], \quad (2.4)$$

where  $\mu_B$  is the Bohr magneton,  $\mathbf{B}$  is the magnetic field,  $g_e \sim -0.5$  is the electron g-factor,  $\vec{\sigma} = (\hat{\sigma}_x, \hat{\sigma}_y, \hat{\sigma}_z)$  is the vector of Pauli operators,  $g_0 \approx 2$  is the free electron g-factor,  $\hat{\mathbf{J}}$  is the spin-3/2 operator and  $q$  and  $\kappa$  are material properties<sup>2</sup> with  $q \ll \kappa$ .

Applying a z-direction magnetic field (known as Faraday geometry) yields simple selection rules:  $\hat{H}_B^e$  and  $\hat{H}_B^h$  break the electron and trion degeneracy but retain

<sup>2</sup>In GaAs:  $\kappa = 1.1$ ,  $q = 0.01$ . In InAs:  $\kappa = 7.68$ ,  $q = 0.04$ , [29].

the  $|J_z\rangle$  and  $|S_z\rangle$  states as eigenstates. As a consequence, the circular dipoles remain. In reality, a weak cross-transition (see figure 2.4a) couples the two manifolds due to a light hole component in the trions<sup>3</sup>. Decays via this transition ( $\approx 1\%$  of the main transition) enable optical spin pumping [30]. The Faraday geometry is not considered further in this work, as it does not allow optical spin rotations.

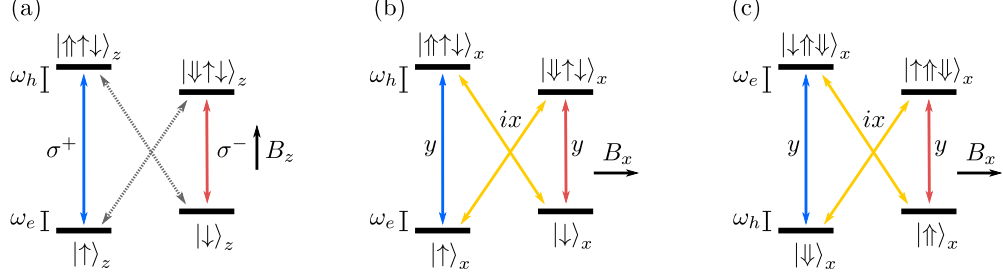


**Figure 2.4:** Level diagrams of charged QDs in a magnetic field. **(a)** Negatively charged QD in a  $z$ -magnetic field resulting in two circularly polarised dipoles. The diagonal transitions (gray) are largely forbidden. **(b)** Negatively charged QD in an in-plane magnetic field, resulting in 4 equally strong linear dipoles. **(c)** Positively charged QD in an in-plane magnetic field. The selection rules are the same as in (b), but the Zeeman splittings are swapped between ground and excited states.

Applying a magnetic field in the  $xy$ -plane (known as Voigt geometry) is more involved, but deserves theoretical attention as the selection rules will play an important role. Taking the magnetic field as  $\mathbf{B} = B(\cos(\phi), \sin(\phi), 0)$ , (2.3) can be rewritten as

$$\hat{H}_B^e = \frac{\mu_B g_e B}{2} \begin{bmatrix} 0 & e^{-i\phi} \\ e^{i\phi} & 0 \end{bmatrix}, \quad (2.5)$$

with the basis states  $|+1/2\rangle$  and  $|-1/2\rangle$ . The resulting eigenstates are

$$|\Phi_e^\pm\rangle = (\pm e^{-i\phi/2} |+1/2\rangle + e^{i\phi/2} |-1/2\rangle) / \sqrt{2}. \quad (2.6)$$

Regarding the hole spin eigenstates, the situation is more complicated. For  $q = 0$ , the heavy hole states with  $J_z = \pm 3/2$  are not coupled by (2.4), i.e.  $\langle +\frac{3}{2} | H_B^h | -\frac{3}{2} \rangle = 0$ , which implies degenerate trions. This is however not the case experimentally. A coupling can be introduced either via  $q > 0$  in (2.4) or by considering light hole-heavy hole mixing, giving the new hole states

$$|\psi_h^\pm\rangle \propto |\pm 3/2\rangle - (\gamma^\pm / \Delta_{hh-lh}) |\mp 1/2\rangle, \quad (2.7)$$

where  $\Delta_{hh-lh}$  is the heavy hole-light hole splitting and  $\gamma^\pm = \gamma e^{\pm 2i\theta}$  is a strain coupling with the phase  $\theta$  depending on the strain direction. These new hole states are still predominantly of heavy hole nature,  $|\gamma^\pm / \Delta_{hh-lh}|^2 \ll 1$ , but can couple to each other via the Zeeman term in (2.4) thanks to the light hole components. Regardless

<sup>3</sup>A low  $B_z$ , the diagonal transitions are additionally opened by the transverse components of the Overhauser field [30]

of the mechanism, the trion eigenstates can be written as a phase superposition

$$|\Phi_h^\pm\rangle = (\pm e^{-i\phi_h/2} |3/2\rangle + e^{i\phi/2} |-3/2\rangle)/\sqrt{2}, \quad (2.8)$$

where we have neglected the light hole component. Inserting (2.6) and (2.8) into (2.2) then yields the dipoles

$$\mathbf{d}_{outer} = \langle \Phi_h^+ | \mathbf{d} | \Phi_e^+ \rangle = \langle \Phi_h^- | \mathbf{d} | \Phi_e^- \rangle = \frac{1}{2} [\cos(\varphi) \mathbf{e}_x + \sin(\varphi) \mathbf{e}_y], \quad (2.9)$$

$$\mathbf{d}_{inner} = \langle \Phi_h^- | \mathbf{d} | \Phi_e^+ \rangle = \langle \Phi_h^+ | \mathbf{d} | \Phi_e^- \rangle = \frac{i}{2} [-\sin(\varphi) \mathbf{e}_x + \cos(\varphi) \mathbf{e}_y], \quad (2.10)$$

with  $\varphi = (\phi_h - \phi)/2$ .  $\mathbf{d}_{outer}$  and  $\mathbf{d}_{inner}$  correspond to the "outer" and "inner" transitions in figure 2.4b. They are linear and fulfill  $\mathbf{d}_{outer} \cdot \mathbf{d}_{inner} = 0$ . If the hole-splitting is dominated by  $q$ ,  $\phi_h = \pi - \phi$ , and the linear dipoles will thus follow the direction of  $\mathbf{B}$  [28]. However, if the hole-splitting is dominated by the hole-mixing in (2.7), then  $\phi_h = \phi + \theta$  and the linear dipoles will be locked along the strain angle  $\theta$ . Thus, depending on the regime, the dipoles may either follow the magnetic field or be locked. In the case of shear strain, the linear polarisation will follow the  $[110]$  or  $[1\bar{1}0]$  crystal axes [28].

Regardless of the underlying mechanism, the hole spin will be treated as a pseudo spin-1/2 particle governed by

$$\hat{H}_B^h = \mu_B \mathbf{B} \bar{\mathbf{g}}_h \vec{\sigma}_h / 2, \quad (2.11)$$

where  $\bar{\mathbf{g}}_h$  is the effective hole spin g-factor tensor and  $\vec{\sigma}$  is the vector of Pauli matrices acting on the hole spin.  $\bar{\mathbf{g}}_h$  is assumed diagonal with  $g_{h,z} > g_{h,x}, g_{h,y} > 0$ . The Zeeman splittings in figure 2.4b are then given by

$$\omega_e = \mu_B B_x |g_{e,x}| / \hbar, \quad (2.12)$$

$$\omega_h = \mu_B B_x g_{h,x} / \hbar, \quad (2.13)$$

where  $\omega_e > \omega_h$  is universally observed.

If the QD is instead charged with a single hole, the excited states are given by positive trions  $X^+$  consisting of a single electron and a hole spin singlet. As the hole singlet does not couple to  $\mathbf{B}$ , the Hamiltonians and selection rules remain the same, except that the level structure is flipped such that the ground state contains the smaller  $\omega_h$  splitting, see figure 2.4c. However, as will be discussed shortly, electrons and holes have different coherence properties.

To summarise: Applying an in-plane magnetic field Zeeman splits the ground and trion states. The selection rules, which are identical for the  $X^-$  and  $X^+$  systems, result in four equally strong optical dipoles with orthogonal linear polarisations. This results in two  $\Lambda$ -systems, which will later be used for optical spin control.

## 2.4 RESONANT EXCITATION

We will now consider three important cases of interaction with a single resonant laser: A continuously driven two-level system, a two-level system under pulsed excitation and a continuously pumped three-level system resulting in optical spin pumping. This section will focus strictly on the results necessary to interpret the experimental results. Ref. [31] which will be cited frequently and is an excellent reference for the details omitted here. The analysis of the four-level Raman scheme used for coherent spin rotations is reserved for section 6.2.

### 2.4.1 TWO LEVEL EMITTER

A fundamental interaction in quantum optics is a 2-level emitter interacting with a classical field (ie. a monochromatic laser) given by  $\mathbf{E}(t) = \mathbf{E}_0 \cos(\omega t)$ , where  $\mathbf{E}_0$  contains the electric field magnitude and polarisation and  $\omega$  is the angular laser frequency. The emitter, with ground state  $|g\rangle$  and excited state  $|e\rangle$ , has the bare Hamiltonian

$$\hat{H}_0 = \hbar\omega_0 |e\rangle\langle e|, \quad (2.14)$$

where  $\hbar\omega_0$  is the energy of the excited state. The coupling with the laser field is given by

$$\hat{H}_I = -\hat{\mathbf{d}} \cdot \mathbf{E}(t), \quad (2.15)$$

where  $\hat{\mathbf{d}}$  is the emitter dipole operator which can be written in terms of the ground and excited state:

$$\hat{\mathbf{d}} = q \langle g|\hat{\mathbf{r}}|e\rangle |g\rangle\langle e| + q \langle e|\hat{\mathbf{r}}|g\rangle |e\rangle\langle g|, \quad (2.16)$$

where  $q$  is the electron charge and  $\hat{\mathbf{r}}$  is the electron displacement operator.

These Hamiltonians can be simplified by applying a rotating wave-approximation and transforming to a rotating frame at frequency  $\omega$  to yield the effective 2-level Hamiltonian [31]

$$\hat{H}_{2lvl} = \Delta |e\rangle\langle e| + \frac{\hbar\Omega}{2} (|e\rangle\langle g| + |g\rangle\langle e|), \quad (2.17)$$

where  $\Delta = \omega_0 - \omega$  is the laser detuning from resonance, and  $\Omega = -\frac{\langle e|\hat{\mathbf{d}}|g\rangle \cdot \mathbf{E}_0}{\hbar}$  is the Rabi frequency, which has been assumed real without loss of generality. Note that  $\Omega$  depends on the projection of the electric field onto the transition dipole. Henceforth, we will set  $\hbar = 1$ .

It is now possible to solve the dynamics. The most convenient method to include the radiative decay of  $|e\rangle$  is to adopt a master equation approach whereby the radiation modes into which the emitter may decay into are traced out. The system is then described by the density operator  $\hat{\rho}$  with dynamics given by the Lindblad

master equation [31]

$$\frac{d}{dt}\hat{\rho} = -i[\hat{H}, \hat{\rho}] + \sum_j \left[ \hat{C}_j \hat{\rho} \hat{C}_j^\dagger - (\hat{C}_j^\dagger \hat{C}_j \hat{\rho} + \hat{\rho} \hat{C}_j^\dagger \hat{C}_j)/2 \right], \quad (2.18)$$

where the  $\hat{C}_j$  are a series of collapse operators representing couplings to a bath. A radiative decay from  $|e\rangle$  corresponds to  $\hat{C}_1 = \sqrt{\gamma}|g\rangle\langle e|$  where  $\gamma$  is the decay rate and the inverse of the excited state lifetime. Solving (2.18) with  $\hat{C}_1$  and the Hamiltonian in (2.17) yields the equations of motion, also known as the optical Bloch equations:

$$\dot{\rho}_{ee} = 1 - \dot{\rho}_{gg} = -\gamma\rho_{ee} + i\frac{\Omega}{2}(\rho_{eg} - \rho_{ge}), \quad (2.19)$$

$$\dot{\rho}_{ge} = \dot{\rho}_{eg}^* = -i\Delta\rho_{ge} - i\frac{\Omega}{2}(\rho_{ee} - \rho_{gg}) - (\gamma/2)\rho_{ge}, \quad (2.20)$$

where the dot superscript denotes a time derivative. The steady state solution yields the excited state population

$$\bar{\rho}_{ee} = \frac{\Omega^2}{2\Omega^2 + \gamma^2 + 4\Delta^2}, \quad (2.21)$$

where the bar denotes steady state. This result, although simple, has several important implications, as the emitted fluorescence is proportional to  $\gamma\bar{\rho}_{ee}$ . Firstly, it is not possible to create a population inversion,  $\lim_{\Omega \rightarrow \infty} \bar{\rho}_{ee} = 1/2$ . Secondly,  $\bar{\rho}_{ee}$  follow a Lorentzian lineshape with a full width half maximum (FWHM) given by

$$\Delta_{FWHM} = \sqrt{\gamma^2 + 2\Omega^2}. \quad (2.22)$$

In the limit  $\Omega \rightarrow 0$ , the linewidth (in angular frequency) is simply  $\gamma$ . This is referred to as the transform-limited linewidth. In practice, the actual linewidth is typically broadened by noise. Increasing  $\Omega$  leads to additional power broadening. It is often convenient to express  $\Omega$  through the optical power  $P$  and a saturation power  $P_{sat}$ :

$$\Omega = \gamma\sqrt{P/P_{sat}}. \quad (2.23)$$

This scaling follows from  $\Omega \propto E$  and  $P \propto E^2$ , where  $E$  is the electric field. Inserting (2.23) into (2.21) yields

$$\bar{\rho}_{ee} = \frac{P/P_{sat}}{1 + 2P/P_{sat} + 4\Delta^2/\gamma^2}. \quad (2.24)$$

Hence, at  $P = P_{sat}$  and  $\Delta = 0$ ,  $\bar{\rho}_{ee} = 1/3$ . The simple form of (2.24) allows  $\Omega$  to be determined experimentally.

### 2.4.2 PULSED EXCITATION

A crucial operation for the generation of single photons is the pulsed resonant excitation of a QD starting in  $|g\rangle$ . A pulse of duration  $T_p \ll \gamma^{-1}$  is used to excite the QD before it can decay, after which a single photon is created under spontaneous

emission. In the absence of emission,  $\gamma = 0$ , the Bloch equations can be analytically solved following a square pulse of duration  $T_p$ :

$$\rho_{ee}(T_p) = \frac{\Omega^2}{\sqrt{\Omega^2 + \Delta^2}} \sin^2 \left( \frac{1}{2} T_p \sqrt{\Omega^2 + \Delta^2} \right), \quad (2.25)$$

Perfect population inversion is possible when  $\Delta = 0$  (laser resonance) and the pulse area  $\Omega T_p$  equals  $\pi$ . This condition is known as a  $\pi$ -pulse. After excitation, the excited state decays according to

$$\rho_{ee}(t) = e^{-\gamma t}, \quad t \geq 0. \quad (2.26)$$

The realistic case of a Gaussian pulse shape and  $\gamma > 0$  is solved numerically in section 10.3.3. The single-photon properties in terms of purity and indistinguishability are introduced and measured in section 9.6.

## 2.5 THREE LEVEL SPIN PUMPING

Adding a second ground state enables many new operations, as the ground states can now be used as a qubit (the exciton makes a poor qubit due to its short lifetime). One important operation is deterministically preparing the QD in one of the ground states. This can be achieved by optical pumping as illustrated in figure 2.5. A y-polarised laser resonant with  $|1\rangle \leftrightarrow |2\rangle$  creates a population in  $|2\rangle$ .  $|2\rangle$  may then decay *vertically* to  $|1\rangle$  with rate  $\gamma_y$  or *diagonally* to  $|0\rangle$  with rate  $\gamma_x$ . Once the QD has decayed to  $|0\rangle$  the QD goes dark<sup>4</sup> as  $|0\rangle$  is uncoupled from the remaining states due to the ground state splitting  $\omega_g$ . This process allows preparation of  $|0\rangle$  as well as conditional spin readout, as fluorescence is (ideally) only generated given the initial state  $|1\rangle$ . Thus, detecting fluorescence from  $|2\rangle \rightarrow |1\rangle$  heralds  $|1\rangle$  as the initial state.

The decay rates  $\gamma_x, \gamma_y$  sum to the trion decay rate,  $\gamma_x + \gamma_y = \gamma_0$ , and fulfil  $\gamma_x = \gamma_y$  in a homogeneous medium and Voigt geometry [21]. A crucial point of this thesis is demonstrating an unequal  $\gamma_y \gg \gamma_x$  induced via an inhomogeneous photonic environment. This asymmetry is quantified by the optical cyclicity

$$C = \frac{\gamma_y}{\gamma_x}. \quad (2.27)$$

As  $C$  can be estimated by measuring  $\gamma_x$  through optical pumping, we now carefully derive the optical pumping rate from a master equation following our previously published derivation in Ref. [32]. In the rotation frame of the laser, the system is governed by the Hamiltonian

$$\hat{H} = \Delta |2\rangle\langle 2| - \omega_g |0\rangle\langle 0| + \frac{\Omega}{2} (|1\rangle\langle 2| + |2\rangle\langle 1|). \quad (2.28)$$

<sup>4</sup>The term dark state will be used loosely and is not limited to the coherent dark states resulting from coherent population trapping.

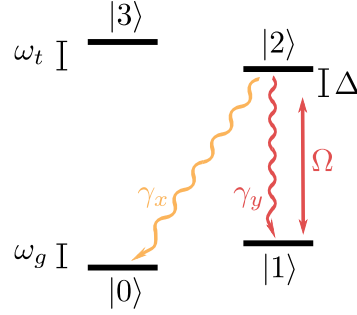


**Figure 2.5:** Level diagram for optical spin pumping. A pump laser populates  $|2\rangle$  until population decays to  $|0\rangle$  after which the QD goes dark. The level  $|3\rangle$  is assumed far detuned.

Level  $|3\rangle$  is neglected on account of the detuning  $\Delta_0 = \omega_g + \omega_t \gg \gamma_0$  where  $\omega_g(\omega_t)$  is the ground state(trion) splitting. Furthermore, the laser coupling between  $|0\rangle \leftrightarrow |2\rangle$  is assumed zero on account of the laser polarisation.

The two decay channels are included through the collapse operators

$$\hat{C}_1 = \sqrt{\gamma_y} |1\rangle\langle 2|, \quad (2.29)$$

$$\hat{C}_2 = \sqrt{\gamma_x} |3\rangle\langle 2|. \quad (2.30)$$

Inserting (2.28, 2.29 2.30) into (2.18) yields the equations of motion

$$\dot{\rho}_{11} = i\frac{\Omega}{2}(\rho_{12} - \rho_{21}) + \gamma_y \rho_{22}, \quad (2.31)$$

$$\dot{\rho}_{22} = -i\frac{\Omega}{2}(\rho_{12} - \rho_{21}) - \gamma_0 \rho_{22}, \quad (2.32)$$

$$\dot{\rho}_{12} = i\frac{\Omega}{2}(\rho_{11} - \rho_{22}) + (i\Delta - \gamma_0/2)\rho_{12}, \quad (2.33)$$

$$\dot{\rho}_{21} = -i\frac{\Omega}{2}(\rho_{11} - \rho_{22}) + (-i\Delta - \gamma_0/2)\rho_{21}, \quad (2.34)$$

$$\dot{\rho}_{00} = \gamma_x \rho_{22}, \quad (2.35)$$

The  $\rho_{10}$  and  $\rho_{20}$  elements are disregarded as there is no coherent coupling to the  $|0\rangle$  state in our approximation.

We then adiabatically eliminate the coherences by setting  $\dot{\rho}_{12} = \dot{\rho}_{21} = 0$  giving the relations

$$\rho_{12} = \frac{-i\frac{\Omega}{2}(\rho_{11} - \rho_{22})}{i\Delta - \gamma_0/2}, \quad (2.36)$$

$$\rho_{21} = \frac{i\frac{\Omega}{2}(\rho_{11} - \rho_{22})}{-i\Delta - \gamma_0/2}. \quad (2.37)$$

This step corresponds to assuming that oscillations between  $|1\rangle$  and  $|2\rangle$  dampen out much faster than population decays to  $|3\rangle$ , which is valid in the limit  $\gamma_0 \gg \gamma_x$ .

Inserting (2.36-2.37) into (2.31-2.35) yields new equations of motion:

$$\dot{\rho}_{11} = -W\rho_{11} + (W + \gamma_y)\rho_{22}, \quad (2.38)$$

$$\dot{\rho}_{22} = W\rho_{11} - (W + \gamma_0)\rho_{22}, \quad (2.39)$$

$$\dot{\rho}_{00} = \gamma_x\rho_{22}, \quad (2.40)$$

where we have defined the rate  $W = \frac{\Omega^2\gamma_0}{4\Delta^2 + \gamma_0^2}$ . This system of differential equations can be solved analytically with the initial conditions  $\rho_{11}(0) = 1, \rho_{22}(0) = \rho_{00}(0) = 0$  corresponding to the QD being initialized in  $|1\rangle$ . In the interest of brevity, we only consider  $\rho_{22}(t)$  as this is the quantity proportional to the fluorescence intensity and thus the quantity measured in the experiment.

$$\rho_{22}(t) = \frac{W}{\lambda} \left( e^{-t(W + \gamma_0/2 - \lambda/2)} - e^{-t(W + \gamma_0/2 + \lambda/2)} \right), \quad (2.41)$$

with

$$\lambda = \sqrt{4W(W + \gamma_y) + \gamma_0^2}. \quad (2.42)$$

The second exponential term in (2.41) has a very fast decay rate and represents states  $|1\rangle$  and  $|2\rangle$  reaching an internal equilibrium. In contrast, the first exponential term represents the slow pumping into  $|0\rangle$  and we thus associate this rate with the spin pumping rate:

$$\gamma_{osp} = W + \frac{\gamma_0}{2} - \frac{1}{2}\sqrt{4W(W + \gamma_y) + \gamma_0^2} \quad (2.43)$$

$$= \frac{1}{2}(2W + \gamma_0) - \frac{1}{2}\sqrt{(2W + \gamma_0)^2 - 4\gamma_x W}, \quad (2.44)$$

where we used  $\gamma_y = \gamma_0 - \gamma_x$ . Finally, we Taylor expand around  $\gamma_x = 0$  to first order to find

$$\gamma_{osp} = \frac{\gamma_x W}{2W + \gamma_0} = \frac{\gamma_x \Omega^2}{2\Omega^2 + 4\Delta^2 + \gamma_0^2}. \quad (2.45)$$

Perhaps unsurprisingly,  $\gamma_{osp}$  saturates according to the 2-level system in (2.21). This is a consequence of the (in our case experimentally valid) assumption  $\gamma_y \gg \gamma_x$  yielding an effective 2-level system with a small leakage from the excited state. In reality, optical Rabi oscillations between  $|1\rangle$  and  $|2\rangle$  will appear at the onset of a sharp pumping pulse with  $\Omega > \gamma_0$ . This feature is lost by performing the adiabatic elimination. However, the result in (2.45) is sufficient for describing the measured exponential decay resulting from optical pumping.

In practice, one cannot perfectly prepare  $|0\rangle$ . A ultimate limit is set by driving  $|0\rangle \rightarrow |3\rangle$  which repumps  $|1\rangle$ , see figure 2.5. Additional repumping is achieved by driving  $|0\rangle \rightarrow |2\rangle$ . Finally, spin-flips with rate  $\kappa$  may couple the ground states.

## 2.6 NOISE SOURCES

Several noise source exists as a consequence of the QD's solid-state environment. This section discusses broadening from phonons and the DC-Stark shift.

### 2.6.1 PHONONS

Phonons are vibrations in the crystal lattice and may couple to the QD excitonic states via the deformation potential [33]. This leads to two distinct forms of broadening.

Firstly, elastic phonon scattering leads to a broadening of the zero-phonon line. This scattering occurs on a  $\sim 100$  ps timescale [33] and is commonly represented as a pure dephasing rate  $\gamma_d \approx 0.05 \text{ ns}^{-1}$  (estimated in section 7.5) and thus a source of Markovian decoherence. This broadens the Lorentzian lineshape, and the FWHM from (2.22) is modified according to [31]

$$\Delta_{FWHM} = \sqrt{(\gamma + 2\gamma_d)^2 + 2 \left(1 + 2\frac{\gamma_d}{\gamma}\right) \Omega^2}. \quad (2.46)$$

More importantly, dephasing results in a loss of photon indistinguishability [33] and, in the entanglement protocol, as loss of fidelity (see section 7.4.2). A common strategy for reducing the impact of pure dephasing is to reduce the  $\gamma_d/\gamma$  ratio by Purcell enhancing  $\gamma$ .

Secondly, inelastic phonon scattering may take place where the QD either absorbs or emits a phonon during its radiative decay. Phonon emission is most prevalent at low temperatures leading to the formation of a broad, red-detuned sideband in the emission spectrum. This sideband contains 5-10% of the emission intensity [16] and can easily be removed by spectral filtering, thus increasing the photon indistinguishability. The magnitude of phonon scattering depends on the QD size, temperature and, as shown in Ref. [33], the mechanical properties of the environment, i.e. the nanostructure.

### 2.6.2 CHARGE NOISE

The DC-stark shift (2.1) also constitutes a broadening mechanism as voltage noise (from the voltage source or charge traps in the surrounding material) inhomogeneously broadens the optical transitions. As the voltage noise is typically on the millisecond time scale [34] it can be treated as static (non-Markovian) on the timescale of all other dynamics. Hence, inhomogeneous in this context refers to the single emitter's resonance frequency shifting from shot to shot. We assume the noise-induced frequency shift  $\delta_s$  follows a normal distribution

$$\mathcal{N}(\delta_s; \sigma) = \frac{e^{-\delta_s^2/(2\sigma^2)}}{\sqrt{2\pi}\sigma}, \quad (2.47)$$

where  $\sigma$  is the standard deviation. The excited state population is then a convolution of the Lorentzian line shape in (2.24) with (2.47):

$$\langle \bar{\rho}_{ee} \rangle = \int_{-\infty}^{\infty} d\delta_s \frac{\Omega^2}{2\Omega^2 + \gamma^2 + 4(\Delta + \delta_s)^2} \mathcal{N}(\delta_s; \sigma), \quad (2.48)$$

where  $\langle \rangle$  denotes an ensemble average and the laser detuning is  $\Delta + \delta_s$ . This lineshape is known as a Voigt profile, and can be more conveniently written as

$$V(\Delta, \gamma, \sigma) = \int_{-\infty}^{\infty} d\delta_s L(\Delta + \delta_s; \gamma) \mathcal{N}(\delta_s; \sigma) \quad (2.49)$$

where  $L$  is a Lorentzian with FWHM  $\gamma$ . Voigt profiles are ubiquitous in spectroscopy, as there is almost always some noise present from charge noise or, as will be discussed in section 2.8, nuclear noise. Slow charge noise and fast noise from phonons thus result in different spectral characteristics, although they are hard to distinguish in practice. The integral in (2.49) must be evaluated numerically, but the resulting linewidth can be approximated [35] with great accuracy by

$$f_V \approx 0.5346 f_L + \sqrt{0.2166 f_L^2 + f_G^2}, \quad (2.50)$$

where  $f_L$  is the Lorentzian FWHM,  $f_G^2 = 2\sqrt{2\ln(2)}\sigma \approx 2.355\sigma$  is the Gaussian FWHM and  $f_V$  is the Voigt FWHM.

## 2.7 SPIN COHERENCE

The concept of spin coherence and  $T_2^*$  time will now be briefly introduced before introducing spin echo in section 6.4.1. Consider a spin-1/2 system in a magnetic field governed by the Hamiltonian

$$\hat{H} = (\omega_g + \delta\omega_g) \hat{\sigma}_z / 2 = \frac{\omega_g + \delta\omega_g}{2} (|0\rangle\langle 0| - |1\rangle\langle 1|), \quad (2.51)$$

where  $\omega_g$  is the ground state splitting given by the magnetic field,  $\delta\omega_g$  is a random perturbation (i.e. noise) of the splitting,  $\hat{\sigma}_z$  is the Pauli z-operator and  $|0\rangle, |1\rangle$  are the two spin eigenstates. A superposition state such as  $|+\rangle = (|0\rangle + |1\rangle)/\sqrt{2}$  will then precess on the Bloch sphere equator at the Larmor frequency  $\omega_g + \delta\omega_g$ . It is often convenient to transform to a frame rotating at frequency  $\omega_g$ . This can be done with the transformation  $\hat{U}(t) = e^{it(\omega_g/2)\hat{\sigma}_z}$  yielding a Hamiltonian in the rotation frame following [36]

$$\hat{\hat{H}} = i\dot{\hat{U}}(t)\hat{U}(t)^\dagger + \hat{U}(t)\hat{H}\hat{U}(t)^\dagger \quad (2.52)$$

$$= \delta\omega_g \hat{\sigma}_z / 2. \quad (2.53)$$

In the rotation frame the state only precesses at the perturbation frequency. Solving the time dependent Schrödinger equation for a constant  $\delta\omega_g$  and initial state

$|\psi(0)\rangle = |+\rangle$  yields the solution

$$\sqrt{2}|\psi(t)\rangle = e^{i\delta\omega_g t/2}|0\rangle + e^{-i\delta\omega_g t/2}|1\rangle. \quad (2.54)$$

If the noise  $\delta\omega_g$  is constant over the relevant experimental time scales but varies from shot to shot, one can write the ensemble averaged state using the density matrix formalism. If we assume  $\delta\omega_g$  to follow a normal distribution, as in (2.47), the ensemble averaged state is

$$2\hat{\rho}(t) = 2 \int_{-\infty}^{\infty} d\delta\omega_g |\psi(t)\rangle \langle\psi(t)| \mathcal{N}(\delta\omega_g; \sigma) \quad (2.55)$$

$$= |0\rangle\langle 0| + |1\rangle\langle 1| + \int_{-\infty}^{\infty} d\delta\omega_g \left( e^{i\delta\omega_g t} |0\rangle\langle 1| + e^{-i\delta\omega_g t} |1\rangle\langle 0| \right) \frac{e^{-\delta\omega_g^2/(2\sigma^2)}}{\sqrt{2\pi}\sigma} \quad (2.56)$$

$$= |0\rangle\langle 0| + |1\rangle\langle 1| + e^{-\sigma^2 t^2/2} (|0\rangle\langle 1| + |1\rangle\langle 0|) \quad (2.57)$$

$$= |0\rangle\langle 0| + |1\rangle\langle 1| + e^{-(t/T_2^*)^2} (|0\rangle\langle 1| + |1\rangle\langle 0|). \quad (2.58)$$

Hence, the off-diagonal coherence terms experience a Gaussian decay with the characteristic time

$$T_2^* = \frac{\sqrt{2}}{\sigma}, \quad (2.59)$$

where  $\sigma$  is the standard deviation of the ground state splitting. This is referred to as inhomogeneous dephasing. Inhomogeneous refers to the inhomogeneous ensemble distribution of  $\delta\omega_g$  and dephasing refers to the fact that coherences are lost but populations and hence  $\langle\hat{\sigma}_z\rangle$  are unaltered. This process will also be referred to as a non-Markovian dephasing, as the noise is slow and correlated. This allows rephasing of the spin using spin-echo (section 6.4.1). Finally, spin-flips between  $|0\rangle$  and  $|1\rangle$  (such as electron co-tunnelling) result in a  $T_1$  time, which is the time scale over which a population inversion decays.

## 2.8 NUCLEAR ENVIRONMENT

In addition to the Zeeman splitting arising from the external magnetic field  $\mathbf{B}_{\text{ext}}$ , the charge carrier spin is perturbed by a hyperfine coupling to the  $\sim 10^5$  nuclear spins over which its wavefunction extends. Indium has spin 9/2 while both Ga and As have spin 3/2 (independent of isotope) [37]. This interaction dominates the dephasing of the electron spin and, to a lesser degree, the hole spin.

The problem of a central spin coupling to a large number of nuclear spins contains incredibly rich physics and the treatment here will focus on explaining the spin  $T_2^*$  times.

### 2.8.1 ELECTRON SPIN COHERENCE

The electron spin  $\hat{\mathbf{S}}$  couples to  $N$  nuclear spins  $\hat{\mathbf{I}}_j$  through the Fermi contact hyperfine interaction [30]

$$H_{hf}^e = \frac{\nu_0}{8} \sum_{j=1}^N A_e^j |\Psi_e(\mathbf{R}_j)|^2 (\hat{\mathbf{I}}_j \cdot \hat{\mathbf{S}}), \quad (2.60)$$

where  $\nu_0$  is the crystal unit cell volume,  $\Psi_e(\mathbf{R}_j)$  is the electron envelope function evaluated at the  $j$ 'th nucleus and  $A_e^j$  is the electron spin hyperfine coupling strength. This interaction occurs when the charge carrier has a non-zero wavefunction at the nuclei, which is true of the conduction band electron.

The nuclear spins are not polarised by  $\mathbf{B}_{\text{ext}}$  due to their weak magnetic moment ( $1000\times$  weaker than the electron). This enables a convenient semi-classical approximation [30], where the QD spin experiences an effective magnetic field, the Overhauser field  $\mathbf{B}_{\text{OH}}$ :

$$\mathbf{B}_{\text{OH}} = \frac{\nu_0}{8} \frac{\bar{A}}{g_e \mu_B} \left\langle \sum_i \hat{\mathbf{I}}_i \right\rangle, \quad (2.61)$$

where  $\bar{A}$  is the mean hyperfine coupling strength. In other words, the Overhauser field is a mean-field approximation of the hyperfine coupling. As a consequence of the unpolarised spin bath, the Overhauser field can be taken to follow a normal distribution [30]

$$P(\mathbf{B}_{\text{OH}}) = \frac{1}{B_N^3 (2\pi)^{3/2}} \exp\left(-\frac{|\mathbf{B}_{\text{OH}}|^2}{2B_N^2}\right), \quad (2.62)$$

where  $B_N$  is the standard deviation along a single axis<sup>5</sup> and is in the range 11 mT to 23 mT [37].  $P(\mathbf{B}_{\text{OH}})$  has predominantly low frequency noise [37] and is taken to be quasi static, i.e. constant over experimental time scales. This approximation, also known as the frozen fluctuation model, provides a good model of the  $T_2^*$  processes.

Equation (2.62) implies the need for an external magnetic field  $|\mathbf{B}_{\text{ext}}| \gg B_N$  to ensure constant selection rules. Applying a large  $\mathbf{B}_{\text{ext}}$ , e.g. in the x-direction, has the effect of suppressing the transverse components of  $\mathbf{B}_{\text{OH}}$ , see figure 2.6. The total magnetic field  $\mathbf{B}_{\text{tot}} = \mathbf{B}_{\text{OH}} + \mathbf{B}_{\text{ext}}$  then has magnitude

$$|\mathbf{B}_{\text{tot}}| = \sqrt{(B_{\text{ext}} + B_{\text{OH}}^{\parallel})^2 + (B_{\text{OH}}^{\perp})^2} \approx B_{\text{ext}} + B_{\text{OH}}^{\parallel} + \frac{(B_{\text{OH}}^{\perp})^2}{2B_{\text{ext}}}, \quad (2.63)$$

where  $B_{\text{OH}}^{\parallel}$  ( $B_{\text{OH}}^{\perp}$ ) are the Overhauser components parallel(perpendicular) to  $\mathbf{B}_{\text{ext}}$ . In (2.63) we assumed  $B_{\text{OH}}^{\parallel}, B_{\text{OH}}^{\perp} \ll B_{\text{ext}}$  to expand in  $B_{\text{OH}}^{\perp}$  to lowest order. In this limit, fluctuations in  $|\mathbf{B}_{\text{tot}}|$  are dominated by parallel fluctuations with standard

<sup>5</sup>Note that some papers including Ref. [37] instead define the RMS of  $|\mathbf{B}_{\text{OH}}|$ , which is  $\sqrt{3}$  times larger than  $B_N$ .

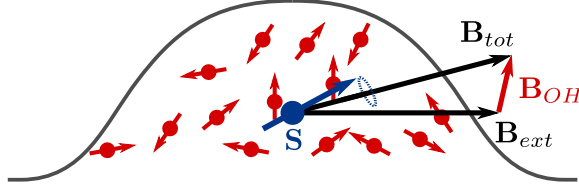


**Figure 2.6:** Graphical representation of the Overhauser field. The electron (blue) precesses around the total magnetic field  $\mathbf{B}_{\text{tot}}$  created by the external magnetic field  $\mathbf{B}_{\text{ext}}$  and the Overhauser field  $\mathbf{B}_{\text{OH}}$  originating from the randomly oriented nuclear spins (red).

deviation  $B_N$ . Using (2.12), the fluctuation of the electron splitting  $\omega_e$  becomes

$$\delta\omega_e = \sigma_{OH} = \frac{\mu_B g_e B_N}{\hbar}. \quad (2.64)$$

Inserting into (2.59) then yields

$$T_2^* = \frac{\sqrt{2}}{\sigma_{OH}} = \frac{\sqrt{2}\hbar}{\mu_B g_e B_N}, \quad (2.65)$$

which yields  $T_2^* = 2.1$  ns for  $g_e = 0.5$  and  $B_N = 15$  mT, which agrees with most experiments [38–40]. In summary, the electron  $T_2^*$  is limited by low frequency components of the Overhauser field produced by the randomly oriented host nuclei.  $\sigma_{OH}$  has the additional effect of broadening the optical lines by  $\sigma_{OH}/(2\pi) \approx 110$  MHz according to (2.64) and  $B_N = 15$  mT.

Applying a spin-echo scheme (described in section 6.4.1) extends the usable coherence time. However, to properly describe the  $T_2$  time one must consider the nuclear spin precession as demonstrated in Ref. [40]. Schemes for reducing  $B_N$  have been experimentally demonstrated [39, 41]. Here, the optically manipulated electron is used to cool the nuclear spin bath leading to an electron spin  $T_2^* = 39$  ns [39].

## 2.8.2 HOLE SPIN COHERENCE

Hole spin dephasing is conceptually similar to electron spin dephasing. However, the hyperfine coupling is anisotropic and additional dephasing arises from charge noise. As discussed, the hole spin mainly consists of heavy holes states with p-like orbitals. These orbitals go to zero at the nuclei and the Fermi contact interaction (2.60) vanished. Heavy holes may still couple to nuclear spins via the weaker dipole-dipole interaction [24]

$$H_{hf}^h = \frac{\nu_0}{8} \sum_{j=1}^N A_{h,z}^j |\Psi_h(\mathbf{R}_j)|^2 I_z^j S_z \quad (2.66)$$

where  $S_z$  is the hole pseudo-spin z-projection,  $\Psi_h$  is the hole envelope function and the hole hyperfine coupling strength  $A_{h,z}^j$  compares to the electron's by  $A_{h,z}^j/A_e^j \approx -0.10$  [24].  $H_{hf}^h$  only results in an Overhauser field along the z-direction which can

efficiently be suppressed with an in-plane magnetic field following the arguments in section 2.8.1. It is thus strongly preferential to operate hole spins in the Voigt geometry. In reality, the non-zero light hole component (introduced in section 2.3.2) experiences the Fermi contact interaction, thus giving an Overhauser field in all 3 dimensions.

Additional noise arises from the hole spin's voltage-dependent  $g$ -factor. Applying an electric field  $F_z$  along  $z$  (as is done in this work by varying  $V_{\text{bias}}$ ) shifts the hole wavefunction's centre of mass [29]. Due to a varying indium concentration along the growth direction, this modulates a number of material properties and thus  $g_h$ . The Zeeman splitting in (2.12) implies that noise on  $F_z$  translates to noise on  $\omega_h$ :

$$(\delta\omega_h)_{\text{electric}} = \frac{B_{\text{ext}}\mu_B}{\hbar} \frac{\partial g_h}{\partial F_z} \delta F_z, \quad (2.67)$$

where  $\partial g_h/\partial F_z$  is the  $g$ -factor tuning and  $\delta F_z$  is the electric field noise. This naturally motivates the development of low noise structure. In summary, three terms contribute [42] to the perturbation of  $\omega_h$  when applying a  $\mathbf{B} = B_x^{\text{ext}}\hat{\mathbf{e}}_x$  external magnetic field:

$$\hbar(\delta\omega_h)_{\text{tot}} = \underbrace{B_x^{\text{ext}}\mu_B \frac{\partial g_{h,x}}{\partial F_z} \delta F_z}_{\text{Electric field noise}} + \underbrace{B_x^{\text{OH}}\mu_B g_{h,x}}_{\text{Parallel overhauser}} + \underbrace{\frac{(B_z^{\text{OH}})^2}{2B_x^{\text{ext}}}\mu_B g_{h,x}}_{\text{Perpendicular overhauser}}, \quad (2.68)$$

where  $B_x^{\text{OH}}$  and  $B_z^{\text{OH}}$  are the Overhauser  $x$  and  $z$  components, respectively, and depend on the amount of hole mixing and other QD properties. To calculate  $T_2^*$  the three components in (2.68) can be assumed independent and added in quadrature to estimate the standard deviation of  $\delta\omega_h$ . Note that the three terms in (2.68) scale as  $(B_x^{\text{ext}})^1$ ,  $(B_x^{\text{ext}})^0$  and  $(B_x^{\text{ext}})^{-1}$ , which implies an optimal value of  $B_x^{\text{ext}}$ . Such an optimum was observed with Ramsey measurements in Ref. [42], where  $T_2^*$  peaked around 70 ns for  $B_x^{\text{ext}} = 4$  T. Longer  $T_2^*$  estimates up to 460 ns at  $B_{\text{ext}} = 3$  T were reported in Ref. [24] but differed by estimating  $T_2^*$  from coherent population trapping measurements. Regardless, the hole can achieve a significantly longer  $T_2^*$  than the electron with nuclear spin manipulation, making it an attractive candidate for quantum information processing.

## 2.9 PHOTONIC NANOSTRUCTURE

A key challenge of photonic quantum information processing is coupling a quantum emitter to a single, well-defined mode. Solid-state emitters such as QDs are uniquely qualified for this, as they can be placed inside photonic nanostructures with feature sizes below the optical wavelength, allowing the light/matter interaction to be tailored to a high degree.

Nanostructures can be divided into two general categories: Cavities and waveguides (WGs). Cavities, such as micropillar cavities and photonic crystal cavities, provide strong light-matter interaction by forming cavity modes with low mode volume (on the order of  $\lambda^3$ ) and high Q-factors [16]. This thesis, however, will focus on employing waveguides, specifically photonic crystal waveguides (PCWs).

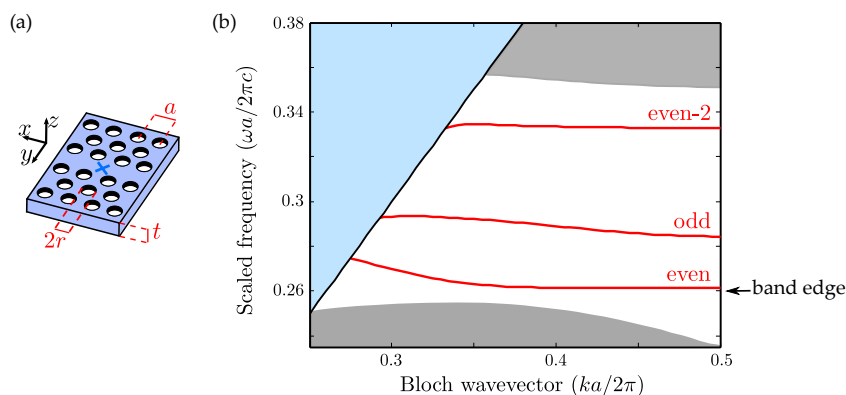


**Figure 2.7:** (a) Schematic of a PCW with lattice constant  $a$ , hole radius  $r$  and thickness  $t$ . (b) PCW Band diagram of a GaAs PCW with  $r = a/3$  and  $t = 2a/3$ . The 3 TE-like modes are drawn and labelled according to the symmetry of the  $y$  electric field component. The lowest frequency mode is the one of interest and exhibits a slow group velocity  $\omega$  near the band edge. Below the band edge, the waveguide ceases to transmit. Gray regions denote slab modes. The blue area denotes radiation modes, ie. out-of-plane propagation. Figures adapted from Ref. [16].

Figure 2.7 illustrates a PCW consisting of a thin GaAs membrane. A periodic lattice of air holes in the membrane act as a periodic modulation of the refractive index  $n$  ( $n_{GaAs} = 3.5$ ,  $n_{air} = 1$ ). This leads to Bragg scattering of light and the optical modes in a photonic crystal are given by Bloch modes, similar to those observed for electrons in a solid-state crystal lattice. A result of this is the formation of a photonic bandgap. Within this bandgap, light cannot propagate inside the membrane. However, removing a single line of holes from the crystal forms a defect in which a discrete number of guided modes can propagate, see figure 2.7. These modes propagate along the  $x$ -direction and are tightly confined in the  $y$ -direction due to Bragg scattering. The main modes of interest are TE-like modes, where the electric field is in the  $xy$ -plane. In practice, only the lowest mode in figure 2.7 needs to be considered, as QDs will be far detuned from the higher-order modes. Thus, the PCW can be treated as being a truly single-mode 1D system, where light propagation is described by a single  $\mathbf{k}$  vector.

Despite the photonic crystal only extending in two dimensions, coupling to the outside radiation modes is suppressed through total internal reflection. Due to the refractive index contrast between air and GaAs, an emitter placed inside the membrane may only couple to a narrow cone of  $k$ -vectors centred around the  $z$ -axis. Thus, the coupling to the continuum of optical modes found in free space and the crystal membrane (also called slab modes) is suppressed, causing the PCW to be the dominant mode into which an emitter radiates. Once emitted, a photon will propagate freely down the WG mode without being reabsorbed by the emitter. The waveguide mode is broadband, although the emitter frequency plays a role through the group index (introduced shortly).

The rate at which an emitter undergoes spontaneous emission is governed by the optical mode density as seen by the emitter and is captured by the local density of states (LDOS). The LDOS may be calculated from the waveguide modes, and, most importantly for our purposes, results in a modification of the radiative decay rate

$$\gamma = \frac{\pi\omega}{\hbar\epsilon_0} |\mathbf{d}|^2 \rho(\omega, \mathbf{r}_0, \hat{\mathbf{e}}_{\mathbf{d}}), \quad (2.69)$$

where  $\omega$  is the optical frequency of the dipole,  $\epsilon_0$  is the vacuum permittivity,  $|\mathbf{d}|$  is the magnitude of the optical dipole,  $\mathbf{r}_0$  is the emitter position,  $\hat{\mathbf{e}}_{\mathbf{d}}$  is the dipole unit vector and  $\rho$  is the LDOS. More conveniently, The LDOS can be re-expressed as a Purcell factor  $F_P$ , which describes the decay rate relative to the rate in a homogeneous medium  $\gamma^{hom}$ :

$$F_P(\mathbf{r}_0, \omega, \hat{\mathbf{e}}_{\mathbf{d}}) = \frac{\gamma(\mathbf{r}_0, \omega, \hat{\mathbf{e}}_{\mathbf{d}})}{\gamma^{hom}(\omega)} \propto \rho(\omega, \mathbf{r}_0, \hat{\mathbf{e}}_{\mathbf{d}}). \quad (2.70)$$

An key feature of a PCW is its highly dispersive nature. Close to the band edge (see figure 2.7) the group velocity  $v_g = \partial\omega/\partial k$  strongly decreases leading to a so-called slow-light regime. This increases the LDOS (more  $\mathbf{k}$ -vectors pr  $\omega$  loosely speaking). An ideally position dipole will experience a WG-induced Purcell factor of [16]

$$F_P^{max}(\omega) \propto n_g(\omega), \quad (2.71)$$

where  $n_g = c/v_g(\omega)$  is the group index. In principle,  $n_g$  diverges at the band-edge. However, this is not experimentally achievable due to fabrication imperfections [43]. Furthermore, the decay dynamics will no longer be markovian (which has thus far been assumed). Values of  $n_g = 50$  has been observed in GaAs PCWs containing QDs [44] correspond to  $F_P = 10$ . The band edge frequency depends on the PCW parameters and can be tailored to the emitter. The  $F_P$  generated by a PCW thus depends on the emitter detuning from the bandedge and, as will be explored in section 5.1, the emitter position and dipole orientation.

An important factor used to quantify the WG coupling is the  $\beta$ -factor,

$$\beta = \frac{\gamma_{wg}}{\gamma_{wg} + \gamma_{ng} + \gamma_{nr}}, \quad (2.72)$$

containing decay rates  $\gamma$  into the waveguide mode (wg), non-guided modes (ng) and non-radiative decays. Hence,  $\beta$  represents the probability of emission into the guided mode.  $\beta = 98.4\%$  has been for a PCW embedded QD [44] as a consequence of the combined inhibition of non-guided modes and enhancement of the guided mode. A high  $\beta$  is the starting point for near-unity collection efficiency but also implies near-deterministic light-matter interaction. By virtue of time-reversal symmetry, a photon propagating in the PCW mode will scatter off the emitter with probability  $\beta$ . If the light-matter interaction is fully coherent and the photon is resonant with the optical dipole, the emitter will radiate  $\pi$  out of phase with the incident field, and the incident photon will be fully reflected. The transmission (with respect to power) of a 1D-waveguide containing a single two-level emitter is given by [45]

$$T = 1 - \frac{\gamma}{\gamma/2 + \gamma_d}\beta + \frac{\gamma}{\gamma + 2\gamma_d}\beta^2, \quad (2.73)$$

in the limit of low power, no detuning and photon bandwidth  $\ll \gamma$ .  $\gamma$  is the radiative decay rate and  $\gamma_d$  is a pure dephasing rate, typically due to the phonon scattering discussed in section 2.6.1.  $T = 0$  for  $\beta = 1$  and  $\gamma_d = 0$ . This important result will be used for spectroscopy in section 4.1, but also leads to exciting non-linear light-matter interactions [45].



## 3 | Experimental Setup

This section describes the experimental setup and relevant equipment. We start by introducing the sample and briefly describe its fabrication. Next, the four laser systems used to excite the QD are described with emphasis on pulse generation and control. The optical setup for combining excitation lasers and detecting fluorescences is presented, and the techniques for measuring waveguide transmission and resonant excitation are described. Finally, the systems for detection and spectral filtering are covered.

### 3.1 SAMPLE

All measurements in this thesis (with the exception of section 6.1) were performed using the same sample. The sample consists of a thin membrane grown on top of a GaAs substrate using molecular beam epitaxy. Figure 3.1a shows the 180 nm-thin membrane which constitutes a p-i-n diode heterostructure with a QD layer in the centre. The extreme thinness is required to ensure single-mode operation of the waveguides, and the QD must be centred to maximize coupling to TE modes. Electric contacts connect to the p and n doped regions allowing QD charging and tuning via the DC stark shift (section 2.2). The contacts are fabricated by vapour deposition of a gold alloy and reactive ion etching is used to form vias to the n-layer. Features of the heterostructure include an AlAs cap on top of the QD layer which reduces coupling to the electron wetting layer states [23]. Additionally, an AlGaAs tunnelling barrier on top of the QD layer reduces the device current to  $\sim$  nA for the  $V_{\text{bias}}$  required to achieve the relevant charge states. The addition of this barrier was

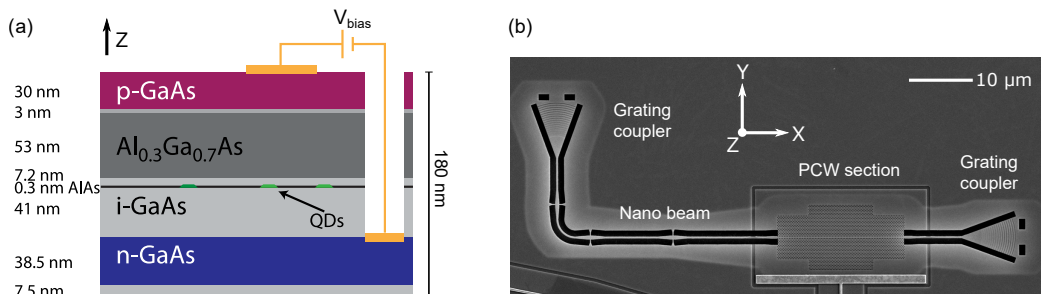


**Figure 3.1:** (a) p-i-n diode heterostructure. Electric contacts are shown in gold. Figure adapted directly from Ref. [18]. (b) SEM image of photonic crystal waveguide.

motivated by the desire to reduce non-radiative exciton recombination through tunnelling. This was indeed successful, as demonstrated by the extremely low blinking measured in Ref. [18]. However, this barrier may be the reason why hole spins are unable to tunnel into the QD as will be investigated in section 4.5. More sample details can be found in Ref. [18].

Photonic nanostructures are created by the process described in Ref. [46]. The structures are defined using electron beam lithography and material is removed through reactive ion etching. Hence, the holes in a PCW are formed by etching through the membrane in figure 3.1a. A sacrificial layer below the heterostructure is also etched causing the membrane to be suspended in air. Figure 3.1b shows a scanning electron microscope (SEM) image of the PCW structure used. The specific PCWs measured here used a lattice constant  $a = 250$  nm and hole radius  $r = 68$  nm. The PCWs are fabricated along the crystallographic axes with the  $x$ -axis in figure 3.1b corresponding to the  $[110]$  or  $[\bar{1}\bar{1}0]$  axes (where  $[001]$  is the growth direction). Both sides of the PCW are coupled to shallow etch grating couplers via nanobeam waveguides. The couplers are described in Ref. [47] and consist of a periodic modulation of the membrane thickness. This results in a diffraction grating which scatters the travelling WG mode out-of-plane in a linearly polarised, near-gaussian mode. The coupler emission propagates at an  $8.4^\circ$  angle with respect to the  $z$ -axis allowing collection without a high NA objective. In Ref. [47] a 60% WG-to-fibre coupling efficiency was measured with a 43 nm -3dB bandwidth.

## 3.2 LASER SYSTEMS

The four laser systems depicted in figure 3.2a will now be introduced.

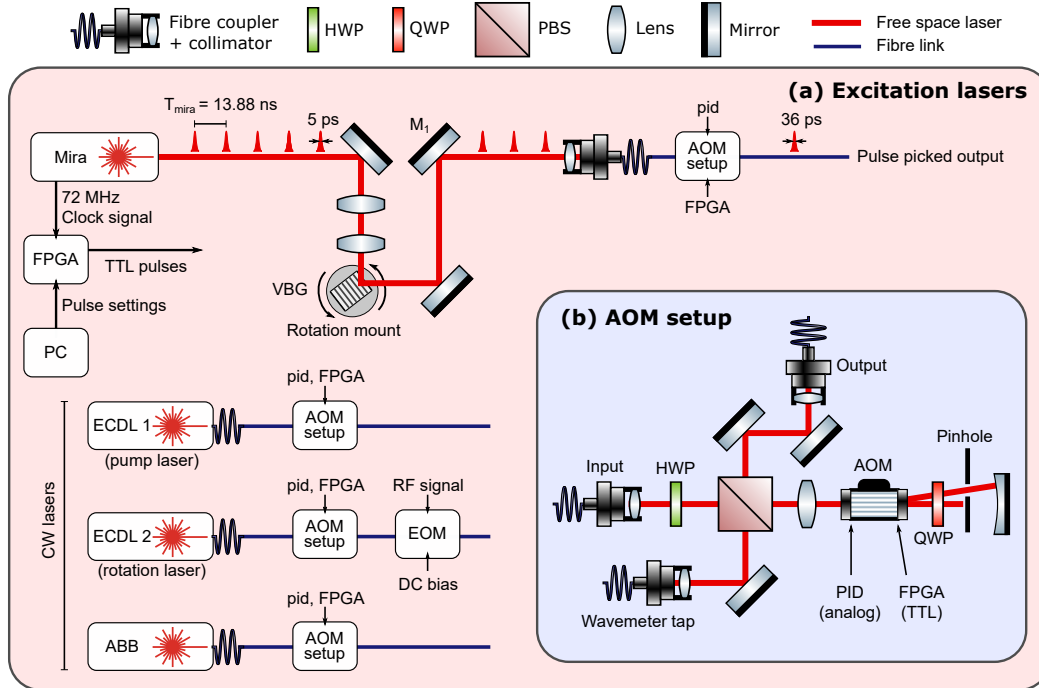


**Figure 3.2:** (a) Laser systems. The Mira generates a train of short pulses which are stretched by a volume Bragg grating (VBG) and pulse picked using an AOM. An FPGA is synchronised to the Mira and sends control pulses to the modulators. 3 CW lasers are modulated with separate AOM setups and EOMs. (b) Diagram of the double pass AOM setup used for power stabilisation, pulse picking and creating pulses from a CW laser. Abbreviations:  $\lambda/2$  plate (HWP),  $\lambda_4$  plate (QWP), polarising beamsplitter (PBS)

### 3.2.1 MODE-LOCKED LASER

A mode-locked Ti:Sapphire laser<sup>1</sup> (henceforth referred to as Mira) is used to generate resonant  $\pi$ -pulses and P-shell excitation. The pulses have a 234 pm (78 GHz) bandwidth (figure 3.3) corresponding to a  $\approx 4$  ps FWHM duration (assuming a bandwidth-limited  $\text{sech}^2$  pulse). To achieve the optimal bandwidth for entanglement generation, the pulses are stretched using a volume Bragg grating<sup>2</sup> (VBG) which reflects the different frequency components into different angles. The central frequency is coupled into a fibre and can be tuned by rotating the VBG and, to a finer degree ( $\sim 200$  MHz precision), using the  $M_1$  mirror in figure 3.2a. The stretched pulse bandwidth is estimated using a spectrometer yielding a raw 44 pm bandwidth, see figure 3.3. Correcting for the 24 pm instrument response of the spectrometer and assuming a non-chirped Gaussian pulse (as promised by the

<sup>1</sup>Coherent Mira 900 P.

<sup>2</sup>Supplied by OptiGrate.

manufacturer) yields a 12.4 GHz FWHM and a 35.6 ps FWHM pulse duration. The central frequency is resolved on a wavemeter which offers greater resolution than the spectrometer.

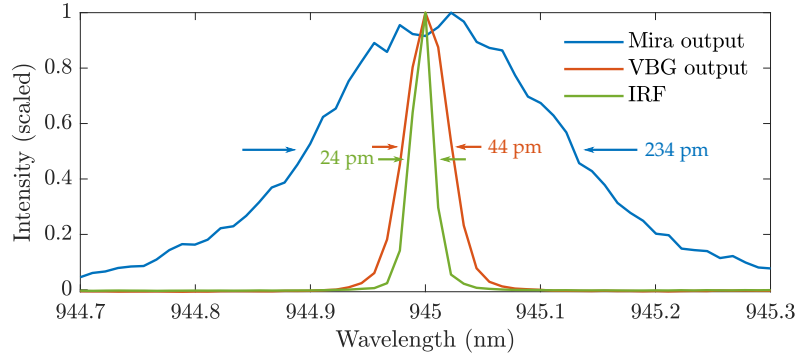


**Figure 3.3:** Spectra of the unstretched Mira pulse and the VBG output measured on a spectrometer. IRF denotes the spectrometer instrument response function measured with an ECDL laser. FWHM values are derived from Gaussian fits (not shown).

### 3.2.2 SYNCHRONISATION AND PULSE PICKING

The Mira produces a constant 72.04 MHz train of optical pulses ( $T_{\text{Mira}} = 13.88$  ns repetition time). However, exciting the QD with the full pulse train is often undesirable, and it is thus necessary to employ pulse picking. This is achieved with the acousto optical modulator (AOM) setup in figure 3.2b. Here, the incoming light is focused using a 35 mm lens to a small spot size inside the AOM<sup>3</sup>. When the AOM is on, light is diffracted into the first-order mode which transmits through a pinhole and is reflected back into the AOM. Having passed through a  $\lambda/4$ -plate twice, the doubly diffracted light is reflected by the PBS and coupled into an output fibre. Using a TTL pulse, the diffraction efficiency can be modulated with an 8 ns rise time. This is used to generate pulsed from CW lasers and, in the case of the Mira, to transmit specific optical pulses from the pulse train. Additionally, an analogue signal delivered from a PID-controller changes the AOM modulation depth and hence the diffraction efficiency. This is used to stabilize the laser power over a 1 kHz bandwidth.

Naturally, pulse picking requires the AOM modulation to be synchronised to the pulse train. This is accomplished using a field-programmable gate array (FPGA). The FPGA delivers TTL signals to the pulse picking AOM and is phase-locked to the pulse train using the output of a fast photodiode, which is exposed to the pulse train. The TTL pulse shape is carefully optimised to realise an extinction of  $\sim 1000$  between two subsequent Mira pulses. We use a Cyclone V FPGA from Intel, which runs a completely custom architecture, which is elaborated in appendix A. In addition to performing pulse picking, the FPGA drives all the optical modulators in figure 3.2a and delivers synchronisation pulses to the timetagger (section 3.4).

<sup>3</sup>MT250-800 from AA Optics with 250 MHz RF driver.

### 3.2.3 CONTINUOUS WAVE LASERS

Two narrowband continuous wave (CW) lasers are used to resonantly excite the QD. Both are extended cavity diode lasers<sup>4</sup> (ECDLs) with  $< 10$  kHz linewidth and continuously tunable wavelength. The laser frequencies are stabilised to an external wavemeter. ECDL 1 is primarily used for spin initialisation and readout and is referred to as the *pump laser*. By applying another AOM setup with 8 ns rise time (same as in figure 3.2b) pumping pulses are generated by modulating the AOM with TTL pulses from the FPGA. ECDL 2 is primarily used as a *rotation laser* for coherent optical spin control. It passes through an AOM for slow power stabilisation and a fibre-coupled Mach-Zehnder based electro optical intensity modulator<sup>5</sup> (EOM). The EOM is used to generate sidebands for spin control (section 6.2.1) but is also used in section 5.2 to generate sharp resonant pumping pulses. When modulated with a square wave, the EOM has a maximal measured extinction of 1300. As the EOM input power is limited to 25 mW, it is advantageous to place it after the lossy AOM setup.

Finally, a fibre-pigtailed 830 nm diode laser<sup>6</sup> is used as an above-band (ABB) laser which plays the role of creating hole spins. The laser is pulsed using an AOM (30 ns rise time) but is not stabilised in frequency.

### 3.2.4 JUSTIFICATIONS FOR A MODE-LOCKED LASER

A mode-locked laser, despite necessitating pulse stretching and intricate synchronisation, is deemed necessary for two reasons. Firstly, the  $\sim 30$  ps pulse duration required for the entanglement generation is on the limit of what is achievable with EOMs. Secondly, a high extinction is needed to avoid driving the QD between pulses. Consider a modulator with an extinction  $\xi$  between peak power and leakage power. A  $\pi$ -pulse requires a peak Rabi frequency  $\Omega_p$  and duration  $T_p$  fulfilling  $T_p\Omega_p = \pi$  (section 2.4.2). The laser leakage will then result in a Rabi frequency of  $\Omega_{\text{leakage}} = \Omega_p/\sqrt{\xi} = \pi/(T_p\sqrt{\xi})$ , where the square root of  $\xi$  is taken due to  $\Omega$  scaling as the electric field. For values of  $T_p = 30$  ps and  $\xi = 1000$  (state-of-the-art-for an EOM),  $\Omega_{\text{leakage}} = 3.3 \text{ ns}^{-1}$ , which will be enough to saturate most QDs. In contrast, a mode-locked laser has near-perfect extinction.

---

<sup>4</sup>DL pro from Toptica and CTL from Toptica.

<sup>5</sup>NIR-MX800-LN lithium niobate modulator from Ix-Blue.

<sup>6</sup>LPS-830-FC from Thorlabs.

### 3.3 OPTICAL SETUP

The sample is held at a temperature of 4.2 K inside a closed cycle cryostat<sup>7</sup>. The sample sits near the cryostat base (figure 3.4a) inside in a 50 mbar helium atmosphere, which transports heat from the sample to a cold finger. The sample is mounted horizontally (growth direction along the optical axis) on top of three piezo stages used for positioning. Above, a 0.81 NA apochromatic objective (focal length 2.91 mm) is used to image the sample. The QD is manipulated by up to four lasers

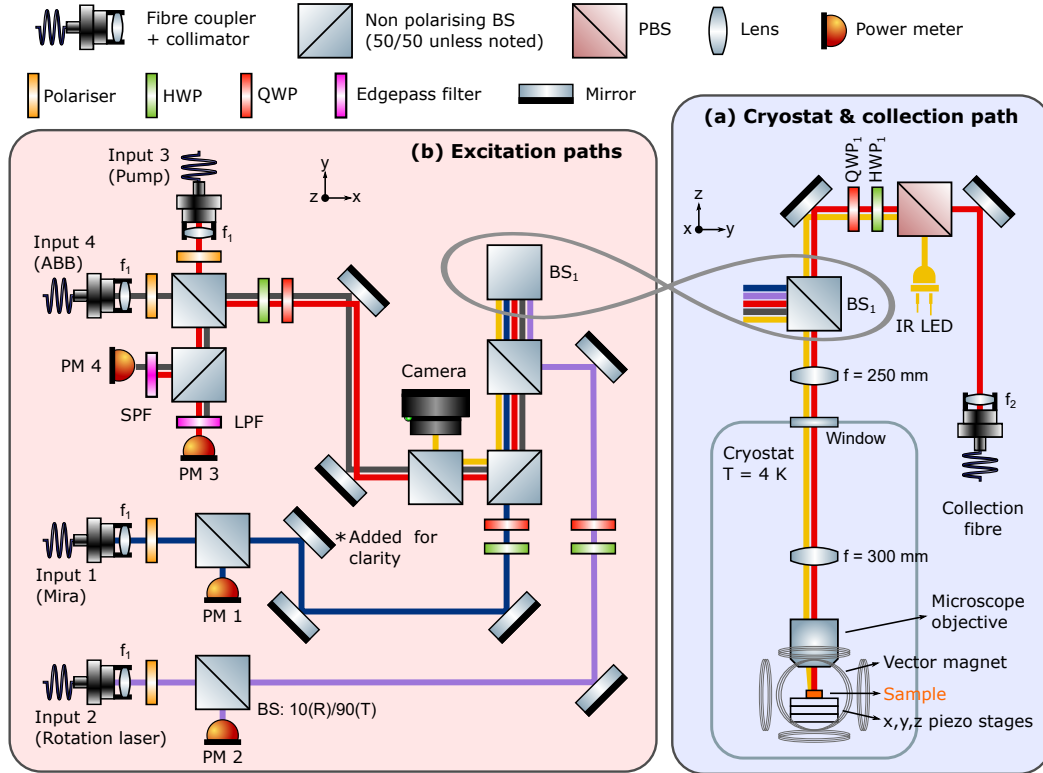


**Figure 3.4:** Optical setup for sample excitation, collection and imaging. **(a)** The sample is held inside a cryostat containing a vector magnet. Emission from the sample is collected by a microscope objective and imaged onto a single-mode collection fibre. **(b)** Four lasers are combined on a breadboard placed on top of the cryostat. Laser names in parentheses denote the configuration used for the entanglement experiment. The beamsplitter  $BS_1$  (appears twice inside  $\infty$  symbol) reflects the lasers into the cryostat. Abbreviations: beamsplitter (BS),  $\lambda/2$ -plate (HWP),  $\lambda/4$ -plate (QWP), polarising beamsplitter (PBS), short-pass filter (SPF), long pass filter (LPF), power meter (PM). Collimator focal lengths:  $f_1 = 18$  mm,  $f_2 = 4.2$  mm.

at once. The fibre-coupled lasers are combined on an optical breadboard (figure 3.4b) placed on top of the cryostat. The lasers are collimated and reflected down the cryostat where a 4F lens system expands the beams by 20% and images the lasers onto the back focal plane of the microscope objective leading to diffraction-limited laser spots on the sample. A linear polariser at the start of each laser path

<sup>7</sup>Attodry1000 from Attocube.

ensures an s-polarised beam. A pair of motorised  $\lambda/2$  and  $\lambda/4$  wave plates are placed in each laser path for precise polarisation control. Each laser path uses a beamsplitter (BS) to expose a power meter, which is used to stabilize the optical power via a PID-controller and an AOM setup (explained in section 3.2). A pair of long-pass and short-pass filters with a 900 nm cut-off are used to separate the ABB laser and pump laser onto separate power meters. Input 2 is used for the rotation laser (chapter 6) as it exhibits the lowest optical loss by having the fewest beamsplitters.

The scattered emission from the collection grating coupler is coupled into a single-mode collection fibre. A short  $f_2 = 4.2$  mm collimation lens is used to image the fibre mode onto the grating couplers. Half of the QD emission is lost on the 50/50 BS<sub>1</sub> beamsplitter (figure 3.4). This loss could be reduced by adopting a 5/95 BS such as in Ref. [18]. However, the need for an extremely high rotation power necessitates a 50/50 splitting ratio in this setup. The total setup efficiency is discussed in appendix G.

The sample can be illuminated using a broadband infrared light-emitting diode, which is reflected down to the sample using the PBS in the collection path (figure 3.4a). The sample reflection is imaged onto a CMOS camera on the breadboard, allowing the sample to be viewed.

A three-axis superconducting magnet housed inside the cryostat can generate a constant magnetic field of arbitrary direction with field strengths up to 5 T in the z-direction but only 2 T in the xy-plane (Voigt geometry). Changing the magnetic field disrupts the optical alignment and is thus rarely done.

### 3.3.1 EXCITATION SCHEMES

Figure 3.5 shows the two schemes used to couple a laser field to a QD. Figure 3.5a shows the configuration used for a transmission experiment. A probe laser is coupled into the WG via the right grating coupler. The probe propagates through the WG, interacts with the QD and the transmitted light is then coupled into the collection fibre via the left grating coupler. Note that the two couplers are orthogonally polarised due to the 90° bend in the WG. The collection optics (QWP<sub>1</sub>, HWP<sub>1</sub> and PBS in figure 3.4) are configured to transmit x-polarised light. This allows all light to be collected from the left grating but rejects y-polarised laser reflections from optical elements and the sample surface. Figure 3.5b shows the setup for resonant excitation where one or more lasers propagating from out-of-plane are tightly focused on the QD position. The resonant excitation lasers, which can not be filtered spectrally, are typically y-polarised to maximize the coupling to the y-polarised dipoles. This also allows effective laser background suppression as the collection and excitation spots are both spatially separated and cross polarised. We observe signal to noise (SNR) ratios up to  $> 10^4$  (figure 4.5a) using this method.

### 3.3.2 ALIGNMENT PROCEDURE

Laser alignment begins by bringing the sample into focus on the camera using the piezo positioners. A laser is sent through the collection fibre and imaged onto the desired collection grating which results in scattering from the opposite grating.

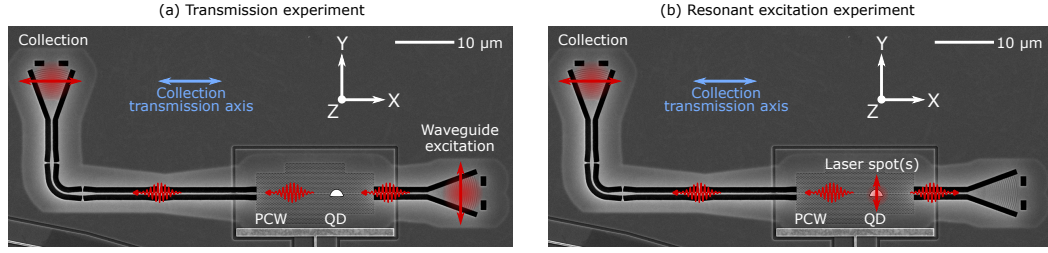


**Figure 3.5:** QD excitation schemes. Red arrows denote laser polarisations. The blue arrow denotes the transmission axis of the polarisation optics.

This scattering is visible on the camera image and is maximised by optimising the collection path mirrors and the fibre collimation. The excitation lasers are initially aligned by resonantly exciting the  $X^0$  with a CW laser (see section 4.4). The rotation laser is aligned to achieve the highest possible fluorescence, thus maximizing the optical Rabi frequency  $\Omega$ . The lasers used for resonant pumping are however aligned to maximize the SNR. The SNR can be monitored by alternating  $V_{\text{bias}}$  between resonance and non-resonance which allows an estimate of the laser background. SNR maximisation often requires tedious beam walking and fine-tuning the laser collimation. Placing the laser spot  $\frac{1}{8}$  to a  $\frac{1}{4}$  spot size from the QD is often found to increase the SNR despite decreasing  $\Omega$ . The exact mechanisms influencing the amount of laser scatter are not completely understood.

### 3.4 DETECTION SYSTEMS

A number of detection systems are used to resolve QD emission on the single-photon level (figure 3.6).

#### 3.4.1 DETECTORS

A spectrometer is an important tool for initial QD spectroscopy as it allows the identification of the different charge states. Otherwise, all experiments use either an avalanche photo diode<sup>8</sup> (APD) or a superconducting nanowire single-photon detector<sup>9</sup> (SNSPD). Both devices are fibre coupled and produce an electric impulse upon photodetection which is registered by a time tagger. The SNSPDs are distinguished by a high quantum efficiency and low rate of dark counts. This is achieved through cryogenic operation at 1.2 K. The entanglement experiment, which relies on the detecting of photon coincidences, greatly benefits from higher detection efficiency and uses the SNSPD exclusively. The remaining experiments, however, applied a mix of the two detectors, partly due to SNSPD reliability issues. The detector properties are summarised in table 3.1.

<sup>8</sup>SPCM-AQ4C from Perkin-Elmer.

<sup>9</sup>From Photonspot.

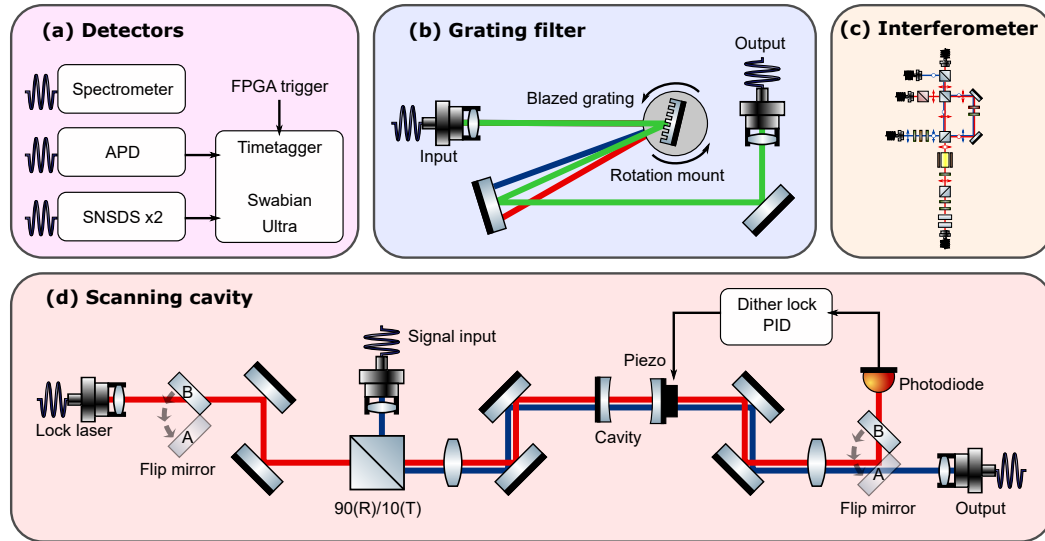


**Figure 3.6:** Overview of detection systems. (a) Photons are either resolved in wavelength on a spectrometer or in detection time on a APD or SNSPD detector. (b) Grating filter used for broadband spectral filtering. (c) Time-bin interferometer described in chapter 8. (d) Scanning Fabry-Perot cavity used for narrow band spectral filtering. Stabilisation is performed by periodically injecting *lock* laser.

	Quantum efficiency at 950 nm	Dark count rate	Deadtime (95% recovery)	Timing jitter (FWHM)
SNSPD	70-90% (polarisation dependent)	$\sim 2$ HZ	55 ns (measured)	260-290 ps (measured)
APD	$\sim 30\%$	$\sim 300$ Hz	50 ns (specified)	350 ps (measured)

**Table 3.1:** Comparison of single-photon detectors.

The time tagger<sup>10</sup> has a jitter of 20 ps FWHM and does not limit timing resolution. The time tagger receives a synchronisation pulse from the FPGA, allowing the photon detections to be tagged relative to the applied pulse sequence.

### 3.4.2 GRATING FILTER

A simple grating filter (figure 3.6b) is used to filter out detuned lasers. A reflective blazed grating reflects the incoming light, separating the different wavelengths. The grating is operated in the Littrow configuration, where the first-order diffraction mode is imaged onto a collection fibre. This setup realises a 65 GHz FWHM bandwidth and a 47% fibre-to-fibre efficiency. Have a wide bandwidth is practical for applications where emission from two Zeeman split transitions has to be detected. The efficiency is in part limited by a lack of polarisation control, as the grating has higher diffraction efficiency for s-polarised light.

<sup>10</sup>Time Tagger Ultra from Swabian.

### 3.4.3 SCANNING CAVITY

Figure 3.6d shows the scanning cavity system used in section 5.3 to finely resolve the QD emission spectrum. Two curved mirrors (50 mm radius of curvature) housed inside a closed tube form a Fabry-Perot cavity with 79 MHz linewidth and  $\nu_{fsr} = 10.45$  GHz free spectral range (FSR). Coupling to higher-order TEM modes is suppressed by a factor of  $>2000$ . The cavity resonance is locked to a *lock laser* by moving the flip mirrors to the A position, allowing light from an ECDL laser to enter the cavity. The cavity transmission is measured by a photodiode and is used for feedback. An Arduino microcontroller sends a dither signal to a piezo which modulates the cavity length. By demodulating the photodiode signal an error signal is derived, which is feed to a digital PID loop that locks the cavity length. Once the cavity transmission exceeds 95% peak value, the flip mirrors are reverted to position B and the cavity is left to drift. When drifting, the cavity remains within a FWHM on a 5 s time scale. During this drift, photons from the signal input impede on the cavity which is coupled to an output fibre for detection with the SNSPD. This cavity setup can be used to finely resolve an emission spectrum by repeatedly incrementing the lock laser frequency, re-locking the cavity and measuring the intensity of signal photons transmitted through the cavity.

## 4 | Spectroscopy

This chapter deals with QD spectroscopy and investigations into basic spin properties. We first describe our procedure for identifying QD through a combination of resonant transmission measurements and photoluminescence measurements. Our priority is finding QDs with an accessible hole spin and strong waveguide coupling. The remaining chapter contains a characterisation of QD<sub>1</sub>, including its radiative lifetime, hole lifetime and hole efficiency. Finally, we demonstrate measurements of resonance fluorescence in Voigt geometry.

### 4.1 RESONANT TRANSMISSION

Resonant transmission (RT) measurements constitute a simple and effective technique for identifying QDs in a two-side waveguide following the excitation scheme described in section 3.3.1. An ECDL laser is coupled to the input grating of the WG, the bias voltage is set to 1.22 V corresponding to  $X^0$  and the laser is scanned in 200 MHz steps across a broad frequency range. The power is attenuated to drive the QDs well below saturation. This yields the PCW transmission spectrum in figure 4.1. The WG band edge is visible around 315.3 THz ( $1/e$  cutoff) and multiple transmission dips associated with individual QDs become apparent. As a deep transmission dip requires both high a  $\beta$ -factor and low levels of dephasing and spectral diffusion (as evident from (2.73)), depth is used to select promising candidates. Fine resolution scans are then repeated for the  $\approx 10$  deepest dips in each PCW. As some QDs exhibit spectral diffusion over very long timescales ( $> 1$  s), the scans are repeated 5 times to reveal the long-timescale linewidth.

Figure 4.2 shows a fine RT scan of our primary QD, QD<sub>1</sub>. This reveals the two  $X^0$  dipoles split by a  $\delta_{f_{ss}} = 6.45$  GHz fine structure splitting (see level structure in figure 2.3). The indicated dipole polarisations are confirmed by subsequent measurements. The unequal dip amplitudes are an early indication of unequal coupling between the dipoles and the waveguide mode. A maximum transmission dip of 83% is observed, which bounds the  $\beta$ -factor to  $> 0.59$  using (2.73). The slightly asymmetric line shape is commonly observed in our devices and is attributed to a Fano-resonance caused by a weak cavity formed between waveguide interfaces [17].

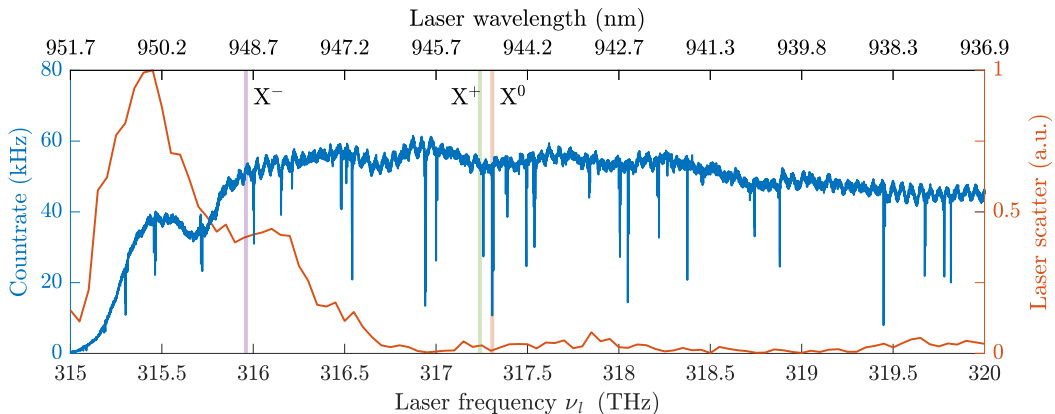


**Figure 4.1:** Left y-axis (blue): RT spectrum of the PCW containing QD<sub>1</sub>.  $V_{\text{bias}}$  is tuned to realise a neutral QD. Each dip corresponds to an individual QD as the plot does not resolve the FSS. The wavelengths of the QD<sub>1</sub> charge states are indicated, but only  $X^0$  is visible in the data. Counts recorded on SNSPD. Right y-axis (red): Laser scatter resulting from a free space laser focused on QD<sub>1</sub> using a non-resonant  $V_{\text{bias}}$ .

Although somewhat overkill for this analysis, we can fit a single transmission dip with the model from Ref. [17]

$$T(\Delta_l; \gamma, \xi, \beta) = \frac{[(\gamma + 2\gamma_d)((\beta - 1)^2\gamma + 2\gamma_d) + 4\Delta_l^2](1 + \xi^2)}{(\gamma + 2\gamma_d)^2 + 4\Delta_l^2 + 4\beta\gamma\Delta_l\xi + [((\beta - 1)\gamma - 2\gamma_d)^2 + 4\Delta_l^2]\xi^2}, \quad (4.1)$$

where  $\Delta_l$  is the laser detuning,  $\gamma$  is the radiative lifetime,  $\beta$  is the  $\beta$ -factor,  $\gamma_d$  is the pure dephasing rate (section 2.6.1) which we assume zero for convenience and  $\xi$  is a parameter of the Fano-resonance. Additionally, (4.1) assumed the limit  $\Omega \ll \gamma$  and reduces to (2.73) in the limit  $\gamma_d, \xi, \Delta_l = 0$ .

We model the full transmission intensity  $I_{\text{tot}}$  with a product of two dips given by (4.1) convolved with a Gaussian spectral diffusion (following section 2.6.2) with standard deviation  $\sigma$

$$I_{\text{tot}}(\omega_l) = I_0 \int_{-\infty}^{\infty} d\Delta \mathcal{N}(\Delta; \sigma) T_1(\omega_l + \Delta - \omega_1; \gamma_1, \xi, \beta_1) T_2(\omega_l + \Delta - \omega_2; \gamma_2, \xi, \beta_2), \quad (4.2)$$

where  $\omega_1$  and  $\omega_2$  are the transition resonance frequencies,  $\omega_l = (2\pi)\nu_l$  is the laser frequency and  $\Delta$  is the random spectral diffusion. With the exception of  $\gamma_1, \gamma_2$ , which are fixed according to the lifetime measurements in figure 4.4a, all parameters in (4.2) are free fit parameters.

This model produces an excellent fit (figure 4.2) and yields useful estimates of the broadening parameter,  $\sigma(X^0) = 87$  MHz. As the  $X^0$  fine structure splitting protects against nuclear noise to first order [34], this broadening is likely the result of charge noise. The main transition has a 755 MHz linewidth, which represents a 8% increase over the transform-limited linewidth  $\gamma_y/(2\pi) = 696$  MHz estimated in section 4.3. Hence, this QD is an example of operating in the near-lifetime limited

regime. However, it is challenging to estimate quantities such as  $\beta$  and  $\gamma_d$  from this fit, as  $\sigma$ ,  $\gamma_d$  and  $\beta$  all diminish the dip height. A more complex RT-based scheme for parameter estimation can be found in Ref. [48].

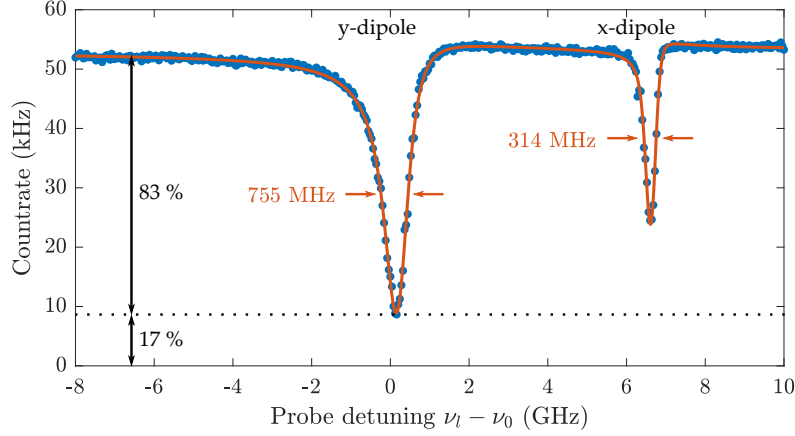


**Figure 4.2:** Narrow RT scan of QD<sub>1</sub>. 5 scans with 40 MHz step size are averaged. The spectrum showing two FSS dipoles is fit (red line) with (4.2) yielding the indicated FWHM values.  $\nu_0 = 317.301$  THz. Counts recorded with SNSPD.

## 4.2 CHARGE STATE IDENTIFICATION

The general approach for identifying the wavelengths and voltage spans of a QD's charge states involves photoluminescence measurements. Here, QDs are excited from free space, allowing spatial selectivity, and the fluorescence collected from a grating coupler is resolved on a spectrometer. An ABB laser is effective at inducing free carriers and populating the relevant charge states. However, due to the high QD density of the investigated sample, this leads to dozens of overlapping spectral lines. Instead, we excited the P-shell as demonstrated in figure 4.3a. The Mira laser is blue-detuned  $\approx 20$  nm from  $X^0$  and pulsed continuously. Scanning  $V_{\text{bias}}$  and resolving the emission on a spectrometer resolves the  $X^+$ ,  $X^0$  and  $X^-$  lines. The charge state identities are later confirmed by applying a magnetic field.

This measurement provides an excellent overview but is time-consuming as the P-shell resonance must first be identified. Alternatively, it was found that strongly pumping  $X^0$  with a CW laser produced weak, yet identifiable emission from the other charge states (figure 4.3b) and revealed the possible presence of  $X^+$ .

This method enabled efficient characterisation through the following steps:

1. Perform an RT-scan of the entire PCW and identify  $X^0$  lines with strong transmission dips.
2. Switch to free space excitation, tune the laser to the  $X^0$  resonance of a specific QD and translate the laser spot along PCW until fluorescence is detected.
3. Pump  $X^0$  strongly and record a photoluminescence spectrum. Check for the existence of an  $X^+$  line close to  $X^0$  but lower in  $V_{\text{bias}}$ .

In total, fine RT scans were performed on 41 QDs across 4 PCWs with identical parameters. Spectroscopy using  $X^0$  pumping was performed on 18 QDs of which 15 produced an identifiable  $X^+$ .

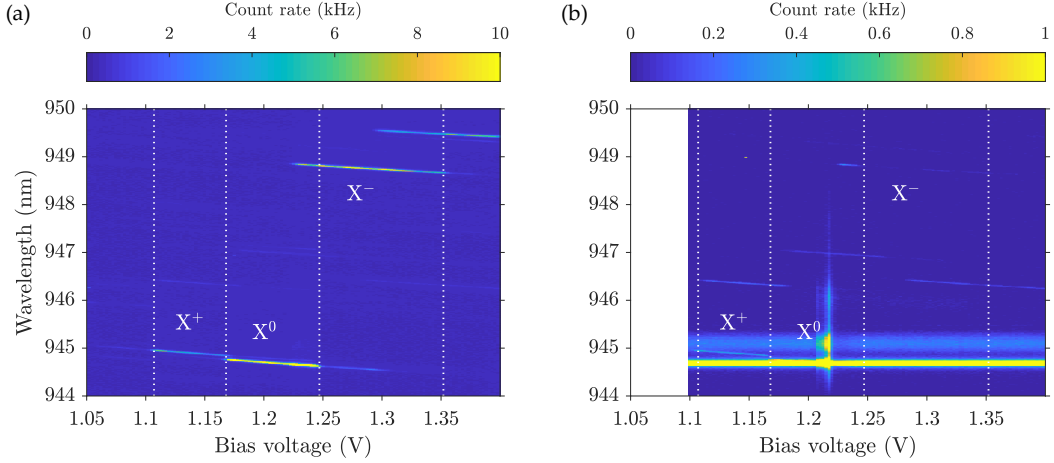


**Figure 4.3:** Photo luminescence from  $QD_1$  at  $\mathbf{B} = 0$  T recorded on a spectrometer. (a) Emission following pulsed excitation of the 925.0 nm P-shell resonance. Dashed lines indicate charge state voltage regions. (b) Emission following strong CW  $X^0$  excitation. Laser scatter gives rise to the strong horizontal line around 944.8 and detector blooming above 945 nm. Importantly, the spectrum faintly reveals the  $X^+$  and  $X^-$ .

### 4.3 LIFETIME MEASUREMENTS

We now measure the radiative lifetimes of the neutral exciton and the charged trions using the method of P-shell excitation just described. The Mira laser remains fixed at the P-shell resonance and is fully rejected by a grating filter in the collection. Switching between the charge states simply amounts to adjusting  $V_{\text{bias}}$  and shifting the grating filter resonance. Figure 4.4a shows the  $QD_1$   $X^0$  decay when exciting with 3 different laser polarisations. The fluorescence decay is modelled by the sum of two exponentials

$$I(t) = I_x e^{-\gamma_x t} + I_y e^{-\gamma_y t} + I_{bg}, \quad (4.3)$$

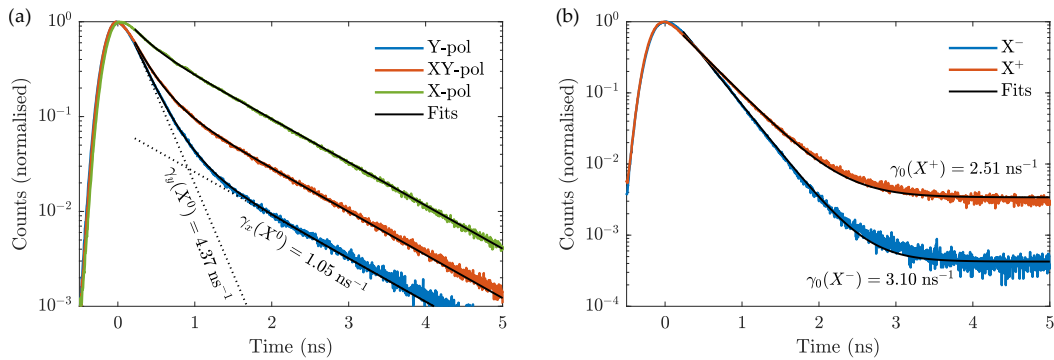
which is motivated by having two dipoles with differing levels of Purcell enhancement. A  $\chi^2$ -fit is applied to the three datasets in figure 4.4a simultaneously, such that  $\gamma_x$  and  $\gamma_y$  are identical across all three fits. A ratio of  $\approx 4$  is found between  $\gamma_y$  and  $\gamma_x$ . This asymmetry is unsurprising based on the observed RT asymmetry (figure 4.1) and will be further explored in chapter 5. The enhanced  $\gamma_y = 4.47 \text{ ns}^{-1}$  (compared to  $\approx 1 \text{ ns}^{-1}$  in bulk) is a direct consequence of the PCW's Purcell enhancement. We also observe a modulating of  $I_x, I_y$  dependent on the laser polarisation. This indicates selective excitation of the x and y-dipoles and polarisation retention in the relaxation from P to S-shell.

Figure 4.4b shows the radiative decay of  $X^-$  and  $X^+$  at  $B_y = 2$  T. As they are less efficiently excited using P-shell, a background appears in the time traces.

Fitting with the model  $I(t) = I_0 e^{-\gamma_0 t} + I_{bg}$  yields estimates of the trion decay rates, which again exceed bulk rates. No difference was observed between  $\mathbf{B} = 0$  T and  $B_y = 2$  T. However, subtle variations in  $I_0$  and  $\gamma_0$  were observed when switching the P-shell laser polarisation between x, xy, and y. This is believed to be an artefact of the SNSPD's (at the time poorly characterised) intensity-dependent IRF. The following lifetimes are averaged over the three laser polarisation, with uncertainty representing an uncertainty of the mean:

$$\gamma_0(X^-) = (3.07 \pm 0.06) \text{ ns}^{-1}, \quad (4.4)$$

$$\gamma_0(X^+) = (2.48 \pm 0.02) \text{ ns}^{-1}. \quad (4.5)$$



**Figure 4.4:** Lifetime measurements on QD<sub>1</sub> using P-shell excitation and SNSPD detectors. **(a)** Decay of both  $X^0$  excitons at  $\mathbf{B} = 0$  T and different laser polarisations (legend). Decays follow the sum of two exponentials with lifetimes indicated by the dashed lines. The first 220 ps are excluded from fitting due to the IRF. **(b)** Decay of  $X^-$  and  $X^+$  trions at  $B_y = 2$  T and  $y$ -polarised excitation, yielding a single exponential decay.

## 4.4 RESONANCE FLUORESCENCE

The main experimental technique used in this work involves resonant excitation from free space as described in section 3.3.1. The simplest example of this is resonantly exciting  $X^0$  at  $\mathbf{B} = 0$  T as demonstrated in figure 4.5. A  $y$ -polarised laser is applied, which predominantly couples to the  $y$ -dipole, although the second dipole is also visible. The order of the two dipoles is swapped compared to figure 4.2 as  $V_{\text{bias}}$  is scanned instead of the laser frequency. Scanning  $V_{\text{bias}}$  gives an estimate of the fluorescence at laser resonance and of the laser background. An extinction  $> 10^4$  is achieved in figure 4.5a, demonstrating the potential laser suppression of the system, although this extinction requires careful alignment and, as evident from figure 4.1, is not possible at all optical frequencies.

The laser Rabi frequency can be estimated by performing a saturation measurement as in figure 4.5b.  $V_{\text{bias}}$  is scanned across the  $y$ -dipole to ensure resonance and the maximum fluorescence intensity is picked out. The resulting intensity is fit with the model for a 2 level emitter (2.24) yielding a saturation power  $P_{\text{sat}}$ .

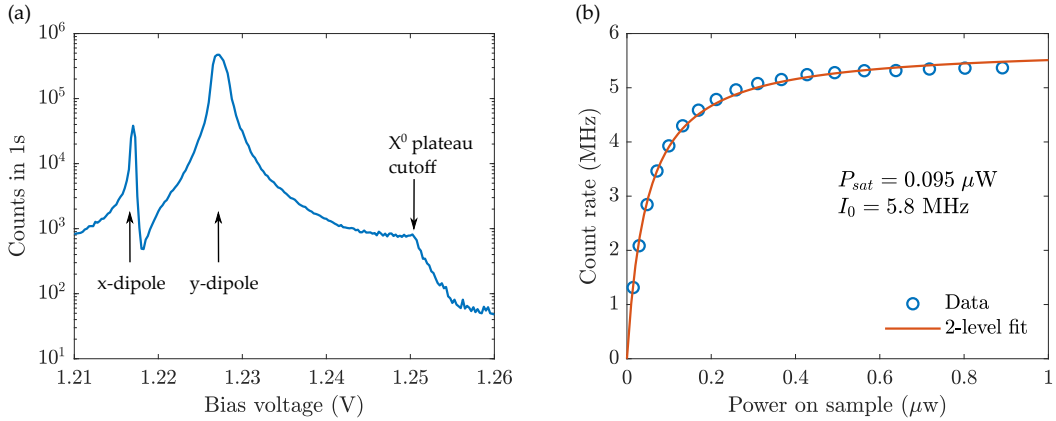


**Figure 4.5:** QD<sub>1</sub> X<sup>0</sup> resonance fluorescence with  $\mathbf{B} = 0 \text{ T}$ . **(a)**  $V_{\text{bias}}$  is scanned revealing both dipoles. The drop in intensity at 1.25 V corresponds to the end of the X<sup>0</sup> charge state.  $P = 0.02 \times P_{\text{sat}}$ . Counts recorded by APD. **(b)** Saturation measurement of the y-dipole in (a). Increasing laser power leads to a saturation of intensity according to (2.24).

## 4.5 HOLE SPECTROSCOPY

### 4.5.1 METHODOLOGY

As the hole state is not intrinsically stable in the sample studied here, holes must be optically induced through the method of photocreation. A method commonly used in the literature is to resonantly pump X<sup>0</sup> at a  $V_{\text{bias}}$  below the X<sup>0</sup> plateau [42, 49]. This causes the electron in the exciton to tunnel out, leaving behind a quasi-stable hole. We were able to reproduce this method of photo creation. However, due to the number of lasers already being used, a dedicated X<sup>0</sup> pump was not experimentally feasible. Instead, an ABB laser at 830 nm was used. It is assumed that photocreation still occurs via the X<sup>0</sup>, but it is also possible that holes created in the surrounding material can directly tunnel into the QD.

Figure 4.6 shows the X<sup>+</sup> plateau resulting from a resonant excitation. A CW ABB laser is used to create the hole and a single laser with  $P \approx 0.3 \times P_{\text{sat}}$  is scanned in frequency. This measurement reveals a single line with a 0.57 GHz/mV Stark shift. In all following measurements,  $V_{\text{bias}}$  is kept between 1.145 and 1.155 corresponding to the region of highest brightness and lowest linewidth.

### 4.5.2 HOLE LIFETIME

We now measure the hole lifetime  $T_0$ . This is the lifetime of the meta-stable charge state and should not be confused with the spin  $T_1$  time. Obviously,  $T_0$  has to exceed the duration of the desired experiments.  $T_0$  is estimated by modulating the ABB laser and probing the hole occupation with a resonant probe laser with power  $P$ . Following Ref. [50] and the previously published derivation in Ref. [32], the dynamics are given by figure 4.7a. Starting from an uncharged state  $|0\rangle$ , a hole  $|h\rangle$  may be initialised by photocreation via the neutral exciton  $|X^0\rangle$ . Once initialised, the hole may tunnel out with rate  $\gamma_t$ . The probe laser populates the trion  $|X^+\rangle$ ,

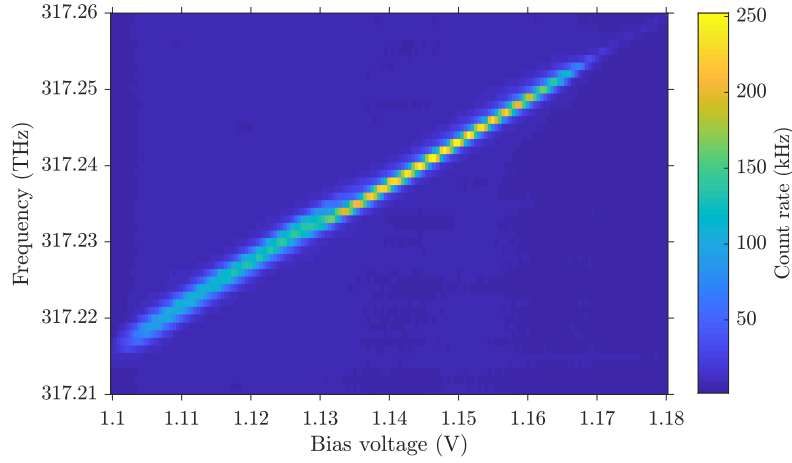


**Figure 4.6:**  $X^+$  plateau at  $\mathbf{B} = 0$  T. A CW ABB laser induces the hole while a resonant laser is scanned in frequency (y-axis). Detected with SNSPD+grating.

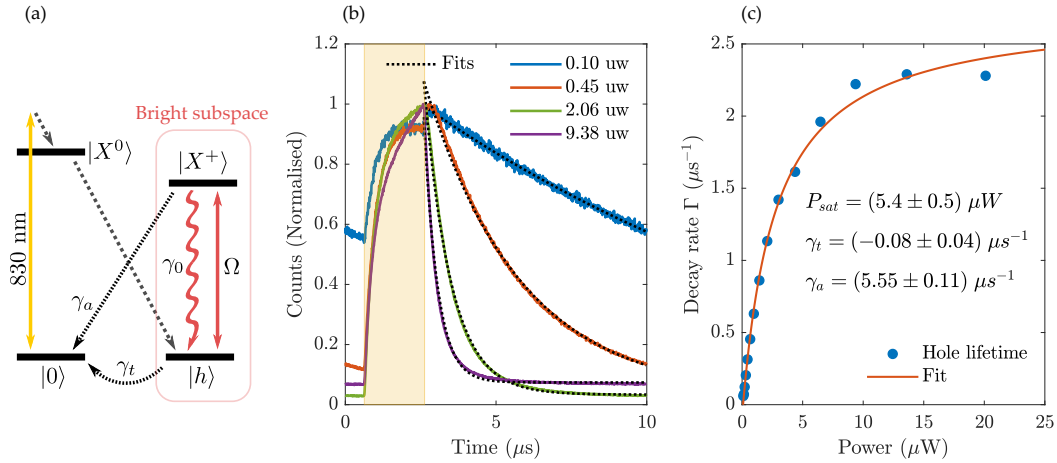


**Figure 4.7:** Hole lifetime measurement. **(a)** Proposed energy level diagram. An ABB laser populates  $|h\rangle$  through photocreation. A probe laser couples  $|h\rangle$  and  $|X^+\rangle$  and generates fluorescence proportional to the population in  $|X^+\rangle$ . **(b)** Fluorescence histogram. A  $2\ \mu\text{s}$  ABB pulse (yellow) populates  $|h\rangle$ , after which fluorescence decays. An exponential fit is used to extract the lifetime. **(c)** Hole decay rate as a function of probe power. Using the model in (4.8) yields estimates of the relevant tunnelling rates.

which may decay radiatively to  $|h\rangle$  with rate  $\gamma_0$  or non-radiatively to  $|0\rangle$  with rate  $\gamma_a$  via an auger process [50].

Consider now the population in the bright subspace,  $n_b = n_h + n_t$ , where  $n_h$  and  $n_t$  are the populations of the  $|h\rangle$  and  $|X^+\rangle$  states, respectively. We assume the limit where the bright subspace is at a constant internal equilibrium given by

$$\Theta = \frac{n_t}{n_b} = \frac{P/P_{sat}}{1 + 2P/P_{sat}}, \quad (4.6)$$

which follows from the steady-state solution of a 2-level system driven at resonance (2.24). The rate at which population leaves the bright subspace then follows

$$\dot{n}_b = -\gamma_t n_h - \gamma_a n_t = -\gamma_t(1 - \Theta)n_b - \gamma_a \Theta n_b = -\Gamma(P)n_b, \quad (4.7)$$

$$\Gamma(P) = \frac{P/P_{sat}}{1 + 2P/P_{sat}}(\gamma_a - \gamma_t) + \gamma_t. \quad (4.8)$$

Hence, the probe signal  $\propto n_b$  decays exponentially with a power-dependent rate. This is indeed observed in figure 4.7b. Probe fluorescence increases during the 2  $\mu$ s ABB pulse but decays exponentially in its absence and is fitted with the model  $I(t) = I_1 e^{-\Gamma t} + I_0$ . The measurement is repeated for a range of probe powers, and  $V_{bias}$  is scanned to ensure probe resonance.

Figure 4.7c shows the extracted  $\Gamma$  as a function of probe power and applies the fit model of (4.8) using  $P_{sat}$ ,  $\gamma_a$  and  $\gamma_t$  as free fit parameters. From this we extract an Auger rate of  $\gamma_a = (5.55 \pm 0.12) \mu\text{s}^{-1}$ . Crucially, this rate should be compared to  $\gamma_0$  to estimate the probability of non-radiative recombination. We calculate  $\gamma_0/\gamma_a = 458 \pm 12$ , which corresponds to the average number of photons that can be scattered before the hole is lost. The fit estimates a  $\gamma_t = (-0.08 \pm 0.04) \mu\text{s}^{-1}$  tunnelling rate which is almost compatible with zero. As a more conservative estimate, we note that the lowest probe power (blue line, figure 4.7c) has an estimated decay rate of  $\Gamma_{min} = 0.06 \mu\text{s}^{-1}$  corresponding to a lower bound hole lifetime of  $T_0 \geq \Gamma_{min}^{-1} = 16 \mu\text{s}$ . Both  $T_0$  and  $\gamma_0/\gamma_a$  are completely sufficient for the entanglement experiments. Similar values have been achieved on other QDs from the same sample.

### 4.5.3 HOLE EFFICIENCY

We now optimise and characterise the probability of charging the QD with a hole. Figure 4.8a shows  $X^+$  fluorescence as a function of ABB power and probe power. A 200 ns ABB pulse is followed by a 600 ns probe pulse of which only the first 50 ns is integrated due to the fluorescence decay demonstrated in figure 4.7b. Increasing the probe power yields a normal 2-level saturation. However, increasing the ABB power yields a local maximum, which could indicate excess noise induced by the ABB.  $V_{bias}$  is scanned for each pixel in figure 4.8a to ensure probe resonance. In general, an ABB pulse corresponding to 0.1  $\mu$ W in figure 4.8a is used for hole spin experiments.

In figure 4.8b, the ABB laser is replaced with the 300 GHz red detuned rotation laser used in chapter 6 to drive Raman transitions. Interestingly, this also enables probe fluorescence but requires considerably higher power. This fact will become important in discussing the spin rotation fidelity.

The probability of charging the QD with a hole is estimated by comparing the brightness of  $X^0$  and  $X^+$  under pulsed resonant excitation. Ideally, the QD should emit a single photon following  $\pi$ -pulse excitation, with both  $X^+$  and  $X^0$  experiencing identical losses from the collection,  $\beta$ -factor etc. For  $X^+$ , a 200 ns ABB pulse initialises the hole followed by a train of 30 Mira<sup>1</sup> pulses with equal intensity. Counts from the pulse train are integrated, and laser background counts measured using

<sup>1</sup>A variable pulse stretcher (not discussed here) was used to produce 24 GHz FWHM pulses.

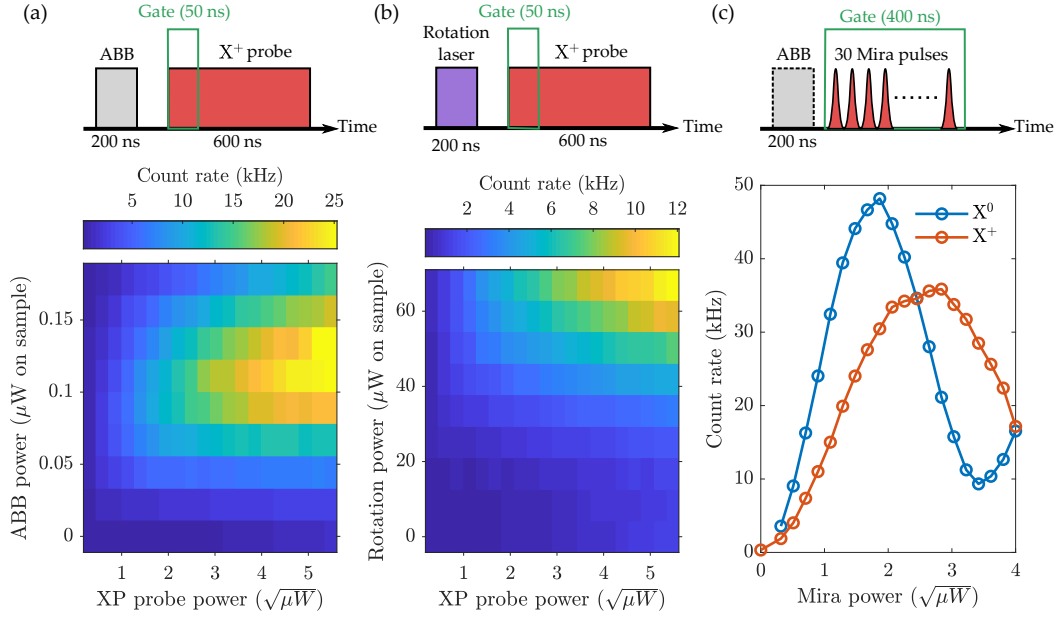


**Figure 4.8:** (a,b) Resonant X<sup>+</sup> fluorescence using a 200 ns pulse of (a) ABB laser or (b) rotation laser to initialise the hole. The power on the y-axis indicates the actual power impeding on the sample while the x-axis powers are measured on the power meters in figure 3.4b. (c) Fluorescence from X<sup>0</sup> and X<sup>+</sup> following pulsed Mira excitation. Count rates are directly comparable. Counts are recorded using a grating filter and APD.

a non-resonant  $V_{\text{bias}}$  are subtracted. A grating in the collection is used to ensure exclusive detection of X<sup>+</sup>. X<sup>0</sup> is measured using the same sequence but omitting the ABB pulse and tuning the Mira and collection grating into X<sup>0</sup> resonance. Figure 4.8c shows X<sup>+</sup> achieving 75% of X<sup>0</sup> counts at  $\pi$ -pulse, which is interpreted as the hole initialisation efficiency. This yields a largely unbiased comparison, as the total detection efficiency should remain constant.

## 4.6 VOIGT GEOMETRY RESONANCE FLUORESCENCE

We now apply a  $B_y = 2\text{T}$  magnetic field to observe the Zeeman splittings and linear dipoles occurring in  $X^+$  and  $X^-$ .

### 4.6.1 ELECTRON SPIN

Figure 4.9a shows the  $X^-$  resonance fluorescence when scanning  $V_{\text{bias}}$  and the frequency of a single laser. Distinct regions of high intensity occur owing to three mechanisms. Firstly, the four levels are Zeeman split and only the  $y$ -dipoles couple to the pumping laser. Secondly, a  $0.50\text{ GHz/mV}$  Stark shift tilts the plateaus. Thirdly, the spin-flip rate  $\kappa$  varies as a function of  $V_{\text{bias}}$ . In the middle of the plateau,  $\kappa \ll \gamma_{osp}$ , and the spin is efficiently pumped into a dark state. In the co-tunnelling regime (section 2.2), the electron spin is randomised by tunnelling with the back contact of the diode, leading to  $\kappa_{co}/(2\pi) \approx 1 - 10\text{ MHz}$  [30]. This recycles the spin and restores the fluorescence. The co-tunnelling regime is useful, as it allows estimation of the laser Rabi frequency as a function of laser power and polarisation. Figure 4.9b shows frequency scans in the co-tunnelling regime for laser polarisations optimised for suppressing the either linear dipole. These optimised polarisations only deviate from the  $x$  and  $y$ -axes of the PCW by a few degrees. A high level of suppression is possible, but precise quantification is complicated by a laser background, which interferes coherently with fluorescence, leading to negative count rates when subtracting laser background. This is not a general problem of  $X^-$ , but rather seems to be related to the spectral position of this  $X^-$  as indicated by figure 4.1. The  $x$ -transitions also feature irregular lineshapes, likely owing to

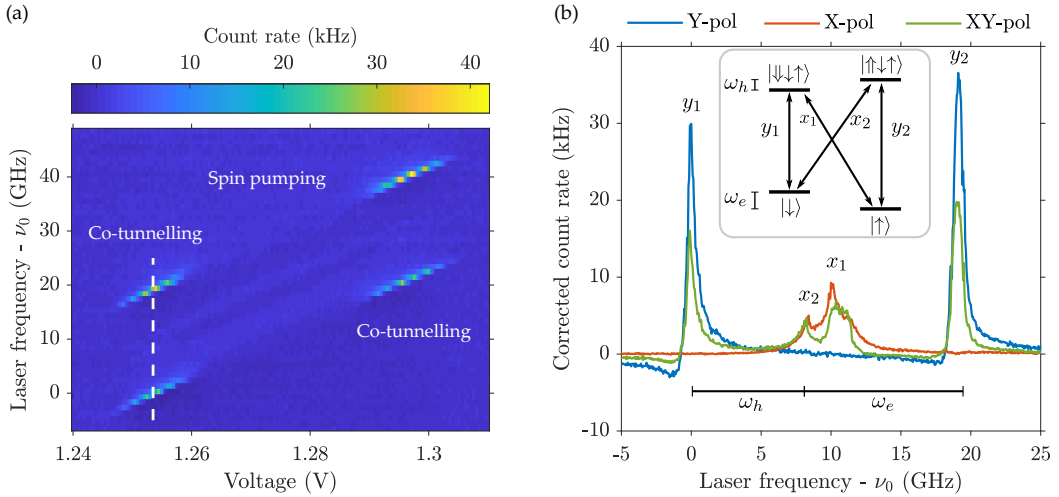


**Figure 4.9:**  $X^-$  resonance fluorescence at  $B_y = 2\text{T}$  using a single CW laser with  $P = 0.02 \times P_{\text{sat}}$ , detected with APD. A laser background measured at  $V_{\text{bias}} = 1.22\text{ V}$  is subtracted. **(a)** Plateau map resulting from a  $y$ -polarised laser, revealing areas of co-tunnelling and spin pumping. **(b)** Frequency scans at  $V_{\text{bias}} = 1.254\text{ V}$  (dashed line in (a)). Optimised laser polarisations (top legend) allow selectively exciting  $x$  and  $y$  dipoles. The annotations correspond to the  $X^-$  level diagram (insert).  $\nu_0 = 315.937\text{ THz}$ .

spin-dragging [51].

When operating in the spin pumping regime, fluorescence can be regained by re-pumping with a second CW laser, see figure 4.10. The intensity is maximized when both lasers are on resonance. Similar to figure 4.9, significant discontinuities are present in the spectrum.

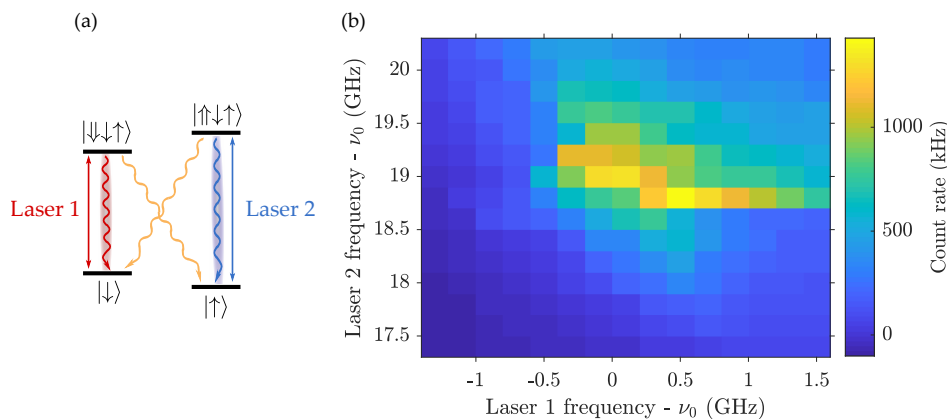


**Figure 4.10:** Two-colour CW spin pumping of  $X^-$  in  $B_y = 2$  T. **(a)**  $X^-$  Energy level diagram with both  $y$ -transitions driven by separate lasers. **(b)** Fluorescence intensity measured at  $V_{\text{bias}} = 1.277$  V (spin pumping regime). The intensity is maximized when both lasers are in resonance with a  $y$ -transition. Measured with SNSPD. A laser background measured at  $V_{\text{bias}} = 1.22$  V is subtracted.  $\nu_0 = 315.949$  THz.

#### 4.6.2 HOLE SPIN

Resonance fluorescence is also possible on  $X^+$ , but is complicated by two factors. Firstly, the hole must be initialised as established in section 4.5. Secondly, there is no co-tunnelling regime. By applying the two-colour pumping scheme in figure 4.11a we observe fluorescence when both pumping lasers are on resonance, see figure 4.11b. In contrast to the  $X^-$  measurement in figure 4.10, we no longer observe clear spin dragging, which seems to be an advantage of the hole spin. Two-colour pumping also allows measuring the  $X^+$  linewidth in the presence of a magnetic field, see figure 4.11c. A weak probe with  $P \approx 0.03 \times P_{\text{sat}}$  is scanned across the  $y_2$ -transition while a strong  $P \approx 2P_{\text{sat}}$  pump ensures re-pumping. A fit to a Voigt lineshape with  $\gamma_0(X^+) = 2.48 \text{ ns}^{-1}$  fixed by lifetime measurements yields a 1045 MHz FWHM corresponding to a broadening  $\sigma(X^+)/ (2\pi) = \sigma^{(XP)} = 345 \text{ MHz}$  which is noticeably broadened compared to  $X^0$  and  $X^-$  and could indicate additional noise owing of the ABB laser.

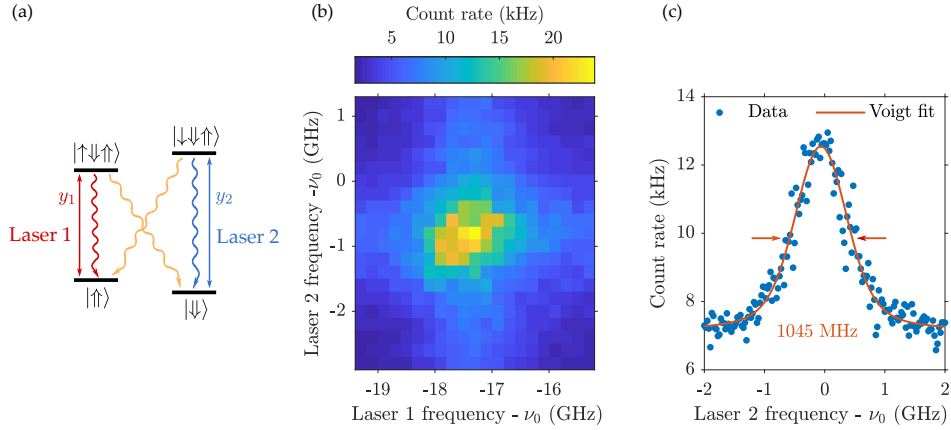


**Figure 4.11:**  $X^+$  resonance fluorescence at  $B_y = 2\text{ T}$  using a CW ABB laser and CW resonant laser(s). **(a)** Two-colour spin pumping level diagram. **(b)** Two-color pumping fluorescence measured at  $V_{\text{bias}} = 1.148\text{ V}$ . Both lasers use  $P \approx 0.03 \times P_{\text{sat}}$ . Detected with grating and SNSPD. **(c)** Two-colour pumping using laser 2 as a weak probe and laser 1 as a strong re-pump. A Voigt lineshape is used to extract the linewidth. Detected with grating and APD.  $\nu_0 = 317.354\text{ THz}$ .

## 4.7 PARAMETER SUMMARY

The properties of  $\text{QD}_1$  are summarised in table 4.1. The  $X^-$  linewidth and g-factors are estimated from figure 5.8b.  $X^+$  linewidth and g-factors are estimated from figure 4.11 and figure 6.5a.

A small note on linewidth: In section 2.8.1 we estimated an electron  $T_2^* = 2.1\text{ ns}$  to result in a  $\sigma_{OH}/(2\pi) \approx 110\text{ MHz}$  broadening of the optical linewidth. This almost perfectly captures the difference between the measured  $\sigma(X^0)$  and  $\sigma(X^-)$ , i.e.  $\sqrt{\sigma(X^0)^2 + \sigma_{OH}^2} = \sqrt{(87\text{ MHz})^2 + (110\text{ MHz})^2} = 140\text{ MHz} = \sigma(X^-)$ . Switching from  $X^-$  to  $X^+$  should not alter the broadening. Remember, we are simply "inverting" the level structure. It would be interesting to explicitly study  $X^+$  broadening as a function of the ABB laser, and investigate if other modes of photocreation are less noisy.

Property	$X^0$	$X^-$	$X^+$
Central frequency (THz)	317.31	315.96	317.24
Decay rate $\gamma_0$ ( $ns^{-1}$ )	4.37 (y-dipole) 1.05 (x-dipole)	$3.03 \pm 0.06$	$2.48 \pm 0.02$
Transform-limited linewidth $\gamma_0/2\pi$ (MHz)	696 (y-dipole) 167 (x-dipole)	482	395
Measured linewidth (MHz)	755 (y-dipole)	660	1045
Broadening, $\sigma/2\pi$ (MHz)	87	140	345
Stark shift (GHz/mV)	0.75	0.50	0.57
Electron splitting (GHz/T)		5.43	4.8
Electron g-factor $g_{e,x}$		0.389	0.34
Hole splitting (GHz/T)		4.17	3.65
Hole g-factor $g_{h,x}$		0.298	0.260

**Table 4.1:** QD<sub>1</sub> properties.  $X^-$   $g$ -factors are measured at  $V_{\text{bias}} = 1.261$  V.  $X^+$   $g$ -factors are measured at  $V_{\text{bias}} = 1.148$  V.



## 5 | Cyclicity

This chapter explores optical cyclicity induced by a PCW. The mechanism of photonically induced cyclicity is covered, and numerical simulations are analysed to estimate the position-dependent decay rates and cyclicity of a QD. A spin pumping measurement is used to estimate the cyclicity and spin pumping fidelity of both  $X^-$  and  $X^+$ . The cyclicity contributions are further explored by measuring the emission spectrum and resonance transmission spectrum of  $X^-$ . Finally, the implications for single-shot readout are analysed and a comparison is made with other methods of cyclicity induction.

### 5.1 PCW SIMULATION

Broadband optical cyclicity can be achieved by placing a QD in a PCW through the simultaneous suppression of  $\gamma_x$  and enhancement of  $\gamma_y$  (see figure 5.1).

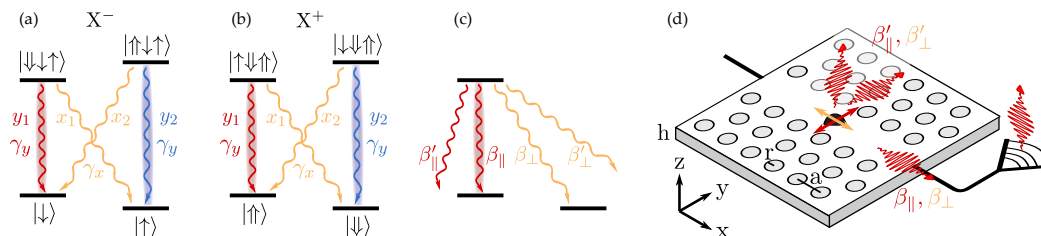


**Figure 5.1:** (a,b) Voigt geometry level diagrams of (a)  $X^-$  (b)  $X^+$ . The  $y$  transitions are enhanced by the PCW. (b) Level diagram of a positively charged QD in the Voigt geometry. (c) The decay of a trion can be decomposed into four  $\beta$ -factors representing the final spin state and emission into either the waveguide mode (unprimed) or radiative modes (primed). (d) PCW schematic. Arrows indicate the ideal placement and dipole orientation for maximal cyclicity.

The LDOS structure in a PCW has previously been analysed using full 3D numerical simulations [52]. This study analysed a two-sided PCW with parameters  $a = 240$  nm,  $r = 80$  nm and  $t = 180$  nm (defined in figure 2.7a), which closely resemble our measured device (section 3.1). The simulation generated Purcell factors for x- and y-dipoles at different spatial positions and four emitter wavelengths corresponding to group indices 5, 20, 56 and 120. Furthermore, the Purcell factors were decomposed into a waveguide (wg) contribution and a non-guided (ng) contribution, which contained both the radiation and slab modes. These simulations are now re-interpreted in the context of cyclicity.

Starting from the four Purcell factors  $F_{x,ng}, F_{y,ng}, F_{x,wg}, F_{y,wg}$ , where subscripts denote dipole polarisation and emission mode, the optical decay rates proportional to Purcell enhancement can be calculated from

$$\gamma_{i,j} = F_{i,j} \gamma_0^{hom} / 2, \quad (5.1)$$

which use the same subscripts and  $\gamma_0^{hom} \approx 1 \text{ ns}^{-1}$  is an estimate of the trion decay rate in bulk GaAs [21]. The factor 2 in (5.1) stems from having two dipoles contribute to the trion decay.

Normalising to  $\gamma_0$  yields the beta factors defined in figure 5.1c:

$$\beta_{\parallel} = \gamma_{y,wg} / \gamma_0, \quad (5.2)$$

$$\beta'_{\parallel} = \gamma_{y,ng} / \gamma_0, \quad (5.3)$$

$$\beta_{\perp} = \gamma_{x,wg} / \gamma_0, \quad (5.4)$$

$$\beta'_{\perp} = \gamma_{x,ng} / \gamma_0, \quad (5.5)$$

$$\gamma_0 = \gamma_{y,wg} + \gamma_{y,ng} + \gamma_{x,wg} + \gamma_{x,ng}, \quad (5.6)$$

where the "l" superscript indicates that the photon is lost and not emitted into the PCW. This notation will be exploited in analysing the entanglement protocol (chapter 7). The cyclicity can then be expressed as

$$C = \frac{\gamma_y}{\gamma_x} = \frac{\gamma_{y,wg} + \gamma_{y,ng}}{\gamma_{x,wg} + \gamma_{x,ng}} = \frac{\beta_{\parallel} + \beta'_{\parallel}}{\beta_{\perp} + \beta'_{\perp}}. \quad (5.7)$$

Note that the non-radiative decay rate  $\gamma_{nr}$  introduced in (2.72) is assumed zero, as we are only interested in the photonic properties. Additionally, no distinction is been made between the left and right propagating waveguide modes. A two-sided waveguide simply incurs a 50% loss when only collecting from one grating coupler.

The analysis will now focus on the  $n_g = 20$  simulation which predict  $\gamma_0 \approx 2 \text{ ns}^{-1}$  using (5.1). Hence, this  $n_g$  bears the greatest resemblance to the measured  $\gamma_0(X^+) = 2.48 \text{ ns}^{-1}$  and  $\gamma_0(X^-) = 3.07 \text{ ns}^{-1}$  (section 4.3). Figure 5.2 shows the spatial dependence of all 4 Purcell factors and the derived  $C$ . Couplings to non-guided modes  $F_{x,ng}$  and  $F_{y,ng}$  are strongly suppressed, have weak spatial structure and only differ by a factor 1.9 at the unit cell centre. By contrast, the waveguide couplings  $F_{x,wg}, F_{y,wg}$  have a strong spatial dependence. The waveguide field can have a strong x-component as it does not fulfil the paraxial approximation [16]. At the waveguide centre,  $F_{y,wg}$  dominates the decay, resulting in a peak cyclicity of 57. Here,  $F_{x,wg} = 0$ , and cyclicity is limited by  $F_{x,ng}$ . Increasing  $n_g$  leads to higher  $C$ , as  $F_{x,ng}$  remains constant but  $F_{y,wg}$  increases linearly with  $n_g$  as given by (2.71). The probability of waveguide emission  $\beta_{wg} = \beta_{x,wg} + \beta_{y,wg}$  remains high across the cell centre. Hence, achieving high  $C$  does not compromise the high  $\beta$ -factor for which PCWs are renowned. As  $C$  depends on minimising  $F_{x,wg}$  it gains a strong spatial dependence.

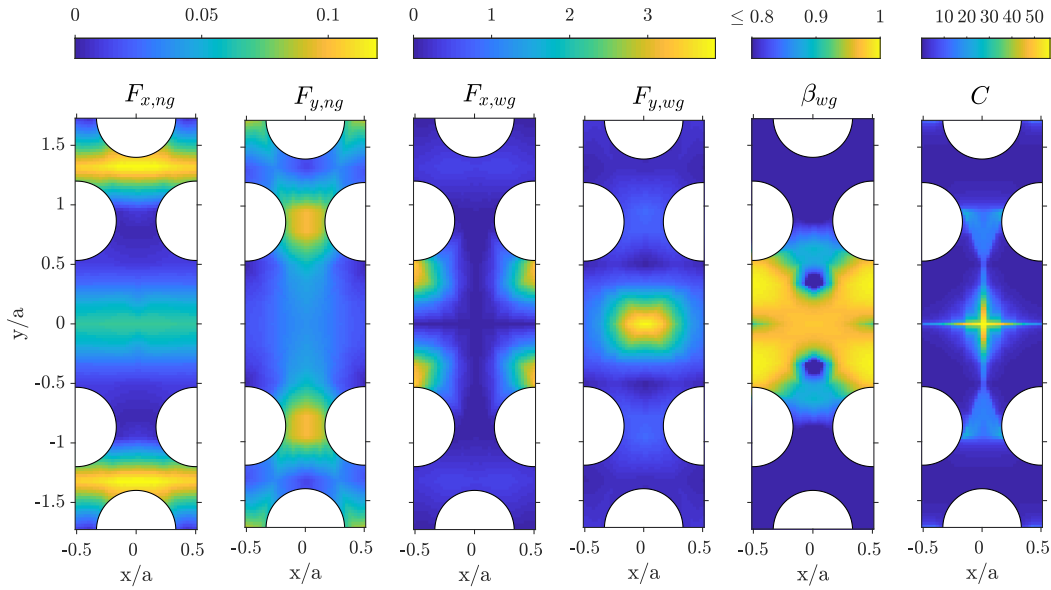


**Figure 5.2:** Numerical simulation of a PCW unit cell (cropped in  $y$ -direction) for  $n_g = 20$  showing Purcell factors, waveguide  $\beta$  and cyclicity. White circles indicate air holes. Axes denote distance in units of the lattice constant  $a = 240$  nm. Values at the origin:  $F_{x,ng} = 0.069$ ,  $F_{y,ng} = 0.037$ ,  $F_{x,wg} = 0.000$ ,  $F_{y,wg} = 3.667$ ,  $F_{tot} = 3.973$ ,  $\beta_{wg} = 0.973$ ,  $C = 56.9$ .

This work has taken the approach of finding a well-coupled QD through spectroscopy. However, it is instructive to consider the requirements for deterministically achieving high  $C$ . One strategy for self-assembled QDs would be to deterministically fabricate the PCW relative to a target QD as demonstrated in Ref. [53]. To evaluate the positioning requirements, imagine placement with perfect accuracy but limited precision, such that the emitter position follows a 2D normal distribution

$$\mathcal{N}(x, y; \sigma) = \exp\left(-\frac{x^2 + y^2}{2\sigma}\right) \frac{1}{2\pi\sigma^2}, \quad (5.8)$$

which assumes an equal uncertainty  $\sigma$  on both  $x$  and  $y$ . An average  $C$  can be estimated by weighting the simulated  $C$  according to (5.8). This dependence is shown in figure 5.3. A high level of precision beyond the current state-of-the-art is required to fully realise the cyclicity. Figure 5.3 also shows the group index  $n_g = 56$  which is realistic (Ref. [44] achieved  $n_g = 50$  in a GaAs PCW) and results in a maximal  $C = 144$ . Deterministic cyclicity also requires optimising the PCW parameters (eg. hole radius) to achieve a certain  $n_g$  for a target QD. Due to the inhomogeneous wavelength distribution of self-assembled dots, this would require spectroscopy prior to fabrication.

Thus far, we have assumed the dipoles to align strictly along  $x$  and  $y$ . As it will be evident from section 5.4, this is generally the case, and the magnetic field does not allow a rotation of the dipoles. Evaluating  $C$  given arbitrary dipoles is not possible given the current simulation data, as it does not contain the phase between the  $x$  and  $y$  field components. E.g. the case  $F_{x,wg} = F_{y,wg}$  could arise from both a

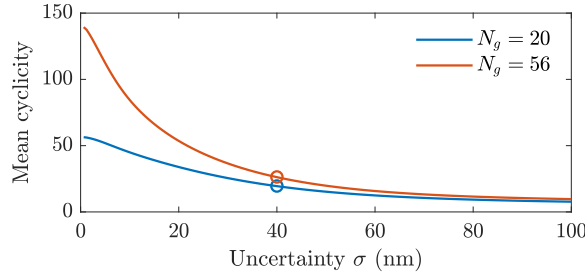


**Figure 5.3:** Mean cyclicity following positioning uncertainty in (5.8). Legends indicate simulation group index. Circles denote the 40 nm precision obtained in Ref. [53].

diagonal or a circular electric field, and only the first case could allow a selective enhancement of orthogonal linear dipoles.

## 5.2 SPIN PUMPING MEASUREMENTS

We now estimate the cyclicity of QD<sub>1</sub> by measuring the spin pumping rate introduced in section 2.5) using the two-colour pumping sequence in figure 5.4a. For X<sup>-</sup>, an AOM generates a 300 ns preparation pulse resonant with  $y_1$  which prepares  $|\uparrow\rangle$ . Next, a 300 ns probe pulse resonant with  $y_2$  pumps the spin back to  $|\downarrow\rangle$ .  $V_{bias}$  is chosen to operate in the spin-pumping region.  $\gamma_{osp}$  is estimated by fitting the fluorescence decay during the probe with the model  $I(t) = I_1 e^{-\gamma_{osp} t} + I_0$ . The probe pulse is generated with an EOM, which achieves a highly square pulse shape (rise time  $\approx 300$  ps). The probe power is then varied, yielding the power-dependent  $\gamma_{osp}$  in figure 5.4b. Measuring X<sup>+</sup> follows the same procedure except for the inclusion of a 100 ns ABB pulse at the start of the pulse sequence used to initialise the hole. Laser background measured at a non-resonant  $V_{bias}$  is subtracted from the histograms. This is mainly relevant for X<sup>-</sup>, which generally features more laser scatter.

Great experimental care is taken to ensure the maximal optical pumping for a given power. Both laser polarisations are optimised to exclusively drive the  $y$ -transitions. Furthermore, the probe frequency is scanned in 200 MHz increments to compensate power tuning, see figure 5.5. The frequency producing the highest  $\gamma_{osp}$  is used in the subsequent analysis. The preparation laser is not scanned, as high fidelity state preparation prior to the probe does not influence the  $\gamma_{osp}$  estimate.  $\gamma_{osp}$  is taken to saturate according to

$$\gamma_{osp} = \gamma_x \int_{-\infty}^{\infty} \frac{\Omega_p^2}{2\Omega_p^2 + \gamma_0^2 + 4\Delta_n^2} \mathcal{N}(\Delta_n; \sigma) d\Delta_n, \quad (5.9)$$

where  $\Omega_p = \gamma_0 \sqrt{P/P_{sat}}$  and  $\gamma_0$  is the already characterised trion lifetime. Equation (5.9) is based on (2.45), but replaces the laser detuning with a spectral diffusion  $\Delta_n \sim \mathcal{N}(\sigma)$ , where  $\sigma$  is the independently characterised broadening. Spectral diffusion subtly modifies the saturation curve, but only affects the  $\gamma_x$  estimate by  $< 3\%$ . The rates in figure 5.4c are fit according to (5.9) with  $\gamma_x$  and  $P_{sat}$  as free

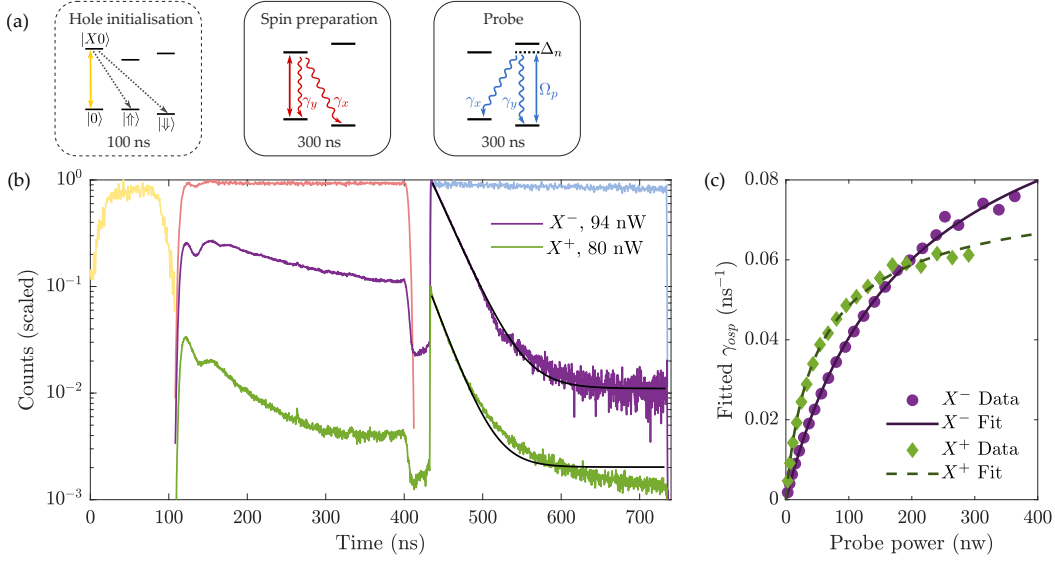


**Figure 5.4:** Two-colour optical pumping experiment for estimating optical cyclicity. **(a)** Energy level diagrams corresponding to optional hole initialisation and optical pumping pulses. **(b)** Examples of optical pumping fluorescence histograms. Yellow, red and blue curves represent laser pulses in (a). Histograms for both  $X^-$  and  $X^+$  are shown in purple and green, respectively, and offset by  $\times 0.1$  for clarity. The probe pulse is fit with an exponential decay (black line) to estimate  $\gamma_{osp}$ . **(c)** Extracted  $\gamma_{osp}$  rates fitted using (5.9).

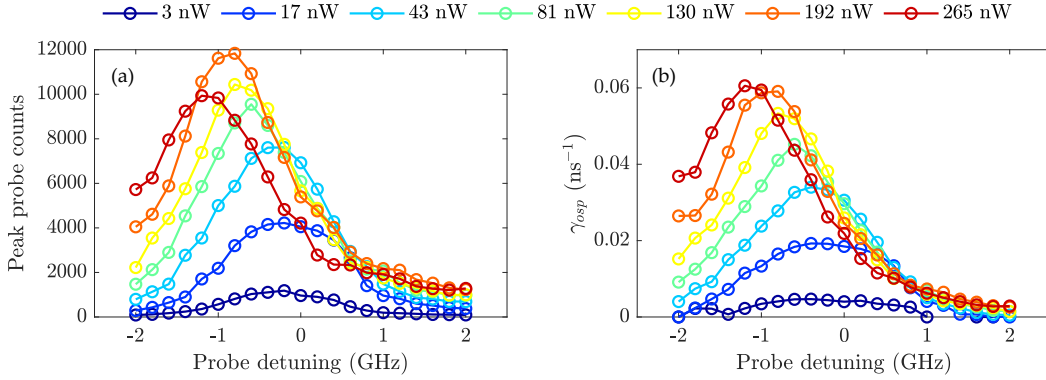


**Figure 5.5:**  $X^+$  spin pumping for various powers (legend) and detunings. **(a)** Maximum count rate during probe pulse. **(b)** Probe pumping rate extracted from fits. Increasing the pumping power monotonically *power tunes* the resonance frequency.

parameters, yielding

$$\gamma_x(X^-) = (0.243 \pm 0.005) \text{ ns}^{-1}, \quad (5.10)$$

$$\gamma_x(X^+) = (0.158 \pm 0.002) \text{ ns}^{-1}. \quad (5.11)$$

The cyclicity is then calculated from  $C = \gamma_y/\gamma_x = (\gamma_0 - \gamma_x)/\gamma_x$  yielding

$$C(X^-) = 11.6 \pm 0.4, \quad (5.12)$$

$$C(X^+) = 14.7 \pm 0.2, \quad (5.13)$$

where the errors from  $\gamma_x$  and  $\gamma_0$  have been propagated. Both  $X^-$  and  $X^+$  exhibit substantially enhanced cyclicity. This is a result of simultaneous  $\gamma_x$  inhibition and  $\gamma_y$  enhancement. Both trions are enhanced despite a 3.8 nm spectral separation, confirming the broadband character of polarisation based enhancement.

### 5.2.1 SPIN PUMPING FIDELITY

An additional quantity of interest derived from spin pumping is the initialisation fidelity  $F_i$ . Given the QD state  $\hat{\rho}$  at the end of the probe pulse, we define the initialisation fidelities as

$$F_i(X^-) = \langle \downarrow | \hat{\rho} | \downarrow \rangle, \quad (5.14)$$

$$F_i(X^+) = \langle \uparrow | \hat{\rho} | \uparrow \rangle. \quad (5.15)$$

We now follow the derivation in Ref. [32] and estimate  $F_i$  by comparing the count rates at the start and the end of the probe pulse. We analyze the dynamics according to the energy level diagram in figure 2.5. Following the preparation laser, the system will be prepared in the state  $\hat{\rho} = \rho_{11}(0) |1\rangle\langle 1| + (1 - \rho_{11}(0)) |0\rangle\langle 0|$ . The probe laser is then turned on. In the limit of  $\gamma_0 \gg \gamma_x$  the states  $|1\rangle$  and  $|2\rangle$  reach an internal equilibrium quantified by  $\Theta = \rho_{22}/(\rho_{11} + \rho_{22})$  before any population is pumped into  $|0\rangle$ . In this approximation the peak fluorescence  $I_{peak}$  at the start of the probe pulse ( $t = t_{peak}$ ) can be expressed as

$$I_{peak} = \alpha \rho_{22}(t_{peak}) = \alpha \Theta \rho_{11}(0), \quad (5.16)$$

where  $\alpha$  relates the population of  $|2\rangle$  to the detected intensity. After a period of optical pumping, the system reached an equilibrium with populations  $\rho_{11}(\infty) = (1 - A)(1 - \Theta)$ ,  $\rho_{22}(\infty) = (1 - A)\Theta$  and  $\rho_{00}(\infty) = A$  where  $0 \leq A \leq 1$ . At this point the fluorescence  $I_{ss}$  follows

$$I_{ss} = \alpha \rho_{22}(\infty) = \alpha \Theta (1 - A). \quad (5.17)$$

When the probe laser is turned off the population in  $|2\rangle$  will decay to  $|0\rangle$  with probability  $\gamma_x/\gamma_0$ . Hence, after the probe pulse, the population in state  $|0\rangle$  and thus the fidelity becomes

$$F_{osp} = \rho_{00}(\infty) + \frac{\gamma_x}{\gamma_0} \rho_{22}(\infty) = A + \frac{\gamma_x}{\gamma_0} (1 - A) \Theta. \quad (5.18)$$

Solving equations (5.16-5.18) gives the final expression

$$F_{osp} = 1 - \rho_{11}(0) \frac{I_{ss}}{I_{peak}} + \rho_{11}(0) \Theta \frac{\gamma_x}{\gamma_0} \frac{I_{ss}}{I_{peak}}. \quad (5.19)$$

In practice we neglect the final term and assume  $\rho_{11}(0) = 1$ , thereby estimating a lower bound. The procedure for obtaining  $I_{peak}$  and  $I_{ss}$  is illustrated in figure 5.6a and the extracted fidelity estimates are given in figure 5.6b. At low powers the system does not reach a steady-state during the finite probe duration, thus resulting in reduced fidelity. We believe the fidelity falloff at high powers is due to a combination of optical repumping and reduced efficiency of the initialization laser resulting in  $\rho_{11}(0) < 1$ . A more accurate measurement should also optimise the detuning of the preparation laser. The best fidelities for the two charges systems are  $F_i(X^-) = 99.1\%$  and  $F_i(X^+) = 98.6\%$ , although the accuracy of the  $X^-$  estimation may be biased by the use of background subtraction, as the laser scatter and QD fluorescence can interfere coherently. The calculated  $F_i$  exceeds the highest values

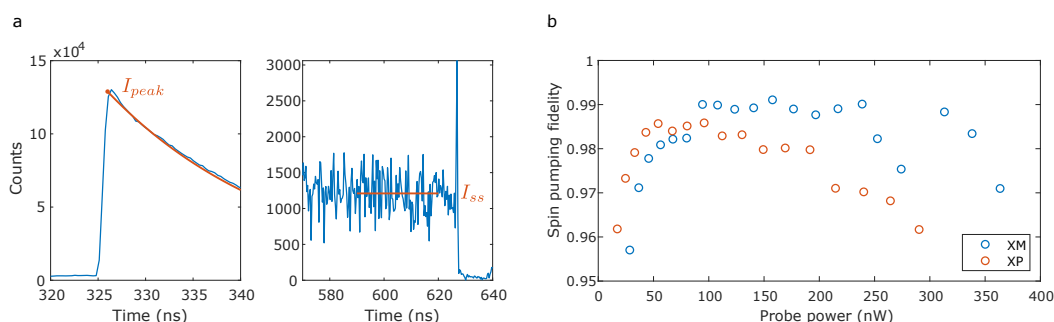


**Figure 5.6:** (a) Spin pumping fidelity estimation of XM with 158 nW probe power. Two different sections of the probe pulse fluorescence are plotted (blue). The peak intensity  $I_{peak}$  is found by fitting the fluorescence with a bi-exponential decay (red) and evaluating the fit at the time where the laser pulse reaches 50% intensity. A bi-exponential is used as an empirical model as it provides an improved fit. The steady-state fluorescence  $I_{ss}$  is estimated by taking a mean (red) over the last 30 ns of the histogram. Laser background correction is performed by subtracting a laser background histogram recorded at a non-resonant  $V_{bias}$ . (b) Estimated spin pumping fidelity as a function of probe power for the XM and XP charge systems.

previously reported in photonic nanostructures [54–56]. Part of the success can probably be attributed to the polarisation control, which reduces optical re-pumping from the x-transitions. A downside of high  $C$  is the prolonged pumping time. The  $1/e$  pumping time using a  $y$ -transition is limited to  $2/\gamma_x(X^+) = 12.7$  ns. Pumping an  $x$  transition would lead to faster initialisation but greatly reduced  $F_i$ , as the two x-transitions have far greater frequency overlap. The fact that x-transitions pump more efficiently than y-transitions further increases requirements on pumping polarisation.

### 5.3 EMISSION SPECTRUM

To further probe the origin of cyclicity, the spectrum of spontaneous  $X^-$  emission is measured. By collecting from a grating coupler, we only detect photons emitted into the PCW mode, thus enabling estimation of  $A_{wg} = \beta_{\parallel}/\beta_{\perp}$ . The QD is excited through P-shell excitation, which we find is effective at populating both  $X^-$  trions

in the presence of a magnetic field. The emission is first filtered by a grating filter to remove the P-shell laser and secondly by a Fabry-Perot cavity (section 3.4.3). Using the locking laser in figure 3.6d, the cavity resonance  $\nu_{cav}$  is scanned with 50 MHz steps. Due to the short cavity FSR  $\nu_{fsr} = 10.55$  GHz, more than one emission line may be in cavity resonance. For this reason, the magnetic field is lowered to  $B_y = 1.3$  T, which provides the best separation between emission lines. The total splitting  $\Delta_0/(2\pi) = 12.47$  GHz still exceeds  $\nu_{fsr}$  causing the highest energy transition to be folded back one FSR as indicated on the inset of figure 5.7.

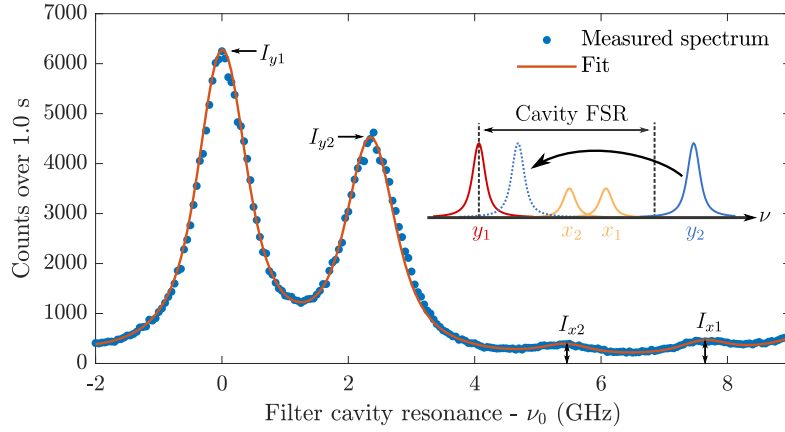


**Figure 5.7:** Emission spectrum of  $X^-$  following P-shell excitation at  $B_y = 1.3$  T resolved by a scanning Fabry-Perot cavity.  $V_{bias} = 1.30$  V. Data shows an average of 10 scans.  $\nu_0 = 315.97$  THz. Emission lines are reordered by the cavity according to the inset. Transition names correspond to figure 5.1a.

The QD emission is modelled according to

$$I_{QD}(\nu) = \sum_{i=1}^4 A_i V(\nu - \nu_0^{(i)}, \gamma_0, \sigma), \quad (5.20)$$

where  $A_i$  is amplitude of the  $i$ -th transition,  $V$  is the Voigt lineshape (2.49),  $\nu_0^{(i)}$  is the  $i$ -th resonance frequency,  $\gamma_0$  is the trion decay rate and  $\sigma$  is the inhomogeneous broadening. This spectrum is numerically convolved with the cavity transmission [57] given by

$$T(\delta) = \frac{1}{1 + F \sin^2(\pi\delta/\nu_{fsr})}, \quad (5.21)$$

where  $\delta$  is detuning from cavity resonance,  $\nu_{fsr}$  is the FSR and  $F$  is the cavity finesse. The detected intensity as function of cavity resonance is then given by

$$I_{detected}(\nu_{cav}) = \int_0^\infty d\nu' I_{QD}(\nu') T(\nu_{cav} - \nu'). \quad (5.22)$$

The parameters  $A_i$ ,  $\nu_0^{(i)}$  and  $\sigma$  are kept free while  $\gamma_0$ ,  $F$  and  $\nu_{fsr}$  are fixed based on lifetime measurements and cavity characterisation.

The measured spectrum and fit are both given in figure 5.7, which reveals all 4 transitions. The data is excellently fit by the model and yields the emission intensity of all four transitions. As the  $y_1$  and  $y_2$  transitions are not equally bright, emission lines originating from the same trion are compared, giving the ratios  $I_{y1}/I_{x1} = 21.8 \pm 0.5$  and  $I_{y2}/I_{x2} = 20.3 \pm 0.6$ . Uncertainties are estimated by analysing 10 separate cavity scans and taking the mean. The two ratios are statically compatible ( $1.9\sigma$  deviation) and quantify the trions' strong preference to decay into the PCW via the  $y$ -transitions. Taking the mean ratio yields an estimate of the waveguide coupling asymmetry  $A_{wg}(X^-) = \gamma_{y,wg}(X^-)/\gamma_{x,wg}(X^-) = 21.1 \pm 0.4$ . This value exceeds  $C$  as it does not include contributions from non-guided modes.

The measurement was attempted on  $X^+$  but P-shell excitation proved too inefficient to achieve sufficient counts.

## 5.4 RESONANT TRANSMISSION

The asymmetric WG coupling can also be explored with RT measurements. A probe laser propagating through the waveguide can couple to all four transitions leading to a probe reflection. However, this interaction will also optically pump the spin. This can be mitigated by measuring the  $X^-$  in the co-tunnelling regime (section 2.2). In the limit  $\kappa \gg \gamma_{osp}$ , spin flips will prepare the thermal state  $\hat{\rho} \approx 0.53|\uparrow\rangle\langle\uparrow| + 0.47|\downarrow\rangle\langle\downarrow|$  as given by the Boltzmann distribution for the temperature  $T = 4.2$  K and  $B_y = 2$  T. Measurements are performed with a weak RT probe,  $\Omega \ll \gamma_0$ . figure 5.8a shows the  $X^-$  RT plateau map, which features a clear spin pumping region and bears a strong resemblance to the fluorescence plateaus observed in resonant excitation (figure 4.9a). Additionally, we perform fine frequency scans at the voltages  $V_{ref} =$

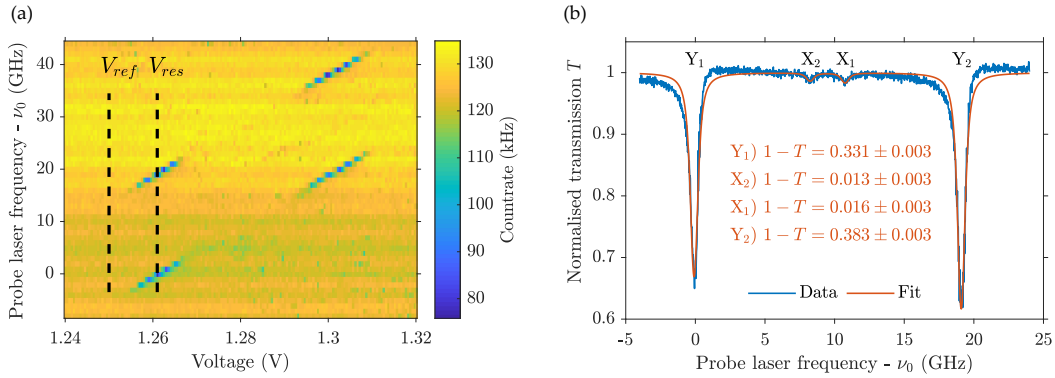


**Figure 5.8:** (a)  $X^-$  resonant transmission plateau map at  $B_y = 2$  T.  $V_{bias}$  and the probe laser frequency are swept, revealing 4 regions of reflection corresponding to the two well coupled  $y$ -transitions and the two cotunnelling regions.  $\nu_0 = 315.941$  THz. (b) Fine transmission scan at with 20 MHz step size. Normalised transmission is calculated by measuring at the two voltages given in (a). The dip amplitudes are based on a fit with (5.23).  $\nu_0 = 315.941$  THz.

1.250 V and  $V_{res} = 1.261$  V (indicated on figure 5.8a) in order to calculate a normalised transmission  $T = T(V_{res})/T(V_{ref})$ . This removes variations in the bare PCW transmission. This method yields the transmission in figure 5.8b where weak transmission dips associated with the  $x$ -transitions become visible. The dips are quantified by fitting to the model

$$T(\nu) = 1 - \sum_{i=1}^4 A_i \cdot V(\nu - \nu_0^{(i)}; \gamma_0, \sigma), \quad (5.23)$$

where  $A_i$  is the  $i$ -th dip amplitude,  $V$  is the Voigt lineshape,  $\nu_0^{(i)}$  is the spectral position of the  $i$ -th dip,  $\gamma_0$  is the trion lifetime and  $\sigma$  is the inhomogeneous broadening. Only  $\gamma_0$  is fixed based on lifetime measurements. This model does not capture the Fano lineshape (similar to  $X^0$  in figure 4.2), but is sufficient for estimating the parameters of interest. From this we estimate an electron Zeeman splitting  $\omega_e/2\pi = 10.7$  GHz and hole splitting  $\omega_h/2\pi = 8.33$  GHz at  $B_y = 2$  T, corresponding to an electron g-factor x-component of  $g_{e,x} = 0.388$  and hole g-factor x-component of  $g_{h,x} = 0.298$ . Furthermore, we find a  $\sigma(X^-)/2\pi = 140$  MHz broadening (discussed in section 4.7).

Similar to the emission spectrum, the RT spectrum features a pronounced ratio between  $y$  and  $x$  dips,  $(1 - T_{y1})/(1 - T_{x1}) = 21 \pm 4$  and  $(1 - T_{y2})/(1 - T_{x2}) = 29 \pm 7$ , again indicating a strong preferential WG coupling. However, relating these ratios to  $A_{wg}$  is more theoretically involved and is not attempted here. The difference between the  $y_1$  and  $y_2$  transitions,  $(1 - T_{y2})/(1 - T_{y1}) = 1.157 \pm 0.014$  is compatible with the Boltzman factor  $e^{-\omega_g \hbar / (k_B T)} = 1.132$ . Hence, the difference is simply a product of the thermal spin state occupations. A pulsed measurement where the spin is initialised through optical pumping yields greater transmission dips but is not covered here.

Next, the CW RT experiment is repeated for 3 different in-plane directions of the magnetic field, see figure 5.9a. Strikingly, no significant change in the dip amplitudes is observed. If the  $X^-$  dipoles were aligned strictly parallel and perpendicular to  $\mathbf{B}$ , rotating  $\mathbf{B}$  by  $90^\circ$  should invert the dip amplitudes and a  $\mathbf{B}$  orientation resulting equal coupling, i.e.  $\beta_\perp = \beta_\parallel$  should exist. Evidently, this is not the case. Hence, we must be in the limit where the hole Zeeman splitting is dominated by hole mixing (section 2.3.2). The strain direction is most likely dictated by crystallographic axes which coincide with the PCW. A change in Zeeman splitting is observed upon rotating  $\mathbf{B}$  (figure 5.9b). However, as  $\omega_e$  and  $\omega_h$  increase by the same ratio, we cannot exclude that  $|\mathbf{B}|$  is simply increasing as the result of an imperfectly calibrated vector magnet.

The observation of preferential  $y$ -dipole coupling is observed across multiple QDs indicating a general trend, see figure 5.10. According to the numerical simulations (figure 5.2), regions should exist where  $x$ -dipoles dominate the WG coupling resulting in an inverted RT spectrum. However, QDs in these regions will be in close proximity to air interfaces and may fail our selection process due to increased broadening.

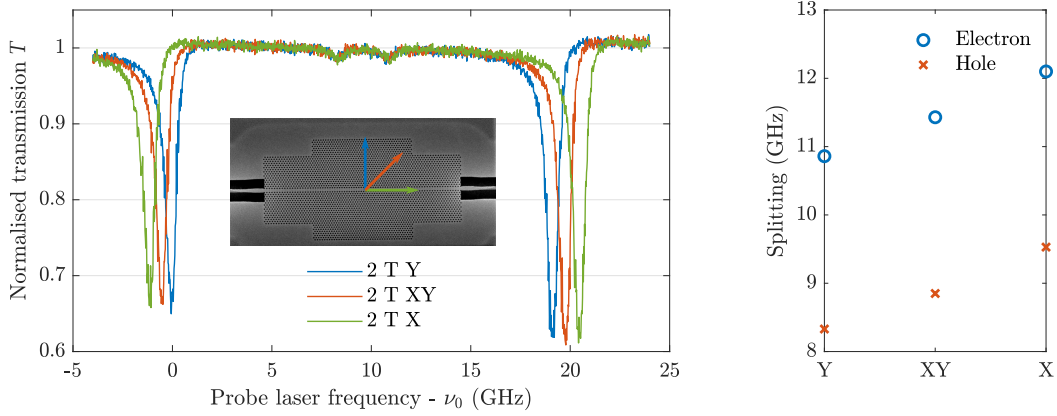


**Figure 5.9:** (a) Normalised  $X^-$  transmission in the cotunnelling regime for 3 different in-plane magnetic field orientations (legend and inset). Rotating the magnetic field does not alter the dip amplitudes. (b) Magnetic field dependent Zeeman splittings extracted from (a).

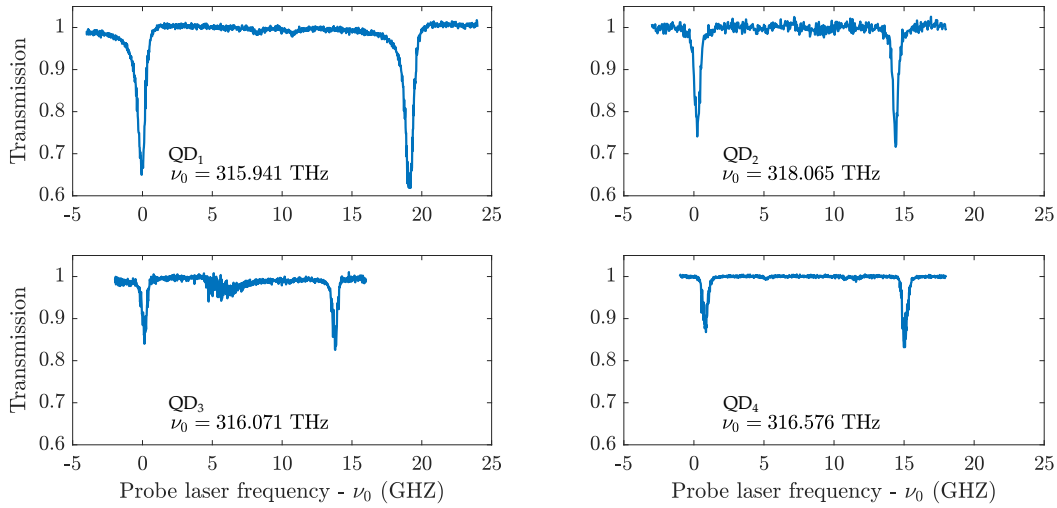


**Figure 5.10:** Resonant  $X^-$  transmission in the cotunnelling regime and  $B_y = 2$  T for multiple QDs. QD<sub>1</sub> is the main QD studied in this work. QD<sub>2</sub> is located in the same PCW as QD<sub>1</sub>. QD<sub>3</sub> and QD<sub>4</sub> are located in a second PCW with identical dimensions.

## 5.5 INTERPRETATION OF MEASURED CYCLICITY

The different experiments conducted on QD<sub>1</sub> now enable a discussion of the observed cyclicity. One concern is that intrinsic factors such as an asymmetric QD shape or strain might contribute to  $C$ . This is hard to completely exclude, as the QD was not characterised before PCW fabrication and direct measurements of oscillator strengths (eg. through resonant saturation measurements) is difficult due to the polarisation dependent coupling to the far-field. However, based on the observed  $X^0$  FFS of 6.45 GHz (26.7  $\mu$ eV) and available literature, a significant asymmetry is unlikely. Firstly, our FFS coincides with the average value for bulk

InAs QDs found in Ref. [58]. Secondly, InAs QDs with FSS values of 120  $\mu\text{eV}$  and 150  $\mu\text{eV}$  were investigated in Ref. [26] without displaying any oscillator strength asymmetry between dipoles. Finally, Ref. [29] performed resonant spectroscopy on  $X^+$  in a Voigt magnetic field. The QDs were grown by the same method as the ones in this study but were placed in a bulk-like nanostructure and displayed  $\approx 20\%$  oscillator strength asymmetry between the  $x$  and  $y$ -dipoles. Hence, we believe that any oscillator strength asymmetry will have a very minor contribution towards the cyclicity.

Understanding the factors limiting cyclicity is complicated by our ignorance of the QD position. Distinguishing non-ideal placement from other errors is non-trivial. However, a qualified guess can be made for  $X^-$  using the using the observed quantities

$$A_{wg}(X^-) = \frac{\beta_{\parallel}}{\beta_{\perp}} = 21.1, \quad (5.24)$$

$$C(X^-) = \frac{\beta_{\parallel} + \beta'_{\parallel}}{\beta_{\perp} + \beta'_{\perp}} = 11.6, \quad (5.25)$$

which, in conjunction with the normalisation of  $\beta$  and the simplified assumption of equal free space coupling,  $\beta'_{\parallel} = \beta'_{\perp} = \beta_{ng}/2$ , gives a solvable system of equations yielding

$$\beta'_{\parallel} = \beta'_{\perp} = \beta_{ng}/2 = \frac{C - A_{wg}}{(1 - A_{wg})(1 + C)} = 0.0374, \quad (5.26)$$

$$\beta_{\parallel} = (1 - \beta_{ng}) \frac{A_{wg}}{1 + A_{wg}} = 0.88, \quad (5.27)$$

$$\beta_{\perp} = (1 - \beta_{ng}) \frac{1}{1 + A_{wg}} = 0.042. \quad (5.28)$$

This implies that  $x$ -transitions couple roughly equally to the WG mode and non-guided modes. Using (5.1) and (5.6), we can estimate the Purcell factor

$$F_{x,ng} = 2 \frac{\gamma_{x,ng}}{\gamma_0^{hom}} = 2\beta'_{\perp} \frac{\gamma_0}{\gamma_0^{hom}} = 0.232. \quad (5.29)$$

This is significantly higher than the 0.069 predicted by simulation and could be the product of fabrication imperfections. Such imperfections become especially important near the band edge [43] and should thus mostly impact  $X^-$ . Such a frequency-dependent  $F_{x,ng}$  could explain our observation of  $C(X^+) > C(X^-)$ . It also interesting to note that  $X^0$  only exhibited a factor 4 asymmetry between the  $\gamma_x$  and  $\gamma_y$  in figure 4.4a. We suspect this as a result of  $X^0$  having slightly differently angled dipoles. When optimising the far-field laser polarisation for a single dipole, we also found a slightly different optimum for  $X^0$  (not shown).

In Ref. [59] we performed optical pumping on a different QD from the same sample and demonstrated  $\gamma_x(X^-) = 0.089 \text{ ns}^{-1}$ ,  $\gamma_y(X^-) = 0.669 \text{ ns}^{-1}$  and  $C = 7.6$ , showing that higher levels of inhibition are indeed possible. In this experiment,  $C$  was

mainly limited by low levels of Purcell enhancement.

## 5.6 CYCLICITY APPLICATIONS: SINGLE-SHOT READOUT

One application of high cyclicity is performing single-shot readout. Single-shot readout refers to the ability to infer the spin state without post-selection and is crucial for applications such as deterministic photon-photon gates [60]. This can be performed with the already demonstrated optical pumping. If fluorescence is detected, one concludes the spin to be in the state resonant with the laser. This has been demonstrated for QDs in Faraday geometry [61] but is difficult for QDs in Voigt geometry, as optical pumping only scatters  $C + 1$  photons on average.

The single shot readout fidelity (derived in appendix C) is

$$F_{ss} = 1 - \frac{1}{2} \left( \frac{1}{1 + C\eta} \right), \quad (5.30)$$

where  $C$  is the cyclicity and  $\eta$  is the total detection efficiency. figure 5.11 shows  $F_{ss}$  for different values of  $\eta$  and  $C$ .  $\eta = 7.2\%$  corresponds to the source-to-fiber efficiency in Ref. [18] while  $\eta = 78\%$  corresponds to the optimal source-to-fiber efficiency predicted in Ref. [18] given realistic improvements. The optimistic values of  $\eta = 78\%$  and  $C = 144$  (achievable with  $n_g = 56$ ) gives  $F_{ss} = 99.56\%$ . This neglects other possible errors such as laser background, spin flips and dark counts. By comparison, experiments on comparable systems have already achieved  $F_{ss} > 95\%$  in NV-centres [62],  $F_{ss} = 94.5\%$  in  $\text{Er}^+$  ions coupled to a nanophotonic cavity [63],  $F_{ss} = 96\%$  in QD molecules [64] and  $99.98\%$  in SiV-centres integrated in a nanophotonic cavity [65]. While Voigt geometry QDs may in principle achieve high  $F_{ss}$ , they will likely never beat systems with intrinsic cyclicity. However, the success probability of heralded spin readout (i.e. post selecting on measuring more than one photon) will naturally benefit from increased  $\eta$  and  $C$ .

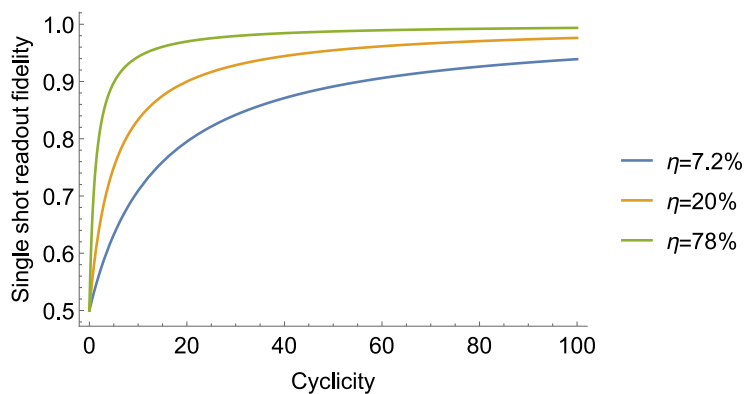


**Figure 5.11:** Single shot readout fidelity for different values of cyclicity and detection efficiency  $\eta$ .

## 5.7 DISCUSSION

This work represents the first demonstration of waveguide induced cyclicity of a QD. A key characteristic is the broadband nature of the enhancement. Both charge states show  $> 10\times$  cyclicity enhancement despite 3.8 nm spectral separation, a comparatively low magnetic field can be applied and no frequency tuning is required as opposed to cavity systems. Furthermore, the ability to excite from free space with arbitrary polarisation represents a flexible side channel, which enables high fidelity spin initialisation and, as will be demonstrated in chapter 6, all-optical coherent spin control. Another possible advantage of the waveguide is easier integration with planar on-chip photonics such as routing [66], frequency conversion [67] and detection [68]. The PCW/QD system constitutes a coherent spin-photon interface in which the spin state can control the WG transmission. This enables applications such as single-photon transistors [69–71], deterministic Bell state analyzers [72], and quantum gates [60, 73].

By contrast, comparable works have focused on using cavity systems. Several works on photonic crystal cavities [55, 71] have achieved selective enhancement, with a convincing  $C = 10$  being measured in Ref. [56] through a time-resolved spin pumping method similar to section 5.2.  $C = 5$  also has been achieved with a micropillar cavity [54]. Elliptical micropillar cavities [74] also show promise, as the cavity  $x$  and  $y$  polarised modes are non-degenerate, although  $C$  has yet to be quantified in this system.

A very strong demonstration of photonically induced cyclicity has recently been made with  $\text{Er}^+$  ions [63] placed in the evanescent field of a nanophotonic cavity, thereby boosting  $C$  by  $\times 100$ . Despite using a cavity, the enhancement is predominantly due to orthogonal optical dipoles coupling to the cavity mode. In contrast to the QDs studied here, the dipole orientations can be manipulated with  $\mathbf{B}$ , allowing  $C$  to be tuned continuously in the range 4-1000.

Overall, PCWs offer a potentially powerful approach for achieving high optical cyclicity in the Voigt geometry. The goal of increasing  $C$  is synergistic with achieving high  $\beta_{wg}$  (deterministic collection) and suppressing decoherence processes through a Purcell enhanced  $\gamma_0$ . The main challenge is the precise fabrication and positing of the nanostructure as the QD dipoles appear locked by the strain profile.

## 6 | Coherent Spin Control

Achieving coherent spin control is the starting point for realising spin-photon entanglement and spin-based quantum gates. Furthermore, spin control facilitates experiments such as Ramsey and spin-echo which provide information on the spin decoherence processes. In most comparable solid-state spin- $\frac{1}{2}$  systems such as NV-centres, SiV-centres and rare earth ions [75], spin control is achieved by subjecting the spin to a microwave (MW) frequency magnetic field typically delivered by a microwave strip-line antenna. MW-control was attempted on InAs QD electron spins [76] but showed little indication of success, most likely due to rapid spin dephasing. Meanwhile, all-optical spin control has proven successful in several experimental settings such as bulk structures [41, 77, 78], micropillar cavities [54] and photonic crystal cavities [55, 56].

Two methods of optical spin control exist: Ultra-fast rotation pulses with durations  $T_p \sim 5$  ps and slow Raman pulses with durations  $T_p \sim 5$  ns. Both methods build upon the selection rules of the Voigt geometry but offer different advantages. In this project, both schemes were successfully realised. We performed the first demonstration of ultra-fast optical spin control in a waveguide geometry using an electron spin and a nanobeam waveguide. This work will be briefly reviewed, as it has proven useful in understanding the challenges of waveguide integration. The majority of this project has focused on implementing the recently developed Raman scheme of Ref. [78], but adapting it to controlling a positively charged QD in a PCW. The remainder of the chapter deals with this approach, as it is ultimately used for entanglement generation but also bears novelty in terms of technique, nanostructure and charge state. The equations of motion will be derived and the experimental scheme will be explained in great detail. Measurements are then carried out to estimate the spin rotation fidelity,  $T_2^*$  and  $T_2$  times. Finally, the methods of slow and fast spin control will be compared, and other methods of spin control will be discussed.

### 6.1 ULTRA-FAST SPIN CONTROL

Ultra-fast QD spin control has been applied in numerous works [40, 55, 56, 77, 79] and is governed by the level structure in figure 6.1. A fast laser pulse with duration  $T_r \ll \omega_g^{-1}$  (typically generated by a mode-locked Ti:Sapphire laser) is red detuned from the trions by  $\Delta_r$ . The pulse is circularly polarised and drives both Voigt geometry  $\Lambda$ -systems. By going via the virtual state formed by the detuned trions, the spin states are coupled. The spin, which is described in the static lab frame, constantly precesses at frequency  $\omega_g$ . However, during the pulse, the spin

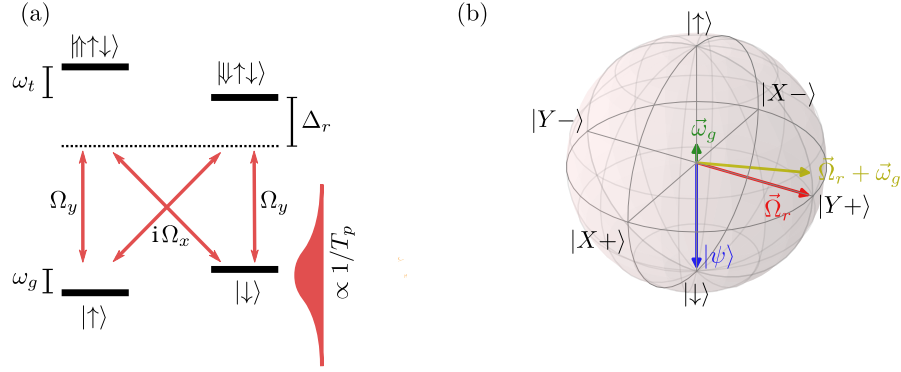


**Figure 6.1:** Overview of ultra-fast spin rotations. **(a)** Level scheme of a Voigt geometry electron spin. A detuned, circularly polarised rotation laser drives both  $\Lambda$ -systems with a pulse of duration  $T_r$  much shorter than the spin precession time  $1/\omega_g$ . **(b)** Effective spin dynamics on the Bloch sphere. The spin always precesses around  $\vec{\omega}_g$ . During a pulse, dynamics are dominated by  $\vec{\Omega}_r$ , but the addition of  $\vec{\omega}_g$  slightly tilts the rotation axis (yellow arrow) away from the equator.

Rabi frequency  $\Omega_r$  momentarily dominates the evolution. Crucially, due to their speed, ultra-fast pulses are largely insensitive to  $T_2^*$  and thereby allow the electron spin to be used as a qubit without nuclear spin narrowing. By implementing spin echo, spin storage times of  $(2.6 \pm 0.3) \mu\text{s}$  have been achieved for electrons [79].

Our work on ultra-fast spin control of a negatively charged QD in a nanobeam waveguide is published in Ref. [80]. A Ramsey experiment was performed in a  $B_y = 2 \text{ T}$  magnetic field yielding the data in figure 6.2. This experiment consisted of a 5 ns optical pumping pulse meant to initialise the spin into  $|\downarrow\rangle$  followed by two  $\pi/2$ -pulses separated by delay  $\tau$ . The first pulse transfers the spin to  $|X-\rangle = (|\uparrow\rangle - |\downarrow\rangle)/\sqrt{2}$  (figure 6.1b) after which the spin freely precesses. The read-out signal is maximized if the delay fulfils  $\tau\omega_g = 2n\pi$ ,  $n \in \mathbb{N}$ , for which the second rotation transfers the spin to  $|\uparrow\rangle$ . The inhomogeneous Overhauser broadening of  $\omega_g$  causes a Gaussian decay of the Ramsey fringes with an inhomogeneous dephasing time of  $T_2^* = (2.2 \pm 0.1) \text{ ns}$ . This is highly comparable with the values observed in bulk structures [38, 40, 79] and indicates that the nanostructure is not further degrading the spin coherence. Another feature of figure 6.2 is the dismal contrast of the Ramsey fringes. This was in part due to an insufficient duration of the pumping pulse, which could not be extended due to a lack of pulse picking at the time. However, modelling indicated that a substantial spin-flip rate of  $\kappa = 0.09 \text{ ns}^{-1}$  was needed to reproduce the visibility. This represented a  $\times 450$  increase over the bare  $\kappa = 0.2 \mu\text{s}^{-1}$  measured in the absence of a rotation laser. Additionally, considerable shifts in the resonant  $V_{\text{bias}}$  were observed with increasing rotation power. It was thus hypothesised, that the intense rotation laser was creating free charge carriers in the material.

Optical spin rotations require a circular polarisation at the position of the QD (derived in section 6.2.2), which is easily achieved in structures with cylindrical

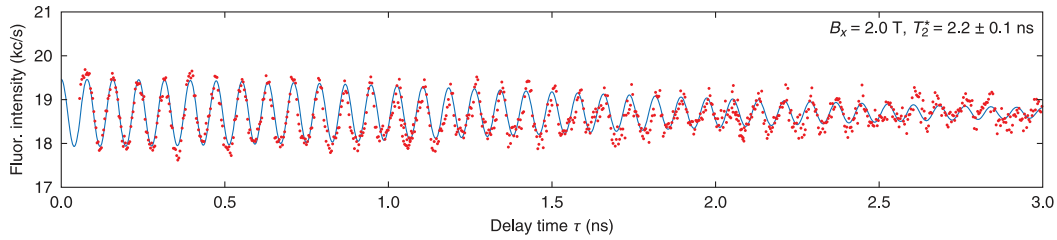


**Figure 6.2:** Ramsey signal measured on an electron spin using two ultra-fast  $\pi/2$  pulses separated by delay  $\tau$ . Using an optical delay line,  $\tau$  is scanned, revealing Ramsey fringes oscillating at  $\omega_g/(2\pi) = (12.70 \pm 0.02)$  GHz. Fitting with the model  $I(t) = A \cos(\omega_g \tau) e^{-(\tau/T_2^*)^2} + B$  yields  $T_2^* = (2.2 \pm 0.1)$  ns and an initial contrast  $A/B = 0.04$ . Figure reproduced directly from Ref. [80].

symmetry. However, as shown in the supplementary material of Ref. [80], the WG results in a non-trivial and non-unitary transformation between the QD-dipoles and the far-field polarisation, which additionally depends on the QD position inside the WG. Thus, the laser polarisation has to be optimised empirically. In the experiment discussed here, the polarisation was optimised by switching the magnetic field to the Faraday geometry and maximizing the laser coupling to the low energy dipole (figure 2.4a), hence yielding a  $\sigma^-$  polarisation.

## 6.2 RAMAN PULSES

The method of slow Raman pulses follows the level structure in figure 6.3a where a rotation laser is detuned by  $\Delta_r$  with respect to the lowest energy transition. In contrast to ultra-fast pulses, the laser field is bichromatic, containing two narrow sidebands detuned  $\pm f$  from the carrier. It is the energy difference of the sidebands which allows an effective coupling between the spin states. Throughout this chapter, a pump laser is used to drive the  $|1\rangle \rightarrow |2\rangle$  transition as indicated on figure 6.3b, allowing spin initialisation and readout.

### 6.2.1 MW SETUP

The sidebands are generated using the MW setup in figure 6.4. A CW MW source produces a sine of frequency  $f/(2\pi) \sim 3$ -4 GHz and fixed power  $\sim 10$  dBm. The signal is split, with one path going through a programmable phase. The two paths, which are equally attenuated, are recombined on a switch. By toggling the switch with a TTL signal from the FPGA, we can switch between MW signals with phase 0 and phase  $\phi_{mw}$ . The calibration of  $\phi_{mw}$  is covered in appendix B. However,  $\phi_{mw}$  can not be modulated quickly and only two different MW phases can be achieved within a pulse sequence. The MW signal is then sent to a secondary switch, which is toggled by a separate FPGA channel and used to cut off the MW signal, allowing the creation of MW pulses. The pulse duration may be incremented in 144 ps steps as limited by the FPGA design. Unfortunately, it is impossible to create pulses separated by less than 8 ns as neighbouring pulses merge due to the non-ideal MW switch. Both switches add considerable switching noise below 1 GHz

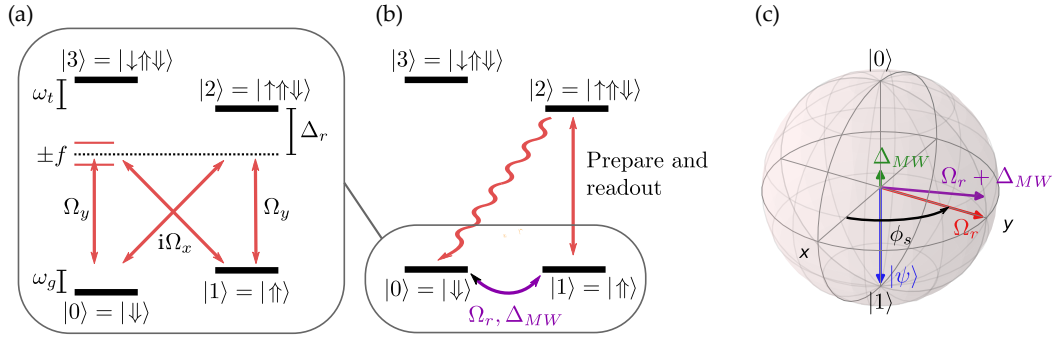


**Figure 6.3:** Principle of Raman pulses. **(a)** Level scheme of a positively charged QD in Voigt geometry. A bi-chromatic laser detuned by  $\Delta_r$  from the lower trion drives both  $\Lambda$ -systems. The laser sidebands match the ground state splitting  $\omega_g$  allowing population transfer. Red arrows indicate the frequency of the suppressed carrier. **(b)** Effective spin dynamics. The laser from (a) results in a ground state coupling with Rabi frequency  $\Omega_r$  and two-photon detuning  $\Delta_{MW}$ . A second laser (red) allows preparation of  $|0\rangle$  and readout of  $|1\rangle$ . **(c)** Spin dynamics on the Bloch sphere. For  $\Omega_r = 0$ , the spin (in the rotating frame) precesses at the detuning  $\Delta_{MW}$ . For  $\Omega_r > 0$ , the spin rotates around the combined axis set by  $\Omega_r$  and  $\Delta_{MW}$  (purple arrow).

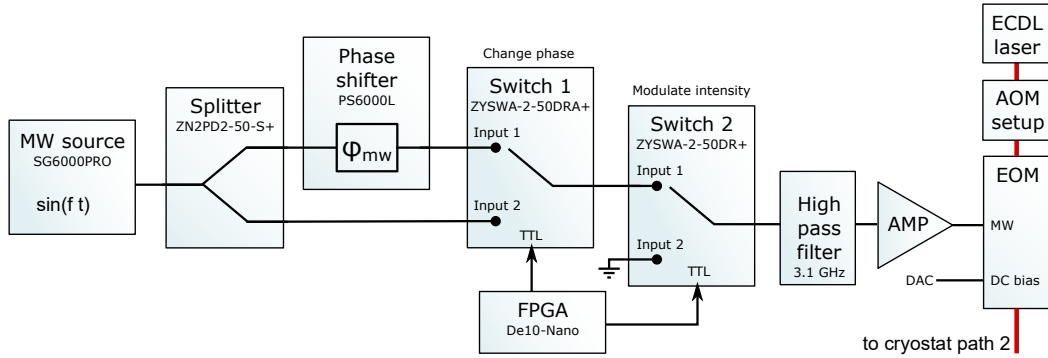


**Figure 6.4:** "Poor man's" setup for MW pulse generation. A source produces a CW MW signal which is divided into two phase-shifted versions. By activating MW switches with an FPGA, the two phases can be toggled and the amplitude can be toggled between fully on and off. The MW field drives an amplitude modulating EOM, which linearly transfers the MW field onto the optical field.

which is filtered by a 3.1 GHz high pass filter. Finally, the MW signal is amplified and drives a fibre-coupled EOM, which provides amplitude modulation using a waveguide-based Mach-Zehnder interferometer.

Given a monochromatic laser input,  $E_{in}(t) = E_0 e^{i\omega_l t}$ , where  $\omega_l$  is the laser frequency, the EOM output field is given by

$$E_{out}(t) = \sin(A \cdot \sin(ft + \phi_{mw}) + \phi_{DC}) E_0 e^{i\omega_l t}, \quad (6.1)$$

where  $f$  is the modulation frequency,  $\phi_{mw}$  is the modulation phase,  $A$  is the modulation index determined by the MW power and  $\phi_{DC}$  is the DC phase shift of

the Mach-Zehnder, which is controlled by a DC voltage bias. Setting  $\phi_{DC} = 0$  and operating in the limit of weak modulation  $A \ll \pi/2$ , the output optical field becomes

$$E_{out}(t) \approx A \cdot \sin(ft + \phi_{mw}) E_0 e^{i\omega t} = \frac{AE_0}{2i} \left( e^{i((\omega_l+f)t+\phi_{mw})} - e^{i((\omega_l-f)t-\phi_{mw})} \right), \quad (6.2)$$

In this limit, the MW signal is linearly transferred onto the optical field. For a sinusoidal modulation, this translates to a pair of sidebands with frequencies  $\pm f$  and phases  $\pm\phi_{mw}$ . By operating at  $\phi_{DC} = 0$ , the carrier is completely suppressed and all the optical power is located in the sidebands needed for spin rotation. Rotation pulses are generated by modulating Switch 2. As only two amplitude levels are permitted by the MW setup, an AOM setup is used to adjust and stabilize the optical power level.  $\phi_{DC}$  is stable on an hour timescale and is periodically optimised by sweeping the DC bias and minimising the transmitted power. When the MW modulation is off (the switches provide 60 dB isolation), the imperfect EOM extinction generates a small laser leakage. Fortunately, the leakage is at the carrier frequency and does not coherently drive the spin. The modulation index  $A$  is optimised to yield high sideband power while remaining in the limit where the output optical power is linear to the MW input power.

### 6.2.2 EFFECTIVE 2-LEVEL DYNAMICS

The starting point for deriving the effective two-level spin dynamics is to adiabatically eliminate the trion states. This approximation is performed and justified in Ref. [77] as well as appendix D. The result of the adiabatic approximation is an effective two-level Hamiltonian of the form

$$\hat{H}_{eff} = \begin{bmatrix} |0\rangle & |1\rangle \\ \omega_{AC} - \omega_g & \frac{\Omega_{eff}}{2} \\ \frac{\Omega_{eff}^*}{2} & 0 \end{bmatrix} \begin{matrix} |0\rangle \\ |1\rangle \end{matrix}. \quad (6.3)$$

$\Omega_{eff}$  is the effective spin coupling and  $\omega_{AC}$  is an AC Stark shift given by

$$\Omega_{eff} = \frac{i}{2} \left( \frac{\Omega_x \Omega_y^*}{\Delta_r} - \frac{\Omega_x^* \Omega_y}{\Delta_r + \omega_t} \right) \stackrel{\Delta_r \gg \omega_t}{\approx} i \frac{\text{Im}\{\Omega_x \Omega_y^*\}}{\Delta_r}, \quad (6.4)$$

$$\omega_{AC} = \frac{\omega_t}{4\Delta_r(\Delta_r + \omega_t)} (|\Omega_y|^2 - |\Omega_x|^2), \quad (6.5)$$

where  $\Omega_x, (\Omega_y)$  is the optical Rabi frequency of the x(y)-transition and  $\omega_t$  is the trion splitting. From (6.4) two important observations are apparent in the limit  $\Delta_r \gg \omega_t$ : Firstly,  $\Omega_{eff}$  is maximised when  $\Omega_x$  and  $\Omega_y$  are  $\pi/2$  out of phase corresponding to circularly polarised light while a linear polarisation gives  $\Omega_{eff} = 0$ . This requirement corresponds to the two  $\Lambda$ -systems interfering constructively. Secondly,  $\omega_{AC} = 0$  for  $|\Omega_y| = |\Omega_x|$  which is also fulfilled for circular polarisation. This motivates the optimisation of the laser polarisation, which was already emphasized in the context of the ultra-fast pulses (section 6.1). All the dynamics of ultra-fast

pulses are contained in (6.3).

Transitioning to the Raman scheme requires modifying  $\Omega_x$  and  $\Omega_y$  to include the time-dependence given by the EOM. Recalling that  $\Omega \propto E_{out}$  (section 2.4.1) and using (6.2) gives

$$\Omega_x(t) = \bar{\Omega}_x(t) \frac{e^{i(ft+\phi_{mw})} - e^{-i(ft+\phi_{mw})}}{2i}, \quad (6.6)$$

$$\Omega_y(t) = \bar{\Omega}_y(t) \frac{e^{i(ft+\phi_{mw})} - e^{-i(ft+\phi_{mw})}}{2i}, \quad (6.7)$$

where  $\bar{\Omega}_x, \bar{\Omega}_y$  are the slowly varying envelopes controlled by the MW switch and the AOM. Inserting into (6.4) yields

$$\Omega_{eff2} = \frac{i}{2} \left( \frac{\bar{\Omega}_x \bar{\Omega}_y^*}{\Delta_r} - \frac{\bar{\Omega}_x^* \bar{\Omega}_y}{(\Delta_r + \omega_t)} \right) \frac{1}{4} \left( 1 - e^{2i(ft+\phi_{mw})} - e^{-2i(ft+\phi_{mw})} + 1 \right), \quad (6.8)$$

where the four last terms represent the four combinations of the two sidebands of which only one is capable of driving the Raman transition. This justifies a rotating wave approximation, and we only keep the  $e^{2i(ft+\phi_{mw})}$  term which, upon insertion in (6.3), gives

$$\hat{H}_{eff3} = \begin{bmatrix} \frac{-\omega_g}{2} & \frac{\Omega_{eff}}{8} e^{2i(ft+\phi_{mw})} \\ \frac{\Omega_{eff}^*}{8} e^{-2i(ft+\phi_{mw})} & \frac{\omega_g}{2} \end{bmatrix}, \quad (6.9)$$

where  $\omega_g/2$  has been added to the diagonals and  $\omega_{AC} = 0$  (circular polarisation). The final step is to remove the time dependence by transforming to the rotating frame  $\hat{U} = |0\rangle\langle 0| e^{-ift} + e^{+ift} |1\rangle\langle 1|$  which, following (2.52) yields the final Hamiltonian

$$\hat{H}_{rot} = \begin{bmatrix} -\Delta_{MW}/2 & \frac{\Omega_r}{2} e^{-i\phi_s} \\ \frac{\Omega_r}{2} e^{i\phi_s} & \Delta_{MW}/2 \end{bmatrix} \quad (6.10)$$

$$= \frac{\Omega_r}{2} (\cos(\phi_s) \hat{\sigma}_x + \sin(\phi_s) \hat{\sigma}_y) - \frac{\Delta_{MW}}{2} \hat{\sigma}_z, \quad (6.11)$$

where the spin Rabi frequency is given by

$$\Omega_r = \frac{1}{8} \left| \frac{\bar{\Omega}_x \bar{\Omega}_y^*}{\Delta_r} - \frac{\bar{\Omega}_x^* \bar{\Omega}_y}{(\Delta_r + \omega_t)} \right| \begin{matrix} \Delta_r \gg \omega_t, \\ \bar{\Omega}_x = i \bar{\Omega}_y \\ \approx \end{matrix} \frac{|\bar{\Omega}_y|^2}{4\Delta_r} \propto \frac{P_{rot}}{\Delta_r}, \quad (6.12)$$

which we can take as being real by moving its phase onto  $\phi_s$ . Hence,  $\Omega_r$  scales linearly with the rotation power  $P_{rot}$  as opposed to the optical Rabi frequencies. Equation (6.10) contains an two-phonon detuning given by

$$\Delta_{MW} = \omega_g - 2f. \quad (6.13)$$

and a phase

$$\phi_s = -2\phi_{mw}, \quad (6.14)$$

which sets the azimuthal angle of the rotation axis (illustrated on figure 6.3c). The factors of two in (6.13) and (6.14) stem from having two sidebands. The Hamiltonian in (6.11) allows greater control than the ultra-fast Hamiltonian (6.3) as  $\Delta_{MW}$ ,  $\Omega_r$  and  $\phi_{mw}$  can all be modulated (with a more advanced MW setup) allowing arbitrary axes of rotation.

From (6.10) simple dynamics can now be derived. If a square rotation pulse of duration  $T_r$  is applied, the resulting unitary transform is given by the time evolution operator

$$\hat{U}_{rot} = e^{-iT_r \hat{H}_{rot}} \quad (6.15)$$

$$= \cos(\theta) \hat{\mathbb{I}} - i \sin(\theta) \frac{[\Omega_r (\cos(\phi_s) \hat{\sigma}_x + \sin(\phi_s) \hat{\sigma}_y) - \Delta_{MW} \hat{\sigma}_z]}{\sqrt{\Omega_r^2 + \Delta_{MW}^2}}, \quad (6.16)$$

$$\theta = \frac{T_r}{2} \sqrt{\Omega_r^2 + \Delta_{MW}^2}, \quad (6.17)$$

where the second equality used the identity [81]

$$e^{i\alpha \vec{n} \cdot \vec{\sigma}} = \cos(\alpha) \hat{\mathbb{I}} + i \sin(\alpha) (\vec{n} \cdot \vec{\sigma}), \quad (6.18)$$

where  $\vec{n}$  is the axis of rotation and  $\vec{\sigma} = (\hat{\sigma}_x, \hat{\sigma}_y, \hat{\sigma}_z)$ .

The probability to transfer the spin from  $|0\rangle$  to  $|1\rangle$  is then given by

$$P_{0 \rightarrow 1} = |\langle 1 | \hat{U}_{rot} | 0 \rangle|^2 = \frac{\Omega_r^2}{\Omega_r^2 + \Delta_{MW}^2} \sin^2 \left( \underbrace{\frac{1}{2} T_r \sqrt{\Omega_r^2 + \Delta_{MW}^2}}_{\text{Pulse area}} \right), \quad (6.19)$$

which is identical to the detuned optical Rabi flopping in (2.25).

### 6.2.3 $\pi$ -PULSE FIDELITY

Several mechanisms may limit the fidelity of the rotation pulses. We will focus on the  $\pi$ -pulse fidelity as defined by the probability of flipping the spin:

$$F_\pi = P_{0 \rightarrow 1}. \quad (6.20)$$

One fundamental limit is given by the inhomogeneous broadening of  $\omega_g$  as quantified by the spin  $T_2^*$ . Assuming the two-photon detuning only receives contributions from the Overhauser field, the fidelity can be evaluated by solving the detuned Rabi

flopping (6.19), setting  $\Delta_{MW} = \Delta_{OH}$  and taking an ensemble average:

$$\langle P_{0 \rightarrow 1} \rangle_{inhom} = \int_{-\infty}^{\infty} d\Delta_{OH} \frac{\Omega_{MW}^2}{\Omega_{MW}^2 + \Delta_{OH}^2} \sin^2 \left( \frac{1}{2} t \sqrt{\Omega_r^2 + \Delta_{OH}^2} \right) \mathcal{N}(\Delta_{OH}; \sigma_{OH}), \quad (6.21)$$

where  $\mathcal{N}(\Delta_{OH}; \sigma_{OH})$  is the Gaussian probability density function of the Overhauser shift. Setting  $\Omega_r = \pi/T_p$  to ensure a  $\pi$ -pulse allows a Taylor expansion of the Rabi-flopping term around  $\Delta_{OH} = 0$ , yielding

$$\frac{(\pi/T_p)^2}{(\pi/T_p)^2 + \Delta_{OH}^2} \sin^2 \left( \frac{1}{2} t \sqrt{(\pi/T_p)^2 + \Delta_{OH}^2} \right) \approx 1 - \frac{T_p^2 \Delta_{OH}^2}{\pi^2} + \mathcal{O}(\Delta_{OH}^4). \quad (6.22)$$

Inserting in (6.21) allows evaluating the Gaussian integral

$$F_\pi = \int_{-\infty}^{\infty} d\Delta_{OH} \left( 1 - \frac{T_p^2 \Delta_{OH}^2}{\pi^2} \right) \frac{e^{-\Delta_{OH}^2/(2\sigma_{OH}^2)}}{\sqrt{2\pi}\sigma_{OH}} = 1 - \left( \frac{T_p \sigma_{OH}}{\pi} \right)^2 \quad (6.23)$$

$$= 1 - \frac{2}{\pi^2} \left( \frac{T_p}{T_2^*} \right)^2 \quad (6.24)$$

$$= 1 - \frac{2}{(\Omega_r T_2^*)^2}, \quad (6.25)$$

using  $T_2^* = \sqrt{2}/\sigma_{OH}$ . The condition  $\Omega_r T_p = \pi$  is assumed in both (6.24) and (6.25). This fidelity applies for a single  $\pi$ -pulse but can be improved by composite pulses and adiabatic approaches [82] which protect against inhomogeneous broadening of  $\Delta_{MW}$  and  $\Omega_r$ . However, composite pulses take longer time, typically require multiple rotation axes and do not protect against markovian decoherence processes. All of these limitations prevent the use of composite pulses for the current entanglement experiment and they will not be given further consideration.

A second fundamental limitation is incoherent scattering from the trions, which contain a non-zero population. This scattering may result in both pure dephasing and spin-flips. Hence, this process is non-reversible. The exact form of the decoherence will not be derived here. Instead, the scattering rate will be calculated, as this forms a worst-case estimate of the effective spin-flip rate  $\kappa$ . The sum of the trion populations (see appendix D), in absence of radiative decays, is given by

$$\rho_{22} + \rho_{33} = \frac{\Omega_x^2}{2\Delta_r^2}, \quad (6.26)$$

where  $|\Omega_x| = |\Omega_y|$  is assumed. (6.26) is similar<sup>1</sup> to the steady solution of a two-level system (2.17) in the limit  $\Delta \gg \Omega, \gamma$ . Inserting the time-dependent form of  $\Omega_x(t)$  from (6.6), averaging over a period of MW modulation, and multiplying with the

<sup>1</sup>A factor two appears in the denominator as opposed to the usual factor four as there are two optical fields per trion.

trion decay rate gives the scattering rate:

$$\begin{aligned} R_{scatter} &= \gamma \langle \rho_{22} + \rho_{33} \rangle = \gamma \left\langle \frac{|\Omega_x(t)|^2}{2\Delta_r^2} \right\rangle \\ &= \gamma \frac{\bar{\Omega}_x^2}{2\Delta_r^2} \left\langle \sin^2(ft + \phi_{mw}) \right\rangle = \frac{\gamma \bar{\Omega}_x^2}{4\Delta_r^2}, \end{aligned} \quad (6.27)$$

which can be expressed by the spin Rabi frequency using (6.12):

$$R_{scatter} = \frac{\gamma |\Omega_r|}{\Delta_r}. \quad (6.28)$$

Hence, when keeping  $|\Omega_r|$  constant, the scattering should depend inversely on the optical detuning. This error combined with the  $T_2^*$  error represents a tradeoff given a fixed  $P_{rot}$ . Lower  $\Delta_r$  allows higher  $\Omega_r$  and lower errors from  $T_2^*$  but produces more scattering. In practice, theoretical optimisation is not fruitful as fidelity turns out to be limited by other forms of laser-induced spin-flips (section 6.3.2).

An additional source of scattering is trion excitation via the phonon sideband.  $\Delta_r$  is always red detuned as phonon-assisted excitation here requires absorbing a phonon in contrast to a blue detuning, which requires phonon emission. The phonon-assisted excitation approximately scales as  $e^{-\Delta_r/(k_B T)}$ , which should result in a fast fall-off with  $\Delta_r$  given  $k_B T/h = 88$  GHz for temperature  $T = 4.2$  K.

Additional infidelity may be caused by fluctuations in the spin control parameters, i.e.  $\Omega_r \propto P_{rot}$  and  $T_r$ . Rewriting (6.19) for  $\Delta_{MW} = 0$  as

$$P_{0 \rightarrow 1} = \sin^2 \left[ \frac{\pi}{2} \left( \frac{T_0 + \epsilon_T}{T_0} \right) \left( \frac{P_0 + \epsilon_P}{P_0} \right) \right] \quad (6.29)$$

where  $T_0$  and  $P_0$  are the ideal unitless duration and power resulting in  $T_0 P_0 = 1$ . Expanding in the small fluctuations  $\epsilon_T$  and  $\epsilon_P$  gives

$$F_\pi \approx 1 - \frac{\pi}{4} \left[ \left( \frac{\epsilon_P}{P_0} \right)^2 + \left( \frac{\epsilon_T}{T_0} \right)^2 \right]. \quad (6.30)$$

Hence, control parameter fluctuations only appear to second order. Given the measured power stability  $\epsilon_P/P_0 = 1.5\%$ , this error will not be given further consideration.

#### 6.2.4 MASTER EQUATION APPROACH

In order to model the spin evolution under both inhomogeneous dephasing and spin-flips, we apply a master equation approach. The evolution of the spin density matrix then follows [31]

$$\frac{d}{dt} \hat{\rho} = -i[\hat{H}_{rot}, \hat{\rho}] + \sum_{j=1}^2 \left[ \hat{C}_j \hat{\rho} \hat{C}_j^\dagger - \frac{1}{2}(\hat{C}_j^\dagger \hat{C}_j \hat{\rho} + \hat{\rho} \hat{C}_j^\dagger \hat{C}_j) \right], \quad (6.31)$$

where  $\hat{H}_{rot}$  is given by (6.11) and the two collapse operators representing spin flips are given by  $\hat{C}_1 = \sqrt{\kappa}|0\rangle\langle 1|$  and  $\hat{C}_2 = \sqrt{\kappa}|1\rangle\langle 0|$ , where  $\kappa$  is the spin flip rate.  $\kappa$  is assumed equal for both collapses as the limit  $k_B T \gg \hbar\omega_g$  roughly applies. For  $\phi_s = 0$ , this gives rise to the equations of motion

$$\frac{d}{dt} \begin{pmatrix} \rho_{00} \\ \rho_{01} \\ \rho_{10} \\ \rho_{11} \end{pmatrix} = \begin{pmatrix} -\kappa & \frac{i\Omega_r}{2} & -\frac{i\Omega_r}{2} & \kappa \\ \frac{i\Omega_r}{2} & -\kappa + i\Delta_{MW} & 0 & -\frac{i\Omega_r}{2} \\ -\frac{i\Omega_r}{2} & 0 & -\kappa - i\Delta_{MW} & \frac{i\Omega_r}{2} \\ \kappa & -\frac{i\Omega_r}{2} & \frac{i\Omega_r}{2} & -\kappa \end{pmatrix} \begin{pmatrix} \rho_{00} \\ \rho_{01} \\ \rho_{10} \\ \rho_{11} \end{pmatrix}. \quad (6.32)$$

The quantity of interest is  $\rho_{11}(t)$  given the initial state  $\hat{\rho}(0) = |0\rangle\langle 0|$  from which  $F_\pi$  may be calculated. For the special case  $\Delta_{MW} = 0$ , an analytical solution exists:

$$\rho_{11}(t) = \frac{1}{2} \left( 1 - e^{-(3/2)T_r\kappa} \left[ \cos\left(\frac{\tilde{\Omega}_r T_r}{2}\right) - \frac{\kappa}{\Omega_r} \sin\left(\frac{\tilde{\Omega}_r T_r}{2}\right) \right] \right), \quad (6.33)$$

where  $\tilde{\Omega}_r = \sqrt{4\Omega_r^2 - \kappa^2}$ . This model is useful if dampening is dominated by  $\kappa$ , as is the case in Ref. [78]. Another special case is  $\Omega_r = 0, \kappa > 0$  in which the state converges towards an equal spin mixture

$$\rho_{11}(t) = \frac{1}{2} (1 - e^{-2\kappa T_r}). \quad (6.34)$$

However, we are interested in the general case where  $\Delta_{MW} = \Delta_{OH} \neq 0$  and  $\kappa > 0$ . In this case,  $\rho(t)$  can not be solved analytically, and one must resort to numerical integration. Inhomogeneous broadening is included by averaging over  $\Delta_{OH}$ :

$$\langle \rho_{11}(t; \Omega_r, \kappa) \rangle_{inhom} = \int_{-\infty}^{\infty} d\Delta_{OH} \rho_{11}(t; \Omega_r, \kappa, \Delta_{OH}) \mathcal{N}(\Delta_{OH}; \sigma_{OH}). \quad (6.35)$$

In practice, 50 values of  $\Delta_{OH}$  are chosen such that they are evenly spaced with respect to the cumulative density function of  $\mathcal{N}(\Delta_{OH}; \sigma_{OH})$ . For each  $\Delta_{OH}$ , (6.32) is integrated numerically with the explicit fifth-order Runge Kutta method. Finally, a weighted average of the  $\rho_{11}(t)$  solutions is taken. This model is used to fit the experimental data in section 6.3.2.

## 6.3 EXPERIMENTAL $\pi$ -PULSE CHARACTERISATION

### 6.3.1 OPTIMISATION

A few steps are required to experimentally optimise the rotation laser. The ground state splitting  $\omega_g$  is approximately known from two-colour spectroscopy but is more precisely confirmed by scanning the MW frequency  $f$  and observing the readout fluorescence as in figure 6.5a. Here a rotation pulse is placed in between an initialisation and readout pulse. This constitutes a measurement of optically detected magnetic resonance (ODMR) as the fluorescence signal detects resonance between

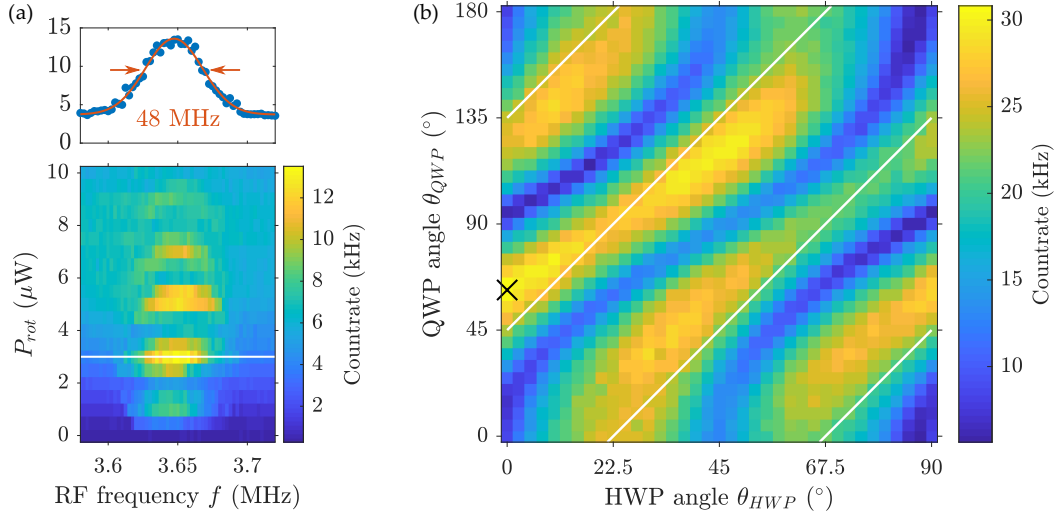


**Figure 6.5:** (a) ODMR of a QD hole spin at  $B_y = 2$  T. Scanning the rotation laser power and MW frequency reveals several fluorescence peaks corresponding to  $\pi$ ,  $3\pi$ ,  $5\pi$  and  $7\pi$  rotations.  $T_r = 50$  ns,  $\Delta_r = 283$  GHz. Top insert shows cut through at  $3 \mu\text{W}$ . Counts are measured by APD and filtered with a grating.  $P_{rot}$  is not comparable with subsequent measurements due to differences in duty cycle. (b) Readout fluorescence as a function of path 2 waveplates. White contours indicate circular polarisation given perfect optics. The black cross indicates the position used henceforth. Counts recorded with SNSPD and etalon filter.  $T_r = 7$  ns,  $f = 3.65$  GHz,  $\Delta_r = 250$  GHz.

the MW-field and the spin. Fitting the ODMR lineshape with a Gaussian yields a precise estimate of the resonance condition  $\omega_g = 2f$ .

Next, the rotation laser polarisation is optimised using the waveplates in path 2 (figure 3.4b). A short rotation pulse  $T_r \sim 7$  ns is applied to reduce the sensitivity to  $\Delta_{OH}$  and increase the measurement contrast. The Rabi frequency is chosen to satisfy  $\Omega_r T_r \approx \pi/3$  such that improved polarisation results in a monotonous increase in readout fluorescence. This measurement is demonstrated in figure 6.5b where the origin corresponds to  $y$ -polarised light propagating down the sample stick. The white contours are given by  $\theta_{QWP} = 2\theta_{HWP} + (1 + 2n)\pi/4$ ,  $n \in \mathbb{N}$  corresponding to circular polarisation in an ideal setup. The contours deviate somewhat from the measured signal demonstrating the value of this optimisation. The deviation may be attributed to the non-trivial dipole to far-field coupling discussed in section 6.1 but can also depend on any birefringent or polarisation dependent optics (e.g. beamsplitters). As non-circular polarisations induce an AC-Stark shift, the measurements in figure 6.5a and figure 6.5b are repeated to check for resonance shifts and to ensure self-consistency. Varying optical alignment shifts the waveplate optimum by a few degrees which necessitates occasional re-optimisation.

### 6.3.2 FIDELITY ESTIMATION

While figure 6.5a demonstrates clear Rabi oscillations, a number of experimental disadvantages are associated with scanning  $P_{rot}$ , namely varying power tuning (demonstrated in figure 5.5) and hole occupation probability. The spin rotation

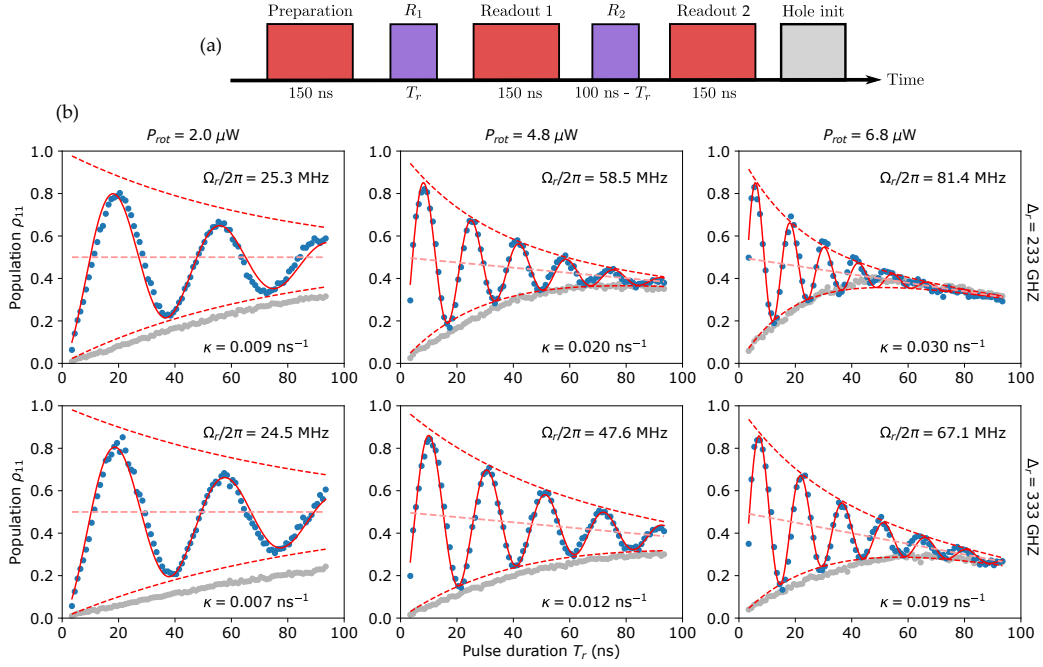


**Figure 6.6:** (a) Pulse sequence used to vary  $T_r$ .  $R_1$  and  $R_2$  pulses are varied in duration while maintaining a 100 ns total duration. Counts from the full duration of Readout 1 are integrated to achieve the Rabi signal. (b) Subset of pulse duration scans. Blue dots show readout fluorescence with  $\Delta_{MW} = 0$ , while gray dots use a large  $\Delta_{MW}$ . The y axis corresponds to the  $\rho_{11}$  population for  $\alpha = 0$ .  $P_{rot}$  and  $\Delta_r$  are indicated on the top and right hand side of the subfigures. Solid red lines indicate fits with (6.36). Top and bottom dashed lines show the envelopes  $(1 - \alpha T_r)(\frac{1}{2} \pm \frac{1}{2} e^{-(3/2)T_r \kappa})$ , which correspond to  $\kappa$  dominated damping. The middle dashed line shows  $(1 - \alpha T_r)/2$  indicating the modelling of decreasing readout efficiency. Counts recorded with APD and grating filter.

fidelity is instead estimated by keeping  $P_{rot}$  fixed but varying the pulse duration  $T_r$ . This is achieved experimentally by the pulse sequence in figure 6.6a where a preparation pulse prepares  $|0\rangle$  and the  $R_1$  pulse duration is varied to produce Rabi oscillations in the fluorescence from the Readout 1 pulse<sup>2</sup>. The  $R_2$  rotation acts as a buffer and maintains a constant duty cycle of the rotation laser. Additionally, based on calibration measurements, the frequency of the pump laser is adjusted as a function of  $P_{rot}$  to compensate for power-tuning.

Clear Rabi oscillations are observed in figure 6.6b when the sidebands are tuned on resonance with the hole spin. Fluorescence for  $T_r = 0$  has been subtracted to remove the contribution from background counts during readout. The measurement is also performed with non-resonant sidebands,  $\Delta_{MW}/(2\pi) = 300$  MHz, which give rise to the gray curves in figure 6.6b. This measurement shows the existence of rotation laser-induced spin-flips, as the coherent coupling is suppressed through  $\Delta_{MW}$ . For low  $P_{rot}$ , the non-resonant series converges towards a steady state value as predicted by (6.34). However, for high powers, e.g.  $P_{rot} = 6.8 \mu\text{W}$ , non-resonant

<sup>2</sup>The spin state resulting from the  $R_2$  rotation is detected by the Readout 2 pulse but is not analysed here.

counts start to decrease for  $T_r > 60$  ns. As spin flips drive the state towards an equal mixture monotonically, this decrease can only be due to a reduction of the readout efficiency. Most likely the power tuning is not perfectly compensated<sup>3</sup>.

Each set of Rabi oscillations are fit using the model

$$I(T_r) = I_0(1 - \alpha T_r) \langle \rho_{11}(T_r; \Omega_r, \kappa, ) \rangle_{inhom}, \quad (6.36)$$

where  $\langle \rho_{11} \rangle$  is calculated from (6.35) and contains  $\Omega_r$  and  $\kappa$  as free fit parameters.  $T_2^* = 23.2$  ns is fixed based on the measurements in section 6.4.1.  $I_0$  is a free intensity scaling parameter and  $\alpha > 0$  is a small empirical fit parameter which accounts for the reduced readout efficiency at long  $T_r$ .

In general, the fits perform acceptably and yield usable estimates of  $\Omega_r$  and  $\kappa$ . From figure 6.6b, a transition from mostly Markovian to non-Markovian dampening is visible. At low  $P_{rot}$ , the Rabi oscillations are only lightly bounded by the  $e^{-(3/2)T_r\kappa}$  envelope, as  $T_2^*$  plays a significant (non-Markovian) role. Conversely, at high  $P_{rot}$ , the oscillations are tightly bounded by the  $e^{-(3/2)T_r\kappa}$  envelope, indicating  $\kappa$  (Markovian) as the dominant dampening mechanism.

The fit results are summarised in figure 6.7. figure 6.7a shows the estimated  $\Omega_r$  as a function of  $\Delta_r$  and  $P_{rot}$ . While  $\Omega_r$  generally scales linearly with  $P_{rot}$ , the dependence on  $\Delta_r$  is weaker than the inverse relation predicted by (6.12). This non-ideal scaling could be the result of only optimised the polarisation and  $f$  at the lowest  $\Delta_r$ . At the highest  $\Delta_r$ , a maximal  $\Omega_r/(2\pi) = 40$  MHz is achieved with an estimated 95  $\mu$ W of optical power hitting the sample during pulses. This is considerably lower than the 150 MHz realised in Ref. [78] for the same detuning and  $\approx 11$   $\mu$ W of input power. This is unsurprising as Ref. [78] employed a planar structure with a solid immersion lens, which provides a far greater far-field coupling than our PCW. Our peak  $\Omega_r$  is limited by the permitted input power to the EOM and optical losses.

Figure 6.7b shows the inferred  $\kappa$  to increase roughly linearly in power with a smaller slope for large detunings. However, the detuning dependence is far weaker than the  $1/\Delta_r^2$  scaling of trion scattering (6.27) or the  $e^{-\Delta_r/(k_B T)}$  scaling of phonon-assisted excitation as illustrated by the figure insert. In absolute numbers the fitted  $\kappa$  also deviates from theory: At  $\Delta_r/(2\pi) = 783$  GHz and max power, (6.28) predicts a scattering rate of  $1.3 \cdot 10^{-4}$  ns<sup>-1</sup>, which is two orders of magnitude lower than the observed  $\kappa$ . This motivates the hypothesis that another source of power-dependent spin-flips exists.

The  $\pi$ -pulse fidelity  $F_\pi$  is calculated by numerically maximizing  $\rho_{11}(T_r)$  with respect to  $T_r$  for the given  $\Omega_r$  and  $\kappa$ . Figure 6.7c shows the power-dependent  $F_\pi$  where a lack of improvement with  $\Delta_r$  becomes apparent as  $F_\pi$  plateaus around 0.88. Figure 6.7d provides a fair comparison between different  $\Delta_r$ , as the  $T_2^*$  contribution is the same for a given  $\Omega_r$ . Fidelity benefits slightly from higher  $\Delta_r$  but is far from reaching the limit set by  $T_2^* = 23.2$  ns.  $F_\pi$  is seen to increase smoothly as opposed to the observations in Ref. [78] where resonances with the nuclear spins diminish  $F_\pi$  at specific values of  $\Omega_r$ . The absence of this signature may either be due to the hole's

<sup>3</sup>Note that when  $T_r$  is increased, the average optical power is constant thanks to the buffer pulse. However, the delay between the  $R_1$  pulse and Readout 1 is reduced.

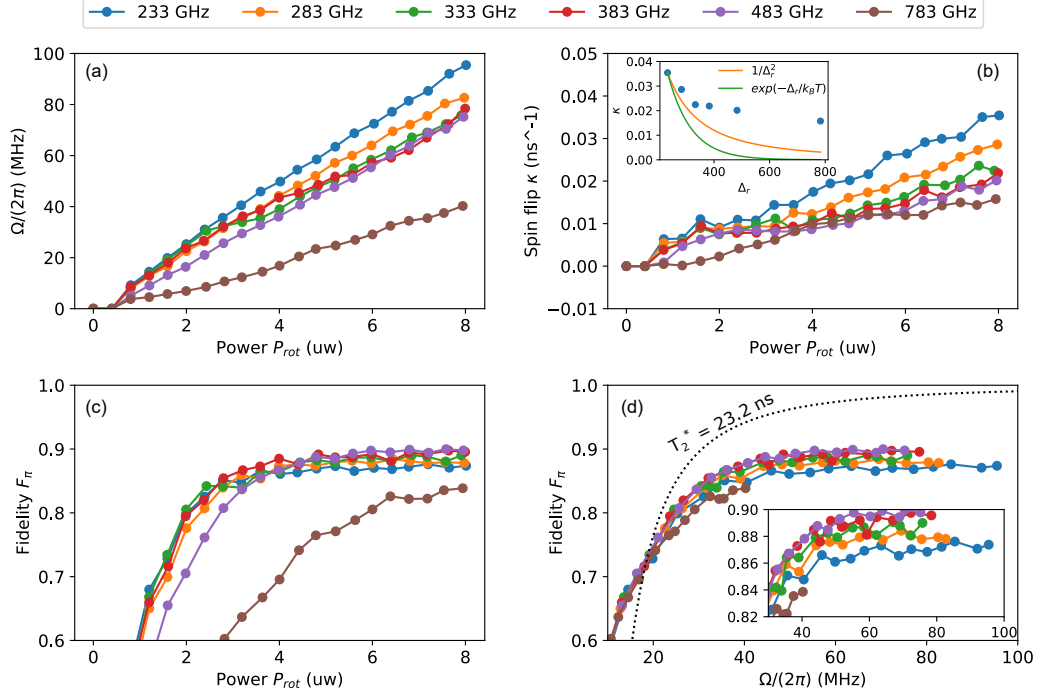


**Figure 6.7:** Parameters estimated from fitting spin Rabi oscillations in figure 6.6. The common top legend indicates the rotation laser detuning  $\Delta_r/2\pi$ . **(a)** Estimated spin Rabi frequency. **(b)** Estimated dampening rate. Inset shows a lorentzian and exponential detuning dependence scaled to  $\kappa(\Delta_r = 233 \text{ GHz})$ . **(c)** Calculated  $\pi$ -pulse fidelity as a function of power. **(d)**  $\pi$ -pulse fidelity as a function of Rabi frequency. The dashed line uses the model in (6.25). Inset shows magnified data.

weaker hyperfine interaction or simply the reduced sensitivity of this measurement. Of special interest is  $F_\pi$  for  $\Omega_r/(2\pi) = 73 \text{ MHz}$  and  $\Delta_r/(2\pi) = 333 \text{ MHz}$  as this is applied in the entanglement experiment of chapter 9. Averaging across the three measurements most closely resembling this condition yields the estimate

$$F_\pi = (88.5 \pm 0.3)\% \quad (\text{Measured}), \quad (6.37)$$

where the error only represents the statistical error from averaging. In comparison, theory predicts

$$F_\pi = 98.2\% \quad (T_2^* \text{ limit using (6.25)}). \quad (6.38)$$

It would seem that fidelity is limited by a power-dependent spin-flip rate which is largely independent of detuning. What may be the cause of these spin flips? One hypothesis relates to the fact, that the rotation laser is capable of photocreation (see section 4.5.3). Regardless of the underlying physical mechanism, photocreation from the rotation laser is undesirable, as this will create random hole spins and thus constituting an effective spin-flip rate. Ideally, the hole spin occupation should not

be perturbed by the rotation laser. This consideration motivates the design of heterostructures with better protection of the hole spin. A second spin-flip mechanism could be related to free charges being induced by the rotation laser [83]. Finally, there is the possibility of the laser driving either the  $X^0$  or the biexciton transitions due to their close spectral proximity. In comparison, the  $X^-$  is further detuned from all other transitions. Interestingly, the estimated  $F_\pi = 88.5\%$  also resembles the observations in Ref. [78] where a limit of  $F_\pi = 91\%$  was reached for hole spins (using both ultra-fast and Raman schemes) in contrast to  $F_\pi = 98.9\%$  achieved with Raman pulses on the electron spin. Here, spin flips independent of detuning were also observed.

## 6.4 HOLE SPIN COHERENCE TIME

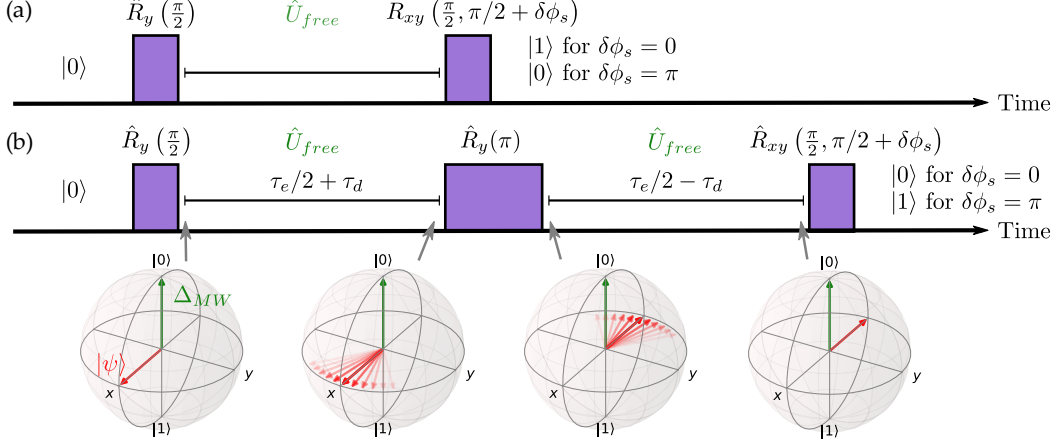


**Figure 6.8:** (a) Ramsey pulse sequence consisting of two  $\pi/2$  pulses separated by delay  $\tau$ . (b) Spin echo pulse sequence.  $\tau_e$  is the total duration of free evolution and  $\tau_d$  is the displacement of the central  $\pi$ -pulse. Bloch sphere diagrams show ensemble spin evolution at different points in time. During the first precession, the ensemble dephases across the  $xy$ -plane. The middle  $\pi$  pulse flips the spins around the  $y$ -axis, causing them to rephase during the second delay.

The hole spin  $T_2^*$  may be estimated using both the Ramsey and Echo pulse sequences illustrated in figure 6.8. The state evolution can be described using the spin unitaries derived from (6.16):

$$\hat{U}_{free}(t) = \cos\left(\frac{t\Delta_{MW}}{2}\right) \hat{\mathbb{I}} - i \sin\left(\frac{t\Delta_{MW}}{2}\right) (-\hat{\sigma}_z) \quad (\text{Free precession}), \quad (6.39)$$

$$\hat{R}_y(\pi) = -i\hat{\sigma}_y \quad (\pi\text{-pulse around } y), \quad (6.40)$$

$$\hat{R}_{xy}(\pi/2, \phi_s) = \frac{1}{\sqrt{2}} \left( \hat{\mathbb{I}} - i(\cos(\phi_s)\hat{\sigma}_x + \sin(\phi_s)\hat{\sigma}_y) \right) \quad (\pi/2\text{-pulse around } \phi_s\text{-axis}), \quad (6.41)$$

$$\hat{R}_y(\pi/2) = \hat{R}_{xy}(\pi/2, \pi/2) = \frac{1}{\sqrt{2}}(\hat{\mathbb{I}} - i\sigma_y) \quad (\pi/2\text{-pulse around } y). \quad (6.42)$$

$\Delta_{MW} = 0$  has been assumed during the rotation pulses, which is justified when  $\Omega_r \gg |\Delta_{MW}|$  and greatly simplifies the following calculations. The total Ramsey unitary for a fixed  $\Delta_{MW}$  is then

$$\hat{U}_{ramsey} = \hat{R}_{xy}(\pi/2, \pi/2 + \delta\phi_s) \hat{U}_{free}(\tau) \hat{R}_y(\pi/2), \quad (6.43)$$

where  $\delta\phi_s$  is the phase shift of the final rotation pulse. As the experimental pulse sequence prepares  $|0\rangle$  and reads  $|1\rangle$ , the measured quantity is the transfer probability

$$P_{0\rightarrow 1} = |\langle 1 | \hat{U}_{ramsey} | 0 \rangle|^2 = \cos\left(\frac{\tau\Delta_{MW} + \delta\phi_s}{2}\right)^2. \quad (6.44)$$

Setting  $\Delta_{MW} = \Delta_{OH}$  and averaging over the inhomogeneous broadening gives

$$\langle P_{0\rightarrow 1} \rangle_{inhom} = \int_{-\infty}^{\infty} d\Delta_{OH} P_{0\rightarrow 1} \mathcal{N}(\Delta_{OH}; \sigma_{OH}) = \frac{1}{2} \left(1 + \cos(\delta\phi_s) e^{-(\tau/T_2^*)^2}\right). \quad (6.45)$$

Hence, when increasing the delay  $\tau$  the final state follows a Gaussian decay towards an equally mixed state. This is a consequence of the inhomogeneous broadening, causing the spin ensemble to spread out over the Bloch sphere equator as indicated by the second Bloch sphere on (6.8)b. The phase  $\delta\phi_s$  of the second  $\pi/2$  pulse determines whether  $|+\rangle$  is mapped to  $|1\rangle$  ( $\phi = 0$ ) or to  $|0\rangle$  ( $\phi = \pi$ ). In contrast to ultra-fast rotations, the Ramsey signal does not contain oscillations at the Larmor frequency as we now work in a rotating frame.

The evolution following spin echo can be evaluated following the exact same steps. The unitary is given by

$$\hat{U}_{echo} = \hat{R}_{xy}(\pi/2, \pi/2 + \delta\phi_s) \hat{U}_{free}(\tau_e/2 - \tau_d) \hat{R}_y(\pi) \hat{U}_{free}(\tau_e/2 + \tau_d) \hat{R}_y(\pi/2), \quad (6.46)$$

which gives the transfer probability

$$P_{0\rightarrow 1} = |\langle 1 | \hat{U}_{echo} | 0 \rangle|^2 = \sin\left(\frac{2\tau_d\Delta_{MW} + \delta\phi_s}{2}\right)^2. \quad (6.47)$$

Performing the same integral as in (6.45) then yields

$$\langle P_{0\rightarrow 1} \rangle_{inhom} = \frac{1}{2} \left(1 - \cos(\delta\phi_s) e^{-4(\tau_d/T_2^*)^2}\right). \quad (6.48)$$

This is similar to Ramsey except for the factor four in the Gaussian time dependence, as changing  $\tau_d$  has the effect of both increasing and decreasing a precession period. In (6.48) there is no  $\tau_e$  dependence as the frozen fluctuation model implicitly assumes a static Overhauser field. Hence, the spin ensemble always perfectly rephases for  $\tau_d = 0$ . In reality, the Overhauser field contains higher frequency components causing a loss in echo visibility for increasing  $\tau_e$ .

We define the echo visibility as

$$\mathcal{V}_{Echo} = \rho_{11}(\delta\phi_s = \pi) - \rho_{11}(\delta\phi_s = 0), \quad (6.49)$$

where  $\rho_{11}(\delta\phi_s)$  is the  $|1\rangle$  population following an echo where the last rotation pulse was phase shifted by  $\delta\phi_s$ . This can be related to measured intensities by

$$\mathcal{V}_{Echo} = \frac{I(\delta\phi_s = \pi) - I(\delta\phi_s = 0)}{I(\delta\phi_s = \pi) + I(\delta\phi_s = 0)}, \quad (6.50)$$

where  $I$  is the intensity of the readout pulse measuring  $|1\rangle$ .

While both Ramsey and Echo may estimate  $T_2^*$ , a Ramsey experiment is difficult given the experimental limitation of  $\tau > 8$  ns. In Ref. [32] we reported a Ramsey measurement on QD<sub>1</sub> yielding  $T_2^* = (21.4 \pm 0.7)$  ns. However, this measurement only sampled the tail of the Gaussian decay. Instead, the remainder of this chapter will focus on the subsequently performed echo measurements on the same QD.

## 6.4.1 SPIN ECHO MEASUREMENTS

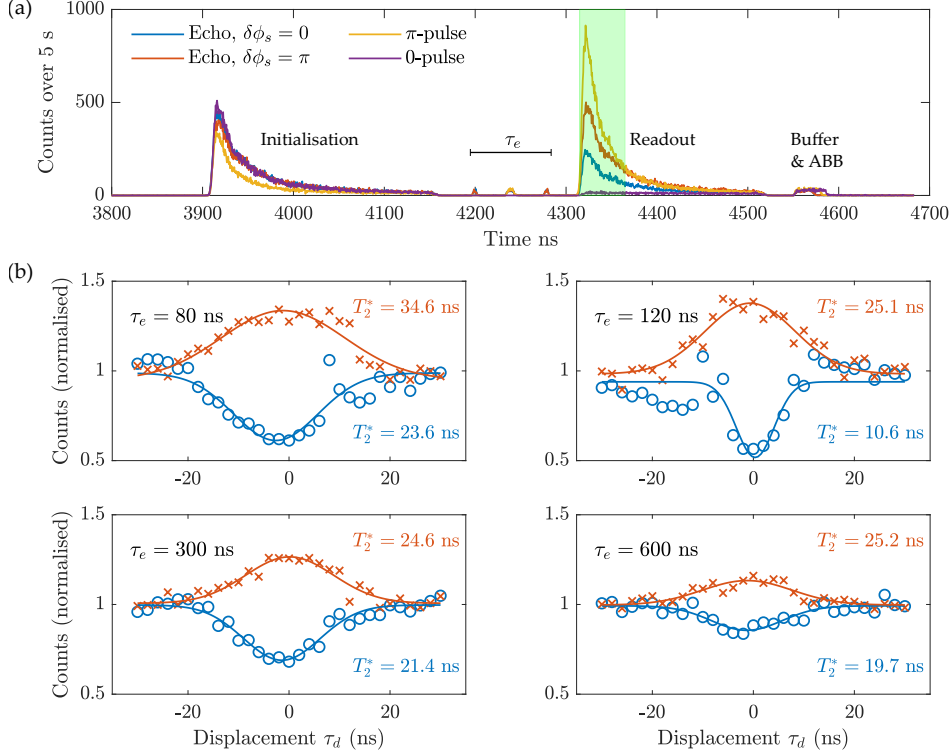


**Figure 6.9:** (a) Spin echo pulse sequence for  $\tau_e = 80$  ns. The initialisation pulse prepares  $|0\rangle$  and the first 50 ns of the readout pulse (green area) is integrated to measure the  $|1\rangle$  population. The legend indicates the different pulse sequences. (b) Echo readout counts for different echo durations. Blue circles denote  $\delta\phi_s = 0$  while red crosses denote  $\delta\phi_s = \pi$ . Counts are normalised to the average value across both settings. Solid lines indicate fits with (6.51) and the extracted  $T_2^*$  values are given on the figure.

The experimental echo pulse sequence is shown in figure 6.9a. A 250 ns initialisation pulse prepares  $|0\rangle$  followed by a series of rotation pulses and a readout pulse. The rotation pulse areas are calibrated using the method described in appendix F.

For each  $\tau_e$  setting the echo is first replaced by a single  $\pi$ -pulse for which  $\Omega_r$  and  $\Delta_{MW}$  are scanned and optimised. The echo sequence is then applied and the central pulse displacement  $\tau_d$  is scanned from -30 to 30 ns. For each  $\tau_d$  the phase of the last  $\pi/2$  pulse assumes values of  $\delta\phi_s = 0$  and  $\delta\phi_s = \pi$ , thus projecting onto both orthogonal spin states. Figure 6.9b shows the echo signal for several echo durations and fits the readout intensity  $I(\tau_d)$  according to

$$I(\tau_d) = I_0 + I_1 \exp\left(\frac{-4(\tau_d - \tau_0)^2}{(T_2^*)^2}\right), \quad (6.51)$$

which is based on (6.48) but introduces the free  $I_0$  and  $I_1$  parameters to model the limited visibility.  $T_2^*$  is taken as a free fit parameter along with  $\tau_0$  which may compensate for small timing offsets. The echo signatures are generally well described

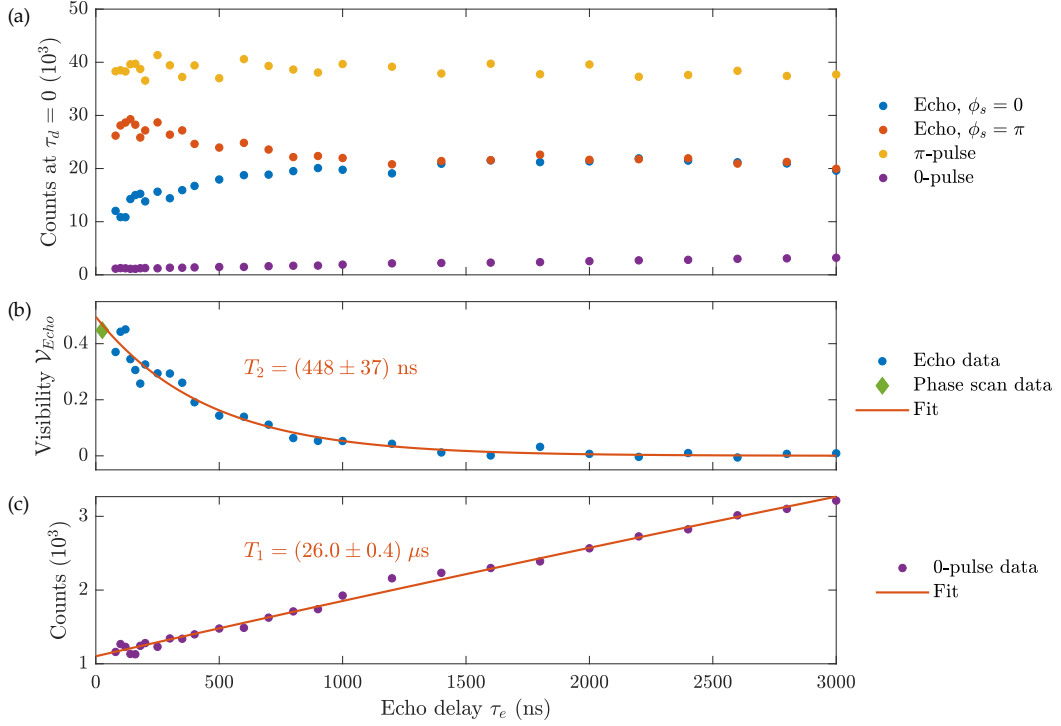


**Figure 6.10:** (a) Readout counts following echo,  $\pi$ -pulse or free evolution. Echo counts are extracted from fits in figure 6.9. (b) Echo visibility fitted with a single exponential with the purpose of extracting the spin  $T_2$ . Diamond indicates visibility extracted in figure 6.11. (c) Zoom in on the 0-pulse counts in (a). A fit using (6.54) is used to extract the spin  $T_1$  time.

by the Gaussian decay and result in  $\tau_0 \approx 0$ . Averaging across 22 measurements with  $\tau_e < 400$  ns yields an average

$$T_2^* = (23.2 \pm 1.3) \text{ ns}, \quad (6.52)$$

where the error represents the uncertainty of the mean. This estimate is compatible with our previous Ramsey estimate of  $T_2^* = (21.4 \pm 0.7)$  ns and will henceforth be used for modelling. Evaluating the fits in figure 6.9 at  $\tau_d = \tau_0$  yields the intensities in figure 6.10a. The two echo signals clearly converge for long  $\tau_e$  which is better illustrated in figure 6.10b, which plots the echo visibility defined in (6.50). Fitting the exponentially<sup>4</sup> decaying echo visibility with

$$\mathcal{V}_{Echo}(\tau_e) = \mathcal{V}_0 e^{-\tau_e/T_2} \quad (6.53)$$

yields a  $T_2 = (448 \pm 37)$  ns coherence time and a peak visibility  $\mathcal{V}_0 = 0.50 \pm 0.02$ .

Figure 6.10c shows a linear increase in counts as  $\tau_e$  is increased and no rotations are applied. Although the spin  $T_1$  time exceeds our measurement duration, it can

<sup>4</sup>Fitting with  $e^{-(\tau_e/T_2)^\alpha}$  yields  $\alpha = 1.06 \pm 0.2$ .

be roughly estimated by applying the model

$$I(\tau_e) = I_0(1 - A \exp(-\tau_e/T_1)), \quad (6.54)$$

where  $I_0$  represents the readout intensity given an equal spin mixture and is estimated by averaging the two echo signals in figure 6.10a, as the spin state will indeed be fully mixed when averaging over both projections. The parameter  $A \approx 1$  gives the y-axis intersection in figure 6.10c and encompasses imperfect spin readout and the fact that the delay between initialisation and readout is  $\approx 100$  ns longer than  $\tau_e$ . We estimate a  $T_1 = (26.0 \pm 0.4)$   $\mu$ s, which is unproblematic for our applications.  $T_1$  may be limited by the weak leakage of the rotation laser carrier. Additionally, our model may overestimate the  $T_1$  slightly as the finite hole lifetime is not included in the model of (6.54).

For short echo durations, we cannot vary  $\tau_d$  sufficiently to map out the Gaussian envelope. Instead, we fix  $\tau_e$  and scan the readout phase  $\phi_s$  to produce echo fringes. Figure 6.11 shows a  $\phi_s$  scan for the entanglement sequences used in section 9.1 for which  $\tau_e = 26$  ns. This data confirms the ability to control the spin readout basis and yields  $\mathcal{V}_{Echo} = 44.8 \pm 0.3\%$  which is fully compatible with the exponential fit in figure 6.10. The plotted  $\phi_{mw}$  is the calibrated phase shift.  $\phi_{mw} = 0$  should result in  $\phi_s = 0$  and a minimum in echo signal following (6.48). However, the measured fringes reveal a small phase offset of  $(6.9 \pm 0.2)^\circ$ . It is unclear whether this is due to imperfect calibration, or a non-zero  $\tau_d \Delta_{MW}$  product, which would shift the minimum according to (6.47). Regardless, this offset only enters to second order in (6.47) and does not explain the low  $\mathcal{V}_{Echo}$  values observed.

The phase scan measurement is repeated using the pulse sequence in figure 6.9a for several delays yielding the dataset in figure 6.12 which extends to shorter  $\tau_e$  and reveals a new structure in the visibility decay: At least two sets of decay and revival are apparent with visibility dips occurring around  $\tau_e = 55$  ns and  $\tau_e = 170$  ns.

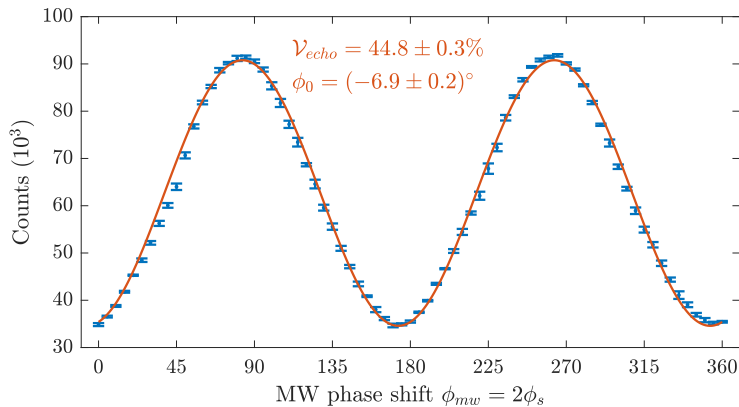


**Figure 6.11:** Echo visibility using the entanglement pulse sequence of section 9.1. The phase of the final  $\pi/2$  pulse is scanned yielding an oscillation with period  $\pi$  with respect to the MW phase  $\phi_{mw}$ . Fitting with the model  $I(\phi_{mw}) = I_0 + I_1 \sin(2\phi_{mw} + \phi_0)$  yields the visibility  $\mathcal{V}_{Echo} = I_1/I_0$ . Error bars denote the average of 5 sweeps.

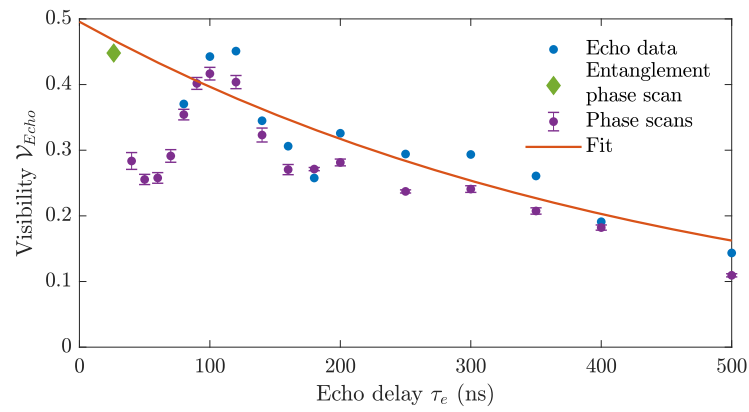


**Figure 6.12:** Summary of echo visibilities for short delays. Blue points represent data from figure 6.10. The green diamond denotes the result from figure 6.11. The purple errorbars represent phase scans for varying  $\tau_e$ . Errorbars are derived from an average of 5 experimental repetitions.

## 6.5 DISCUSSION

We now discuss our observed spin coherence, compare against other works, and discuss the improvements needed to achieve better spin rotations.

### 6.5.1 SPIN COHERENCE

In Ref. [42] the authors also investigate hole spin coherence at  $B_y = 2$  T, thus providing an excellent point of comparison. Noticeably, the authors observe two rounds of collapse and revival in the echo visibility, which are highly similar to our observations in figure 6.12. This modulation is attributed to a precession of the nuclei, which gives rise to a varying longitudinal Overhauser component  $B_{OH}^{\parallel}$  during the echo. This effect is also commonly observed on the electron spin [38, 40]. Hence, we feel confident that hyperfine interactions continue to affect spin coherence at  $B_y = 2$  T. Our  $T_2^* = 23.2$  ns is shorter than the  $\approx 55$  ns demonstrated in Ref. [42]. This difference could be related to our larger hole spin g-factor  $g_{h,y} = 0.26$  (vs. 0.145 [42]) or higher charge noise in our sample. Interestingly, Ref. [42] showed benefits from increasing the magnetic field to 4 T, both in terms of  $T_2^*$  and a longer, more monotonous echo visibility. This motivates measurements at higher magnetic fields, which we could achieve in our cryostat by mounting the sample vertically and exploiting the stronger z-magnet.

To estimate the dephasing contributions from charge noise, we consider the measured hole g-factors in table 4.1. Assuming a constant  $\frac{\partial g_h}{\partial V_{\text{bias}}}$ , we estimate  $\frac{\partial g_h}{\partial V_{\text{bias}}} = 0.31 \text{ V}^{-1}$ . Additionally, assuming that the observed  $\sigma(X^+)$  broadening is solely due to electronic noise acting via the DC-Stark shift, we estimate a voltage noise  $\delta V_{\text{bias}} < 0.61$  mV. This is an upper bound, as nuclear spin noise and phonons also contributes to  $\sigma(X^+)$ . By combining (2.67) and (2.59) we estimate a lower bound on  $T_2^*$  set by charge noise

$$(T_2^*)_{\text{charge noise}} \geq \frac{\sqrt{2}\hbar}{B_{\text{ext}}\mu_B \left| \frac{\partial g_h}{\partial V_{\text{bias}}} \right| \delta V_{\text{bias}}} = 42 \text{ ns}, \quad (6.55)$$

which exceeds our measured  $T_2^*$  and supports the notion, that hyperfine interactions remain important for spin dephasing and decoherence. However, attempts to reduce charge noise, e.g. reduced use of the ABB laser, may also benefit  $T_2^*$ .

Finally, we compare the measured peak spin-echo visibility  $\mathcal{V}_0 = (50 \pm 2)\%$  to a simulation using the Monte Carlo framework explained in chapter 10. This simulation assumes a perfectly static Overhauser field during the spin-echo and will produce a  $\mathcal{V}_{\text{echo}}$  independent of  $\tau_e$ . However,  $\mathcal{V}_{\text{echo}}$  will depend on spin rotation errors, and spin initialisation and readout errors. We attempt to replicate our echo experiment by assuming  $T_r = 7$  ns,  $\Omega_r = \pi/T_r$ ,  $T_2^* = 23.2$  ns and  $\kappa = 0.021$  ns (figure 6.7b for  $\Delta_r/(2\pi) = 333$  GHz and  $P_{\text{rot}} = 7$   $\mu$ W). Additionally, we include a  $F_i = 98\%$  spin initialisation fidelity and  $F_r = 96.8\%$  spin readout fidelity (both estimated in section 9.2.2). This simulation yields  $\mathcal{V}_0 = 79.0\%$ , which significantly exceeds our measured visibility. This suggests imperfect echo rephasing (due to the discussed nuclear spin precession) or imperfections in the echo pulse sequence.

### 6.5.2 OTHER WORKS

Several other works have characterised InAs QD hole spins and found similar  $T_2^*$  times (26 ns [84], 21 ns [85] and 15 ns [86]), and a considerably longer<sup>5</sup>  $T_2^* > (460 \pm 80)$  ns is reported in Ref. [24]. However, all these works utilized bulk-like nanostructures. Few works have achieved quantum control in photonic nanostructures capable of inducing optical cyclicity. Ref. [54] reported  $T_2^* = 2.1$  ns for a positively charged QD in a micropillar cavity, while negatively charged QDs in photonic crystal cavities have produced  $T_2^* = 0.94$  ns [55] and  $T_2^* \sim 0.4$  ns [56]. Hence, our experiment presents an unprecedented combination of broadband optical cyclicity and all-optical coherent spin control in a QD with a relatively long  $T_2^*$ . This is achieved by having the optical decay dominated by the waveguide coupling through which one decay channel is strongly preferred. However, the Voigt  $\Lambda$ -systems may still be driven by a far-field laser. This is in contrast to the Faraday geometry, where diagonal transitions are suppressed due to the selection rules. Optical spin rotations in this geometry would likely require an infeasible amount of power. An attempt to solve this problem was recently made in Ref. [87] where the Faraday  $\Lambda$ -systems were driven via so-called hot trions. So far, it is unclear if the coupling is strong and coherent enough for fast rotations. Additionally, Faraday does not provide ideal decoupling of the hole spin from the Overhauser field (section 2.8.2).

### 6.5.3 IMPROVING SPIN ROTATIONS

Given the demonstrated  $T_2^* = 23.2$  ns,  $F_\pi = 98.2\%$  should be achievable, yet only  $F_\pi = (88.5 \pm 0.3)\%$  is measured. The main error mechanism is thus the experimentally observed laser-induced spin-flips. The observed spin-flip rate cannot be explained by trion scattering, neither in terms of absolute values of observed scaling with  $\Delta_r$ . Most likely, the spin-flip mechanism is related to the rotation lasers capability to photocreate hole spins. Hopefully, an improved heterostructure design may better protect the hole. Prolonging  $T_2^*$  through increased magnetic fields and reduced charge noise would however be needed for  $F_\pi > 99\%$ . As an alternative to the hole spin, the nuclear spin narrowing and electron spin control demonstrated in Ref. [78] could be adopted. We see no fundamental obstacles to this scheme, although it would require a larger magnetic field and an arbitrary waveform generator (AWG) for generating MW pulses. An AWG could anyway be beneficial, as it would enable more advanced pulse sequences and remove the tedious fine-tuning currently required. A final challenge is achieving high  $\Omega_r$  despite the poor QD far-field coupling. This coupling could perhaps be improved with the use of a spatial light modulator. As the PCW mode is linearly polarised, it is not possible to drive Raman transitions through the waveguide.

---

<sup>5</sup>This impressive measurement is undoubtedly the result of extremely low charge noise. However,  $T_2^*$  is estimated from modelling coherent population trapping and may not be completely comparable to the other works.

## 6.6 COMPARISON OF ULTRA-FAST AND RAMAN SCHEMES

The ultra-fast and Raman schemes for spin control differ in several ways as summarised in table 6.1, and we now discuss their merits in the context of entanglement generation.

	Ultra-fast	Raman
$\pi$ -pulse duration	$\sim 5$ ps	$\sim 5$ ns
Fidelity (single pulse)	$\text{sech}^2(\omega_g T_p/2) \approx 1 - \frac{(\omega_g T_p)^2}{4}$ [88]	$1 - \frac{2}{\pi^2} \left(\frac{T_p}{T_2^*}\right)^2$
Other errors	Polarisation, $\Delta_r$ noise, trion scattering	Polarisation, $\Delta_{MW}$ , trion scattering
Laser type	Mode locked laser	CW laser
Axis of rotation	Fixed	Arbitrary
Pulse sequence flexibility	Low (requires pulse picking, delay stages, interferometers)	High (electronically defined)
Spectral filtering	Grating	Grating or cavity
Previous works on QDs	$F_\pi = 0.91$ ( $X^-$ , [77]) $F_\pi = 0.96$ ( $X^-$ , [89]) $F_\pi = 0.89$ ( $X^+$ , [42])	$F_\pi = 0.9886 \pm 0.0004$ ( $X^-$ and nuclear narrowing, [78])

**Table 6.1:** Summary of difference between the ultra-fast and Raman approaches towards coherent spin control.

The main advantage of ultra-fast pulses is their insensitivity to  $T_2^*$  allowing control of electron spins without nuclear-spin narrowing. The fidelity of ultra-fast pulses is reduced at high magnetic fields as the natural spin precession tilts the rotation axis. However, this can be overcome with composite pulses [88]. Raman pulses require  $T_2^* > T_r$ , which rules out the bare electron spin. However, the long  $T_2^* \approx 40$  ns demonstrated with both hole spins [42] and electron spins with nuclear-spin narrowing [78] should in principle enable Raman pulses with per mille  $T_2^*$  errors. Again, composite pulses can further reduce the  $T_2^*$  dependence [82]. For both approaches, fidelity is likely limited by the noise and decoherence induced from the rotation pulse. Here ultra-fast pulses may be unfavourable, as their increased optical Rabi frequency could lead to phonon induced dephasing [90]. When reviewing the experiments performed thus far, Raman pulses also hold a clear record.

Regarding the experimental implementation, ultra-fast pulses, unsurprisingly, hold the advantage of being faster, potentially allowing some protocols to run at a higher rate. In all other regards, Raman pulses are strongly advantageous. The requirement of a mode-locked laser for ps pulse generation is a big downside if ultra-fast resonant excitation is also needed. This is the definitive reason why ultra-fast pulses were not considered in this project. Having two synchronised mode-locked lasers for both spin rotation and optical excitation was simply not a possibility.

For complex pulse sequences, e.g. the sequence in figure 9.11, ultra-fast pulses become very cumbersome<sup>6</sup>, requiring pulse picking, translation stages for variable delays, interferometers and compensation of varying optical coupling efficiencies. Additionally, the bi-chromatic spectrum of Raman pulses can be efficiently filtered with a Fabry-Perot cavity or an etalon. In this work, an etalon filter is anyway required and yields low loss filtering. The huge bandwidth of ultra-fast pulses necessitates other types of frequency filtering.

## 6.7 SUMMARY

Throughout this project, many improvements have been made to the spin control capabilities. Switching from the electron to the hole spin has given a  $\times 10$  increase in spin dephasing time consistent with measurements in bulk structures. The main challenge waveguide operation seems to be optimising the laser polarisation. Due to the higher visibility of hole spin Rabi oscillations, this optimisation can now be performed without changing the magnetic field geometry. An additional challenge of waveguides seems to be power delivery, which currently limits the obtainable  $\Omega_r$ . Currently, our main limitations arise from the laser-induced spin-flips which limit the spin rotation fidelity to  $F_\pi = (88.5 \pm 0.3)\%$ . These can hopefully be overcome by adopting new heterostructures or the electron spin. Increasing the magnetic field will likely aid in further decoupling the hole spin from the nuclei and avoiding the observed collapses of spin echo visibility. Assuming that these challenges can be overcome, our platform constitutes a powerful combination of optical cycling transitions and coherent optical spin control. The Raman pulse scheme allows great flexibility which may be further expanded with better electronics.

---

<sup>6</sup>Realising five ultra-fast rotation pulses with different delays and amplitudes is left as an exercise to the reader... on second thoughts, please carry on reading.

## 7 | Theory of Multi-Photon Entanglement

This chapter delves into the question of how to generate multi-photon entangled states from QD spins. After defining the entangled states of interest, the influential protocol of Lindner and Rudolph is described along with the parameter regime required for successful operation. Next, the protocol for time-bin entanglement is described in great detail: The intrinsic infidelity mechanisms are presented and the crucial role of the nanostructure leads to an optimisation of the entanglement fidelity. Finally, the procedure for measuring entanglement fidelity is laid out with a focus on GHZ states and the time-bin interferometer used for detecting photonic qubits.

### 7.1 ENTANGLED STATES OF INTEREST

We will now briefly review some basic properties of Bell states, GHZ states and 1D-cluster states, and the types of photonic qubits.

#### 7.1.1 BELL STATES

The simplest entangled states are the four Bell states [81]

$$|\Phi^\pm\rangle = \frac{1}{\sqrt{2}} (|00\rangle \pm |11\rangle), \quad (7.1)$$

$$|\psi^\pm\rangle = \frac{1}{\sqrt{2}} (|01\rangle \pm |10\rangle). \quad (7.2)$$

These states are maximally entangled and form a complete basis for the four-dimensional Hilbert space consisting of two qubits. The Bell states can be created by combining the Hadamard and the controlled NOT (CNOT) gates [81], which are ubiquitous in entanglement generation. The Hadamard is given by

$$\hat{H} = \frac{1}{\sqrt{2}} \begin{bmatrix} 1 & 1 \\ 1 & -1 \end{bmatrix}, \quad (7.3)$$

and acts to initialise super positions via  $\hat{H}|0\rangle = (|0\rangle + |1\rangle)/\sqrt{2} = |+\rangle$  and  $\hat{H}|1\rangle = (|0\rangle - |1\rangle)/\sqrt{2} = |-\rangle$ . In this work, the Hadamard will be replaced by  $\pi/2$  rotations around the y-axis, which generates the same states but requires keeping track of

phases as discussed in Ref. [19]. The CNOT is a two-qubit gate given by

$$\hat{U}_{CNOT} = \begin{array}{cccc|c} |00\rangle & |01\rangle & |10\rangle & |11\rangle & \\ \left[ \begin{array}{cccc} 1 & 0 & 0 & 0 \\ 0 & 1 & 0 & 0 \\ 0 & 0 & 0 & 1 \\ 0 & 0 & 1 & 0 \end{array} \right] & \begin{array}{c} |00\rangle \\ |01\rangle \\ |10\rangle \\ |11\rangle \end{array} & , & (7.4) \end{array}$$

and has the effect of flipping the second qubit (the target qubit) if the first qubit (the control qubit) is in  $|1\rangle$ . A Bell state may then be created by preparing two qubits in a pure, separable state and applying  $\hat{H}$  followed by  $\hat{U}_{CNOT}$  as illustrated in figure 7.1. This quantum circuit maps the four possible inputs  $|00\rangle, |01\rangle, |10\rangle, |11\rangle$  to the four Bell states in (7.1,7.2).

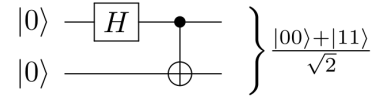


**Figure 7.1:** Quantum circuit for creating  $|\Phi^+\rangle$  by applying a Hadamard and CNOT gate on the initial state  $|00\rangle$ .

Photonic Bell states are by themselves important, as they form the backbone of quantum teleportation, super-dense coding and the E91 quantum key distribution protocol [81]. Notable experimental approaches for generating photonic Bell states include SPDCs [91] and the QD biexciton-cascade [92]. QDs have also been used to create entanglement between a QD spin a frequency-encoded photon [89,93], which has been used to mediate entanglement between distant QDs [94].

### 7.1.2 GHZ STATE

The  $N$ -qubit Greenberger–Horne–Zeilinger (GHZ) state is given by [81]

$$|\text{GHZ}^{(N)}\rangle = \frac{1}{\sqrt{2}} \left( |0\rangle^{\otimes N} + |1\rangle^{\otimes N} \right), \quad (7.5)$$

which represents an equal superposition of all qubits in  $|0\rangle$  or  $|1\rangle$ . Note that  $|\text{GHZ}^{(2)}\rangle = |\Psi^+\rangle$ . The GHZ state has enabled strong rejections of local realism [95], but has also been proposed as the key resource for ballistic universal computing in Ref. [96]. As will be discussed in section 7.6, the simple form of (7.5) makes it highly favourable to measure.

### 7.1.3 CLUSTER STATE

The two and three-qubit linear cluster states are given by [20]

$$\left| \text{Cluster}^{(2)} \right\rangle = \frac{1}{2} (|00\rangle + |01\rangle + |10\rangle - |11\rangle), \quad (7.6)$$

$$\left| \text{Cluster}^{(3)} \right\rangle = \frac{1}{\sqrt{8}} (|000\rangle + |001\rangle + |010\rangle - |011\rangle + |100\rangle + |101\rangle - |110\rangle + |111\rangle). \quad (7.7)$$

In contrast to the GHZ state, the linear cluster cannot be written in a compact form and has an exponentially increasing number of terms. An important feature of the cluster state is its tendency to remain entangled following single-qubit measurements. In contrast, a GHZ state fully collapses following a single z-measurement. It is this feature that makes the cluster state attractive for protecting against photon loss in the context of photonic repeaters [10, 11]. In a graph state representation, (7.7) is represented by three qubits on a string where qubits are entangled with the nearest neighbours, hence the name linear-cluster state. In general, two-dimensional cluster states are required for measurement-based quantum computing and photonic quantum repeaters. This can be achieved either by fusing smaller one-dimensional clusters [97] or by using two coupled emitters [98].

### 7.1.4 ENCODING SCHEMES

Photons can encode information using their polarisation, path, time and frequency degrees of freedom in addition to the number of photons. The photon number is often a poor qubit, as photon loss acts to decohere the state. For the other encodings, photon loss is detectable and reduces detection probability but not fidelity. This is often referred to as dual-rail encoding, as the qubit levels correspond to two separate, orthogonal photonic modes. The different dual-rail encodings offer various experimental advantages and disadvantages. For example, path qubits require an interferometrically stable transmission channel. Polarisation qubits require a polarisation maintaining transmission channel, but can be easily measured using linear polarisation optics. Time-bin qubits can easily be transmitted over a long distance, as the early and late photon components propagate through the same transmission channel separated by a short time delay over which the channel remains phase-stable. However, as will be shown in section 7.7, time-bin qubits require a stabilised, unbalanced interferometer for detection.

## 7.2 THE LINDNER-RUDOLPH PROTOCOL

In 2009, Netanel H. Lindner and Terry Rudolph proposed a simple method for creating on-demand linear photonic cluster states by utilizing solid-state emitters such as quantum dots [19]. The protocol follows the level scheme in figure 7.2a where a negatively charged QD is subjected to a small magnetic field in the y-direction (Voigt geometry). However, the dynamics are analysed using the z-projection spin states giving rise to ground state and excited state Larmor precession with the rates

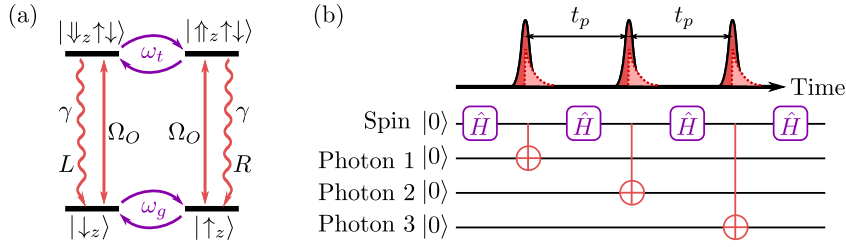


**Figure 7.2:** The Lindner-Rudolph protocol. **(a)** Level structure of a negative charged QD in the Voigt geometry analysed with the z-spin states.  $\omega_g$  ( $\omega_t$ ) indicates the rate of ground state (trion) precession. **(b)** Entanglement Protocol consisting of periodic QD excitation with period  $t_p$ . Precession periods correspond to Hadamard gates  $\hat{H}$  in the quantum circuit diagram while photon emission corresponds to CNOT gates due to the photon polarisation being determined by the spin z-projection.

$\omega_g$  and  $\omega_t$ , respectively. Letting the spin precess for a period  $t_p = \pi/(2\omega_g)$  realises a  $\hat{R}_y(\pi/2) = e^{-i(\pi/4)\hat{\sigma}_y}$  rotation of the electron spin.

Initialising the system in  $|\uparrow_z\rangle$  and allowing a  $\pi/2$  precession creates the even superposition state  $|\psi\rangle = (|\uparrow_z\rangle + |\downarrow_z\rangle)/\sqrt{2}$ . Exciting the QD with a linearly polarised  $\pi$ -pulse coherently transfers the superposition to the trions,  $|\psi\rangle = (|\uparrow_z\uparrow\downarrow\rangle + |\downarrow_z\uparrow\downarrow\rangle)/\sqrt{2}$  which then decay radiatively and gives the spin-photon Bell state  $|\psi\rangle = (|\uparrow_z\rangle|R\rangle + |\downarrow_z\rangle|L\rangle)/\sqrt{2}$  where  $R(L)$  indicates a right(left)-handed circular polarised photon. The sequence of  $\pi/2$  precession and optical excitation is then repeated, leading to the creation of a linear cluster state.

In summary, the protocol simply consists of periodic optical excitations corresponding to the quantum circuit in figure 7.2b. Had the  $\pi/2$  precessions been omitted, a GHZ state would instead have been produced. The role of the spin is to act as an entangler, retaining a quantum memory and ensuring correlations between the emitted photons. This gives rise to the picture of a cluster state machine gun or, perhaps more elegantly put, a knitting machine where the electron spin is the knitting needles braiding photons together into an entangled braid.

What are then the physical requirements for realising the protocol? Primarily, the radiative decay rate  $\gamma$  must satisfy  $\gamma \gg \omega_g$ . In the z-basis picture of figure 7.2a, the requirement springs from the fact that an uncertainty in photon emission time translates to an uncertainty in the precession angle. In the Voigt picture, where the magnetic field gives rise to Zeeman split states, each trion may decay via two channels emitting photons of different frequencies. The photon frequency provides which-path information unless the splitting is much smaller than the linewidth, i.e.  $\gamma \gg \omega_g$ . Reducing  $\omega_g$  and increasing  $t_p$  comes at the cost of increased sensitivity to the fluctuating Overhauser field as quantified by  $T_2^*$ . Hence, the difficulty of the Lindner-Rudolph protocol can be summarised by the condition

$$\gamma \gg \omega_g \gg (T_2^*)^{-1}, \quad (7.8)$$

necessitating either high levels of Purcell enhancement to boost  $\gamma$  or a spin with a long coherence time. A long  $T_2^*$  at low magnetic fields is especially challenging as

the transverse components of the Overhauser field are no longer suppressed. This is especially problematic for the hole spin (which might otherwise be well suited, see discussion in section 2.8). The low  $\mathbf{B}$  regime also prevents spin initialisation through optical pumping. This can however be circumvented by measuring the polarisation of the first photon in the  $\{|R\rangle, |L\rangle\}$  basis to project the spin state. An advantage of the Lindner-Rudolph protocol is its immunity to phonons. As long as phonons couple equally to both trions, no which-path information is gained through phonon scattering. However, for applications such as fusion of multiple cluster states indistinguishability remains important [99].

In assessing the feasibility of the Lindner-Rudolph protocol, we must also consider the experimental requirements and in particular nanostructure compatibility. The photon encoding requires a polarisation preserving nanostructure such as a cylindrically symmetric bullseye cavity or micropillar cavity. Polarisation encoding also excludes the cross polarisation technique commonly associated with the aforementioned structures, as this would project the emitted photons onto a single polarisation. To extinguish the excitation laser, one must either use non-resonant excitation (associated with reduced indistinguishability [100]), excitation from a side-channel or extremely tight temporal filtering. The use of most waveguide structures is also excluded as both circular dipoles will be projected onto the same waveguide mode and the polarisation information lost. A possible exception is the use of a chiral waveguide coupling whereby the polarisation is mapped onto the propagation direction of the photon [101, 102]. The degree of chirality will then become an additional source of infidelity. Additionally, off-chip applications will require the now path-encoded photons to be coupled into two interferometrically stable output modes which is very challenging<sup>1</sup>.

### 7.2.1 EXPERIMENTAL REALISATIONS OF LINDNER-RUDOLPH

An experimental realisation of the Lindner-Rudolph was performed by I. Schwartz et. al. in 2016 [20]. The experiment used a QD loaded with a quasi-stable dark exciton. The dynamics and selection rules of this system are functionally identical to figure 7.2. However, the precession is given by intrinsic strain and no magnetic field is applied. The dark exciton has been shown to possess a long  $T_2^* \approx 100$  at zero magnetic field [104], although a complete understanding of the physics is somewhat lacking. Crucially, the system can be excited non-resonantly solving the issue of laser rejection. The QD was placed in a bulk-like structure with DBR layers and a solid immersion lens used to improve collection efficiency.

A localised entanglement between photons two emissions apart was measured with  $1.5\sigma$  significance, thus justifying a claim of three-qubit entanglement. The infidelity was primarily given by the spin precession during the optical decay which could not be optimised due to the non-tuneability of  $\omega_g$ . This experiment remains an impressive experimental achievement and continues to inspire work into spin-photon entanglement. However, it is unclear if this approach is truly scaleable given the lack of tunable parameters. Additionally, the emitted photons in the dark

<sup>1</sup>A possible solution is to interfere the two paths on-chip with a polarisation-preserving grating coupler [103], thereby converting back to polarisation.

exciton system have a poor indistinguishability of 63% [105] (a consequence of the non-resonant excitation) which is a serious obstacle for most applications.

### 7.3 TIME-BIN PROTOCOL

Related to the Lindner-Rudolph is a protocol of time-bin entanglement capable of deterministically generating GHZ and linear cluster states. Here, information is encoded in the emission time of the photons. The ideal protocol follows the

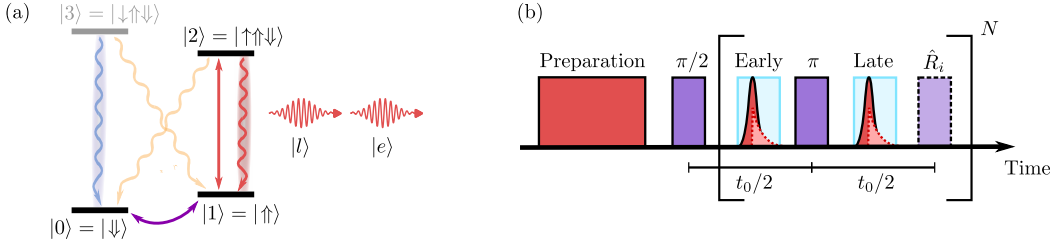


**Figure 7.3:** Ideal time-bin protocol. **(a)** Level structure of a positively charged QD in an in-plane (Voigt) magnetic field. Raman pulses connect the two ground states and the  $|1\rangle \leftrightarrow |2\rangle$  transition is excited to generate single photons in the early and late time-bins. Diagonal decays are suppressed by the nanostructure. **(b)** Pulse sequence consisting of spin preparation and alternations between spin rotation and optical excitation. The square brackets indicate a single round of the protocol which generates a single photon in either the early or late time-bin. Running the protocol  $N$  times yields an  $N+1$  qubit GHZ state (when  $\hat{R}_i = \hat{R}_y(\pi)$ ) or linear cluster state (when  $\hat{R}_i = \hat{R}_y(\frac{\pi}{2})$ ).

level structure and pulse sequence in figure 7.3. The conventions in Ref. [106] are followed assigning  $|0\rangle = |\downarrow\rangle$  and  $|1\rangle = |\uparrow\rangle$  and the  $|0\rangle, |1\rangle$  notation will be used hence forth. This also encourages a more general treatment without committing to a negatively or positively charged QD. The QD is subjected to a strong in-plane magnetic field and placed in a PCW to achieve high optical cyclicity as explained in chapter 5.

The protocol relies on repeating two different operations:

1.  $\pi$  and  $\pi/2$  rotations of the ground state spin around the y-axis<sup>2</sup> according to

$$\hat{R}_y(\pi) = e^{-i(\pi/2)\hat{\sigma}_y} = -|0\rangle\langle 1| + |1\rangle\langle 0|, \quad (7.9)$$

$$\hat{R}_y(\frac{\pi}{2}) = e^{-i(\pi/4)\hat{\sigma}_y} = (|0\rangle\langle 0| - |0\rangle\langle 1| + |1\rangle\langle 0| + |1\rangle\langle 1|)/\sqrt{2}. \quad (7.10)$$

2. Optical  $\pi$ -pulses resonant with  $|1\rangle \leftrightarrow |2\rangle$ . These pulses serve to "append" a photon to the  $|1\rangle$  terms in the wavefunction. Formally, the operation can be represented by the generalised creation operators  $\hat{A}_{e,j}^\dagger = |0\rangle\langle 0| + |1\rangle\langle 1| \hat{a}_{e,j}^\dagger$  and  $\hat{A}_{l,j}^\dagger = |0\rangle\langle 0| + |1\rangle\langle 1| \hat{a}_{l,j}^\dagger$ , where  $a^\dagger$  is the photon creation operator, the

<sup>2</sup>The actual axis of rotation is completely arbitrary and only generates a global phase. What matters is the relative phase between subsequent pulses. Y-rotations look nicer on paper as the resulting states have real amplitudes.

$e(l)$  subscript denotes the early(late) time-bin and  $j$  denotes the repetition number.

A GHZ or cluster state with one spin and  $N$  photons can be created through the following steps:

1. Optical pumping on  $|1\rangle \leftrightarrow |2\rangle$  prepares  $|0\rangle$  after which a  $\hat{R}_y(\pi/2)$  rotation prepares the spin in  $|\psi\rangle = (|0\rangle + |1\rangle)/\sqrt{2}$ .
2. The early excitation pulse  $\hat{A}_{e,j}^\dagger$  is applied.
3. The ground states are flipped with  $\hat{R}_y(\pi)$ .
4. The late excitation pulse  $\hat{A}_{l,j}^\dagger$  is applied.
5. In the case of GHZ, an additional  $\hat{R}_y(\pi)$  rotation is applied. For cluster state,  $\hat{R}_y(\pi/2)$  is instead applied.
6. Steps 2-5 are repeated  $N$  times.

The evolution during a single round of the GHZ protocol is then as follows:

$$\begin{aligned} \frac{1}{\sqrt{2}}(|0, \emptyset\rangle + |1, \emptyset\rangle) &\xrightarrow{2} \frac{1}{\sqrt{2}}(|0, \emptyset\rangle + |1, e\rangle) \xrightarrow{3} \frac{1}{\sqrt{2}}(|1, \emptyset\rangle - |0, e\rangle) \\ &\xrightarrow{4} \frac{1}{\sqrt{2}}(|1, l\rangle - |0, e\rangle) \xrightarrow{5 \text{ (GHZ)}} \frac{-1}{\sqrt{2}}(|0, l\rangle + |1, e\rangle), \end{aligned} \quad (7.11)$$

where  $\emptyset$  denotes the photon vacuum,  $|e\rangle$  denotes an early photon and  $|l\rangle$  denotes a late photon. This state is a spin-photon  $|\Phi^+\rangle$  Bell state when assigning the logical levels  $|l\rangle \rightarrow |0\rangle$  and  $|e\rangle \rightarrow |1\rangle$ . It is easily seen that repeating steps 2-5 will yield a three-qubit GHZ state. The effect of repeating steps 2-5 can be summarised by the ideal single round operator:

$$\hat{O}_{j,GHZ}^\dagger = -(|0\rangle\langle 0| a_{l,j}^\dagger + |1\rangle\langle 1| a_{e,j}^\dagger), \quad (7.12)$$

which adds an early/late photon in the  $j$ 'th repetition of the protocol.  $\hat{O}_{j,GHZ}^\dagger$  is also equivalent to a CNOT gate between the spin qubit and the  $j$ 'th photon from which the generation of a GHZ state also becomes evident. In regards to a quantum circuit, steps 2-5 play the same role as the optical excitation in the Lindner-Rudolph protocol as they create a photon fully correlated with the spin state. If instead a  $\hat{R}_y(\pi/2)$  rotation is applied in step 5 the first round yields the state

$$\xrightarrow{5 \text{ (Cluster)}} (|1, l\rangle - |0, l\rangle - |0, e\rangle - |1, e\rangle)/2, \quad (7.13)$$

which is the beginning of a cluster state. The  $\hat{R}_y(\pi/2)$  serves to "split up" the wavefunction and plays the same role as the  $\hat{R}_y(\pi/2)$  precessions in the Lindner-Rudolph protocol. The choice of  $\hat{R}_i = \hat{R}_y(\pi/2)$  as opposed to  $\hat{R}_i = \hat{R}_y(3\pi/2)$  is driven by an experimental desire to minimize the total area of rotation pulses. The generated state is the same but for a change in signs.

Since the protocols for GHZ and cluster state generation are near identical and suffer from the same infidelities (albeit with slightly difference scaling), the GHZ state will henceforth be the main experimental focus of this work due to its significantly easier verification (section 7.6).

A few remarks are in place about this protocol: It is important to emphasize that there is only ever one photon emitted in each repetition of the protocol. Until any measurement is performed, the photon exists both in the early and late time-bin and is entangled with the spin. The emission time of the photon does not need to be resolved, but it is assumed that time-bin durations and separations are long enough ( $> 1/\gamma$ ) that the photon is always contained within the time-bin and that early and late photon modes are orthogonal.

## 7.4 INTRINSIC INFIDELITIES

The four main intrinsic error mechanisms are now considered separately. This section will follow the treatment in Ref. [106], highlighting the key results but omitting the theoretical details. The four error mechanisms are illustrated in figure 7.4. The calculated fidelities represent the operational fidelity as defined by

$$\mathcal{F}^{(N)} = Tr_{env}\{\langle\psi_i|\rho_{exp}|\psi_i\rangle\}, \quad (7.14)$$

where the trace over the environment represents our ignorance of unobserved degrees of freedom such as scattered phonons or lost photons. We also integrate over the emission time of the photons. Additionally, the fidelity is conditioned on measuring at least one photon in each round of the protocol. This allows filtering to prevent certain erroneous trajectories from being detected. A Franson interferometer such as the one in figure 7.4b is needed to interfere the early and late photon components to realise photonic xy-measurements.

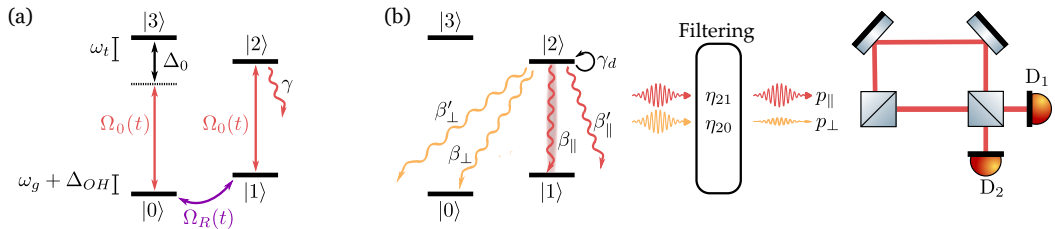


**Figure 7.4:** Illustration of intrinsic infidelities in time-bin entanglement. **(a)** Errors during excitation and spin control. The excitation laser with Rabi Frequency  $\Omega_0(t)$  drives both  $|0\rangle \leftrightarrow |3\rangle$  and  $|1\rangle \leftrightarrow |2\rangle$ . Only the finite detuning  $\Delta_0$  limits the excitation of  $|3\rangle$ . During free, evolution  $\Delta_{OH}$  contributes an unknown phase which is cancelled out by spin echo. **(b)** Errors during optical decay. While in  $|2\rangle$ , the QD scatters phonons with rate  $\gamma_d$  causing the entangled state to dephase. Additionally, 4 possible decay paths exist. A filter may be used to suppress detection of the undesired  $\beta_{\perp}$  decay.

### 7.4.1 GROUND STATE DEPHASING

As discussed in section 2.8, the spin states experience a slowly fluctuating magnetic field contribution  $\Delta_{OH}$  from the nuclear Overhauser field as quantified by  $T_2^*$ . Remarkably, the protocol is insensitive to  $T_2^*$  for two reasons: Firstly, the  $\pi$ -pulses in the protocol act as spin echo pulses. Using an equal delay  $t_0/2$  (figure 7.3b) between rotation pulses ensures that the spin spends the same amount of time in  $|0\rangle$  and  $|1\rangle$ , causing  $\Delta_{OH}$  to only contribute a global phase. Secondly, when the photon is measured through the interferometer, we can't tell if it was emitted in the early or late time-bin. Regardless of early or late emission, the QD spent equal time in the excited  $|2\rangle$  state during both time-bins and  $\Delta_{OH}$  (alongside any slow fluctuation of the excited state energy) once again gives a global phase. Ultimately,  $T_2^*$  poses a limit on fidelity as with any echo scheme. More importantly,  $T_2^*$  will limit the fidelity of Raman pulses as discussed in section 6.2.2.

### 7.4.2 PHONON INDUCED DEPHASING

While in the excited state  $|2\rangle$ , the QD may scatter a phonon with rate  $\gamma_d$ . This scattering preserves the spin but induces a random phase on the state and thus removes the coherence. Put differently, the spin becomes entangled with the phononic environment which, when traced out, kills the coherence. Experimentally, this results in reduced detection visibility of xy-measurements. Considering only single-phonon scattering events, the N-photon GHZ fidelity becomes [106]

$$\mathcal{F}_{ph}^N[GHZ] = \frac{1}{2} + \frac{1}{2} \left( \frac{\gamma}{\gamma + 2\gamma_d} \right)^N = \frac{1 + I^N}{2}, \quad (7.15)$$

where

$$I = \frac{\gamma}{\gamma + 2\gamma_d} \quad (7.16)$$

is the photon indistinguishability, which may be measured with a Hong-Ou-Mandel experiment.  $I = 0$  gives  $\mathcal{F}_{ph}^N[GHZ] = 1/2$  corresponding to perfect z-correlations but no coherence. In the limit  $\gamma_d \ll \gamma$ , the fidelity can be approximated as

$$\mathcal{F}_{ph}^N[GHZ] \approx 1 - N \frac{\gamma}{\gamma + 2\gamma_d} = 1 - N \frac{1 - I}{2}. \quad (7.17)$$

### 7.4.3 EXCITATION ERRORS

In the ideal protocol, the optical  $\pi$ -pulses were assumed to be instantaneous and the level  $|3\rangle$  was neglected. In reality, the excitation pulse will have a finite duration  $T_{opt}$ , the excited state a lifetime  $\gamma$  and the unwanted transition  $|0\rangle \leftrightarrow |3\rangle$  will be detuned by  $\Delta_0 = \omega_g + \omega_t$  from the driving pulse, see figure 7.4a. Consequently, two errors may occur: Firstly, the QD may emit a photon during the  $\pi$ -pulse (a pulse-photon) leading to the possibility of two-photon emission. The pulse-photon

is nearly fully distinguishable from the spontaneously emitted photon<sup>3</sup> and, similar to the phonon scattering, provides which-path information on when the QD was excited. Secondly, the laser may excite  $|0\rangle \leftrightarrow |3\rangle$  causing an off-resonant photon to be emitted from  $|3\rangle$  which similarly causes dephasing. Filtering can improve the fidelity by decreasing the chance of detecting the "bad" photons, which will often lead to the trajectory being discarded by post selection. The off-resonant photon is easily removed by frequency filtering as  $\Delta_0 \gg \gamma$ . The pulse-photon may either be fully filtered by time-gating detection<sup>4</sup> to after the  $\pi$ -pulse or partially filtered with narrowband frequency filtering, as the pulse-photon has a bandwidth  $\propto 1/T_{opt} \gg \gamma$ .

Minimizing the excitation errors poses an optimisation problem. The first error is minimized when  $T_{opt} \ll \gamma^{-1}$  (fast, wideband pulses) while the second error is minimized when  $T_{opt} \gg \Delta_0^{-1}$  (slow, narrowband pulses). As a simplified model, assuming square excitation pulses with duration  $T_{opt}$  and perfect frequency filtering, one can choose  $T_{opt}$  such that a perfect  $\pi$ -pulse is achieved for  $|1\rangle \rightarrow |2\rangle$  and a  $2\pi$ -pulse is achieved for  $|0\rangle \rightarrow |3\rangle$ , thereby minimizing the emission from  $|3\rangle$ . The  $N$ -photon conditional fidelity then becomes [106]

$$\mathcal{F}_{exc,sq}^N = 1 - N \frac{\sqrt{3}\pi}{8} \frac{\gamma}{\Delta_0} \quad (7.18)$$

for the optimised pulse duration  $T_{opt} = \sqrt{3}\pi/\Delta_0$ .

#### 7.4.4 BRANCHING ERRORS

Due to the finite optical cyclicity, the QD has a chance to decay via the non-spin-preserving  $|2\rangle \rightarrow |0\rangle$  transition (figure 7.4b). This error is more complex in the sense that the spin is no longer conserved and the wavefunction branches into multiple combinations of spin and photonic states. The branching errors depend on the dynamics in figure 7.4b, which are parametrised by the four  $\beta$ -values introduced in chapter 5.1 which account for the internal efficiencies of the PCW. The measurement setup and frequency filtering adds external efficiencies  $\eta_{21}$  and  $\eta_{20}$  for transitions  $|2\rangle \rightarrow |1\rangle$  and  $|2\rangle \rightarrow |0\rangle$ . The  $\eta$ 's contain all efficiencies except for the PCW's and are in this work much smaller than unity. The probabilities of detecting photons from the vertical or diagonal transitions then become

$$p_{\parallel} = \eta_{21}\beta_{\parallel}, \quad (7.19)$$

$$p_{\perp} = \eta_{20}\beta_{\perp}, \quad (7.20)$$

<sup>3</sup>They are emitted during different times and have different bandwidth, see discussion in Ref. [107].

<sup>4</sup>Ideally, a shutter in the detection path would only open after the excitation pulse. The shutter should be placed before any frequency filtering as frequency filtering erases the temporal information. Such filtering is currently possible with integrated EOM devices however with considerable insertion loss.

and the corresponding probability of losing the photons become

$$p'_{\parallel} = \beta'_{\parallel} + (1 - \eta_{21})\beta_{\parallel}, \quad (7.21)$$

$$p'_{\perp} = \beta'_{\perp} + (1 - \eta_{20})\beta_{\perp}. \quad (7.22)$$

The full state after a single round of the GHZ protocol then reads [106]

$$\begin{aligned} |\psi^{(1)}\rangle = & \frac{1}{\sqrt{2}} \hat{R}_i(|0\rangle [\sqrt{p_{\parallel}} |e, \emptyset\rangle + \sqrt{p'_{\parallel}} |1_{e\parallel}, \emptyset\rangle + \sqrt{p_{\perp}} |l', \emptyset\rangle + p_{\perp} |l', e'\rangle \\ & + \sqrt{p_{\perp} p'_{\perp}} |l', 1_{e\perp}\rangle + \sqrt{p'_{\perp}} |1_{l\perp}, \emptyset\rangle + \sqrt{p_{\perp} p'_{\perp}} |e', 1_{l\perp}\rangle + p'_{\perp} |1_{e\perp}, 1_{l\perp}\rangle] \\ & + |1\rangle [\sqrt{p_{\parallel}} |l, \emptyset\rangle + \sqrt{p_{\parallel} p_{\perp}} |l, e'\rangle + \sqrt{p_{\parallel} p'_{\perp}} |l, 1_{e\perp}\rangle \\ & + \sqrt{p'_{\parallel}} |1_{l\parallel}, \emptyset\rangle + \sqrt{p'_{\parallel} p_{\perp}} |e', 1_{l\parallel}\rangle + \sqrt{p'_{\parallel} p'_{\perp}} |1_{l\parallel}, 1_{e\perp}\rangle]), \end{aligned} \quad (7.23)$$

where  $e'(l')$  denotes detecting a photon from the diagonal decay during early(late) excitation and "1" denotes a lost photon with the subscript indicating emission time and decay channel. " $\parallel$ " indicates vertical decay and " $\perp$ " indicates diagonal decay. The full expression is difficult to grasp and it is easier to consider the trajectories resulting in one or more photons which are illustrated in figure 7.5. Both ideal trajectories occur with amplitude  $\sqrt{p_{\parallel}}$  (figure 7.5a:b). Starting in  $|0\rangle$  can only result in a late error with amplitude  $\sqrt{p_{\perp}}$  (figure 7.5c) which can be completely removed with filtering. However, starting in  $|1\rangle$  allows an early error which can result in an additional error once the QD is re-excited by the late pulse (figure 7.5d). Perfect filtering,  $p_{\perp} = 0$ , increases the fidelity as the only the  $\sqrt{p'_{\perp} p_{\parallel}} |1\rangle |1_{e\perp}, l\rangle$  term survives postselection. This term has two interesting consequences. The first consequence is an overweight of late photons as quantified by the late/early ratio

$$\frac{P_l}{P_e} = \frac{|\langle l | \psi^{(1)} \rangle|^2}{|\langle e | \psi^{(1)} \rangle|^2} = \frac{p_{\parallel} + p_{\parallel} p'_{\perp}}{p_{\parallel}} = 1 + p'_{\perp} \stackrel{\eta_{20} \ll 1}{\approx} 1 + \beta_{\perp} + \beta'_{\perp} = \frac{C + 2}{C + 1}, \quad (7.24)$$

using equations (7.23, 7.22, 5.7), where  $C$  is the optical cyclicity. Intuitively speaking, the early pulse slightly polarises the spin.

The second consequence is that while the evolution  $|1\rangle \rightarrow |1\rangle |1_{e\perp}, l\rangle$  following an early error is non-ideal, the spin and photon remain correctly correlated. If this error occurs during the first round of the entanglement protocol it only results in dephasing but not a spin-flip error.

In the limit  $C \gg 1$  and low collection efficiency but no filtering, i.e.  $\eta_{20} = \eta_{21} \ll 1$ , the conditional  $N$ -photon GHZ error can be approximated by [106]

$$\mathcal{F}_{br}^{(N)}[GHZ] = 1 - N \left( \frac{3\beta_{\perp} + \beta'_{\perp}}{2} \right) + \frac{\beta'_{\perp}}{4}. \quad (7.25)$$

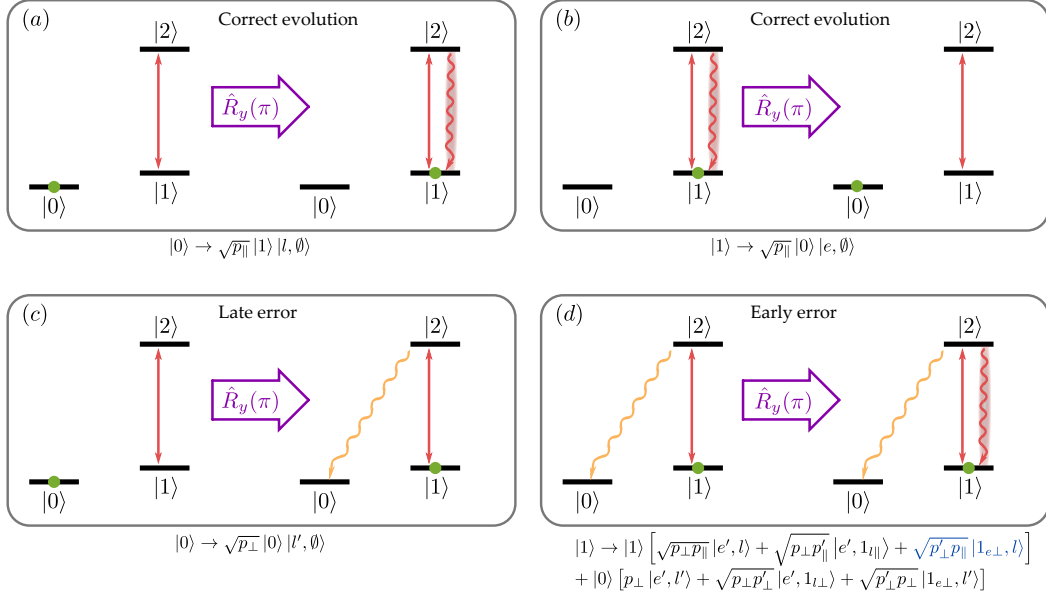


**Figure 7.5:** Possible trajectories during a single protocol round resulting in one or more detected photons. Level diagrams indicate evolution following an early excitation pulse,  $\pi$ -rotation and late excitation. Green dots indicate the state before excitation and squiggly lines indicate decay path. **(a,b)** ideal evolution without branching errors. **(c)** evolution with a diagonal decay during the late excitation. **(d)** evolution with an early diagonal decay followed by a late decay which may either decay correctly (vertical) or incorrectly (diagonal). The blue term in the output state is the only surviving term in the limit of perfect filtering  $p_{\perp} = 0$ .

Adding perfect filtering,  $\eta_{20} = 0$  gives the improved fidelity

$$\mathcal{F}_{br}^{(N)}[GHZ] \approx 1 - \left(N - \frac{1}{2}\right) \left(\frac{\beta_{\perp} + \beta'_{\perp}}{2}\right) = 1 - \frac{1}{2(C+1)} \left(N - \frac{1}{2}\right). \quad (7.26)$$

The  $(N - \frac{1}{2})$  term stems from the previously discussed fact, that the late error only causes dephasing during the first round<sup>5</sup>.

## 7.5 FIDELITY OPTIMISATION

The combined fidelity resulting from the three aforementioned errors can approximated by the product

$$\mathcal{F}[GHZ] = \mathcal{F}_{ph} \cdot \mathcal{F}_{exe} \cdot \mathcal{F}_{br}, \quad (7.27)$$

which can be expanded to first order giving

$$\mathcal{F}[GHZ] \approx 1 + \frac{1}{4(C+1)} - N \left( \frac{\gamma_d}{\gamma + 2\gamma_d} + \frac{1}{2(C+1)} + \frac{\sqrt{3}\pi}{8} \frac{\gamma}{\Delta} \right). \quad (7.28)$$

<sup>5</sup>50% discount on your first photon!

The fidelity may now be optimised which is done in Ref. [108]. The essence of the problem is that the photonic environment of the QD influences all error mechanisms. Optimising the QD position and increasing the group index  $n_g$  provides higher  $C$  and a Purcell enhanced  $\gamma$  as discussed in section 5.1. Enhancing  $\gamma$  decreases the phonon error as  $\gamma_d$  is assumed intrinsic to the QD but, conversely, worsens the excitation error. Thus, for a fixed set of QD parameters  $\gamma_d, \gamma_0^{hom}$  and  $\Delta_0$  there exists an optimal  $n_g$  which maximizes the total fidelity. The effect of the PCW

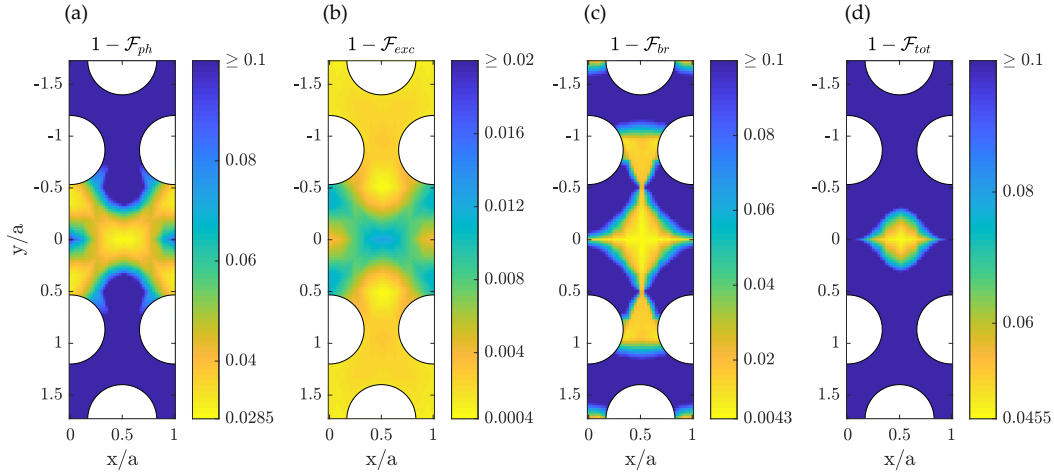


**Figure 7.6:** Spatially resolved infidelity contributions from (a) phonon dephasing, (b) excitation errors, (c) branching errors and (d) all errors for a group index  $n_g = 20$ . Physical parameters are given in the main text. Simulation data courtesy of Ref. [52].

can be explored using the numerical simulations presented in section 5.1. Figure 7.6 shows the infidelity contributions as a function of QD position for  $n_g = 20$ . The fidelities are calculated using (7.17), (7.18), (7.26) and (7.28) for  $N = 1$  using  $\Delta_0 = (2\pi) \times 17$  GHz (QD<sub>1</sub> at  $B_y = 2$  T) and  $\gamma_0^{hom} = 1$  ns<sup>-1</sup> (homogeneous decay rate introduced in (5.1)). Using equation (7.16),  $\gamma_d = 0.06$  ns<sup>-1</sup> is estimated based on Ref. [18] where  $I = 0.96$  and  $\gamma = 2.89$  ns<sup>-1</sup> were observed for a PCW embedded QD originating from the same wafer as QD<sub>1</sub>. The infidelity maps in figure 7.6a and figure 7.6b are perfectly anti-correlated due to their scaling with  $\gamma^{-1}$  and  $\gamma$ , respectively. The optimal region in figure 7.6c differs in shape as high cyclicity requires an additional suppression of the x-dipole. The ideal overall fidelity is given by a centrally placed QD as indicated by figure 7.6d. For a centrally positioned QD,  $n_g = 20$  results in  $\gamma = 2.0$  ns<sup>-1</sup> (comparable to QD<sub>1</sub> X<sup>+</sup>) and fidelity  $\mathcal{F}^{(1)} = 95.45\%$  with the infidelity contributions  $1 - \mathcal{F}_{ph} = 2.85\%$ ,  $1 - \mathcal{F}_{exc} = 1.27\%$ ,  $1 - \mathcal{F}_{br} = 0.43\%$ .

Figure 7.7 shows  $\mathcal{F}[GHZ](N = 1)$  as a function of  $\Delta_0$  for a centrally position QD at different  $n_g$ . Higher  $n_g$  enable higher fidelities, but only once  $\Delta_0 \gg \gamma$  is satisfied. Strong magnetic fields up to 8 T have been used to demonstrate coherent hole spins [42, 109] but can inhibit  $T_2^*$  via charge noise (section 2.8.2). Going beyond the 10 T in figure 7.7 seems questionable given existing demonstrations.

Going to a higher but realistic  $n_g = 56$ , we consider a realistic parameter set with  $C = 140$ ,  $\Delta_0 = 2\pi \times 64$  GHz,  $\gamma_d = 0.06$  ns<sup>-1</sup> and  $\gamma = 5.3$  ns<sup>-1</sup> which results in

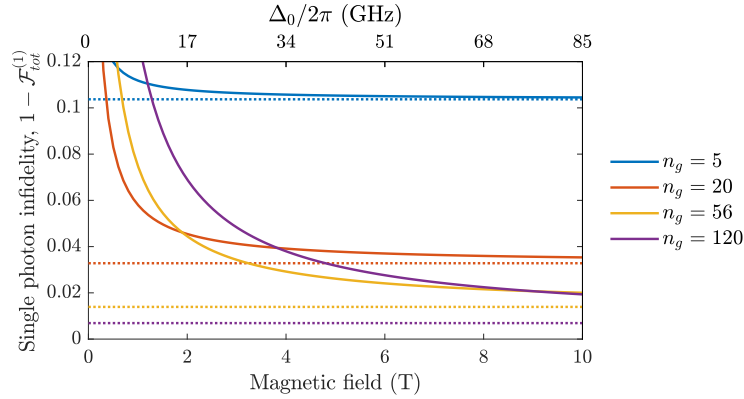


**Figure 7.7:** Total infidelity as a function of splitting  $\Delta_0$  for 4 different group indices given a QD placed in the PCW unit cell centre. Dashed lines indicate fidelity in the limit  $\Delta_0 \rightarrow \infty$ . Physical parameters are given in the main text. Conversion from magnetic field to  $\Delta_0$  assumes the measured  $(|g_{e,y}| + |g_{h,y}|)\mu_B/\hbar = (2\pi) \times 8.5 \text{ GHz/T}$  for QD<sub>1</sub>.

a 2.1% infidelity per qubit and a 10 qubit GHZ or cluster state with  $\approx 80\%$  fidelity [108]. This is in the ball-park of the 1.4% error threshold for quantum computing with two-dimensional cluster states [110]. Decreasing the dephasing rate  $\gamma_d$  (either through QD design, temperature or phononic engineering of the environment) would be of huge benefit in order to reach a 1% error level. Given the current  $\gamma_d$  estimate, high values of  $\gamma$  are required to increase indistinguishability, which in turn induce excitation errors. Neglecting branching errors, the tradeoff can be summarised by

$$\Delta_0 \gg \gamma \gg \gamma_d. \quad (7.29)$$

In addition to  $T_2^*$ -insensitivity and PCW-compatibility, a big strength of this protocol is likely the high entanglement generation rate ensured by fast radiative decays and optical spin rotations. A delay of only 10 ns between subsequent photonic qubits is reasonable. As opposed to entanglement generation based on probabilistic SPDC sources and probabilistic fusion [13], this protocol represents a near-deterministic source of multi-photon entanglement. Apart from outcoupling losses, efficiency is in principle only limited by the internal  $\beta$ -factor (close to unity) and losses related to phonon side-band filtering ( $\sim 5\%$  at 1.6 K [18]).

## 7.6 FIDELITY MEASURES

The question of how to best characterise entangled states is nontrivial. One approach is quantum state tomography which attempts to reconstruct the full density matrix from which the fidelity may be calculated. However, tomography requires an exponentially increasing number of measurement settings [111] rendering it infeasible for large numbers of qubits. A different approach is performing a limited set of measurements to either estimate a lower bound on the fidelity or produce an entanglement witness.

### 7.6.1 GHZ METHOD

Fortunately, the fidelity of an  $N$ -qubit GHZ state may be estimated exactly using only  $1 + N$  measurement settings. The method is derived in Ref. [112] and can be understood by re-writing the fidelity as

$$\mathcal{F} = \langle \psi_i | \rho_{exp} | \psi_i \rangle = Tr\{\rho_{exp} |\psi_i\rangle\langle\psi_i|\}, \quad (7.30)$$

where  $\rho_{exp}$  is the experimentally produced density matrix and  $|\psi_i\rangle$  is the ideal GHZ state given in (7.5). The projection operator can be expanded as

$$2 |\psi_i\rangle\langle\psi_i| = \hat{P}_z + \hat{\chi}, \quad (7.31)$$

$$\hat{P}_z = |0\rangle\langle 0|^{\otimes N} + |1\rangle\langle 1|^{\otimes N}, \quad (7.32)$$

$$\hat{\chi} = |0\rangle\langle 1|^{\otimes N} + |1\rangle\langle 0|^{\otimes N}. \quad (7.33)$$

Here,  $\hat{P}_z$  measures the degree of classical correlations and can be directly evaluated by measuring all qubits in  $z$ -basis.  $\hat{\chi}$  is constructed from  $N$  measurements using

$$\hat{\chi} = \frac{1}{N} \sum_{k=1}^N (-1)^k \hat{\mathcal{M}}_k, \quad (7.34)$$

$$\hat{\mathcal{M}}_k = \left[ \cos\left(\frac{k\pi}{N}\right) \hat{\sigma}_x + \sin\left(\frac{k\pi}{N}\right) \hat{\sigma}_y \right]^{\otimes N}, \quad (7.35)$$

which is shown in Ref. [112] and can easily be verified through direct calculation. Hence, all qubits should be measured along  $N$  different, equally spaced axes on the equator of the Bloch sphere as shown in figure 7.8.

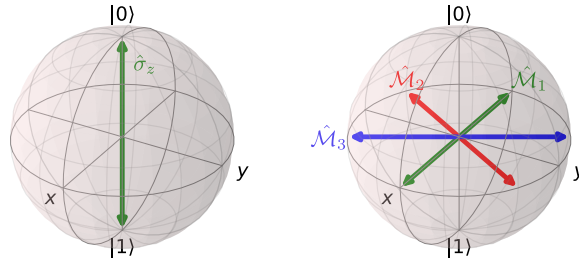


**Figure 7.8:** The  $N+1$  measurement bases required by the GHZ-method illustrated on the Bloch sphere for  $N = 3$ . All qubits are measured in the same basis.

Combining (7.30) and (7.31) gives the final fidelity

$$\mathcal{F} = \frac{\langle \hat{P}_z \rangle + \langle \hat{\chi} \rangle}{2}. \quad (7.36)$$

This method will be referred to as the GHZ-method and also applies to Bell states. The role of the  $\hat{\chi}$  operator can be better understood by considering the operator

$$\hat{\mathcal{M}}(\phi) = [\cos(\phi)\hat{\sigma}_x + \sin(\phi)\hat{\sigma}_y]^{\otimes N} = \begin{bmatrix} 0 & e^{-i\phi} \\ e^{i\phi} & 0 \end{bmatrix}^{\otimes N}, \quad (7.37)$$

which for the N-qubit GHZ state has the expectation value

$$\langle \hat{\mathcal{M}}(\phi) \rangle = \cos(N\phi). \quad (7.38)$$

In other words, measuring all qubits on the equator of the Bloch sphere and sweeping the azimuthal angle  $\phi$  gives a  $2\pi/N$  period oscillation.  $\hat{\mathcal{M}}(\phi)$  samples the oscillation at the angles  $\phi = k\pi/N$ ,  $k = 1..N$ , which gives  $(-1)^k$  following (7.38). The experimental requirement is thus the ability to precisely vary  $\phi$  for all qubits and be able to realise  $\phi = 0$ .

### 7.6.2 RELATION TO LOWER BOUND METHODS

A second method frequently used to measured spin-photon Bell states is given in Ref. [113]. This method differs by only measuring the two operators  $\sigma_z^{\otimes 2}$  and  $\sigma_x^{\otimes 2}$  and yields a lower fidelity bound of

$$\mathcal{F}_{bound} \geq \frac{1}{2} (\rho_{00,00} + \rho_{11,11} - 2\sqrt{\rho_{01,01}\rho_{10,10}} + \tilde{\rho}_{00,00} + \tilde{\rho}_{11,11} - \tilde{\rho}_{01,01} - \tilde{\rho}_{10,10}), \quad (7.39)$$

where  $\tilde{\rho} = \hat{R}_x(\pi/2)\rho\hat{R}_x^\dagger(\pi/2)$  is the density matrix after rotating both qubits  $\pi/2$  around  $x$ . Equation (7.39) can be recast in terms of the operators in section 7.6.1 to give

$$\mathcal{F}_{bound} \geq \frac{1}{2} (\langle \hat{P}_z \rangle + |\langle \hat{\mathcal{M}}_1 \rangle| - 2\sqrt{\rho_{01,01}\rho_{10,10}}). \quad (7.40)$$

Hence, by adopting the lower bound method and omitting a  $\sigma_y^{\otimes 2}$  measurement,  $\mathcal{F}_{bound}$  is reduced according to the magnitude of imperfect z-correlations  $\sqrt{\rho_{01,01}\rho_{10,10}}$ .

## 7.7 EXPERIMENTAL APPROACH

Despite looking simple on paper, translating the GHZ-method into a list of concrete measurements takes some consideration. For the sake of clarity, a distinction will be made between the *measured operators* ( $\hat{P}_z, \hat{\mathcal{M}}_k$ ), of which  $N + 1$  are required, and the *measurement settings*, which refer to the experimental pulse sequence and detection setting.

Realising the  $\hat{P}_z$  measurement is simple. Detecting the photon emission time reveals the photon z-projection without error<sup>6</sup>. Spin z-readout is performed with the combination of a  $\hat{R}_r$  rotation pulse and a readout pulse utilizing optical pumping. If one or more readout photons are detected, the spin is taken to be  $|\uparrow\rangle$ . However,

<sup>6</sup>This simplicity should not go unappreciated as virtually all other operations have errors.

since the readout can only detect  $|\uparrow\rangle$ ,  $\hat{R}_r$  is used to map the spin state of interest onto  $|\uparrow\rangle$ . Hence, to measure the spin projector  $|s\rangle\langle s|$ , we must apply  $\hat{R}_r$  such that

$$\hat{R}_r |s\rangle = |\uparrow\rangle. \quad (7.41)$$

Since the readout only measures a single projector, two measurement settings are required for each operator. For example, to measure  $\hat{P}_z$  we use one sequence with  $\hat{R}_r = \hat{\mathbb{I}}$  to measure  $|\uparrow\rangle\langle\uparrow|$  and a second sequence with  $\hat{R}_r = \hat{R}_y(\pi)$  to measure  $|\downarrow\rangle\langle\downarrow|$ .

In constructing the  $\hat{\mathcal{M}}_k$  operators it is useful to define the single qubit operator

$$\hat{\sigma}_{xy}(\phi) = \cos(\phi)\hat{\sigma}_x + \sin(\phi)\hat{\sigma}_y = \begin{bmatrix} 0 & e^{-i\phi} \\ e^{i\phi} & 0 \end{bmatrix} = |+(\phi)\rangle\langle+(\phi)| - |-(\phi)\rangle\langle-(\phi)|, \quad (7.42)$$

with the eigenstates

$$|+(\phi)\rangle = (|0\rangle + e^{i\phi}|1\rangle)/\sqrt{2}, \quad (7.43)$$

$$|-(\phi)\rangle = (|0\rangle - e^{i\phi}|1\rangle)/\sqrt{2}, \quad (7.44)$$

corresponding to the states on the equator of the Bloch sphere with azimuthal angles  $\phi$  and  $\phi + \pi$ . In the case of the spin, (7.41) dictates a  $\pi/2$  rotation around the azimuthal angle  $\phi_s$ :

$$\hat{R}_{xy}(\pi/2, \phi_s) = \frac{\hat{\mathbb{I}}}{\sqrt{2}} - \frac{i}{\sqrt{2}}(\cos(\phi_s)\hat{\sigma}_x + \sin(\phi_s)\hat{\sigma}_y) = \frac{1}{\sqrt{2}} \begin{bmatrix} 1 & -ie^{-i\phi_s} \\ -ie^{i\phi_s} & 1 \end{bmatrix} \quad (7.45)$$

which is given by (6.16) for  $\Delta_{MW} = 0$  and  $\Omega_r T_r = \pi/2$ . (7.45) then performs the desired mappings using  $\phi_s = \phi \pm \pi/2$ :

$$\hat{R}_{xy}(\pi/2, \phi + \pi/2) |+(\phi)\rangle = e^{i\phi} |1\rangle = e^{i\phi} |\uparrow\rangle \quad (7.46)$$

$$\hat{R}_{xy}(\pi/2, \phi - \pi/2) |-(\phi)\rangle = -e^{i\phi} |1\rangle = -e^{i\phi} |\uparrow\rangle \quad (7.47)$$

In the case of a time-bin qubit, the early and late parts of the photon must be interfered. This can be done using a Franson interferometer such as the one in figure 7.9a which is comprehensively discussed in chapter 8. Here, the late photon component is sent through a long arm with a delay equal to the time-bin separation such that the early and late photon components interfere on a 50:50 beam splitter and the photon is detected on either of the output detectors. A passive interferometer (lack of active switching) will lead to the 3 detection windows depicted in figure 7.9b, which herald the photonic detection basis [114]. Early and late detections herald a z-measurement, as the emission time is unambiguous, while the middle window erases the timing information, thus constituting an xy-measurement. For now, consider the middle bin where the early and late photon modes are transformed according to

$$\begin{pmatrix} \hat{a}_{D1}^\dagger \\ \hat{a}_{D2}^\dagger \end{pmatrix} = \underbrace{\frac{1}{\sqrt{2}} \begin{bmatrix} -ie^{-i\chi} & 1 \\ e^{-i\chi} & -i \end{bmatrix}}_{\hat{U}_{inf}} \begin{pmatrix} \hat{a}_e^\dagger \\ \hat{a}_l^\dagger \end{pmatrix}, \quad (7.48)$$

where  $\hat{a}_e^\dagger(\hat{a}_l^\dagger)$  are the early(late) photon creation operators and  $\hat{a}_{D1}^\dagger(\hat{a}_{D2}^\dagger)$  are the photon annihilation operators of the detector  $D_1(D_2)$  in the middle bin.  $\chi$  is the phase accumulated in the long arm and the  $i$ 's come from the reflections of the 50:50 BS. One can then simply define that the photon state  $|+\rangle = (\hat{a}_e^\dagger + \hat{a}_l^\dagger)|\emptyset\rangle/\sqrt{2}$  maps to detector 1 and  $|-\rangle = (\hat{a}_e^\dagger - \hat{a}_l^\dagger)|\emptyset\rangle/\sqrt{2}$  maps to detector 2, which is true for  $\chi = -\pi/2$ :

$$U_{inf}(\chi = -\pi/2)|+\rangle = \frac{1}{\sqrt{2}} \begin{bmatrix} 1 & 1 \\ i & -i \end{bmatrix} \frac{1}{\sqrt{2}} \begin{pmatrix} 1 \\ 1 \end{pmatrix} = \begin{pmatrix} 1 \\ 0 \end{pmatrix}. \quad (7.49)$$

Which detector is which is not ultimately important, as they can anyway be swapped by  $\chi \rightarrow \chi + \pi$ . What matters is that the interferometer is stable and has the correct time delay. Additionally, the early and late excitation pulses must have a well defined relative phase. One approach is to use two separate excitation and detection interferometers, which share the same path length difference and interferometer phase. We will pursue a more elegant solution by applying the double-pass interferometer in figure 7.9a.

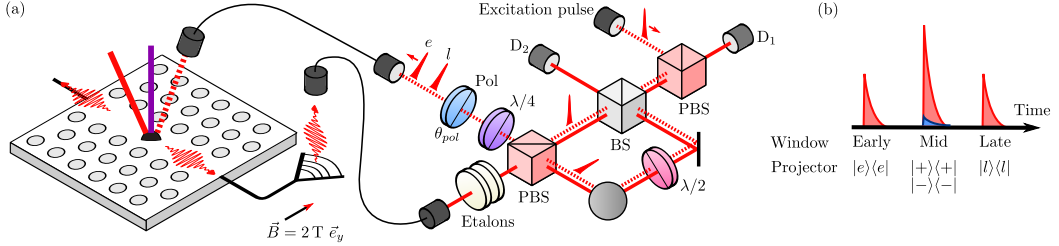


**Figure 7.9:** (a) Simplified experimental setup using a double pass interferometer. A single excitation pulse enters from the top and is split into an early and late excitation pulse. These pulses excite the QD in conjunction with the rotation and pumping lasers. The early and late photon components enter the same interferometer and have a chance to interfere on a 50/50 beamsplitter (BS) leading to detection on  $D_1$  or  $D_2$ . Abbreviations: Linear polariser (Pol), polarising beamsplitter (PBS). (b) The three possible detection patterns in time. Early and late herald a photonic z-measurement while the middle bin heralds a rotated basis.

Here, the same interferometer is used to create the excitation pulses and to detect the photonic qubits. The photonic readout basis is set by adjusting the excitation phase. While this might seem wrong (indeed, one could argue that the quantum state rather than the measurement basis is being changed) the only quantity of importance is the relative phase between excitation and detection. To illustrate this notion, consider the following example where a spin-photon Bell state is produced and the  $\hat{\mathcal{M}}(\phi)$  operator is measured. The late excitation operator is

modified to be  $\hat{A}_l^\dagger \rightarrow |0\rangle\langle 0| + |1\rangle\langle 1| e^{i\phi_l} \hat{a}_l^\dagger$  where  $\phi_l$  is the phase of the late excitation pulse. The first round then evolves according to

$$|0\rangle \xrightarrow{\hat{R}_y(\pi/2)} \frac{|0\rangle + |1\rangle}{\sqrt{2}} \quad (7.50)$$

$$\xrightarrow{\hat{A}_e} \frac{|0\rangle |\emptyset\rangle + |1\rangle |e\rangle}{\sqrt{2}} \quad (7.51)$$

$$\xrightarrow{\hat{R}_y(\pi)} \frac{|1\rangle |\emptyset\rangle - |0\rangle |e\rangle}{\sqrt{2}} \quad (7.52)$$

$$\xrightarrow{\hat{A}_l} \frac{e^{i\phi_l} |1\rangle |l\rangle - |0\rangle |e\rangle}{\sqrt{2}} \quad (7.53)$$

$$\xrightarrow{\hat{R}_{xy}(\pi/2, \pi/2 + \phi_s)} \frac{-(|0\rangle + e^{i\phi_s} |1\rangle) |e\rangle + e^{i\phi_l} (-e^{i\phi_s} |0\rangle + |1\rangle) |l\rangle}{2} \quad (7.54)$$

$$\xrightarrow{\hat{U}_{inf}} \frac{(-ie^{i\chi} - e^{i(\phi_l - \phi_s)}) |0, D_1\rangle + (-e^{i\chi} - ie^{i(\phi_l - \phi_s)}) |0, D_2\rangle}{\sqrt{8}} + \frac{(-ie^{i(\phi_s + \chi)} + e^{i\phi_l}) |1, D_1\rangle + (-e^{i(\phi_s + \chi)} + ie^{i\phi_l}) |1, D_2\rangle}{\sqrt{8}}, \quad (7.55)$$

where  $|D_1\rangle, |D_2\rangle$  represent the two detectors. The detection probabilities then follow

$$P_{0,D1} = P_{1,D2} = \frac{1}{4}(1 + \sin(\phi_l - \chi - \phi_s)), \quad (7.56)$$

$$P_{1,D1} = P_{0,D2} = \frac{1}{4}(1 - \sin(\phi_l - \chi - \phi_s)). \quad (7.57)$$

The coincidence probabilities only depend on the phase of the spin rotation  $\phi_s$  and the difference between the photonic excitation and detection phase ( $\phi_l - \chi$ ). There is thus no distinction between scanning the excitation and detection phase. The advantage of the double-pass interferometer is that  $(\phi_l - \chi)$  is stable over time, and  $\phi_l$  can be scanned using the polariser in figure 7.9 which is shown in chapter 8.

## 7.8 SUMMARY

The Lindner-Rudolph protocol offers a simple approach for deterministic multi-photon entanglement but suffers from the short coherence time of most QD spins, especially at low magnetic fields, and has problematic requirements for the nanostructure. The time-bin protocol offers several advantages: It utilises spin echo for  $T_2^*$ -insensitivity, operates at high magnetic fields allowing better spin coherence and spin initialisation, and has great compatibility with nanostructures, especially PCWs. However, successfully inducing optical cyclicity is crucial for its success.

The protocol is of higher complexity, with more operations required per generated photon yielding a wider range of error. These errors can be minimised with clever optimisation of the photonic environment but trade-offs between the three intrinsic error sources result in a global optimum. Another element in fidelity optimisation

is the use of filtering and post selection to reject detection of bad state evolutions. In terms of state verification, the GHZ is considerably easier than the linear cluster state as it only requires a linear number of measurements for an exact fidelity measurement. This scheme requires the spin and photonic qubits to be projected along arbitrary axes on the equator of the Bloch sphere. This can be realised with  $\pi/2$  spin rotations and with an interferometer.



**Figure 7.10:** A popular mantra in quantum photonics. Unfortunately, due to excitation errors, Purcell enhancement has limited benefit for time-bin entanglement. Figure reproduced from Ref. [115] and modified in accordance with the Creative Commons Attribution-Non Commercial 2.5 License.



## 8.1 THEORETICAL ANALYSIS

### 8.1.1 EXCITATION INTERFEROMETER

The Mira laser is connected to the FC<sub>1</sub> port (figure 8.1) and has a s-polarised electric field  $E_{L1}$  represented by the Jones vector

$$\mathbf{E}_{L1} = \Phi(t) \begin{pmatrix} 0 \\ 1 \end{pmatrix}, \quad (8.1)$$

where  $\Phi(t)$  contains the laser envelope function (the optical frequency has been removed by working in a rotation frame), and  $\begin{pmatrix} 1 \\ 0 \end{pmatrix}$  and  $\begin{pmatrix} 0 \\ 1 \end{pmatrix}$  are the basis vectors for p and s-polarisation, respectively. On encountering the BS the laser pulse is divided. The long interferometer arm creates the late pulse which becomes p-polarised thanks to HWP<sub>3</sub> and QWP<sub>3</sub>. After being recombined by PBS<sub>2</sub>, the fields of the early and late pulses are given by

$$\mathbf{E}_{L2}^e = \sqrt{T_{\text{short}}} \Phi(t - t_{\text{short}}) \begin{pmatrix} 0 \\ 1 \end{pmatrix}, \quad (8.2)$$

$$\mathbf{E}_{L2}^l = \sqrt{T_{\text{long}}} \Phi(t - t_{\text{long}}) e^{i\phi'} \begin{pmatrix} 1 \\ 0 \end{pmatrix}, \quad (8.3)$$

where the e(l) superscripts denote early(late), and  $T_{\text{short}}(T_{\text{long}})$  are the intensity transmission coefficients of the short(long) arms including BS splitting ratio and other losses.  $t_{\text{short}}$  and  $t_{\text{long}}$  are the short and long arm time delays, respectively, and together define the interferometer delay  $T_{TB} = t_{\text{long}} - t_{\text{short}}$ .  $\phi'$  is the phase accumulated in the long arm relative to the short arm. Subsequently, the  $\Phi$  terms will be ignored.

Consider now the transformation  $M_{tot}$  due to QWP<sub>4</sub>, linear polariser and HWP<sub>4</sub>

$$M_{tot} = M_{hwp}(\theta_{pol}/2) M_{pol}(\theta_{pol}) M_{qwp}(\theta_{qwp}) \quad (8.4)$$

$$= \begin{pmatrix} 1+i \\ 2 \end{pmatrix} \begin{bmatrix} \cos(\theta_{pol}) - i \cos(\theta_{pol} - 2\theta_{qwp}) & \sin(\theta_{pol}) + i \sin(\theta_{pol} - 2\theta_{qwp}) \\ 0 & 0 \end{bmatrix}. \quad (8.5)$$

Here  $M_{hwp}$ ,  $M_{pol}$  and  $M_{qwp}$  are the Jones matrices given in appendix E. HWP<sub>4</sub> always has the angle  $\theta_{hwp} = \theta_{pol}/2$  such that the output is p-polarised. Applying (8.5) to (8.2) and (8.3) gives the p-polarised field in front of FC<sub>2</sub>:

$$E_{L3}^e = \left( \frac{1+i}{2} \right) \sqrt{T_{\text{short}}} (\sin(\theta_{pol}) + i \sin(\theta_{pol} - 2\theta_{qwp})) \quad (8.6)$$

$$E_{L3}^l = \left( \frac{1+i}{2} \right) e^{i\phi'} \sqrt{T_{\text{long}}} (\cos(\theta_{pol}) - i \cos(\theta_{pol} - 2\theta_{qwp})), \quad (8.7)$$

with the intensities (modulo conversion constants)

$$I_{out}^e = |E_{L3}^e|^2 = \frac{T_{short}}{4} (2 - \cos(2\theta_{pol}) - \cos(2\theta_{pol} - 4\theta_{qwp})), \quad (8.8)$$

$$I_{out}^l = |E_{L3}^l|^2 = \frac{T_{long}}{4} (2 + \cos(2\theta_{pol}) + \cos(2\theta_{pol} - 4\theta_{qwp})), \quad (8.9)$$

and phase difference

$$\delta\phi = \text{Arg}(E_{L3}^l) - \text{Arg}(E_{L3}^e) \quad (8.10)$$

$$= \phi' + \text{Arg} \left( \frac{\cos(\theta_{pol}) - i \cos(\theta_{pol} - 2\theta_{qwp})}{\sin(\theta_{pol}) + i \sin(\theta_{pol} - 2\theta_{qwp})} \right). \quad (8.11)$$

The goal is then to scan  $\delta\phi$  while maintaining  $I_{out}^e = I_{out}^l$ . For  $T_{short} = T_{long}$ , we can simply fix  $\theta_{qwp} = \pi/4$  which results in the phase difference

$$\delta\phi = \phi' + 2\theta_{pol} - \pi/2. \quad (8.12)$$

Hence, by scanning  $\theta_{pol}$  through  $\pi$  we can sweep a full  $2\pi$  phase difference. In practice  $T_{short} = T_{long}$  can be achieved: While the long arm has more optical loss, one can preferentially couple the long arm into the FC<sub>2</sub> coupler, as the spatial modes of the short and long arm do not perfectly overlap. In the interest of generality, there also exists a general solution for  $T_{short} \neq T_{long}$  which allows a  $2\pi$  scan of  $\delta\phi$  while maintaining  $I_{out}^e = I_{out}^l$ . This is given by

$$\theta_{qwp} = \frac{1}{4} \left( \pm \arccos \left( \frac{4T_{laser}^S}{T_{laser}^S + T_{laser}^L} - 2(1 + \cos(2\theta_{pol})) \right) + 2\theta_{pol} + 2n\pi \right). \quad (8.13)$$

This approach however increases complexity, as  $\theta_{pol}$  and  $\theta_{qwp}$  must both be precisely controlled. The excitation interferometer is also capable of exclusively generating early pulses using  $\{\theta_{qwp} = 0, \theta_{pol} = \pi/2\}$  or late pulses using  $\{\theta_{qwp} = 0, \theta_{pol} = 0\}$ .

### 8.1.2 DETECTION INTERFEROMETER

We now consider the time-bin photons propagating from the FC<sub>3</sub> port. After frequency filtering (discussed in section 8.6), a pair of waveplates are used to fix the polarisation coming from the single-mode input fibre. This is done by minimizing the reflection of PBS<sub>1</sub>. Next, QWP<sub>2</sub> and the EOM are used to control the splitting ratio of PBS<sub>2</sub>. In passive operation, the EOM is turned off but in practice adds some birefringence, and the splitting ratio can be scanned around 50:50 with QWP<sub>2</sub> alone. The electric field at the detectors can then be written as

$$\begin{pmatrix} E_{D1}^e \\ E_{D2}^e \\ E_{D1}^m \\ E_{D2}^m \\ E_{D1}^l \\ E_{D2}^l \end{pmatrix} = \begin{bmatrix} \eta_{S1} & 0 \\ \eta_{S2}e^{i\phi_2} & 0 \\ \eta_{L1}e^{i(\phi_1+\phi)} & \eta_{S1} \\ \eta_{L2}e^{i\phi} & \eta_{S2}e^{i\phi_2} \\ 0 & \eta_{L1}e^{i\phi_1} \\ 0 & \eta_{L2} \end{bmatrix} \begin{pmatrix} E_1^e \\ E_1^l \end{pmatrix} \quad (8.14)$$

where  $D1$  and  $D2$  denote the two detector outputs in figure 8.1, and the super scripts denote the early(e), middle(m) and late(l) detection windows.  $\eta_{ij}$  is the electric field transmission from  $FC_3$  to detector  $j$  via path  $i$ .  $\phi_1$  and  $\phi_2$  are the BS reflection phase shifts defined in Ref. [116] which equate  $\phi_1 = \phi_2 = \pi/2$  for a lossless BS. A balanced input with  $E_1^e = 1$  and  $E_1^l = e^{i\psi}$  results in the middle window detector intensities

$$I_{D1}^m = |E_{D1}^m|^2 = \eta_{L1}^2 + \eta_{S1}^2 - 2\eta_{L1}\eta_{S1} \sin(\phi_1 + \phi - \psi), \quad (8.15)$$

$$I_{D2}^m = |E_{D2}^m|^2 = \eta_{L2}^2 + \eta_{S2}^2 + 2\eta_{L2}\eta_{S2} \sin(\phi_2 - \phi + \psi). \quad (8.16)$$

Equal  $\eta$  and  $\phi_1 = \phi_2 = \pi/2$  then yield a detector contrast with unit visibility:

$$\frac{I_{D1}^m - I_{D2}^m}{I_{D1}^m + I_{D2}^m} = -\cos(\phi - \psi) = -\cos(\phi - \phi' + 2\theta_{pol} - \pi/2), \quad (8.17)$$

where the last equality substituted  $\psi$  with  $\delta\phi$  from (8.12). Thus, if the excitation interferometer output is connected to the detection interferometer input, the phase of the detector fringes depends on  $\theta_{pol}$  and  $\phi - \phi'$ , which is the difference in long-arm phase between the two interferometers. Crucially,  $\phi - \phi'$  is expected to remain constant as interferometric drift affects both passes equally. This makes the interferometer "self stabilising". However, the value of  $\phi - \phi'$  can not be known a priori and must be calibrated as it depends on the concrete alignment.

For a non-equal values of  $\eta$ , the detection contrast is given by

$$\frac{I_{D1}^m - I_{D2}^m}{I_{D1}^m + I_{D2}^m} = -\nu_{TBI} \cos(\phi - \phi' + 2\theta_{pol} - \pi/2), \quad (8.18)$$

where the TBI visibility is given by

$$\nu_{TBI} = \frac{2(\eta_{L1}\eta_{S1} + \eta_{L2}\eta_{S2})}{\eta_{L1}^2 + \eta_{S1}^2 + \eta_{L2}^2 + \eta_{S2}^2}. \quad (8.19)$$

## 8.2 LASER SCATTER REJECTION

One challenge of the double pass design is preventing excitation laser reflections from entering the detectors, which can lead to unwanted background or, in the case of high intensity, deactivation of the SNSPD detectors. As each excitation pulse contains on the order of  $10^8$  photons, significant rejection is required. This is achieved by  $PBS_3$  and  $PBS_4$  and by vertically (out-of-plane) raising the excitation pass by 3 mm. This imposes strict requirements for the lens system in the long arm. Ideally, the optical mode of the detection pass should undergo the same transformation from both arms to ensure equal fibre couplings. Additionally, the excitation laser should enter and exit the long arm with the same beam height despite entering off-axis. These requirements are met with the lens system in figure 8.2. In the experiment, we achieve fibre coupling efficiencies between 81% and 88% for  $FC_4$  and  $FC_5$  for both arms. Ultimately, only one in  $\approx 2 \cdot 10^{11}$  excitation photons are reflected into a detector. This is sufficient, although some reflections are visible in the entanglement data (see figure 9.1).

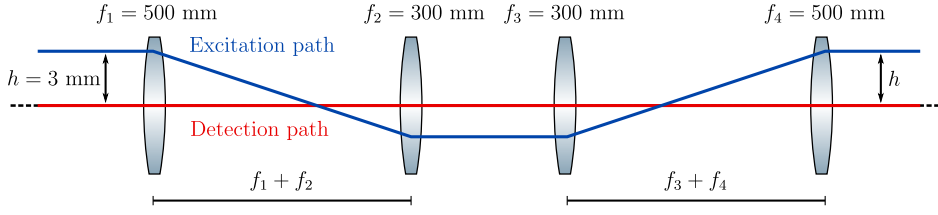


**Figure 8.2:** A four-lens system in the long interferometer arm preserves the height of both counter propagating beams and ensures correct mode transformation for high fibre coupling efficiency. Translation of the entire assembly and increasing the distance between lenses 2 and 3 gives 2 degrees of freedom for optimising fibre coupling.

### 8.3 TIMING CONSIDERATIONS

The interferometer delay is  $T_{TB} = 11.81$  ns corresponding to a distance of 3.541 m. This delay has been chosen as a compromise between the following factors:

1.  $T_{TB}$  should be short to facilitate optical stability and high repetition rate.
2.  $T_{TB}$  should be long enough to permit spin-rotations between excitations.
3. The photon detection windows should be unambiguous.

These requirements are met by the design in figure 8.3. By pulse picking every other Mira pulse, a repetition of the entanglement sequence has a duration  $2T_{Mira}$ . This duration is long enough to allow a 7 ns rotation pulse (figure 8.3c) without overlapping with the photons. Finally, the late detection of the first photon ( $l_1$ ) is distinguishable from the second photon's early window ( $e_2$ ).

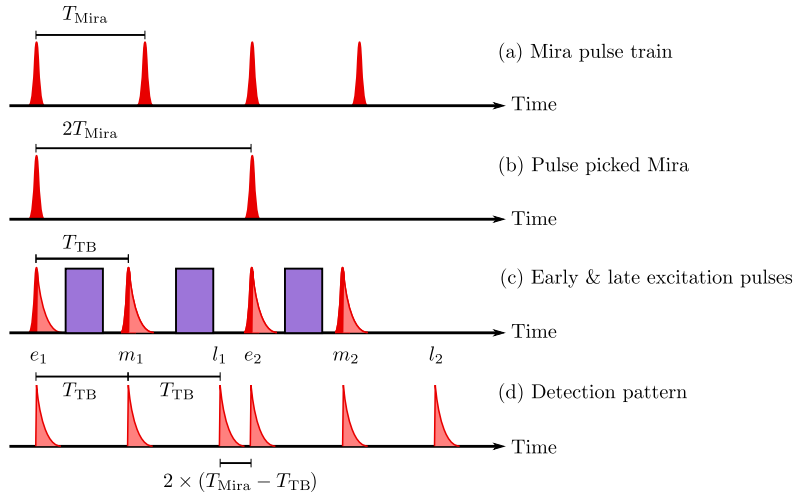


**Figure 8.3:** Timing dictated by the TBI. The Mira pulse train (a) is pulse picked giving the pulses in (b). The interferometer doubles the excitations pulses (c) which are interleaved with rotation pulses (purple). These are the pulses seen by the QD. (d) Photon detection using the TBI resulting in three detection windows pr repetition.

## 8.4 INTERFEROMETER CHARACTERISATION

We will now cover the three steps taken to optimise and characterise the TBI performance. As a first step, we measure the intensities of the pulses generated by the excitation interferometer for different angles of  $\theta_{pol}$  as shown in figure 8.4. By optimising the FC<sub>2</sub> coupling, we achieve a ratio  $R_{el} = I_{out}^e/I_{out}^l$  close to 1. Since a 180° range is sufficient to scan a full fringe,  $\theta_{pol}$  is restricted to the range  $\theta_{pol} \in [60^\circ, 240^\circ]$  where  $R_{el}$  has a mean  $\langle R_{el} \rangle = 1.004$  and standard deviation  $\sigma(R_{el}) = 0.017$ . This fluctuation has negligible impact on the probability to drive a  $\pi$ -pulse, as variations in power enter to second order (see equation (2.25)).

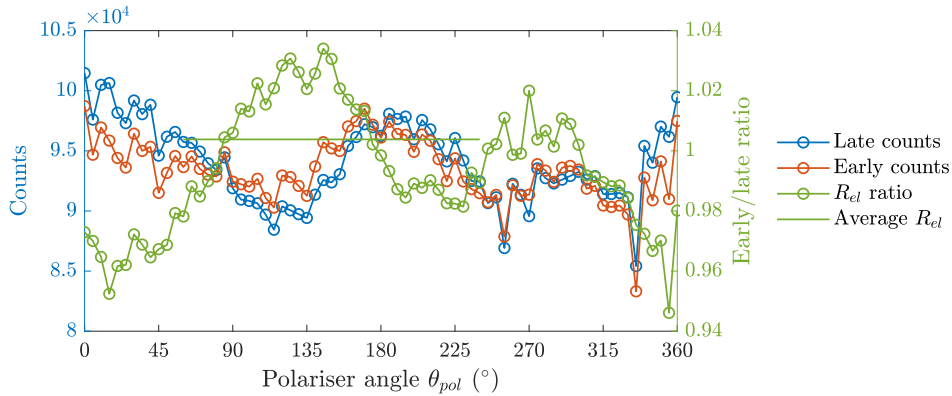


**Figure 8.4:** Attenuated output of excitation interferometer measured with an APD. Green dots show the intensity ratio  $R_{el}$  which should ideally be 1 for all  $\theta_{pol}$ . The solid green line indicates the mean  $R_{el}$  on  $\theta_{pol} \in [60^\circ, 240^\circ]$  used for successive measurements.

As a second step, we connect the FC<sub>2</sub> port to the cryostat path 2 (figure 3.4b) and connect the cryostat collection to FC<sub>3</sub> of the TBI. A non-resonant  $V_{bias}$  is selected to only collect laser scatter. Hence, this setup is equivalent to coupling the TBI excitation output to the detection input<sup>1</sup>. The PBS<sub>2</sub> ratio is varied by scanning  $\theta_D$  yielding the early and late intensities in figure 8.5.  $\theta_D$  is chosen to maximize the visibility defined in (8.19).

As a final step, we scan the early/late phase using  $\theta_{pol}$ . The counts in the middle detection bin are integrated and plotted in figure 8.6. Figure 8.6 shows two separate measurements taken 142 hours apart without intermediate alignment. Series 1 and 2 both show high levels of visibility as characterised by fits to (8.18) (99.74% and 99.90% respectively) and single data points (99.7% and 99.8% respectively). Furthermore, the fringe phase only shifts by  $(4.1 \pm 0.2)^\circ$  between the two measurements. The 5 minutes required to calibrate the fringe phase is negligible compared to the duration of stability, and the "self-stabilising" claim is thus well justified. Slight systematic fit deviations are visible in figure 8.6, which may be due to the  $R_{el}$  variations observed in figure 8.4.

<sup>1</sup>We choose to go via the sample to keep the fibre couplings necessary for the entanglement experiment.

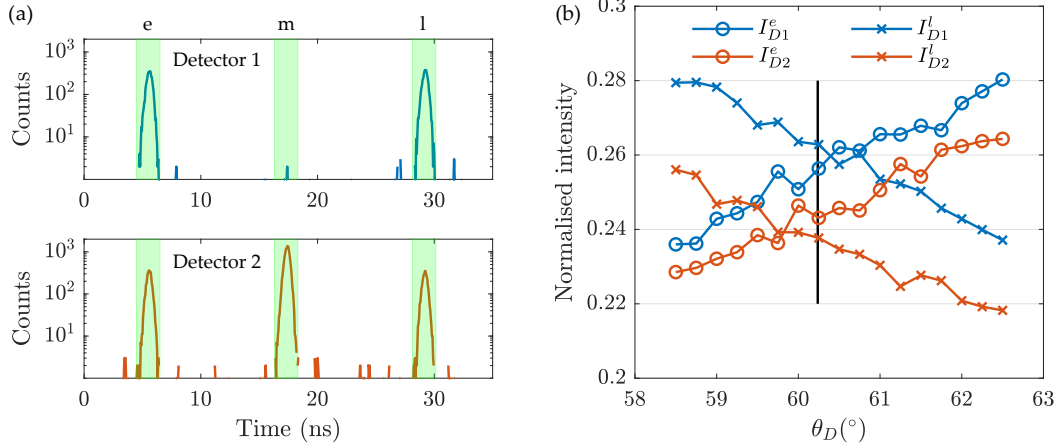


**Figure 8.5:** Measurement of excitation pulses reflected off the sample surface. **(a)** Histograms recorded from both detectors showing the early(e), middle(m) and late(l) detection windows (green boxes). The applied  $\theta_{pol}$  setting corresponds to the minimum in figure 8.6 yielding a near-zero  $I_{D1}^m$ . **(b)** Early and late intensities vs the polariser  $\theta_D$ , which sets the PBS<sub>2</sub> splitting ratio. The black line indicates the optimal  $\theta_D$ .

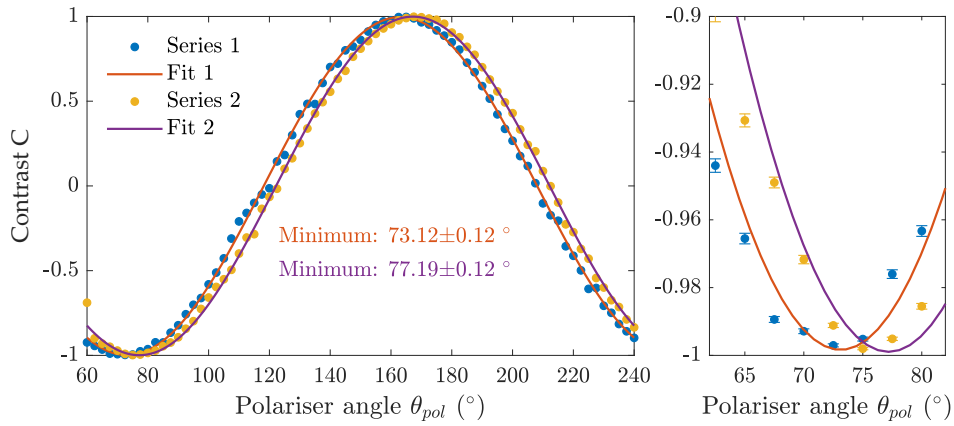


**Figure 8.6:** Middle time-bin detection contrast  $C = (I_{D1}^m - I_{D2}^m)/(I_{D1}^m + I_{D2}^m)$  for different values of  $\theta_{pol}$  using excitation pulses reflected of the sample. The right subplot shows a data zoom in. Errorbars are derived from shot noise. Fits following (8.18) are used to estimate the fringe phase.

## 8.5 ACTIVE SWITCHING

So far we have described the passive operation of the TBI, where the selection between a photonic z and x-measurement is probabilistic but heralded by the detection time. The chance to measure  $N$  photons in the intended basis is thus  $1/2^N$ , which imposes considerable loss when trying to realise the GHZ measurement scheme of section 7.6.1 for  $N \gg 1$ . A deterministic  $\hat{\sigma}_z^{\otimes N}$  measurement simply requires all photons to be transmitted through PBS<sub>2</sub> (figure 8.1) which is easily implemented. However, a deterministic  $\hat{\sigma}_x^{\otimes N}$  measurement requires a reflection of the early photon

and transmission of the late photon on encountering  $\text{PBS}_2$ . This can be achieved by modulating the polarisation of  $\mathbf{E}_2$  in time. The detection time continues to herald the measurement basis, but the active modulation increases the heralding chance, provided that the modulator adds less than 3 dB loss. An ideal modulator for our TBI is a resonant free space polarisation modulating EOM, as it combines low loss with the ability to switch photons every  $T_{TB} \approx 12$  ns.

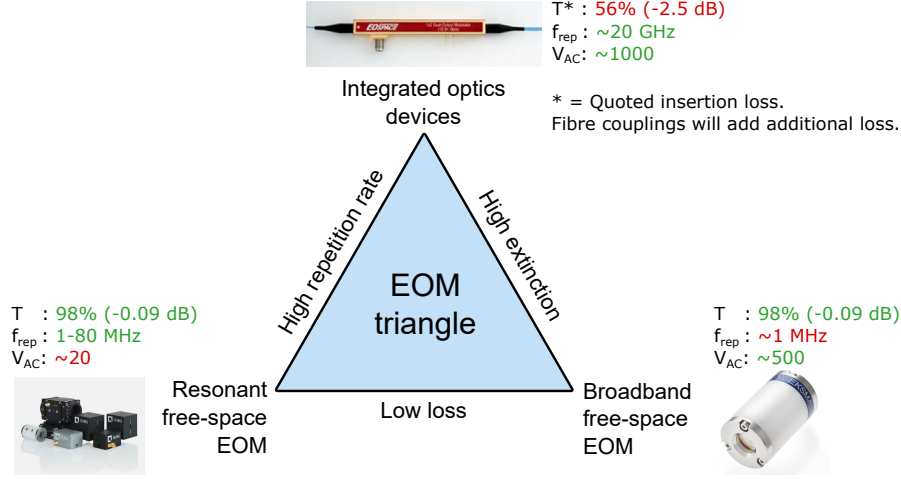


**Figure 8.7:** Current state-of-the-art electro optical modulators represented as a triangle: You can only have two sides at once.  $T$  is optical transmission,  $f_{\text{rep}}$  is the maximum modulation frequency and  $V_{\text{AC}} = T_{\text{max}}/T_{\text{min}}$  is the AC extinction. The broadband EOM's  $f_{\text{rep}}$  is mainly limited by the required high voltage drivers. Sources for performance metrics: [117–119].

An ideal free-space polarisation-modulating EOM consists of an electro optically active crystal angled  $45^\circ$  with respect to horizontal [120]. Capacitors across the crystal apply an electric field, which modulates the refractive index along a single axis, as described by the Jones Matrix

$$M_{EOM}(\Phi) = \frac{e^{-i\Phi/2}}{2} \begin{bmatrix} 1 + e^{i\Phi} & 1 - e^{i\Phi} \\ 1 - e^{i\Phi} & 1 + e^{i\Phi} \end{bmatrix}, \quad (8.20)$$

where  $\Phi$  is the retardation proportional to the applied voltage. A resonant EOM uses an LC circuit to amplify the driving voltage, which must be harmonic leading to the time dependent retardation

$$\Phi(t) = A \frac{\pi}{2} \sin(2\pi f_{EOM} t + \alpha), \quad (8.21)$$

where  $A$  is the modulation index,  $f_{EOM}$  is the modulation frequency and  $\alpha$  is the modulation phase. We can bias the EOM with a  $45^\circ$  QWP and set  $A = 1$ . The EOM then oscillates between a  $+\lambda/4$  and  $-\lambda/4$  waveplate which, summed with the fixed QWP, corresponds to a  $45^\circ \lambda/2$  wave plate being turned on and off. This

configuration requires half the driving voltage and results in the optical field

$$\mathbf{E}_2 = \begin{pmatrix} E_{2,x} \\ E_{2,y} \end{pmatrix} = M_{EOM}(\Phi)M_{qwp}(\pi/4) \begin{pmatrix} 1 \\ 0 \end{pmatrix} = e^{i(\pi/4-\Phi)} \begin{pmatrix} \sin(\Phi/2 + \pi/4) \\ i \sin(\Phi/2 - \pi/4) \end{pmatrix}, \quad (8.22)$$

leading to a PBS transmitted intensity

$$I_T(t) = |E_{2x}|^2 = \frac{1}{2}(1 + \sin(\Phi(t))) = \frac{1}{2} + \frac{1}{2} \sin\left(\frac{\pi}{2} \sin(2\pi f_{EOM}t + \alpha)\right), \quad (8.23)$$

which is plotted in figure 8.8. By choosing  $f_{EOM} = 1/(2T_{Mira}) \approx 36$  MHz and fine tuning the modulation phase  $\alpha$ , the desired reflection(transmission) of the early(late) photons is achieved as indicated on figure 8.8 leading a near unity probability of detecting photons in the middle bin (excluding experimental imperfections).  $f_{EOM}$  can be derived from a phase locked loop in the FPGA (see appendix A for details).

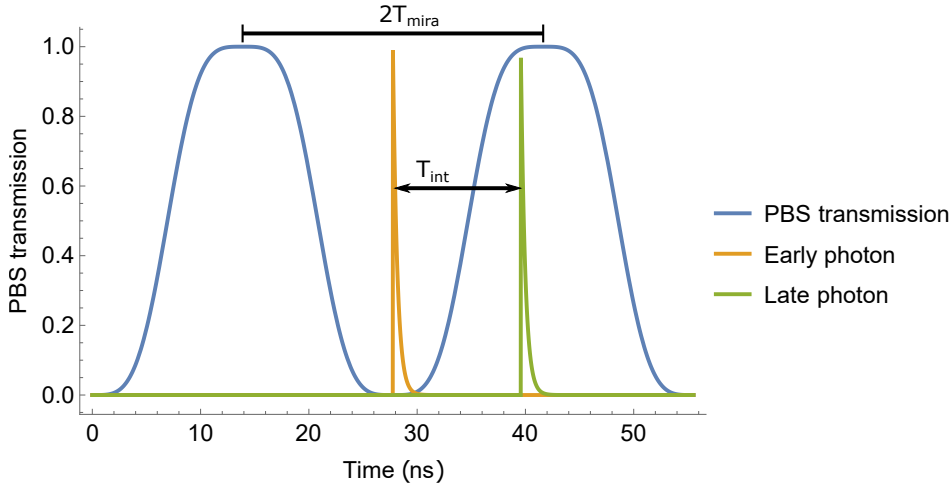


**Figure 8.8:** Calculated transmission through PBS<sub>2</sub> when modulating a perfect EOM. Optimisation of the modulation phase gives early (late) photons a very low (high) probability of being transmitted into the short interferometer arm.

Ultimately, this method of switching was not used experimentally due to challenges with temperature stabilisation of the EOM. Additionally, the time dependent  $e^{-i\Phi}$  term in (8.22) gives an additional phase to the early and late photons requiring the detector fringe phase to be recalibrated. However, it is still interesting to consider how the switching requirements intrinsic to time-bin encoded photons can be solved with current technologies. It should also be mentioned that the proposed EOM scheme does not allow deterministic measurement of operators such as  $\hat{\sigma}_x \hat{\sigma}_z \hat{\sigma}_x$  and  $\hat{\sigma}_z \hat{\sigma}_x \hat{\sigma}_z$ . These operators switch between z and x-basis and are interesting, as they constitute a witness for linear cluster states [121]. These new measurements ideally require  $I_T(t)$  to be a square wave with 3/4 duty cycle, as only the early photon in the  $\sigma_x$  measurement should be reflected. This could be approximated by two cascaded resonant EOMs operating at frequencies  $f_1 = 1/(2T_{mira})$  and

$f_2 = 1/(T_{mira})$ , which are the two lowest Fourier components of the aforementioned square wave.

## 8.6 FREQUENCY FILTERING

The detection interferometer begins with two etalons for frequency filtering. Each etalon has a 100 GHz FSR and 3 GHz FWHM. By controlling the etalon temperature with a Peltier element and a PI-controller, the etalon thickness and thus resonance frequency can be tuned with a high degree of stability and accuracy. The filtering accomplishes several functions vital to the entanglement protocol:

1. Scattering from the strong rotation laser is greatly suppressed, especially when  $\Delta_r = (0.5 + n) \cdot \nu_{fsr}$ ,  $n \in \mathbb{N}$ .
2. The QD phonon sideband is rejected, yielding higher indistinguishability.
3. Mira laser scattering and QD photons emitted during optical  $\pi$ -pulses are partly rejected due to their large bandwidth, thus decreasing  $g^{(2)}(0)$ .
4. Emission from undesired QD decay channels is rejection.

Using two low finesse etalons as opposed to one of higher finesse results in a more square transmission profile more adept at picking out a single emission line. Figure 8.9 shows the measured double etalon transmission. The asymmetric spectrum is likely due to an unwanted coupling between the two cavities, which could be removed by tweaking the alignment. Nevertheless, the unwanted QD transitions are suppressed by between 18.6 and 35.5 dB relative to the  $y_1$ -transition. The entire etalon system incurs an additional frequency-independent loss of 10% (0.46 dB).

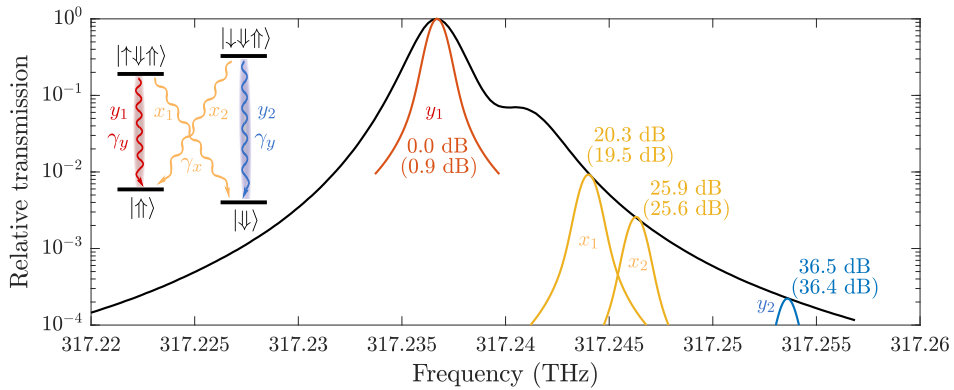


**Figure 8.9:** Transmission of double etalon system measured with a power meter by scanning an ECLD laser in 200 MHz steps. The black line shows transmission normalised to the target 317.2367 THz resonance. Other lines indicate the spectra of the four  $X^+$  transitions of  $QD_1$  as defined by the level structure insert. Losses for narrow-band light are given without parentheses while numbers in parentheses include the linewidth of  $QD_1$ .

## 9 | Entanglement Measurement

This chapter contains the experimental methodologies and results concerning spin-photon entanglement. The general pulse sequence is presented and the operations of  $\pi$ -pulse excitation and spin readout are optimised and quantified. The case of two-qubit entanglement is then treated in great detail: The procedure for post-selection and background correction is discussed, and the ability to control the readout basis of the spin and photon is verified, thus facilitating the GHZ-method. The generalisation to three qubits is straight forward and the fidelity of a three-qubit GHZ state is quantified along with a qualitative investigation of the cluster state. Finally, the single-photon properties of photon purity and indistinguishability are estimated. These quantities are estimated using a modified version of the entanglement scheme and are relevant to assessing the protocol errors. All measurements are performed on QD<sub>1</sub> and detected using the TBI interferometer of chapter 8 and SNSPDs.

### 9.1 EXPERIMENTAL PULSE SEQUENCE

Figure 9.1 shows the pulse sequence and recorded fluorescence histogram of the two-qubit entanglement pulse sequence consisting of a 200 ns preparation pulse, early/late excitation pulses surrounded by rotation pulses, a 200 ns spin readout pulse, a rotation buffer pulse and an ABB pulse. The full sequence has a duration of  $T_{rep} = 44 \times T_{mira} = 606$  ns where  $T_{mira}$  is the Mira laser repetition period. The exact timing and calibration of the rotation pulses are given in appendix F.

Detecting fluorescence with the TBI gives rise to a doubling of all pulses and three *photon detection windows*: early(e), middle(m) and late(l). Each photon detection window spans 2 ns which captures 97.3% of emitted photons. The *spin readout window* comprises the first 50 ns of the readout pulse following the optimisation in section 9.2.2. The delay from the e,m,l windows to the spin readout is chosen to exceed the 55 ns detector dead time such that readout detection efficiency is independent of previous photon detections.

As discussed in section 7.7, the  $R_3$  pulse in figure 9.1 is used to control the spin readout basis leading to the different pulse sequences summarised in table 9.1. The total area of rotation pulses is kept constant by adding a buffer pulse after the readout which offsets changes made to the  $R_3$  pulse and keeps a constant duty cycle and optical power.

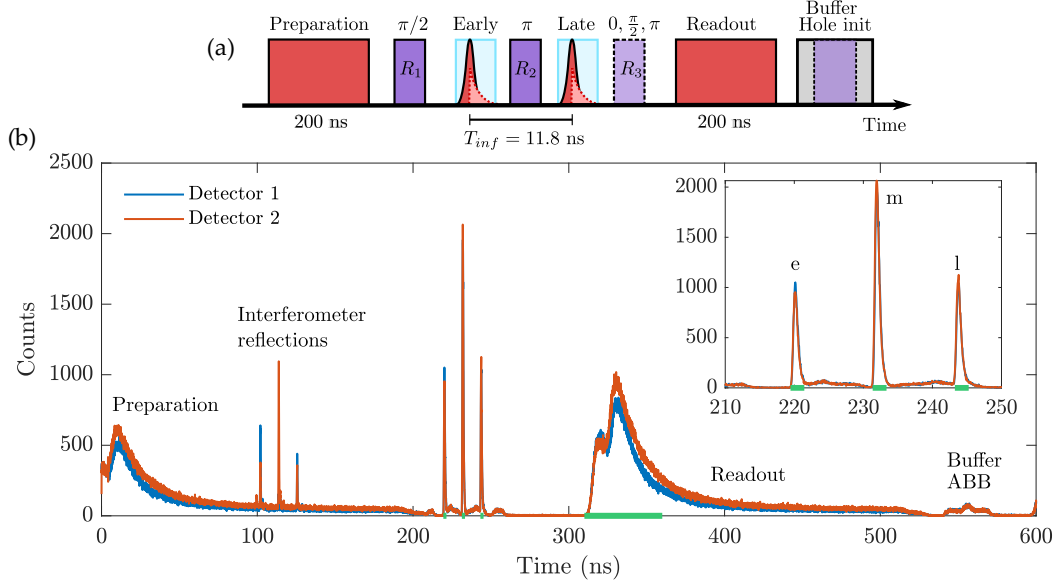


**Figure 9.1:** (a) Two qubit entanglement pulse sequence. Only the  $R_3$  is varied to set the spin readout basis. (b) Histogram of counts recorded on both detectors using the sequence in (a). Green lines indicate the four detection windows. The inset shows a magnified view of the same histogram. Peaks around 100 ns arise from optical reflections of the excitation pulses in the interferometer. Around 550 ns the rotation buffer is overlain on the 100 ns ABB pulse (not visible). Integration time: 30 s. Bin width: 50 ps.

Experiment	Spin readout projection	$R_1$	$R_2$	$R_3$	Buffer
Two-qubit entanglement	$ \uparrow\rangle$	$0.5\pi$	$1\pi$	0	$3.5\pi$
	$ \downarrow\rangle$	$0.5\pi$	$1\pi$	$1\pi$	$2.5\pi$
	$ +\rangle,  -\rangle$	$0.5\pi$	$1\pi$	$0.5\pi$	$3\pi$
Prepare $ \uparrow\rangle$		$1\pi$	0	0	$4\pi$
Prepare $ \downarrow\rangle$		0	0	0	$5\pi$

**Table 9.1:** Pulse areas of all 3 rotation pulses and buffer for various experiments experiments. Rotation pulses and buffer always sum to  $5\pi$ .

## 9.2 CALIBRATION MEASUREMENTS

To fully realise the desired sequence, the frequencies and powers of all lasers are carefully tuned as described in this section. An overarching principle is keeping the applied pulse sequence as close to the full entanglement sequence as possible to avoid shifts and systematic errors.

### 9.2.1 ACHIEVING RESONANCE

Resonance between the etalons, QD and lasers is achieved by the following method: A target frequency is chosen such that the QD is at resonance in the middle of the  $X^+$  plateau. The pump laser and Mira laser (fine-tuned using the VBG) are tuned to this frequency using a wavemeter and the etalon temperature is adjusted to maximize the transmission of the pump laser as measured by a power meter. The full entanglement sequence is applied and histograms are recorded at different  $V_{\text{bias}}$ . Counts in the readout window are plotted in figure 9.2 from which  $V_{\text{bias}}$  is selected. This procedure is intended to compensate power tuning induced from the pulse sequence.

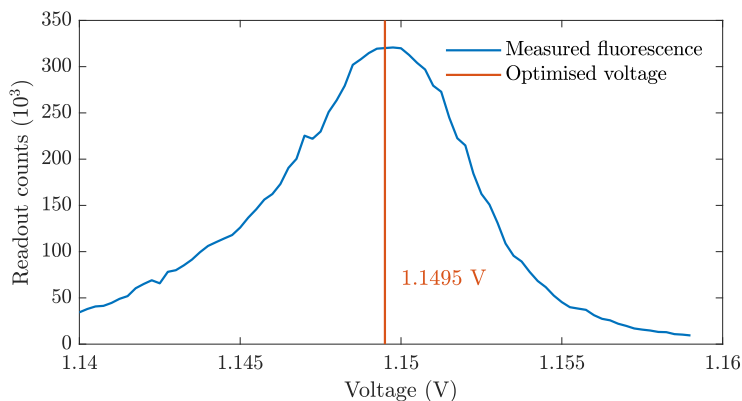


**Figure 9.2:** Spin readout counts from the full pulse sequence as a function of  $V_{\text{bias}}$ . Integration time: 5 s.

### 9.2.2 READOUT FIDELITY

The pump power should be optimised to achieve a good balance of readout and initialisation fidelity. The readout fidelity  $F_r$  is the probability that the QD spin was in  $|\uparrow\rangle$  given one or more clicks during the readout pulse and can be written using Bayes' theorem:

$$\begin{aligned}
 F_r = P(\uparrow | \text{click}) &= \frac{P(\text{click} | \uparrow)P(\uparrow)}{P(\text{click})} \\
 &= \frac{P(\text{click} | \uparrow)P(\uparrow)}{P(\text{click} | \uparrow)P(\uparrow) + P(\text{click} | \downarrow)P(\downarrow)} = \frac{P(\text{click} | \uparrow)}{P(\text{click} | \uparrow) + P(\text{click} | \downarrow)}, \quad (9.1)
 \end{aligned}$$

where the relation  $P(\uparrow) = P(\downarrow) = 1/2$  corresponding to zero prior information has been applied. In the limit of low collection efficiency (negligible multi-photon probability), the conditional probabilities in (9.1) are proportional to the mean number of detected readout photons conditioned on the spin state,  $I_{\uparrow}$  and  $I_{\downarrow}$ :

$$F_r = \frac{I_{\uparrow}}{I_{\uparrow} + I_{\downarrow}}. \quad (9.2)$$

These intensities are measured by preparing either  $|\uparrow\rangle$  or  $|\downarrow\rangle$  according to table 9.1. The two sequences result in the readout intensities

$$I_{1\pi} = \underbrace{[F_i F_{\pi} + (1 - F_i)(1 - F_{\pi})]}_{\text{Spin prepared in } \uparrow} N_{rep} I_{\uparrow} + \underbrace{[F_i(1 - F_{\pi}) + (1 - F_i)F_{\pi}]}_{\text{Spin prepared in } \downarrow} N_{rep} I_{\downarrow}, \quad (9.3)$$

$$I_{0\pi} = (1 - F_i)N_{rep}I_{\uparrow} + F_i N_{rep}I_{\downarrow}, \quad (9.4)$$

where the  $0\pi$  and  $1\pi$  subscripts indicate the applied rotation pulse. Equations (9.3) and (9.4) account for the fact that the finite preparation fidelity  $F_i$  and rotation fidelity  $F_{\pi}$  may lead to the wrong spin state being initialised.  $N_{rep}$  is the number of experimental repetitions. Solving (9.2), (9.3) and (9.4) yields

$$F_r = \frac{1}{2} \left( 1 + \frac{K - 1}{(2F_i - 1)(2F_{\pi} + K - 1)} \right), \quad (9.5)$$

where  $K = I_{1\pi}/I_{0\pi}$ . An advantage of this method is that no assumptions have been made about the physical mechanisms influencing  $I_{\uparrow}$  and  $I_{\downarrow}$ .  $I_{\downarrow}$  (ideally zero) may have contributions from both laser background and spin recycling, but modelling this is not required for fidelity estimation. Furthermore, a small uncertainty in  $F_i$  has negligible impact on the product  $F_i F_r$  which to first order describes the combined initialisation and readout fidelity.

Figure 9.3a shows the measured fluorescence for both pulse sequences and different powers. Integrating the histograms from 0 to  $\tau_{read}$  yields the cumulative counts in figure 9.3b from which  $K(\tau_{read})$  is calculated (figure 9.3c). The freedom in picking  $\tau_{read}$  presents a trade-off: A longer  $\tau_{read}$  yields more counts (higher post-selection probability) but reduced  $K$  as "bad" counts from laser scatter and spin recycling become more prominent. When choosing readout power one should ask: What is  $K(\tau_{read})$  for the  $\tau_{read}$  which gives  $x$  percentage of possible readout counts? In this regard the high power  $P_{pump} = 16 \mu\text{W}$  always performs best, yielding  $K = 15.9$  while detecting 79% of the cumulative counts<sup>1</sup> for the standard duration  $\tau_{read} = 50 \text{ ns}$  used henceforth. It is noticeable that the cumulative  $I_{0\pi}(\tau_{read})$  counts in figure 9.3b are near equal across the different pump powers. In this light, the preference for a high readout power is obvious as a shorter  $\tau_{read}$  is required to reach the same number of counts.

Assuming  $F_{\pi} = 0.885$  (section 6.3.2) and  $F_i = 0.98$  (matching  $\gamma_{osp}$  in figure 9.3a to power and spin pumping rates in figure 5.4 and figure 5.6), we estimate the readout fidelity  $F_r = 0.966$ .

<sup>1</sup>As this cumulative count also includes "bad counts" unrelated to the spin state, more than 79% of "good counts" will have been detected.

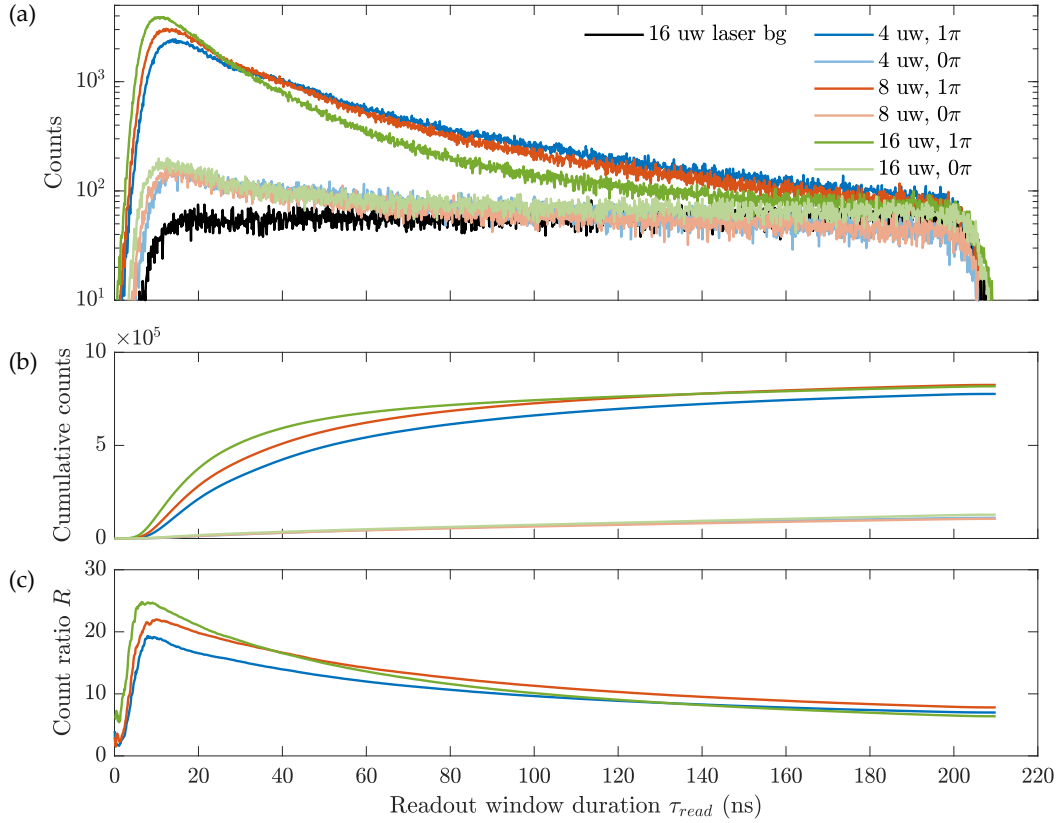


**Figure 9.3:** Measurement of readout fidelity. **(a)** Fluorescence histograms for different pump powers where either a 0 or  $1\pi$  rotation pulse has been placed between initialisation and readout. A  $\pi$  rotation prepares  $|\uparrow\rangle$  which yields much higher fluorescence allowing the spin state to be inferred. Black line indicates laser background at 16  $\mu$ W measured at non-resonant  $V_{bias}$ . **(b)** Cumulative counts calculated by integrating histograms in (a) from 0 to  $\tau_{read}$ . **(c)** Ratio between cumulative counts with  $1\pi$  and  $0\pi$  rotations as a function of integration window length  $\tau_{read}$ . Counts recorded using TBI (short arm only).

The analysis can be expanded by subtracting the measured laser background to achieve background-corrected values of  $I_{1\pi}$  and  $I_{0\pi}$  leading to  $K^{(bg,corr)} = 25.0$  and  $F_r^{(bg,corr)} = 0.984$  for  $P_{pump} = 16 \mu$ W and  $\tau_{read} = 50$  ns. However, this bluntly assumes no interference between the laser scatter and QD fluorescence. Furthermore, laser background subtraction is not possible in real applications requiring spin readout. Hence, not subtracting laser background but using the lower, uncorrected value of  $F_r$  yields a more accurate analysis with fewer assumptions.

## 9.2.3 MIRA POWER CALIBRATION

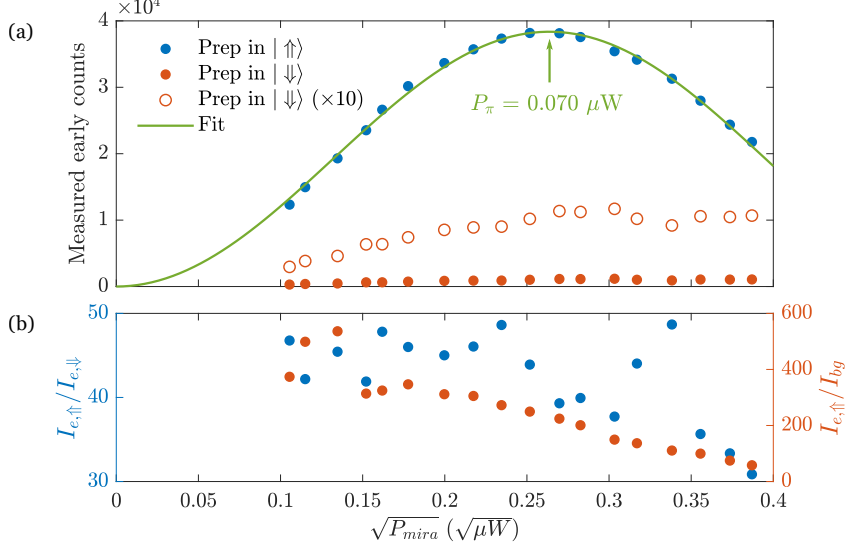


**Figure 9.4:** (a) Early pulse fluorescence following preparation in  $|\uparrow\rangle$  or  $|\downarrow\rangle$ . Unfilled circles have been scaled by  $\times 10$  for clarity. Counts recorded by TBI (short arm only). Laser background counts (not shown) have been subtracted. (b) Left y-axis: Ratio between fluorescence intensities of the two different spin states. Right y-axis: Fluorescence given  $|\uparrow\rangle$  divided by laser background.

The Mira power  $P_{mira}$  is optimised by preparing  $|\uparrow\rangle$  and exciting with a single early pulse. Figure 9.4 shows early fluorescence  $I_{e,\uparrow}$  as a function of  $P_{mira}$ . The  $\pi$ -pulse power  $P_\pi$  is determined by fitting to the model

$$I_{e,\uparrow}(P_{mira}) = I_{max} \times \sin\left(\frac{\pi}{2} \sqrt{\frac{P_{mira}}{P_\pi}}\right)^2, \quad (9.6)$$

derived from (2.25). This measurement also allows estimation of the spin dependent photon emission by instead preparing  $|\downarrow\rangle$  giving the measurement of  $I_{e,\downarrow}$  in figure 9.4a.  $I_{e,\downarrow}$  is ideally zero but received contributions from

1. Imperfect initialisation in  $|\downarrow\rangle$ .
2. Emission from  $|\downarrow\uparrow\downarrow\rangle$  (see figure 7.3a).
3. Cross excitation from  $|\downarrow\rangle$  to  $|\uparrow\uparrow\downarrow\rangle$  (see figure 7.3a).

For the 5 lowest  $P_{mira}$ , the spin dependent extinction has an average value  $\langle I_{e,\uparrow}/I_{e,\downarrow} \rangle = 44.8$  which is consistent with the limit set by the initialisation fidelities

$$\left(\frac{I_{e,\uparrow}}{I_{e,\downarrow}}\right)_{\text{initialisation limit}} = \frac{F_i F_\pi + (1 - F_i)(1 - F_\pi)}{(1 - F_i)} = 43.5, \quad (9.7)$$

for  $F_\pi = 0.885$  and  $F_i = 0.98$ . However, for higher  $P_{mira}$ , a decrease in  $I_{e,\uparrow}/I_{e,\downarrow}$  is observed which cannot be attributed to initialisation errors. As fluorescence is

filtered by the etalons, photons from the  $|\uparrow\downarrow\rangle \rightarrow |\downarrow\rangle$  transition are suppressed by 35 dB. Hence, the most likely contribution is the aforementioned cross excitation from  $|\downarrow\rangle$  to  $|\uparrow\downarrow\rangle$ , indicating a small error in the Mira polarisation.

Using a non-resonant  $V_{\text{bias}}$  allows estimation of the Mira laser background  $I_{bg}$ . Figure 9.4b shows the laser extinction  $I_{e,\uparrow}/I_{bg}$  reaching an excellent value of 237 at  $P_{\text{mira}} = P_{\pi}$ .

#### 9.2.4 ROTATION LASER AND STABILITY CONCERNS

The optical detuning of the rotation laser is fixed at  $\Delta_r/2\pi = 350$  GHz to ensure relatively good spin rotations (section 6.3.2) and maximal etalon filtering. The rotation power  $P_{\text{rot}}$  is optimized by preparing  $|\uparrow\rangle$  according to table 9.1 and maximizing the spin readout by varying  $P_{\text{rot}}$ . Due to pointing instabilities in the optical setup caused by 2-hour temperature fluctuations in the lab,  $P_{\text{rot}}$  and  $P_{\text{mira}}$  are automatically recalibrated every 10 minutes using the methods described. This calibration also includes a re-optimisation of the rotation EOM bias voltage.

### 9.3 TWO-QUBIT ENTANGLEMENT RESULTS

#### 9.3.1 DATA FORMAT

Running the entanglement experiment yields a data stream from the time tagger containing timestamps of the detected photons and the clock signals from the FPGA. Subtracting the FPGA clock signal from the photon timestamps yields the photon detection time relative to the start of the pulse sequence. If a single photon is detected within the pulse sequence, it is added to a histogram. If multiple photons are detected, their detection time and detector number are saved as a tuple, allowing the post-selection criteria to be applied. The term *coincidence* will be used for multiple photons detected within the same experimental repetition despite occurring at different times.

#### 9.3.2 BACKGROUND CORRECTION

Due to the non-ideal timing of the rotation pulses and the time delay of the TBI, background counts from the rotation pulses occur during the photon detection windows. The problem is especially severe for the  $l$  detection window when applying  $|\downarrow\rangle$  readout as illustrated in figure 9.5 where rotation background accounts for  $\approx 10\%$  of the measured counts. As evident from figure 9.5, the background only appears at a resonant  $V_{\text{bias}}$  and is presumably made of incoherent QD scattering. As this pollution could be removed by better pulse generation equipment, the analysis will apply background subtraction. The background subtraction assumes two sources of photons: Signal photons (s) occurring from the QD and background photons (b). The probability  $P(\text{photon}, \text{readout})$  of measuring a coincidence between a qubit photon and spin readout is given by

$$P(\text{photon}, \text{readout}) = P(s_p, s_r) + P(b_p)P(b_r) + P(b_p)P(s_r) + P(s_p)P(b_r) \quad (9.8)$$

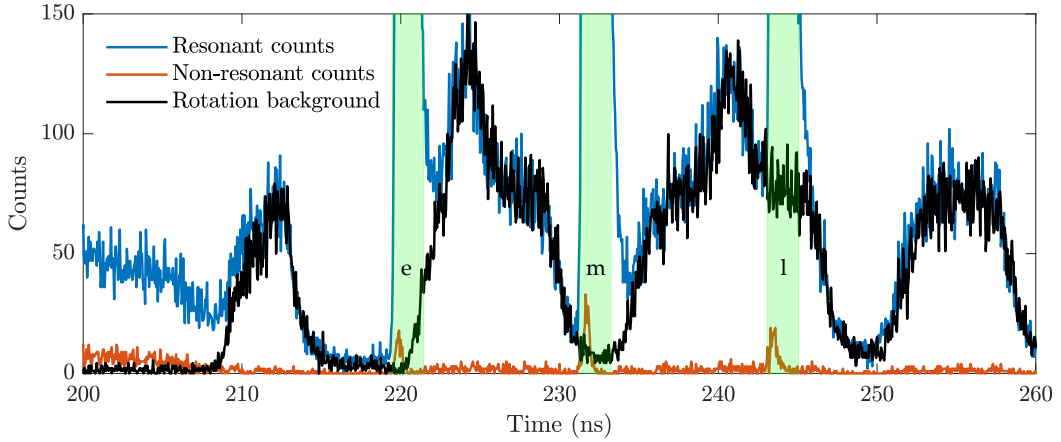


**Figure 9.5:** Estimation of rotation pulse background. Blue (red) curves show fluorescence histograms from the full entanglement experiment using a  $|\downarrow\rangle$  spin readout and resonant (non-resonant)  $V_{\text{bias}}$ . The black curve shows fluorescence generated by the rotation laser at resonant  $V_{\text{bias}}$ . All histograms were acquired over 30 s. Green windows represent the  $e$ ,  $m$ ,  $l$  detection windows. Especially the  $l$  window is contaminated by rotation background.

where  $P(s_p, s_r)$  is the true probability of coincidences. The remaining terms represent undesired coincidences through combinations of signal and background with  $p$  and  $r$  subscripts indicating photon or readout window. By estimating the single count probabilities in (9.8) by  $P(a) = N_a/N_{\text{rep}}$  where  $N_a$  is the number of detections of type  $a$  and  $N_{\text{rep}}$  is the total number of experimental repetitions, the number of true coincidences can be estimated by

$$\langle N(s_p, s_r) \rangle = N(\text{coinc, meas}) - \frac{1}{N_{\text{rep}}} (N(b_p)N(b_r) + N(b_p)N(s_r) + N(s_p)N(b_r)) \quad (9.9)$$

where  $N(\text{coinc, meas})$  is the measured number of coincidences and the  $N()$  terms represent the number of single detections (no coincidences) of background and signal counts. The estimator variance is calculated through standard error propagation and assuming Poissonian statistics.

$N(b_p)$  is the rotation pulse background estimated in figure 9.5. Our background correction approach is justified by the observation that the rotation background is completely incoherent, as it never exhibits any interferometric visibility between the two detectors. While (9.9) enables subtraction of readout laser scatter, this is not performed following the discussions in section 9.2.2, i.e. we set  $N(b_r) = 0$ . Ultimately, the discussed background correction only increases Bell state fidelity by  $\approx 1\%$ .

### 9.3.3 2 QUBIT Z AND X BASIS MEASUREMENTS

In order to test the control over readout basis, all four spin readout settings in table 9.1 are applied for a range of  $\theta_{\text{pol}}$  (introduced in section 8.1.1). Figure 9.6 shows the total number of counts across the 4 detection windows. Ideally,  $\theta_{\text{pol}}$  should not

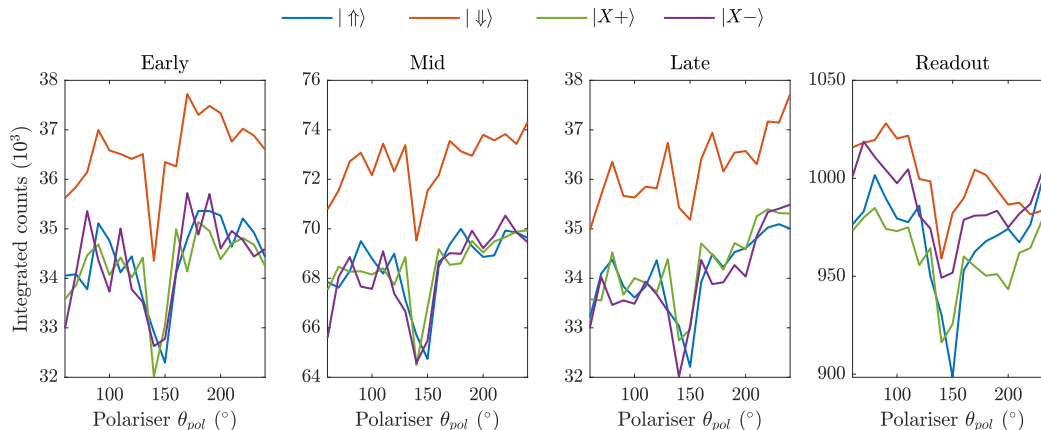


**Figure 9.6:** Total counts in the 4 detection windows as a function of polariser angle  $\theta_{pol}$  and spin readout (legend). Counts from rotation pulses have been subtracted.  $\theta_{pol}$  is varied from  $60^\circ$  to  $240^\circ$  in  $10^\circ$  increments and each readout setting is integrated for 30 s using both interferometer arms and detectors.

influence the count rate, as it only alters the excitation pulse phases. This is almost the case apart from the dip at  $\theta_{pol} \approx 145^\circ$  which is attributed to fluctuations in optical alignment<sup>2</sup>. Counts in  $e, m, l$  should also not be influenced by the choice of spin readout. However, a consistent increase in counts is found by applying the  $|\downarrow\rangle$  readout, possibly indicating a pulse sequence imperfection or a different effect leading to an overall increase in fluorescence, eg. improved hole spin occupation. As expected, the middle bin contains approximately twice the counts of the early/late bins owing to the TBI. The greatly increased number of counts in the spin readout is a result of the cyclicity allowing the QD to scatter on average  $C$  photons before decaying to the dark state.

Next, coincidences between the  $e, m, l$  windows and spin readout from the same dataset are examined. Our post-selection criteria require at least one photon in  $e, m$  or  $l$  and at least one in spin readout. Detectors  $D_1$  and  $D_2$  (defined in figure 8.1) are only distinguished in the case of the middle window. Coincidences between spin readout and photonic  $z$ -basis readout are plotted in figure 9.7a by normalising early counts according to  $P_{e,r} = N_{e,r}/(N_{e,r} + N_{l,r})$ , where  $N$  denote the number of coincidences between an early( $e$ ) or late( $l$ ) photon and readout. A clear contrast is observed only when measuring the spin in  $z$ -basis. Measuring the spin in  $x$ -basis reveals a consistent bias towards late photon detection in accordance with theory (section 7.4.4). Additionally, no significant dependence upon  $\theta_{pol}$  is observed. Error bars are derived from Poissonian statistics.

Figure 9.7b shows coincidences between photonic  $xy$ -basis readout using the middle window and spin readout. The detection contrast between the two detectors is quantified by  $P_{D1} - P_{D2} = (N_{m1,r} - N_{m2,r})/(N_{m1,r} + N_{m2,r})$  where the  $m1$  and  $m2$  subscripts denote detection on detector 1 or 2 in the middle bin. Clear interferometer fringes are visible when reading the spin in  $x$ -basis. Crucially, the

<sup>2</sup>Such dips commonly occur over multiple runs of the experiment but at different values of  $\theta_{pol}$ .

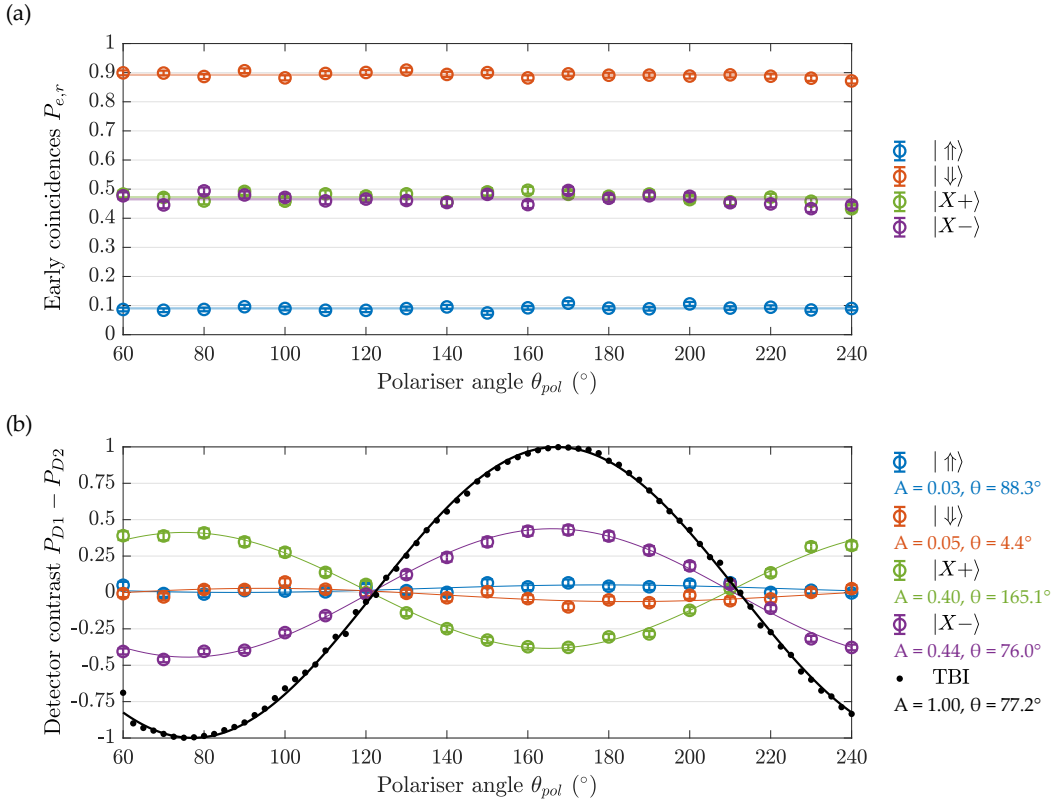


**Figure 9.7:** Coincidences between photonic qubit and spin readout. **(a)** Coincidences conditioned on an early/late detection heralding a photonic z-measurement. The probability of the photon being early is plotted vs  $\theta_{pol}$  for the 4 different spin projections (indicated by legend). The solid lines indicate averages. **(b)** Probability difference between detectors D1 and D2 for different  $\theta_{pol}$  and spin projections. Data is fit with the model  $P_{D1} - P_{D2} = -A \cdot \cos(\theta_{pol}/2 - \theta_0)$ . Fit values are given below legends. The TBI characterisation represents series 2 in figure 8.6.

coincidence fringes are in near-perfect phase with the TBI characterisation. This proves that the photon can be measured in the general  $|\pm(\phi)\rangle$  basis and that the fringe phase corresponds to the phase measured with a coherent state of light. The considerable difference between z- and x-visibility is expected, as far more errors impact x-visibility as discussed in chapter 10.

### 9.3.4 ENTANGLEMENT GENERATION EFFICIENCY

The probabilities to collect qubit photons and readout photons are estimated from the background-corrected data in figure 9.6 by averaging over all spin readout settings and values of  $\theta_{pol}$ . Assuming an ideal 1/4 chance of the photonic qubit going to the early window yields a total detection efficiency of  $P_{detec,qubit} = 0.282\%$ . Similarly, assuming a perfectly mixed spin state when averaging over all spin measurement settings, the readout detection efficiency conditioned on  $|\uparrow\rangle$  is estimated as  $P_{detec,spin} = 3.96\%$ . This yields an expected coincidence probability of  $P_{coinc} = P_{detec,qubit}P_{detec,spin}/2 = 5.57 \cdot 10^{-5}$ , where the factor 2 stems from the

mean  $|\uparrow\rangle$  projection. The measured coincidence rate averaged over all measurement settings is 124 Hz corresponding to  $P_{coinc} = 7.52 \cdot 10^{-5}$ . This 35% increase over the expected probability can be explained by blinking, which is shown to have a similar magnitude in section 9.6.1. It should be noted that specifying a specific photonic measurement basis reduces the coincidence rate due to the probabilistic basis choice of the TBI.

Out of the measured coincidences, the fraction of coincidences with more than one click with the photon detection windows is  $1.48 \cdot 10^{-4}$ . This rarity originates from the low detection efficiency and the fact that a second photon can only be generated by rotation errors, laser scatter or two-photon emission during excitation<sup>3</sup>. While all two-photon states have zero fidelity, they are excluded from further analysis on account of their rarity.

### 9.3.5 2 QUBIT GHZ MEASUREMENT

The final capability required by the GHZ-method is the ability to co-rotate the spin  $\phi_s$  and photonic  $\phi_p$  readout angles. This is demonstrated in figure 9.8 where the interferometer polariser  $\theta_{pol}$  and MW phase shift  $\phi_{mw}$  are varied with either the same or opposite signs. Recall that  $\phi_{mw}$  is the MW-phase of the  $R_3$  pulse relative to the prior pulses. As predicted by (7.56),  $\theta_{pol} = -\phi_{mw}$  is required to observe fringes. The measured oscillation has a  $90^\circ$  period since  $\phi_p = 2\theta_{pol}$  and  $\phi_s = 2\phi_{mw}$ .

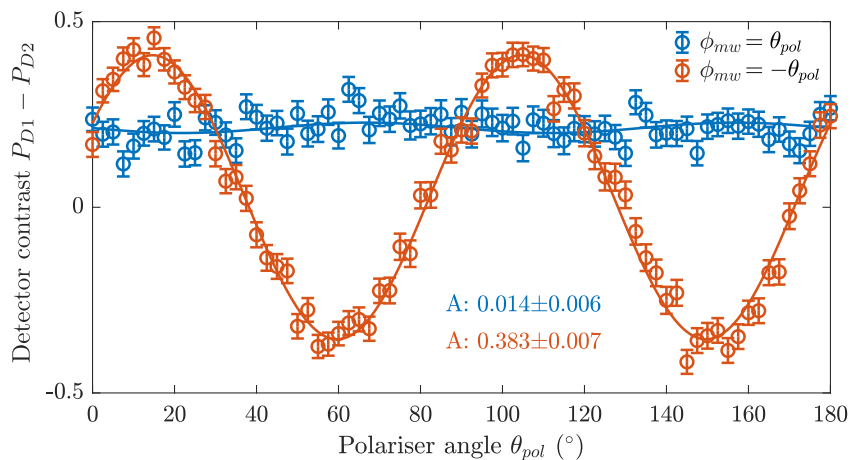


**Figure 9.8:** Normalised middle bin coincidences when projection the spin on  $|+(\phi)\rangle$  as a function of  $\theta_{pol} = \pm\phi_{mw}$ . Data is fit according to  $y = A \sin(4\theta_{pol} - \phi_0) + B$ . This measurement utilized a  $\Delta_r = 250$  GHz rotation laser detuning and the visibility is not directly comparable to figure 9.7b. The constant offset in the  $\theta_{pol} = \phi_{mw}$  series bears no significance, as the  $\theta_{pol}^0$  offset was not compensated.

We are now ready to realise the GHZ-method for two qubits. The final settings are summarised in table 9.2. The polariser offset  $\theta_{pol}^0 = 76^\circ$  corresponds to the fringe phase in figure 9.7b. By performing the six measurement settings we obtain

<sup>3</sup>The discussion in section 7.4.4 explains why branching errors don't generate multi-photon states.

Operator	Projectors	Rotation pulse $\tilde{R}_3$	Polariser $\theta_{pol}$
$\hat{P}_z$	$ e\rangle \uparrow\rangle,  l\rangle \uparrow\rangle$	0	$\theta_{pol}^0$ (irrelevant)
	$ e\rangle \downarrow\rangle,  l\rangle \downarrow\rangle$	$\pi$	$\theta_{pol}^0$ (irrelevant)
$\hat{\mathcal{M}}_1$	$ X+\rangle_p X+\rangle_s,  X-\rangle_p X+\rangle_s$	$\pi/2, \phi_{mw} = 0$	$\theta_{pol}^0$
	$ X+\rangle_p X-\rangle_s,  X-\rangle_p X-\rangle_s$	$\pi/2, \phi_{mw} = \pi/2$	$\theta_{pol}^0$
$\hat{\mathcal{M}}_2$	$ Y+\rangle_p Y+\rangle_s,  Y-\rangle_p Y+\rangle_s$	$\pi/2, \phi_{mw} = -\pi/4$	$\theta_{pol}^0 + \pi/4$
	$ Y+\rangle_p Y-\rangle_s,  Y-\rangle_p Y-\rangle_s$	$\pi/2, \phi_{mw} = -\pi/4 + \pi/2$	$\theta_{pol}^0 + \pi/4$

**Table 9.2:** Specific measurement settings required to realise the GHZ-method a spin-photon Bell state. Two measurement settings are required per operator as the pulse sequence only permits projection onto one spin state. The third column indicates the area and MW phase of the rotation pulses.

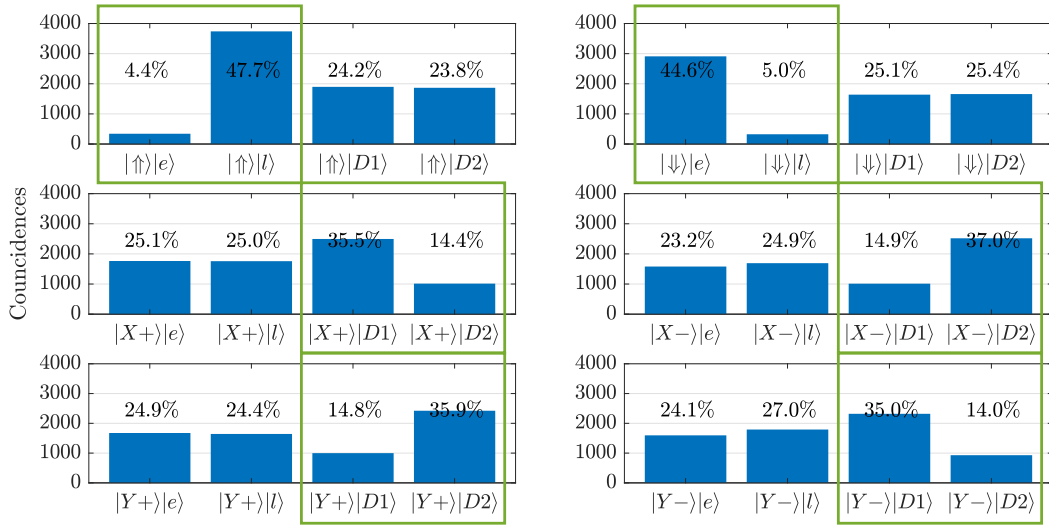


**Figure 9.9:** Coincidence counts from the 6 measurement settings of the 2 qubit GHZ measurement. Each subplot corresponds to one of the measurement settings listed in table 9.2 with green boxes indicating the projectors of interest. A 60 s integration time was applied for each measurement setting.

the coincidences plotted in figure 9.9. Due to the passive TBI switching, only half the measured projectors are of interest. The values of the projectors are calculated according to

$$\langle \hat{P}_z \rangle = \frac{N_{\downarrow,e} + N_{\uparrow,l}}{N_{\downarrow,e} + N_{\uparrow,l} + N_{\uparrow,e} + N_{\downarrow,l}}, \quad (9.10)$$

$$\langle \hat{\mathcal{M}}_1 \rangle = \frac{-N_{X+,D1} - N_{X-,D2} + N_{X+,D2} + N_{X-,D1}}{N_{X+,D1} + N_{X-,D2} + N_{X+,D2} + N_{X-,D1}}, \quad (9.11)$$

$$\langle \hat{\mathcal{M}}_2 \rangle = \frac{-N_{Y+,D1} - N_{Y-,D2} + N_{Y+,D2} + N_{Y-,D1}}{N_{Y+,D1} + N_{Y-,D2} + N_{Y+,D2} + N_{Y-,D1}}, \quad (9.12)$$

where subscripts denote spin and photon projection. Normalisation is ensured as the measured projectors in the denominator sum to the identity operator. Figure

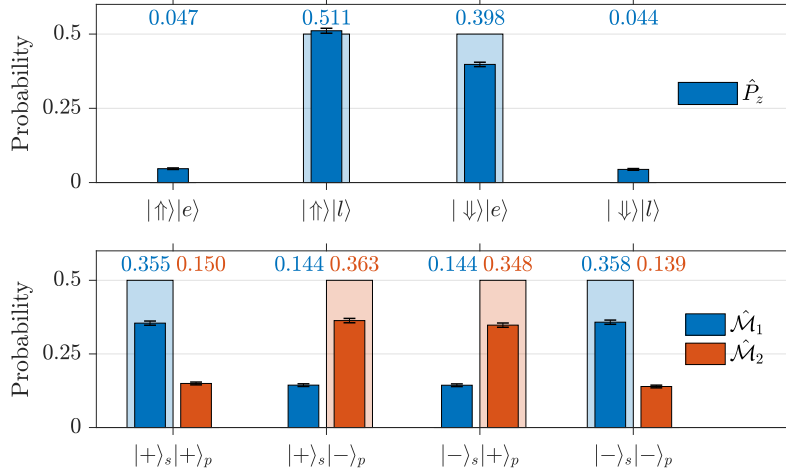


**Figure 9.10:** Normalised spin-photon Bell state measurement. The top row shows z-basis measurement outcomes. Bottom row shows the two rotated bases in the xy-plane. The shaded bars show ideal measurement outcomes.

9.10 shows coincidence counts according to this normalisation. An overweight of  $|\uparrow\rangle|l\rangle$  is clearly apparent, which is due to a combination of branching and spin rotation errors as shown in section 10.2. Using (9.10,9.11,9.12, 7.34,7.36), we find the final projectors and fidelity estimate

$$\langle \hat{P}_z \rangle = 0.909 \pm 0.004, \quad (9.13)$$

$$\langle \hat{\mathcal{M}}_1 \rangle = -0.425 \pm 0.011, \quad (9.14)$$

$$\langle \hat{\mathcal{M}}_2 \rangle = 0.421 \pm 0.011, \quad (9.15)$$

$$\langle \hat{\chi} \rangle = \frac{-\langle \hat{\mathcal{M}}_1 \rangle + \langle \hat{\mathcal{M}}_2 \rangle}{2} = 0.423 \pm 0.008, \quad (9.16)$$

$$\mathcal{F}_{GHZ}^{N=1} = \frac{\langle \hat{P}_z \rangle + \langle \hat{\chi} \rangle}{2} = 0.666 \pm 0.005. \quad (9.17)$$

Thus, we exceed the  $\mathcal{F} = 0.5$  threshold for entanglement by 22 standard deviations using only 6 minutes of acquisition. The only correction applied in this estimate is the subtraction of rotation laser counts. The  $\theta_{pol}$  scans in 9.7 also contain the measurement settings used for  $\hat{P}_z$  and  $\hat{\mathcal{M}}_1$ , and it is thus no surprise that the detected visibilities match between the two experiments. The GHZ-method, however, is faster than a full  $\theta_{pol}$  scan and, by additionally measuring  $\hat{\mathcal{M}}_2$ , provides an exact fidelity.  $|\langle \hat{\mathcal{M}}_1 \rangle|$  and  $|\langle \hat{\mathcal{M}}_2 \rangle|$  are statically compatible implying that x- and y-Pauli errors are equally likely.

If we ignore  $\hat{\mathcal{M}}_2$  and resort to the lower bound method of section 7.6.2 we find

$$F_{bound} = \frac{1}{2} \left( \langle \hat{P}_z \rangle + |\langle \hat{\mathcal{M}}_1 \rangle| \right) - \sqrt{\rho_{\uparrow e, \uparrow l} \rho_{\downarrow l, \downarrow e}} = 0.621 \pm 0.006, \quad (9.18)$$

where  $\rho_{\uparrow e, \uparrow e}$  and  $\rho_{\downarrow l, \downarrow l}$  correspond to the measured probabilities in the top row of figure 9.10. Unless one cannot measure  $\hat{M}_2$ , there is little reason to only perform the lower bound measurement. However, this bound provides a convenient point of reference against other works.

## 9.4 THREE-QUBIT ENTANGLEMENT

The experiment is extended to three photons by adding a second round of excitation as shown in figure 9.11. The second pair of excitation pulses are delayed by  $6 \times T_{mira} = 82.6$  ns to ensure a 59.0 ns delay between the  $l_1$  and  $e_2$  windows, exceeding the detector dead time. The total sequence duration then becomes  $50 \times T_{mira} = 689$  ns. The post-selection criteria are modified to require at least one photon in

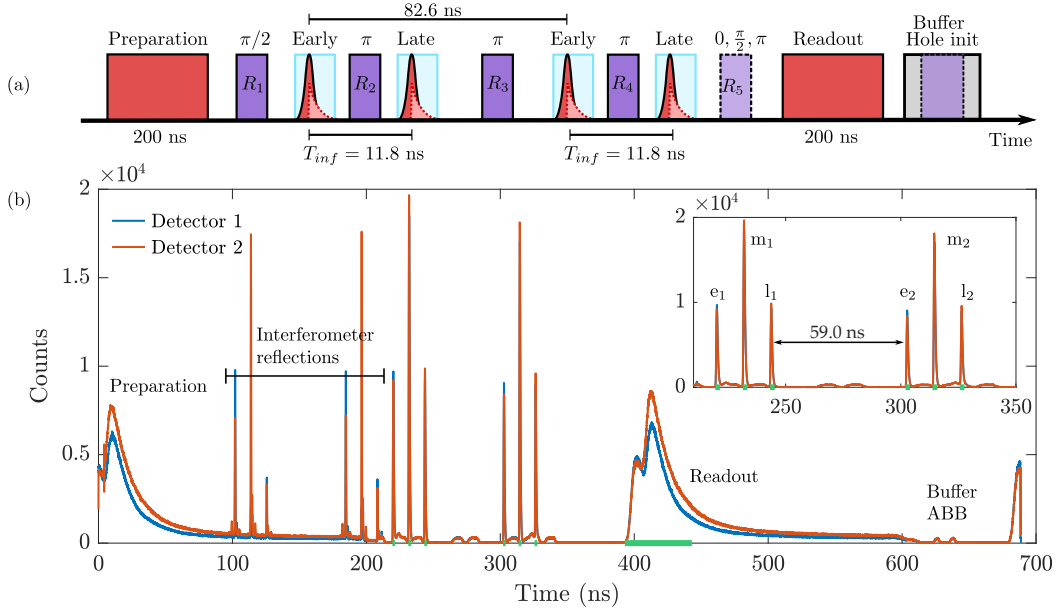


**Figure 9.11:** Three-qubit entanglement sequence. **(a)** Pulse sequence diagram. Only the  $R_5$  pulse is varied to set the spin readout basis. **(b)** Fluorescence histogram of all counts recorded from for both detectors for  $|\downarrow\rangle$  spin readout. Green lines indicate the  $2 \times 3 + 1$  detection windows. Inset shows magnified view of the same histogram. A second triplet of interferometer reflections also becomes visible at 200 ns but does not overlap with any detection windows. Integration time: 300 s.

each round of excitation. As the three-photon coincidence rate is only 0.68 Hz, a more limited set of measurements are performed to investigate the presence of entanglement.

Firstly, photonic xy-measurements are performed for different  $\theta_{pol}$  when projecting the spin on  $|X+\rangle$ . This allows an measurement of the operator

$$\hat{V}_2 = |X+\rangle\langle X+|_s \hat{\sigma}_{xy}^{\otimes 2}(\phi_p) \quad (9.19)$$

$$\begin{aligned} &= |X+\rangle\langle X+|_s (|+(\phi_p)\rangle\langle +(\phi_p)|_1 - |-(\phi_p)\rangle\langle -(\phi_p)|_1) \\ &\quad \times (|+(\phi_p)\rangle\langle +(\phi_p)|_2 - |-(\phi_p)\rangle\langle -(\phi_p)|_2), \end{aligned} \quad (9.20)$$

where the  $s$ , 1 and 2 subscripts denote the spin qubit and the two separate photonic qubits. This operator has the expectation value

$$\langle \hat{V}_2 \rangle = \sin(2\phi_p) = \sin(4(\theta_{pol} - \theta_{pol}^0)), \quad (9.21)$$

and can be experimentally estimated by

$$\langle \hat{V}_2 \rangle = \frac{N_{m1,m1,r} + N_{m2,m2,r} - N_{m1,m2,r} - N_{m2,m1,r}}{N_{m1,m1,r} + N_{m2,m2,r} + N_{m1,m2,r} + N_{m2,m1,r}}, \quad (9.22)$$

where the first two subscripts denote the detection window and detector of the first and second time-bin photon. The result of this measurement is shown in figure 9.12 which reveals a small but significant oscillation with period  $\pi/2$  as predicted by (9.21). Furthermore, the fringe phase  $\theta_{pol}^0$  is statistically compatible with previous measurements. Hence, control of photonic readout is generalisable to several qubits.

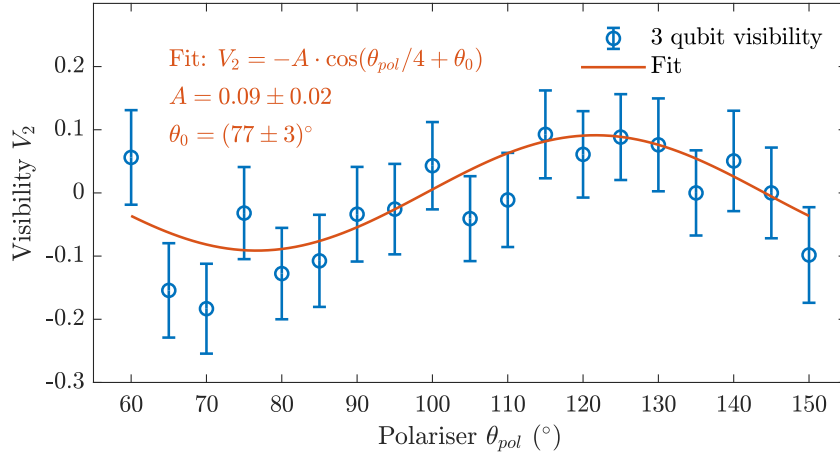


**Figure 9.12:** 3 qubit correlations when measuring all qubits in the rotated basis and varying  $\theta_{pol}$ . The  $\theta_{pol}$  scan was repeated 7 times and the coincidences from each scan were summed. Each datapoint corresponds to 35 minutes of integration leading to a total acquisition time of 11 hours.

To quantify the degree of entanglement, the GHZ measurement is performed on 3 qubits. The measurement strategy is an exact extension of the two qubit measurement, the difference being that 4 operators are being measured for a total of

8 measurement settings.  $\theta_{pol}$  and  $\theta_{mw}$  are now incremented in steps of  $\pi/3$ . The measurement results are given in figure 9.13, yielding the fidelities

$$\langle \hat{P}_z \rangle = 0.755 \pm 0.016, \quad (9.23)$$

$$\langle \hat{\mathcal{M}}_1 \rangle = -0.11 \pm 0.04, \quad (9.24)$$

$$\langle \hat{\mathcal{M}}_2 \rangle = 0.11 \pm 0.04, \quad (9.25)$$

$$\langle \hat{\mathcal{M}}_3 \rangle = -0.05 \pm 0.04, \quad (9.26)$$

$$\langle \hat{\chi} \rangle = 0.09 \pm 0.02, \quad (9.27)$$

$$F_{GHZ}^{N=2} = 0.423 \pm 0.014. \quad (9.28)$$

The z-correlations remain significant but reduced compared to the two-qubit case. A reduction is expected from the addition of imperfect spin rotation pulses and the possibility of branching errors occurring in the second excitation round. The off-diagonal measurements as quantified by  $\chi$  reveal a small but significant signature of coherence identical with the visibility in figure 9.12. However,  $F_{GHZ}^{N=2} < 0.5$  and a claim of genuine 3-partite entanglement cannot be made. Despite this, the results from the three-qubit experiment are in good qualitative agreement with expectation and demonstrate the relative experimental ease with which more photonic qubits may be added.

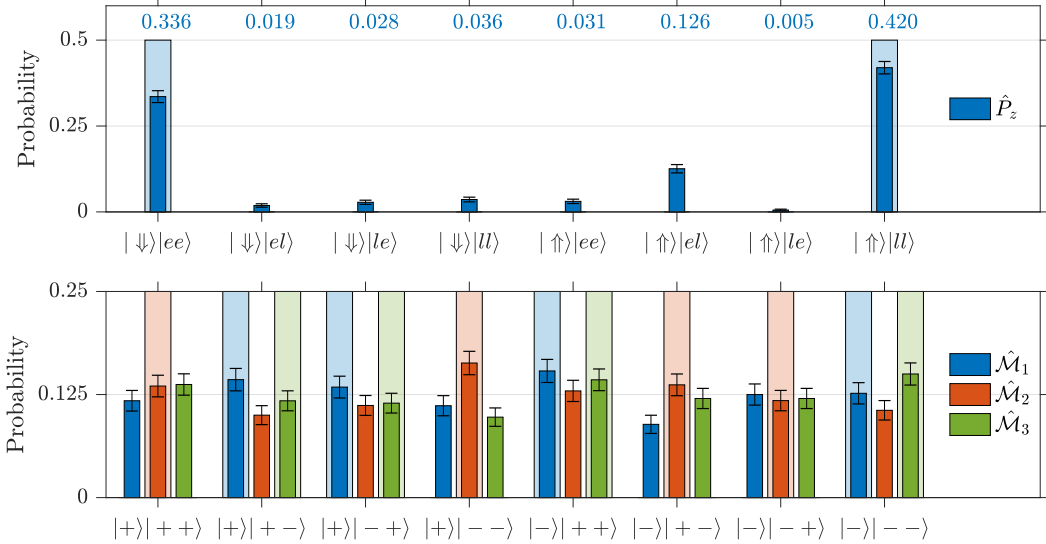


**Figure 9.13:** Fidelity measurement of a three-qubit GHZ state. Top row represents z-measurement and bottom row represents the three measurements in the xy-plane. Kets show the measured projector of the spin and the two photons. Shaded bars indicate the ideal state's detection pattern. 2 hours of data were acquired for each of the four operators.

Finally, we have superficially attempted cluster state creation by replacing the

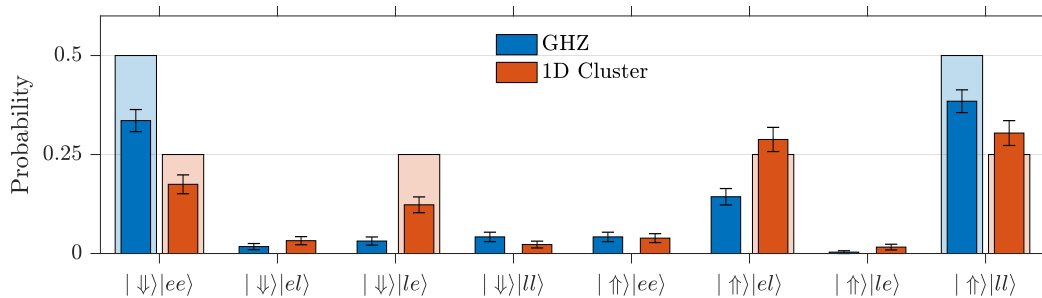


**Figure 9.14:** Comparison of z-measurements between the GHZ and cluster protocol. The measurement alternated between the GHZ and Cluster protocol 5 times to event out any slow experimental drifts. Each dataset corresponds to 3000 s of acquisition time. Shaded bars indicate the ideal state’s detection pattern.

$\hat{R}_3$  rotation (figure 9.11a) with a  $\pi/2$  rotation, thus realising the cluster state protocol described in section 7.3. We did not perform a full characterisation of the cluster fidelity, be we instead measured the z-correlations, which are presented in figure 9.13 and show promising agreement with the ideal outcome. Contrary to the 3-qubit state in (7.7) which contains every combination of spin and photon, we only expect four projectors to be non-zero. This is because our pulse sequence has omitted the final  $\hat{R}_y(\pi/2)$  spin rotation in the protocol.

## 9.5 DISCUSSION OF ENTANGLEMENT EXPERIMENT

While the observed of entanglement fidelity will be discussed in chapter 10, a few observations are in place regarding the experimental methodology. Overall, the measured detection patterns show a strong qualitative agreement with theory and the ability to control the spin and photonic readout basis has been convincingly demonstrated. Only a calibration of the interferometer phase  $\theta_{pol}^0$  is required, which can be rapidly performed using a single laser. Letting the TBI passively choose the photonic readout basis is experimentally simple and the heralding is unambiguous. However, the  $2^N$  penalty from the passive basis choice in conjunction with the overall low detection rate makes a four-qubit experiment with this setup infeasible. The repetition rate  $f_{rep} = 1/T_{rep}$  is primarily limited by the duration of the readout and preparation pulses, which are long due to  $C \gg 1$ . If not for the rotation buffer and ABB pulse, one could use the pumping pulse to perform spin readout and initialisation. Another current limit on  $f_{rep}$  is the detector deadtime. Using faster detectors or detector multiplexing could remove delays from the pulse sequence. Furthermore, the long 70 ns delay between the first early and second late excitation could be non-ideal, as it corresponds to the first echo visibility dip observed in figure 6.12. The use of slow Raman pulses for spin rotation does not currently limit  $f_{rep}$ . In addition to better detectors, it would be beneficial to generate the pulse sequence using an arbitrary waveform generator (AWG) to allow fine-tuning of the rotation pulse areas. In general, running the protocol without pulsed excitation and optimising the spin-echo visibility could be an efficient strategy to optimise the

overall fidelity. An AWG could also allow the spin readout basis to be cycled on a fast shot-to-shot basis to eliminate systematic effects from slow experimental drifts.

### 9.5.1 COMPARISON TO OTHER WORKS

We will now compare our experimental results to two existing works with strong points of similarity.

In Ref. [54] the authors apply the same time-bin protocol on a positively charged QD in the Voigt geometry. However, they apply a micropillar cavity and a 6 T magnetic field to achieve a cyclicity of  $C = 5$ . Additionally they estimate an  $F_i = 92.3 \pm 3\%$  initialisation fidelity,  $T_2^* = (2.11 \pm 0.11)$  ns and an  $F_\pi = 83 \pm 3$  spin rotation fidelity. Noticeably,  $F_\pi$  is limited by the difficulty of coupling a detuned rotation pulse into the cavity. This marks one of the key challenges of the micropillar, which is only exacerbated if the cavity Q is increased to further enhance  $C$ . The authors do not measure the qubits in the rotated basis but note the z-correlations<sup>4</sup> leading to  $\langle \hat{P}_z \rangle = 72.5\%$ . While the approach in Ref. [54] may allow faster state generation, our approach improves all other relevant metrics, and we see a great benefit of the PCW's higher  $C$  and free space excitation.

In Ref. [122] an NV-centre is used to generate a time-bin spin-photon Bells state. Again, a single optical transition is used to emit the early and late photon, but the spin is controlled by a microwave field. Also different is the use of a time-to-polarisation interferometer which converts the time-bin qubit to a polarisation qubit. This does not remove the requirement of a stable interferometer but allows the photonic readout basis to be controlled using polarisation optics. Using the lower bound method (section 7.6.2), the authors measure a raw  $\mathcal{F}_{bound} \geq (56.0 \pm 0.9)\%$ , which is below our value. Upon applying background correction, they measure  $\mathcal{F}_{bound} \geq (64.7 \pm 1.3)\%$  comparable to ours. Noticeably, their rate of entanglement is limited to 25 per hour (6.9 mHz), which is more than 4 magnitudes below our rate. This is a result of the low (3% [122]) zero-phonon-line efficiency and the much longer 177  $\mu$ s repetition time. However, the NV-centre does offer some simplifications in terms of intrinsic cyclicity and high fidelity MW spin control.

---

<sup>4</sup>The authors observed correct spin/photon z-correlations with a probability of 77% and 68% depending on the spin projection.  $\langle \hat{P}_z \rangle$  is taken as the average of these two numbers.

## 9.6 $g_2$ AND HONG-OU-MANDEL VISIBILITY

We will now investigate two important figures of merit in the generation of single photons, namely the photon purity and indistinguishability. An ideal source of pure single photons will never emit two photons in the same mode, and the purity can therefore be quantified by the second-order intensity autocorrelations function [123]

$$g^{(2)}(t, \tau) = \frac{\langle a^\dagger(t)a^\dagger(t+\tau)a(t+\tau)a(t) \rangle}{\langle a^\dagger(t)a(t) \rangle^2}. \quad (9.29)$$

Of special interest is  $\mathcal{G} = g^{(2)}(\tau = 0)$  which is zero for a single photon state and one for a coherent state [123].  $\mathcal{G}$  can be measured with a Hanbury Brown and Twiss (HBT) setup in which the light field is incident on a 50/50 BS with both outputs monitored by detectors.

The Hong-Ou-Mandel (HOM) effect states that interfering two indistinguishable photons on a beamsplitter will always result in both photons bunching into the same exit port. This phenomenon is a result of the bosonic nature of photons [123]. The degree to which this bunching occurs quantifies the indistinguishability through the Hong-Ou-Mandel visibility  $\mathcal{V}_{hom}$ . Hence, this measurement requires interfering two photons from the same source on a beamsplitter.

Thankfully, the HBT and HOM setups are both contained in the TBI as illustrated in figure 9.15. A combined experiment is performed by preparing  $|\uparrow\rangle$ , exciting with both early and late  $\pi$ -pulses generated by the TBI and measuring counts with the TBI. The photon detection time heralds which experiment was performed: early and late detection windows herald  $g^{(2)}$  while the middle window heralds HOM. This allows both properties to be measured under the same conditions. Furthermore, perfect temporal overlap of photons interfering in the middle bin is automatically ensured.

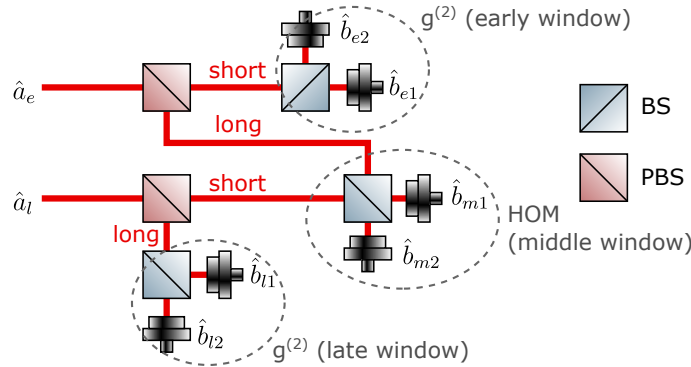


**Figure 9.15:** Path representation of the TBI. The early and late inputs are mapped to the six possible combinations of detector and detection time. It is clearly seen that early and late detection applies a  $g^{(2)}$  measurement while the middle time-bin applies a HOM measurement.

We apply two different methods of spin preparation:

1. *Pump method.* The pump laser is moved in frequency to drive  $|\downarrow\rangle \leftrightarrow |\uparrow\downarrow\downarrow\rangle$  and directly initialise  $|\uparrow\rangle$  (see figure 7.3).
2.  *$\pi$ -pulse method.*  $|\uparrow\rangle$  is prepared according to table 9.1, thus maximally replicating the conditions of the entanglement experiment.

Unfortunately, these methods limit the repetition rate to  $f_{rep} = 1/T_{rep} = 1.65$  MHz which is slow compared to the  $f_{rep} \sim 70 - 150$  MHz used in most QD experiments [18, 100, 124].

### 9.6.1 INTENSITY AUTOCORRELATION

First, the  $g^{(2)}$  is estimated. Figure 9.16a shows a histogram of the delay  $\Delta n_{rep}$  between detecting a photon on detector  $D_1$  and  $D_2$  in units of experimental repetitions,  $T_{rep} = 606$  ns. Coincidences are conditioned on both photons being detected within the same detection window (i.e. early or late) giving rise to an early and late dataset. The detection windows are identical to the 2 ns windows shown in figure 9.1. Figure 9.16c and figure 9.16d show fine time resolved histograms for  $\Delta n_{rep} = 0$  and  $\Delta n_{rep} = 1$ .

In figure 9.16a the occurrence of late coincidences is reduced by 0.884 with respect to early coincidences. This is an effect of a non-spin-preserving decay during the early decay, which should result in a coincidence reduction of  $(C/(C+1))^2 = 0.876$  for a cyclicity  $C = 14.7$ , well in agreement with data. A bunching is observed for low  $|\Delta n_{rep}|$  which is quantified in figure 9.17a by fitting to an exponential decay following the method in Ref. [125]. This reveals a bunching time-scale of  $(3.7 \pm 0.4)T_{rep} = (2.2 \pm 0.2) \mu\text{s}$  (averaged over early and late). Such an effect is commonly observed in  $g^{(2)}$  experiments and is referred to as blinking, as the QD is thought to "blink" in and out of being optically active with a certain correlation time. For the neutral excitons, blinking may be caused by shelving into long-lived dark exciton states [125]. Since  $X^+$  only has bright excitons and spectral diffusion has a negligible effect on pulsed excitation efficiency, the most probable source of blinking is the non-deterministic initialisation of the hole spin. In other words, the state of an uncharged quantum dot acts as a dark state. Blinking is hard to quantify precisely when  $T_{rep}$  is long. However, the estimated blinking magnitude of  $\approx 25\%$  is relevant to the probability of observing photon coincidences. In light of the blinking time scale, coincidences are normalised according to the values at  $30 \leq |\Delta n_{rep}| < 40$  giving the normalised coincidences in figure 9.16b and separate  $\mathcal{G}$  estimates for early and late, which are statistically compatible.

To shed some light on the observed  $\mathcal{G}$  we consider the contribution from unwanted excitation laser scatter. In the limit where the detected light is a statistical mixture of QD photons and small amounts of laser scatter, the laser scatter contribution to  $\mathcal{G}$  can be approximated [126] by

$$\mathcal{G}_\xi \approx 2\xi - \xi^2, \quad (9.30)$$

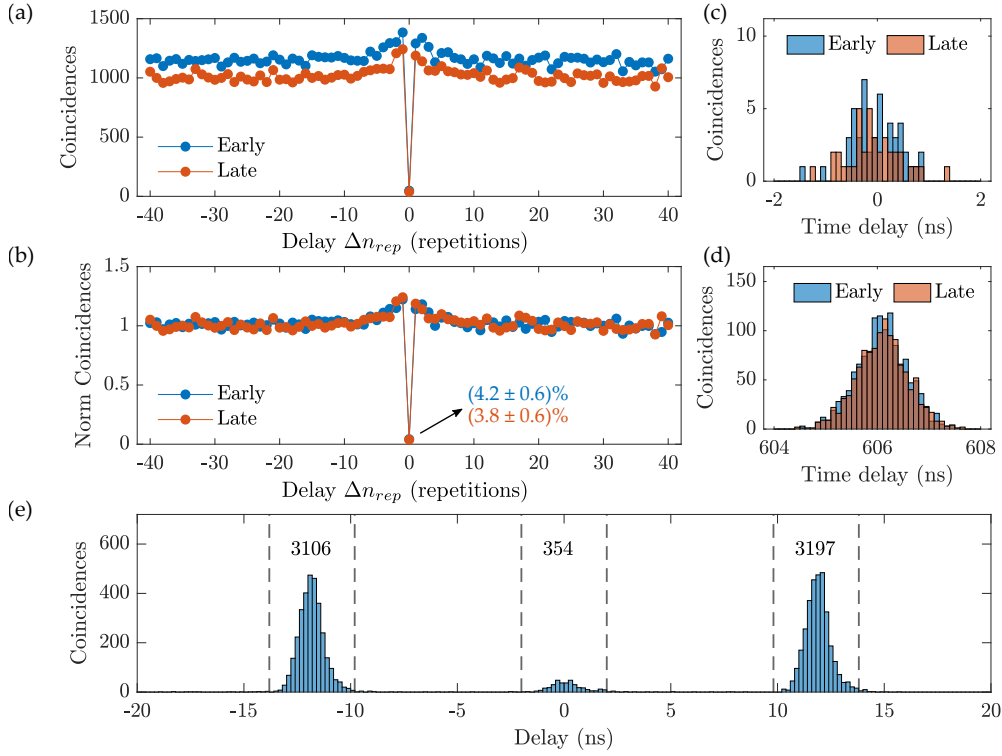


**Figure 9.16:** Combined  $g^{(2)}$  and HOM measurement using the pump sequence. Integration time: 20 minutes. (a) Delays between photons of different repetitions with both photons recorded in early or late time-bin. (b) Coincidences in (a) normalised. (c,d) Coincidence histograms for  $\Delta n_{rep} = 0$  and  $\Delta n_{rep} = 1$ . (e) Histogram of delays between two photons in the same repetition where at least one photon was detected in the middle bin.

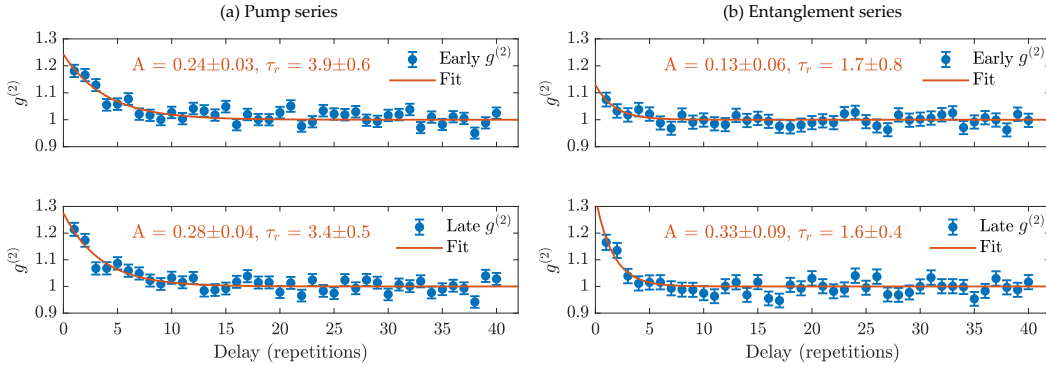


**Figure 9.17:** Observation of  $g^{(2)}$  bunching in both the pump and  $\pi$ -pulse measurements series. Data is fit with the model  $g^{(2)}(n_{rep}) = 1 + Ae^{-\Delta n_{rep}/\tau_r}$ . Data error bars are derived from Poisson statistics.

where the laser impurity  $\xi$  is the ratio between laser scatter intensity and single photon intensity

$$\xi = \frac{I_{\text{laser}}}{I_{\text{single photons}}} = \frac{I_{\text{off}}}{I_{\text{on}} - I_{\text{off}}}, \quad (9.31)$$

where  $I_{\text{on}}$  ( $I_{\text{off}}$ ) is the fluorescence intensity measured with a resonant (non-resonant)  $V_{\text{bias}}$ .  $I_{\text{off}}$  is measured with the exact same experimental sequence and yields  $\xi_{\text{early}} = (0.56 \pm 0.05)\%$  giving  $\mathcal{G}_{\xi, \text{early}} = (1.12 \pm 0.10)\%$ . Hence, laser scatter is only estimated to account for a quarter of the observed  $g^{(2)}(0)$ , the remainder of which may originate from multiphoton excitation, which will be estimated by Monte Carlo simulation in section 10.4.2, or from other sources of fluorescence.

### 9.6.2 HOM ESTIMATION

Most methods for measuring the Hong-Ou-Mandel visibility  $\mathcal{V}_{\text{hom}}$  rely on varying the degree of two-photon interference, either by temporally shifting the photons [127] or by varying the photon polarisation [18]. Since neither method is permitted by the construction of the TBI, we will follow the method of Ref. [124] in which two photons are injected into an unbalanced Michelson interferometer which thus closely resembles the TBI. The raw visibility is calculated by

$$\mathcal{V}_{\text{hom}}^{\text{raw}} = 1 - \frac{N_{m1,m2}}{(N_{m1,e2} + N_{m2,e1} + N_{m1,l2} + N_{m2,l1})/2} \quad (9.32)$$

where  $N_{ij,kl}$  is the number of coincidences between a photon in detection window  $i$  and detector  $j$  and a second photon in detection window  $k$  and detector  $l$  with both photons being detected within the same experimental repetition. In other words: Coincidences between both detectors at the middle bin are normalised to the coincidences between a middle and an early/late detection.

Figure 9.16e shows these 3 coincidence bins and gives the value  $\mathcal{V}_{\text{hom}}^{\text{raw}} = (88.8 \pm 0.6)\%$  for the pump series. While the indistinguishability discussed in section 7.4.1 was exclusive due to pure dephasing, the measured  $\mathcal{V}_{\text{hom}}^{\text{raw}}$  has more contributions. It is therefore instructive to calculate a corrected visibility  $\mathcal{V}_{\text{hom}}^{\text{corr}}$  which only contains the dephasing contribution. Commonly three corrections [124] are applied :

1. The unequal splitting ratio the beamsplitters used to interfere photons.
2. The classical interferometer visibility (in our case quantified by  $\mathcal{V}_{\text{TBI}}$ .)
3. The single-photon impurity  $\mathcal{G} > 0$ .

Corrections 1 and 2 both compensate extrinsic imperfections of the measurement setup while correction 3 is intrinsic to the source. Correcting for  $\mathcal{G}$  does not make sense in the context of a single-photon source. However, in the context of entanglement generation, it is insightful to separate indistinguishability and purity as they are caused by different errors and have different effects on fidelity.

The corrected visibility is calculated by following the approach in Ref. [124]. A source of perfectly indistinguishable photons subjected to the discussed imperfections will give the measured visibility

$$\mathcal{V}_{\text{hom}}^{\text{ideal}} = 1 - \frac{R_P T_P [(2g + 1)(R^2 + T^2) - 2RT\mathcal{V}_{\text{TBI}}^2]}{RT(R_P^2 + T_P^2)(\mathcal{G} + 1)} \quad (9.33)$$

where the equations in Ref. [124] have been modified to accommodate the fact that the TBI (figure 9.15) contains a PBS with reflectivity  $R_P$  and transmission  $T_P$  (with respect to intensity) and a 50/50 BS with reflectivity  $R$  and transmission  $T$ . To better appreciate the contributions of the different errors, one can Taylor expand (9.33) to lowest order in all variables:

$$\mathcal{V}_{hom}^{\text{ideal source}} \approx 1 - 2\mathcal{G} - 2\epsilon - 2(R - 0.5)^2 - 2(T - 0.5)^2. \quad (9.34)$$

The corrected visibility can then be calculated from

$$\mathcal{V}_{hom}^{\text{corr}} = \frac{\mathcal{V}_{hom}^{\text{raw}}}{\mathcal{V}_{hom}^{\text{ideal}}}. \quad (9.35)$$

Using the correction factors in table 9.3, a corrected  $\mathcal{V}_{hom}^{\text{corr}} = (96.9 \pm 0.7)\%$  is calculated for the pump series.

Correction	Values	Visibility reduction $1 - \mathcal{V}_{hom}^{\text{ideal}}$
Splitting ratio	$R_P = 0.485$ , $T_P = 0.515$ , $R = 0.513$ , $T = 0.487$	0.14%
Classical TBI visibility	$\mathcal{V}_{TBI} = 0.997$	0.60%
Intensity autocorrelation	$\mathcal{G} = 0.040$ (pump series) $\mathcal{G} = 0.047$ ( $\pi$ -pulse series)	7.7% (pump series) 9.0% ( $\pi$ -pulse series)
Summed contributions		8.4% (pump series) 9.7% ( $\pi$ -pulse series)

**Table 9.3:** Correction factors used to calculate  $\mathcal{V}_{hom}^{\text{ideal}}$ . The  $\mathcal{V}_{TBI}$  estimate is taken from figure 8.6. The beamsplitter parameters  $R_P, T_P, R, T$  are measured with a power meter.

The  $g^{(2)}$  and HOM measurements are summarised in table 9.4 including results from the  $\pi$ -pulse series (figure 9.18). Overall, the estimated values of  $\mathcal{V}_{hom}^{\text{corr}}$  are in agreement with the  $\mathcal{V}_{hom}^{\text{corr}} = (96 \pm 2)\%$  measured in Ref.[18] which investigated photon generation from a neutral exciton ( $\gamma = 2.89 \text{ ns}^{-1}$ ) and employed the same wafer material and photonic nanostructure as investigated here. Based on this data, there is no reason to believe that the  $X^+$  generates inferior indistinguishability, which should also be the case with phonon scattering as the dominant dephasing mechanism. Our higher  $\mathcal{G}$  is likely a result of the long 35.6 ps excitation pulse duration. Repeating the combined  $g^{(2)}$ -HOM experiment with the  $X^0$  exciton of the same QD would indeed be insightful and offer a more direct comparison<sup>5</sup>. A general increase in  $\mathcal{G}$  is observed for the  $\pi$ -pulse sequence, which is a combination of less QD emission (worse  $|\uparrow\rangle$  initialisation from  $\pi$ -pulse sequence) and small amounts of background emission from the rotation laser. The pump and  $\pi$ -pulse series differ in  $\mathcal{V}_{hom}^{\text{corr}}$  by  $1.1\sigma$  given the number the coincidences accumulated. Hence, there is no statistically significant indication of  $\mathcal{V}_{hom}^{\text{corr}}$  being reduced due to the rotation laser.

<sup>5</sup>Alas, fate would have it that the Mira laser failed shortly after acquiring the presented data, thus rendering an  $X^0$  measurement impossible.

Property	Symbol	Pump series (%)	$\pi$ -pulse series (%)
$\mathcal{G}$ early time bin	$\mathcal{G}_e$	$4.2 \pm 0.6$	$4.4 \pm 0.8$
$\mathcal{G}$ late time bin	$\mathcal{G}_l$	$3.8 \pm 0.6$	$4.9 \pm 0.9$
Laser impurity (early)	$\xi_e$	$0.337 \pm 0.003$	$0.526 \pm 0.005$
Laser impurity (late)	$\xi_l$	$0.383 \pm 0.004$	$0.562 \pm 0.005$
Mean impurity limited $\mathcal{G}$	$\mathcal{G}_\xi$	$0.720 \pm 0.005$	$1.085 \pm 0.007$
Raw HOM visibility	$\mathcal{V}_{hom}^{raw}$	$88.8 \pm 0.6$	$86.5 \pm 0.7$
Corrected HOM visibility	$\mathcal{V}_{hom}^{corr}$	$96.9 \pm 0.7$	$95.7 \pm 0.8$

**Table 9.4:** Summary of  $g^{(2)}$  and HOM estimates for both pump and  $\pi$ -pulse series.

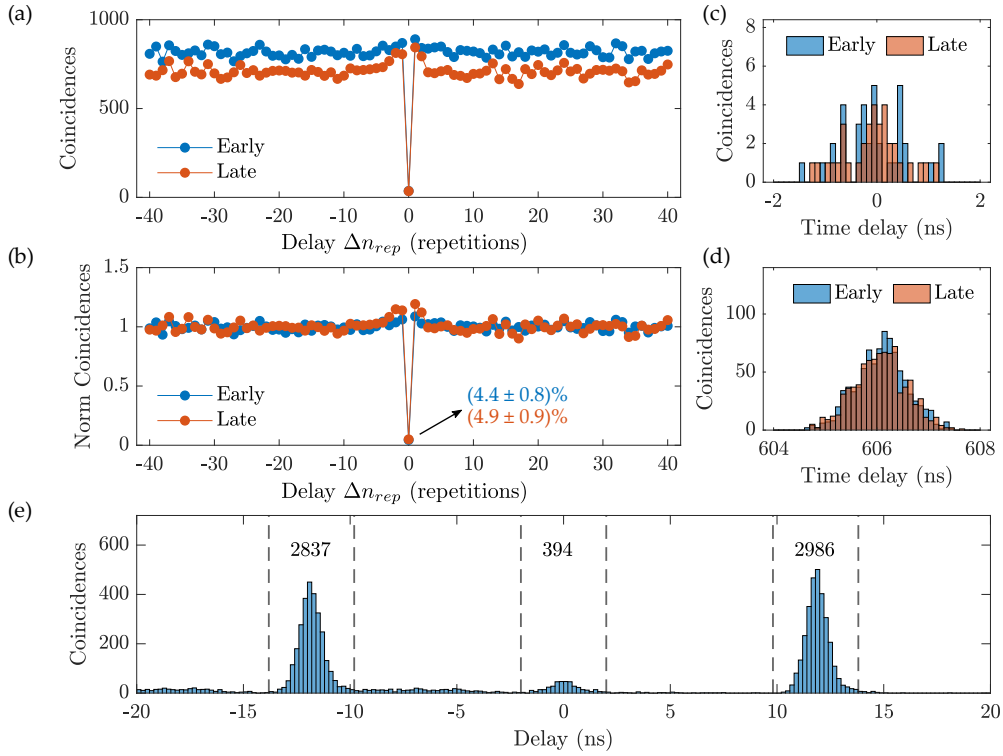


**Figure 9.18:** Combined  $g^{(2)}$  and HOM measurement using the  $\pi$ -pulse series. Subfigures are explained in figure 9.16. Background counts from the rotation pulse preparing  $|\uparrow\rangle$  are visible between -20 to -15 ns and -10 to -5 ns. The rotation pulse appears doubled due to the interferometer.

## 10 | Entanglement Modelling

Chapter 7 presented an analysis of the three intrinsic errors of the time-bin entanglement protocol. However, there are additional errors to consider in order to make sense of the experimentally measured fidelity. Especially spin rotations, which were shown to be non-ideal in chapter 6 must be included to properly replicate the experiment.

This chapter opens by enumerating the additional errors not yet analysed and providing analytical fidelity expressions when possible. A simple model is used to show how cyclicity and spin rotation errors combine to cause an overweight of certain Z-measurement outcomes. The remaining sections present an exhaustive Monte Carlo (MC) simulation of the two-qubit entanglement which aims to incorporate all relevant errors. This gives insight into the importance of parameters such as  $T_2^*$ ,  $\kappa$  and  $T_{opt}$  and the difference between Z and X-measurements. Ultimately, simulations yield good qualitative agreement with the experiment, and we conclude the chapter by summarising the main errors.

### 10.1 ADDITIONAL ERRORS

Additional errors are listed below and are approximately ordered from most to least important.

#### 10.1.1 SPIN ROTATION ERRORS

Spin rotation errors have a large impact as each round of the GHZ protocol uses 2  $\pi$ -rotations. This error contains both a Markovian contribution from laser-induced spin-flips with the rate  $\kappa$  and a non-Markovian contribution from the quasi-static Overhauser shift  $\Delta_{OH}$  (section 2.8). These error leads to both spin-flips and dephasing and will be visible in both Z and XY basis measurements. Control errors, e.g. rotation power fluctuations, will also contribute but are not considered here.

#### 10.1.2 SPIN INITIALISATION AND READOUT

Spin initialisation and readout errors both result in a state orthogonal to the ideal. However, the two errors result in different detection patterns. Incorrectly initialising  $|1\rangle$  and applying a  $\pi/2$  pulse followed by the single round operator (7.12) gives

$$\hat{O}_{1,GHZ}^\dagger \hat{R}_y \left( \frac{\pi}{2} \right) |1\rangle = \frac{|0\rangle |l\rangle - |1\rangle |e\rangle}{\sqrt{2}} = |\Phi^-\rangle, \quad (10.1)$$

as opposed to the ideal Bell state  $|\Phi^+\rangle$ . This corresponds to a Pauli Z-error on the spin or the photon. Measuring the usual operators will result in  $\langle\Phi^-|\hat{P}_z|\Phi^-\rangle = 1$  as spin and photon are correctly correlated, but  $\langle\Phi^-|\hat{\chi}|\Phi^-\rangle = -1$ , thereby correctly yielding  $\mathcal{F} = 0$  using (7.36). By contrast, a spin readout error causes reduced visibility across all operators.

We can quantify these errors by considering how the operators in (9.10) and (9.11) are impacted by imperfect initialisation and readout. It is easy to show that the expectation values are given by

$$\langle\hat{P}_z\rangle = F_r, \quad (10.2)$$

$$|\langle\hat{\mathcal{M}}_i\rangle| = 1 - 2F_i - 2F_r + 4F_iF_r, \quad (10.3)$$

where  $F_r(F_i)$  is the spin readout(initialisation) error. As discussed above,  $\langle\hat{P}_z\rangle$  is only affected by readout errors, while  $|\langle\hat{\mathcal{M}}_i\rangle|$  is affected by both errors. This gives a higher order term in (10.3) where two errors cancel each other out. The total fidelity is given by

$$\mathcal{F} = \frac{\langle\hat{P}_z\rangle + |\langle\hat{\mathcal{M}}_i\rangle|}{2} = \frac{1}{2} + 2F_rF_i - \frac{F_r}{2} - F_i. \quad (10.4)$$

This is a surprising result.  $\mathcal{F}(F_r = 0, F_i = 1) = -\frac{1}{2}$ , as a completely imperfect readout inverts all the detection patterns. This seems gravely concerning, as fidelity by construction is limited to  $0 \leq \mathcal{F} \leq 1$ . However, this result makes sense in terms of Pauli errors as the  $\hat{\mathcal{M}}_i$  measurements are performed along different axes. For two qubits, a completely imperfect readout corresponds to applying a Y-Pauli error before measuring  $\hat{\mathcal{M}}_1$  and an X-Pauli error before measuring  $\hat{\mathcal{M}}_2$ . In effect, the different operators are not measuring the same state, thus permitting  $\mathcal{F} < 0$ . The key point is that readout errors are worse than initialisation errors.

### 10.1.3 LASER SCATTERING

Laser scatter from the optical  $\pi$ -pulses will give additional detections across all photonic windows without any correlation to the spin state. For simplicity, this is modelled by mixing the ideal state  $|\psi_{id}\rangle$  with a single laser photon. For small impurity  $\xi \ll 1$  (defined in (9.31)) and low collection efficiency (negligible chance of two-photon detection), the post selected state from a two qubit experiment is

$$\hat{\rho}_{exp} = (1 - 2\xi)\hat{\rho}_{id} + 2\xi\hat{\rho}_{scatter}, \quad (10.5)$$

$$\hat{\rho}_{id} = |\psi_{id}\rangle\langle\psi_{id}|, \quad (10.6)$$

$$\hat{\rho}_{scatter} = \left( \frac{|e\rangle\langle e| + |l\rangle\langle l| + e^{-i\phi_l}|e\rangle\langle l| + e^{i\phi_l}|l\rangle\langle e|}{2} \right) \times \left( \frac{|\uparrow\rangle\langle\uparrow| + |\downarrow\rangle\langle\downarrow|}{2} \right), \quad (10.7)$$

where the factor 2 in (10.5) comes from having two laser pulses but only one QD emission, and  $\phi_l$  is the phase of the late excitation. The fidelity of (10.5) can be

directly evaluated

$$\begin{aligned}\mathcal{F}_{scatter} &= (1 - 2\xi) \langle \psi_{id} | \hat{\rho}_{id} | \psi_{id} \rangle + 2\xi \langle \psi_{id} | \hat{\rho}_{scatter} | \psi_{id} \rangle \\ &= (1 - 2\xi) + 2\xi \frac{1}{4} = 1 - \frac{3}{2}\xi.\end{aligned}\quad (10.8)$$

When  $\hat{\rho}_{scatter}$  is detected through the TBI, the middle detection window intensity will depend on  $\phi_l$ . In other words, for X-measurements, laser scatter will mix in the interference fringes observed when characterising the TBI (figure 8.6). This may explain the visibility difference between the  $|X+\rangle$  and  $|X-\rangle$  readout curves in figure 9.7. Laser background adds constructively with the actual coincidences of  $|X-\rangle$  but destructively with  $|X+\rangle$ . However, since the experiment projects onto both spin states this systematic effect is averaged out.

#### 10.1.4 INTERFEROMETER

The visibility of XY measurements exactly follow the classical TBI visibility. This follows from  $\langle \hat{\mathcal{M}}_1 \rangle$  in (9.11) having the exact same form as  $\mathcal{V}_{TBI}$  in (8.19) for a perfect input state.  $\hat{P}_z$  is in principle independent of the interferometer, as it only checks if the spin is correctly correlated to the photon time. A bad interferometer cannot convert  $|e\rangle$  to  $|l\rangle$ . However, if erroneous states such as  $|\uparrow\rangle|e\rangle$  are more prevalent than  $|\downarrow\rangle|l\rangle$ , an increased chance to project onto  $|l\rangle$  will slightly improve  $\langle \hat{P}_z \rangle$ . Given the measured interferometer values in figure 8.5,  $(\eta_{S1}^2 + \eta_{S2}^2)/(\eta_{L1}^2 + \eta_{L2}^2) = 0.998$ . Hence, there is no preference for measuring early or late photons, and it is fair to state the two-qubit TBI limited fidelity as

$$\mathcal{F}_{TBI}^{N=1} = \frac{\langle \hat{P}_z \rangle + \langle \hat{\chi} \rangle}{2} = \frac{1}{2} + \frac{\mathcal{V}_{TBI}}{2}, \quad (10.9)$$

giving 99.8% for the observed  $\mathcal{V}_{TBI} = 99.6\%$ .

#### 10.1.5 CROSS EXCITATION

An additional excitation error occurs if the excitation laser drives the diagonal  $|0\rangle \rightarrow |2\rangle$  and  $|1\rangle \rightarrow |3\rangle$  transitions, which have a high probability of producing spin-flips. In a PCW with out-of-plane excitation, this coupling can be well suppressed via the laser polarisation. However, this error may be a big hindrance for nanostructures such as photonic crystal cavities, which employ cross polarisation techniques and thus don't discriminate the optical dipoles based on polarisation.

#### 10.1.6 $T_2$ TIME

A finite  $T_2$  time will contribute to an imperfect spin echo. We have so far assumed that the echo time duration  $\tau_e$  is much shorter than  $T_2$ . This seems to be a good approximation for the two-qubit experiment with  $\tau_e \approx 20$  ns and  $T_2 = 448$  ns<sup>-1</sup> (measured in section 6.4.1). However, the echo visibility dips observed in figure 6.10 may be relevant for even short  $\tau_e$ .

### 10.1.7 EXCITATION INDUCED DEPHASING

A more speculative error is related to the dampening of optical  $\pi$ -pulses, which is almost universally observed in QD systems [90,128,129]. This dampening is referred to as excitation-induced dephasing, with most works attributing the effect to a phonon coupling [90,129]. If this is the case, the entangled state may dephase during excitation in addition to the previously modelled phonon dephasing, which only occurs during the decay. This effect would encourage the use of longer excitation pulses following the scaling predicted in Ref. [90].

## 10.2 EXPLAINING EARLY/LATE ASYMMETRY

A simple model combining spin rotation errors and cyclicity is presented here in order to shed light on asymmetries in the Z-basis measurement (figure 9.10). Consider the state in (7.23) following a single round. Assuming perfect filtering,  $\hat{R}_i = \hat{\mathbb{I}}$  (the last rotation has not yet been performed), tracing out unobserved photons and postselecting on one photon, the state is given by the density matrix

$$\hat{\rho} = \frac{A}{2} [p_{\parallel} |0, e\rangle\langle 0, e| + p_{\parallel}(1 + p'_{\perp}) |1, l\rangle\langle 1, l| + p_{\parallel}(|0, e\rangle\langle 1, l| + |1, l\rangle\langle 0, e|)], \quad (10.10)$$

$$A = \frac{2}{p_{\parallel}(2 + p'_{\perp})}, \quad (10.11)$$

where  $A$  is the postselection probability. The state in (10.10) contains an overweight of late photons as discussed in section 7.4.4. The probability of measuring states with the spin in  $|1\rangle$  simply correspond to evaluating

$$P_{1,e} = \text{tr}\{|1, e\rangle\langle 1, e| \hat{\rho}\} = 0, \quad (10.12)$$

$$P_{1,l} = \text{tr}\{|1, l\rangle\langle 1, l| \hat{\rho}\} = \frac{A}{2} p_{\parallel}(1 + p'_{\perp}). \quad (10.13)$$

However, to project onto states containing  $|0\rangle$ , we must first apply a  $\hat{R}_y(\pi)$  rotation. We approximate an imperfect  $\pi$ -pulse with the transformation

$$\hat{\hat{\rho}} = F_{\pi} \hat{X}_{spin} \hat{\rho} \hat{X}_{spin}^{\dagger} + (1 - F_{\pi}) \hat{\rho}, \quad (10.14)$$

where  $\hat{\hat{\rho}}$  is the state after  $\hat{R}_y(\pi)$ ,  $F_{\pi}$  is the  $\pi$ -pulse fidelity and  $\hat{X}_{spin}$  applies  $\hat{\sigma}_x$  on the spin. Evaluating the remaining detection probabilities then gives

$$P_{0,e} = \text{tr}\{|1, e\rangle\langle 1, e| \hat{\hat{\rho}}\} = \frac{A}{2} F_{\pi} p_{\parallel}, \quad (10.15)$$

$$P_{0,l} = \text{tr}\{|1, l\rangle\langle 1, l| \hat{\hat{\rho}}\} = \frac{A}{2} (1 - F_{\pi}) p_{\parallel} (1 + p'_{\perp}). \quad (10.16)$$

Note that the  $P$  subscripts no longer match the projection operators as the transformed  $\hat{\hat{\rho}}$  is being measured. Finally, (10.13) and (10.15) allow calculating the

relative probabilities of observing  $|1, l\rangle$  and  $|0, e\rangle$ :

$$\frac{P_{1,l}}{P_{0,e}} = \frac{1 + p'_\perp}{F_\pi} = \frac{1}{F_\pi} \frac{C + 2}{C + 1}, \quad (10.17)$$

where the last equality used (7.22) for  $\eta_{20} = 0$  and  $C$  is the cyclicity. Hence, the existing late bias is further increased as projection onto  $|0, e\rangle$  requires an imperfect rotation. For the measured values,  $C = 14.7$  and  $F_\pi = 0.885$ , (10.17) yields a ratio of 1.20. This treatment neglected errors on the first two rotation pulses but can explain a large part of the 1.28 ratio observed in figure 9.10.

### 10.3 A MONTE CARLO SIMULATION

A Monte Carlo (MC) simulation of the two-qubit experiment is now performed to better include the relevant errors. The central idea of the MC approach is to constantly check if the system has coupled to the environment. If so, the system is subjected to a random collapse. This allows us to work with wavefunctions instead of density matrices and provides a higher level of physical intuition at the expense of having to simulate many trajectories. This is not a big problem, as we anyway need to integrate over an ensemble of  $\Delta_{OH}$ .

The simulation Hilbert space consists of the four QD spin states, an early pulse-photon, an early qubit photon, a late pulse-photon and a late qubit photon:

$$\mathcal{H} = \{0, 1, 2, 3\} \otimes \{\emptyset, e_p\} \otimes \{\emptyset, e\} \otimes \{\emptyset, l_p\} \otimes \{\emptyset, l\}, \quad (10.18)$$

where  $\emptyset$  denotes photon vacuum,  $e(l)$  denotes early(late) and the  $p$  subscript indicates a photon emitted during the optical  $\pi$ -pulse. Figure 10.1 shows the simulation steps which will now be elaborated.

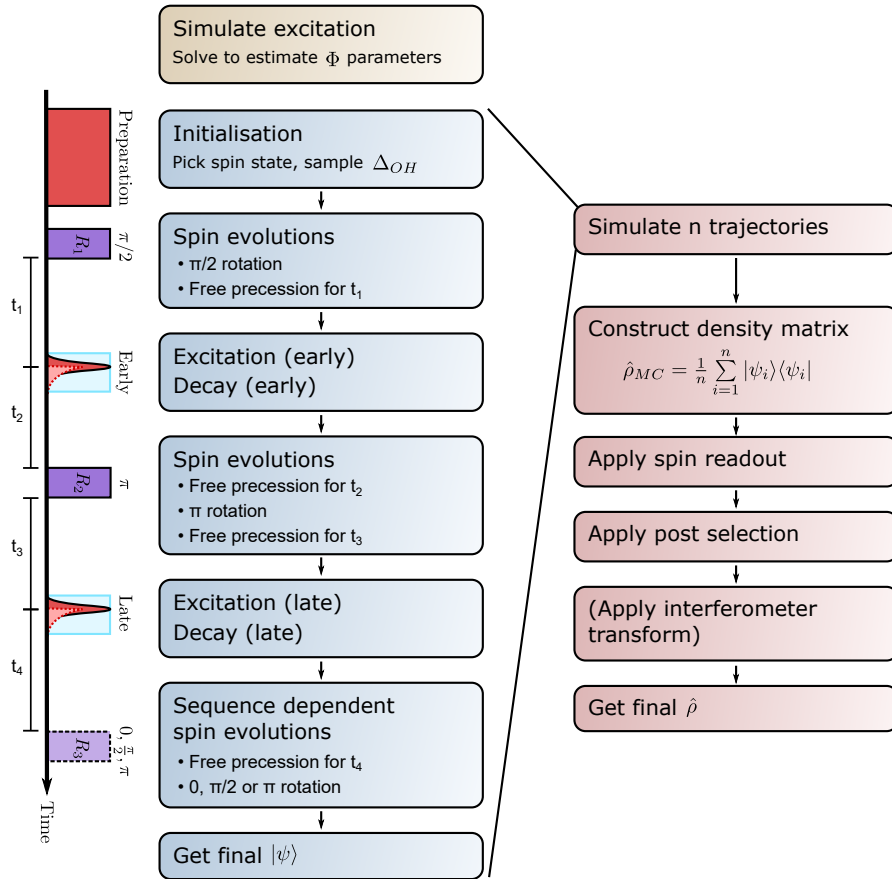


**Figure 10.1:** Operations performed in a MC simulation of a single trajectory and the construction of a final density matrix from multiple trajectories. The simulations steps relate to the pulse sequence on the left.

### 10.3.1 INITIALISATION

The spin initialisation fidelity  $F_i$  corresponds to choosing the initial state following

$$|\psi\rangle = \begin{cases} |0\rangle |\emptyset\rangle^{\otimes \text{photons}} & \text{if } r \leq F_i \\ |1\rangle |\emptyset\rangle^{\otimes \text{photons}} & \text{if } r > F_i \end{cases}, \quad (10.19)$$

where  $r \sim \mathcal{U}(0, 1)$  is random number and  $\mathcal{U}(0, 1)$  denotes the uniform distribution on  $[0, 1]$ . In addition, a  $\Delta_{OH}$  is drawn from  $\mathcal{N}(\sqrt{2}/T_2^*)$  (following section 2.8) which is used throughout the trajectory evolution.

### 10.3.2 SPIN ROTATION

For simplicity, rotation pulses are assumed square, permitting unitary evolution by

$$\hat{U}_{rot} = \hat{U}_{spin} \otimes \hat{\mathbb{I}}_{trions} \otimes \hat{\mathbb{I}}_{photons}, \quad (10.20)$$

where  $\hat{U}_{spin}$  only acts on the two ground states and is given by (6.16).

This unitary is used during rotation pulses ( $\Omega_r > 0$ ) and during periods of delay ( $\Omega_r = 0$ ). During rotation pulses, spin-flips are introduced by the collapse operators

$$\hat{C}_1 = \sqrt{\kappa} |0\rangle\langle 1| \otimes \hat{\mathbb{I}}_{photons}, \quad (10.21)$$

$$\hat{C}_2 = \sqrt{\kappa} |1\rangle\langle 0| \otimes \hat{\mathbb{I}}_{photons}, \quad (10.22)$$

which are the same operators applied in the master equation of section 6.2.4. Due to the common  $\kappa$  in  $\hat{C}_1$  and  $\hat{C}_2$ , the rate of spin-flips is  $\kappa$  regardless of the spin state. The probability of a spin-flip occurring after time  $\tau_f$  is then given by the exponential distribution

$$P(\tau_f) = \kappa e^{-\kappa\tau_f}, \quad \tau_f \geq 0. \quad (10.23)$$

This enables efficient simulation: A  $\tau_f$  is randomly drawn from (10.23) and  $|\psi\rangle$  is evolved according to (10.20) for duration  $\tau_f$  after which a collapse as applied according to standard MC techniques [130]

$$|\psi_1\rangle = \frac{\hat{C}_i |\psi_0\rangle}{\sqrt{p_i}}, \quad (10.24)$$

where  $|\psi_0\rangle$  is the initial state,  $|\psi_1\rangle$  is the post-collapse state, and the randomly chosen  $\hat{C}_i$  has probability

$$p_i = \frac{\langle \psi_0 | \hat{C}_i^\dagger \hat{C}_i | \psi_0 \rangle}{\sum_i \langle \psi_0 | \hat{C}_i^\dagger \hat{C}_i | \psi_0 \rangle}. \quad (10.25)$$

Following the collapse, a new  $\tau_f$  is sampled and the procedure is repeated until the next spin-flip occurs or the end of the rotation pulse is reached.

The experimental pulse sequence is approximated by choosing the  $\pi$ -pulse duration  $T_{r,\pi} = 7$  ns,  $\pi/2$ -duration  $T_{r,\pi/2} = 3.5$  ns, spin Rabi frequency  $\Omega_r = \pi/T_r$  and pulse delays  $(t_1, t_2, t_3, t_4) = (6.5, 3.5, 2, 8)$  ns defined in figure 10.1.

### 10.3.3 EXCITATION

During optical excitation, several outcomes are possible. Ideally, the  $|1\rangle$  state is coherently excited to  $|2\rangle$  and any superposition is maintained. However, the QD can decay radiatively during the excitation pulse, thus emitting a pulse-photon. This collapses the wavefunction, and the pulse-photon can either be detected or lost. After the emission of the pulse-photon, the QD may be re-excited to  $|2\rangle$ . It will be assumed that photons emitted from transitions other than  $|2\rangle \rightarrow |1\rangle$  are perfectly filtered based on the excellent etalon filtering observed in figure 8.9.

We model the excitation by applying one of the following<sup>1</sup> collapse operators

$$\hat{C}_1 = \Phi_{00} |0\rangle\langle 0| + \Phi_{30} |3\rangle\langle 0| + \Phi_{21} |2\rangle\langle 1| + \Phi_{11} |1\rangle\langle 1| \text{ (Ideal)}, \quad (10.26)$$

$$\hat{C}_2 = \sqrt{\eta_p} \Phi_{11}^p |1\rangle\langle 1| \hat{a}_p^\dagger \text{ ( } 2 \rightarrow 1 \text{ decay, detected)}, \quad (10.27)$$

$$\hat{C}_3 = \sqrt{\eta_p} \Phi_{21}^p |2\rangle\langle 1| \hat{a}_p^\dagger \text{ ( } 2 \rightarrow 1 \text{ decay, detected, reexcitation)}, \quad (10.28)$$

$$\hat{C}_4 = \sqrt{1 - \eta_p} \Phi_{11}^p |1\rangle\langle 1| \text{ ( } 2 \rightarrow 1 \text{ decay, lost)}, \quad (10.29)$$

$$\hat{C}_5 = \sqrt{1 - \eta_p} \Phi_{21}^p |2\rangle\langle 1| \text{ ( } 2 \rightarrow 1 \text{ decay, lost, reexcitation)}, \quad (10.30)$$

$$\hat{C}_6 = \Phi_{00}^p |0\rangle\langle 0| \text{ (Excite } 0 \rightarrow 3, \text{ decay } 3 \rightarrow 0)}, \quad (10.31)$$

$$\hat{C}_7 = \Phi_{01}^p |0\rangle\langle 1| \text{ (Excite } 1 \rightarrow 2, \text{ decay } 2 \rightarrow 0)}, \quad (10.32)$$

$$\hat{C}_8 = \Phi_{10}^p |1\rangle\langle 0| \text{ (Excite } 0 \rightarrow 3, \text{ decay } 3 \rightarrow 1)}, \quad (10.33)$$

where the  $p$  superscript indicates a pulse-photon emission,  $\eta_p$  is the detection probability of a pulse-photon from  $2 \rightarrow 1$  and  $\hat{a}_p^\dagger$  creates a pulse-photon in the appropriate early or late mode. All operators apply the identity on unaffected qubits.

Following standard MC techniques [130], the state after excitation is given by

$$|\psi_1\rangle = \frac{\hat{C}_i |\psi_0\rangle}{\sqrt{p_i}}, \quad (10.34)$$

where  $|\psi_0\rangle$  is the initial state and  $\hat{C}$  is chosen according to

$$p_i = \langle \psi_0 | \hat{C}_i^\dagger \hat{C}_i | \psi_0 \rangle. \quad (10.35)$$

By construction, the probabilities in (10.35) sum to unity.

The task at hand is then to evaluate the  $\Phi$  amplitudes. This is done with a separate MC simulation where the optical Bloch equations are solved. The Hermitian

<sup>1</sup>The full list of projects is longer still, including rare events such as exciting  $1 \rightarrow 2$ , decaying  $2 \rightarrow 0$  and re-exciting  $0 \rightarrow 3$ . These events are included in the simulation.

evolution is governed by (D.4) with the assumptions<sup>2</sup>  $\Omega_x = 0$  and  $\Delta_{OH}=0$ :

$$\begin{aligned} \hat{H}_1 = & -\omega_g |0\rangle\langle 0| + \Delta_l |2\rangle\langle 2| + (\Delta_l + \omega_t) |3\rangle\langle 3| \\ & + \frac{\Omega(t)}{2} (|2\rangle\langle 1| + |3\rangle\langle 0|) + h.c. \end{aligned} \quad (10.36)$$

Here,  $\omega_g$  ( $\omega_t$ ) is the ground state (trion) splitting,  $\Delta_l$  is the laser detuning from the  $|1\rangle \leftrightarrow |2\rangle$  transition and  $\Omega(t)$  is the optical Rabi frequency of the y-transitions. Thus, we neglect cross-excitation but note that it can easily be incorporated by adding the appropriate coupling terms to (10.36). In effect, (10.36) describes two separate two-level systems. However, all four levels must be included as optical decays can couple the two manifolds.

The optical Rabi frequency is given a Gaussian time dependence

$$\Omega(t) = \Omega_0 e^{-t^2/(2\tilde{T}_{opt}^2)}, \quad (10.37)$$

where  $\tilde{T}_{opt}$  is the standard deviation of  $\Omega(t)$ . This is related to  $T_{opt}$  (the FWHM of the pulse intensity) through<sup>3</sup>  $\tilde{T}_{opt} = T_{opt}/(2\sqrt{\ln(2)}) \approx 0.601 \times T_{opt}$ . In principle, the excitation pulse has infinite temporal extent meaning that the QD will always decay within the pulse. This motivates a truncation of the pulse: The pulse is truncated to the interval  $[-(3/\sqrt{2})\tilde{T}_{opt}, (3/\sqrt{2})\tilde{T}_{opt}]$ , see figure 10.2.  $\Omega_0$  is chosen

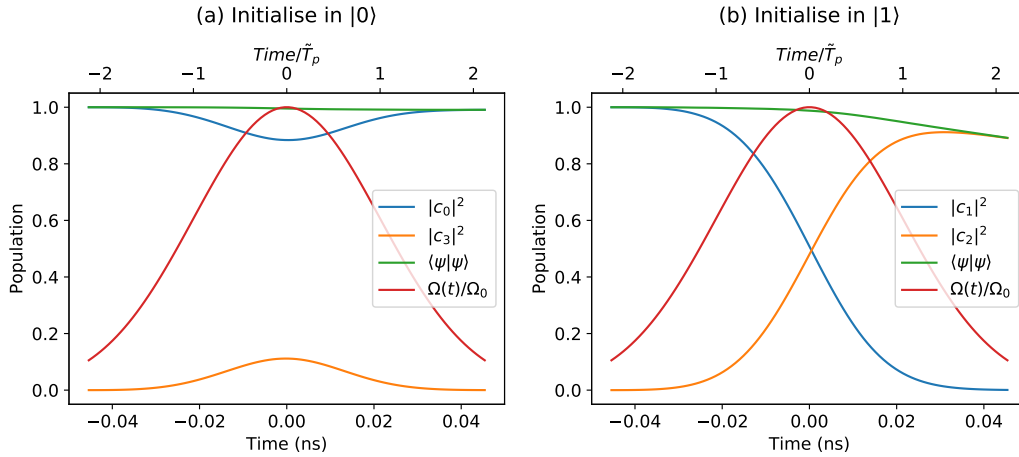


**Figure 10.2:** Solution to the optical Bloch equations for a QD subjected to a truncated  $\pi$ -pulse resonant with the  $|1\rangle \rightarrow |2\rangle$  transition. Blue and orange curves indicate populations of the relevant states. The QD is initialised in (a)  $|0\rangle$  and (b)  $|1\rangle$ . The wavefunction norm  $\langle\psi|\psi\rangle$  decays due to radiative decays. Simulation parameters:  $T_{opt} = 35.6$  ps,  $\Delta_l = 0$ ,  $\Delta_g + \Delta_t = \Delta_0 = 2\pi \times 17$  GHz and  $\gamma = 2.54$  ns<sup>-1</sup>.

<sup>2</sup> $\Delta_{OH}=0$  is justified by the short duration of the excitation relative to overall spin evolution and that  $\Delta_{OH} \ll \Delta_0, \Omega(t)$ . This assumption removes the need of re-evaluating the excitation for every value of  $\Delta_{OH}$ .

<sup>3</sup>The conversion involves a  $\sqrt{2}$  conversion from intensity to Rabi frequency and a  $2\sqrt{2\ln(2)}$  conversion from Gaussian FWHM to standard deviation.

to fulfill the  $\pi$ -pulse condition:

$$\int_{-(3/\sqrt{2})\tilde{T}_{opt}}^{(3/\sqrt{2})\tilde{T}_{opt}} dt \Omega(t) = \pi \Rightarrow \Omega_0 = \sqrt{\frac{\pi}{2}} \frac{1}{\tilde{T}_p \operatorname{erf}(\frac{3}{2})}, \quad (10.38)$$

where  $\operatorname{erf}()$  is the error function.

Optical decays are included with the 4 collapse operators:

$$\hat{C}_1 = \sqrt{\gamma_y} |1\rangle\langle 2|, \quad (10.39)$$

$$\hat{C}_2 = \sqrt{\gamma_y} |0\rangle\langle 3|, \quad (10.40)$$

$$\hat{C}_3 = \sqrt{\gamma_x} |1\rangle\langle 3|, \quad (10.41)$$

$$\hat{C}_4 = \sqrt{\gamma_x} |0\rangle\langle 2|. \quad (10.42)$$

Building of Ref. [130], the evolution is governed by the non-Hermitian Hamiltonian

$$\hat{H}_{eff} = \hat{H}_1 - \frac{i}{2} \sum_i \hat{C}_i^\dagger \hat{C}_i \quad (10.43)$$

$$= \hat{H}_1 - \frac{i\gamma_0}{2} (|3\rangle\langle 3| + |2\rangle\langle 2|), \quad (10.44)$$

where  $\gamma_0 = \gamma_x + \gamma_y$ . The dynamics owing to (10.36), (10.37) and (10.44) are then integrated numerically yielding the state evolution  $|\psi(t)\rangle$ , which is plotted in figure 10.2. Quantum jumps are incorporated [131] through the following steps:

1. Sample a random number  $r \sim \mathcal{U}(0, 1)$ .
2. Integrate the Schroedinger equation until time  $\tau$  at which  $\langle \psi(\tau) | \psi(\tau) \rangle \leq r$ . If this condition is never met the systems evolves without collapse.
3. Draw a random collapse from (10.39)-(10.42) with probabilities

$$p_i = \frac{\langle \psi(\tau) | \hat{C}_i^\dagger \hat{C}_i | \psi(\tau) \rangle}{\sum_i \langle \psi(\tau) | \hat{C}_i^\dagger \hat{C}_i | \psi(\tau) \rangle} \quad (10.45)$$

and transform the state according to

$$|\psi_{after}\rangle = \frac{\hat{C}_i |\psi(\tau)\rangle}{\sqrt{p_i}}. \quad (10.46)$$

Note which collapse occurred, as this indicates the decay path.

4. Repeat steps 1-3 starting at time  $\tau$ .

In practice, the Schrödinger equation only has to be integrated once over the full pulse. Upon sampling  $r$  one can skip to the point in time where the jump occurs, apply a collapse operator, and only then compute a fresh numerical integration starting at  $\tau$ . Most of the time, no jump occurs.

The simulation is repeated a large number of times with the spin initialised in both  $|0\rangle$  and  $|1\rangle$ . The amplitudes  $\Phi_{00}, \Phi_{30}, \Phi_{21}$  and  $\Phi_{11}$  are estimated by multiplying the amplitudes following coherent evolution with the root probability of a coherent evolution. The  $\Phi^p$  amplitudes are computed by counting the occurrences of the different collapses and noting the final state. The phases of these amplitudes are irrelevant as their corresponding operators anyway collapse the state.

In this work, we approximate pulse-photons as inheriting the bandwidth of the excitation pulse. This enables evaluation of their detection probability  $\eta_p$  by multiplying the laser spectrum with the measured etalon transmission. The actual physics is more complicated, as the pulse-photon's spectrum is correlated with its emission time and should be computed with the quantum regression theorem [132].

#### 10.3.4 OPTICAL DECAY

We now consider the optical decay occurring after the optical excitation. The optical decay is treated as being instantaneous following the discussion of section 7.4.1. The decay can then simply be treated by randomly applying collapse operators in the same manner as for the excitation. The collapse operators are given by

$$\hat{C}_1 = |0\rangle\langle 0| + |1\rangle\langle 1| + \sqrt{p_{\parallel}}\sqrt{I} |1\rangle\langle 2| \hat{a}^{\dagger} \text{ (Correct evolution, photon detected),} \quad (10.47)$$

$$\hat{C}_2 = \sqrt{p'_{\parallel}} |1\rangle\langle 2| \text{ (Correct decay, photon lost),} \quad (10.48)$$

$$\hat{C}_3 = \sqrt{p_{\parallel}}\sqrt{1-I} |1\rangle\langle 2| \hat{a}^{\dagger} \text{ (Correct decay, phonon scattering),} \quad (10.49)$$

$$\hat{C}_4 = \sqrt{\gamma_y/\gamma_0} |0\rangle\langle 3| \text{ (3} \rightarrow \text{0 decay, photon lost),} \quad (10.50)$$

$$\hat{C}_5 = \sqrt{\gamma_x/\gamma_0} |1\rangle\langle 3| \text{ (3} \rightarrow \text{1 decay, photon lost),} \quad (10.51)$$

$$\hat{C}_6 = \sqrt{\gamma_x/\gamma_0} |0\rangle\langle 2| \text{ (2} \rightarrow \text{0 decay, photon lost).} \quad (10.52)$$

where  $I$  is the indistinguishability from (7.16) and  $p_{\parallel}, p'_{\parallel}$  are the probabilities defined in (7.19) and (7.21). Like before, only photons from the  $2 \rightarrow 1$  decay are assumed detected. Note how (10.48) and (10.49) both collapse the wavefunction despite using the correct decay channel as which way information is gained through a lost photon and scattered phonon, respectively. State evolution is found by following (10.34) and (10.35).

#### 10.3.5 DENSITY MATRIX CONSTRUCTION

After having simulated  $N$  trajectories the wavefunctions are summed to create a density matrix:

$$\hat{\rho}_{MC} = \frac{1}{N} \sum_{i=1}^N |\psi_i\rangle\langle\psi_i|. \quad (10.53)$$

As in the experiment, most trajectories will contain zero detected photons. Following the experimental approach, postselection is applied by

$$\hat{\rho}_{MC}^{(1)} = \frac{\hat{P}_{N=1} \hat{\rho}_{MC} \hat{P}_{N=1}^\dagger}{\text{tr}\{\hat{P}_{N=1} \hat{\rho}_{MC} \hat{P}_{N=1}^\dagger\}}, \quad (10.54)$$

$$\hat{P}_{N=1} = \hat{\mathbb{I}}_{QD} \otimes (|e_p \emptyset \emptyset \emptyset\rangle\langle e_p \emptyset \emptyset \emptyset| + |\emptyset e \emptyset \emptyset\rangle\langle \emptyset e \emptyset \emptyset| + |\emptyset \emptyset l_p \emptyset\rangle\langle \emptyset \emptyset l_p \emptyset| + |\emptyset \emptyset \emptyset l\rangle\langle \emptyset \emptyset \emptyset l|)_{photons}, \quad (10.55)$$

which projects onto having one photon. The simulation Hilbert space implies that pulse and qubit photons can be distinguished based on emission time and that states with a pulse-photon have zero fidelity. To emulate the experiment where this distinction is lacking, the density matrix is transformed by

$$\hat{\rho}_{MC}^{(2)} = \hat{\mathcal{P}} \hat{\rho}_{MC}^{(1)} \hat{\mathcal{P}}^\dagger, \quad (10.56)$$

$$\hat{\mathcal{P}} = [|\emptyset e \emptyset \emptyset\rangle (\langle e_p \emptyset \emptyset \emptyset| + \langle \emptyset e \emptyset \emptyset|) + |\emptyset \emptyset l \emptyset\rangle (\langle \emptyset \emptyset \emptyset l_p| + \langle \emptyset \emptyset l \emptyset|)] \otimes \hat{\mathbb{I}}_{QD}, \quad (10.57)$$

which has the effect of changing pulse-photons to qubit-photons. The result is that pulse-photons may correctly contribute to Z-correlations but not to X-correlations. The spin readout fidelity  $F_r$  is incorporated by the transform

$$\hat{\rho}_{MC}^{(3)} = F_r \hat{\rho}_{MC}^{(2)} + (1 - F_r) \hat{X}_{spin} \hat{\rho}_{MC}^{(2)} \hat{X}_{spin}, \quad (10.58)$$

$$\hat{X}_{spin} = \hat{\sigma}_{x,spin} \otimes \hat{\mathbb{I}}_{trions} \otimes \hat{\mathbb{I}}_{photons}, \quad (10.59)$$

which has the effect of flipping the spin with probability  $1 - F_r$ . The fidelity may now be directly evaluated from the definition in (7.30), giving the operational fidelity:

$$\mathcal{F}_{MC}^{op} = \langle \psi_{ideal} | \hat{\rho}_{MC}^{(3)} | \psi_{ideal} \rangle. \quad (10.60)$$

Alternatively, one can evaluate the operators used by the GHZ-method. The interferometer is implemented by letting the ideal TBI operator (7.48) work on the  $e$  and  $l$  elements of  $\hat{\rho}_{MC}^{(3)}$ .

## 10.4 MONTE CARLO RESULTS

### 10.4.1 ADDING SINGLE ERRORS

Figure 10.3 shows a series of simulations where only a single error is present at a time. We simulate the two-qubit entanglement, set the  $R_3$  pulse to a  $\pi/2$  rotation, and report the operational fidelity in (10.60). All simulations utilize an  $\eta = 0.01$  collection efficiency which achieves the same low-efficiency regime as the experiment but a higher postselection chance.

Figure 10.3a:b shows great agreement with theory for both cyclicity and indistinguishability except in the limit of low  $C$ , for which the approximation in (7.26) does not apply. Figure 10.3c tests spin echo by adopting the rotation pulse delays  $(t_1, t_2, t_3, t_4) = (0, 30 \text{ ns} - \tau_d, 30 \text{ ns} + \tau_d, 0)$  and varying  $\tau_d$  to displace the central  $\pi$ -pulse. The entanglement MC is performed for  $T_2^* = 23.2 \text{ ns}$ . In addition, an echo

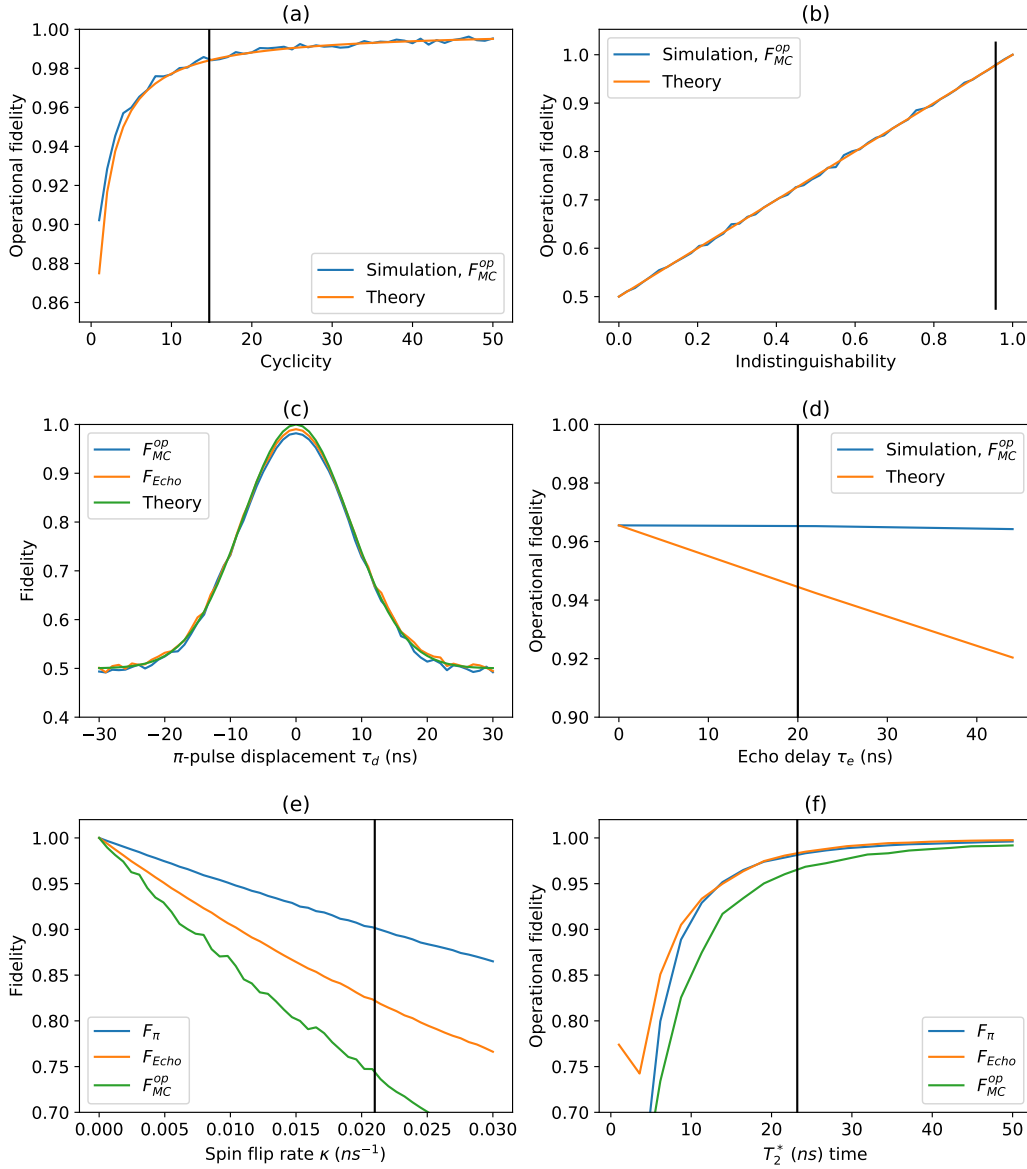


**Figure 10.3:** Two-qubit entanglement simulations with single error sources. All simulations use  $n = 5 \cdot 10^5$  trajectories and collection efficiency  $\eta = 0.01$ . Black lines indicate experimental values. **(a)** Cyclicity errors compared against (7.26) for  $N = 1$ . **(b)** Indistinguishability errors compared against (7.17) for  $N = 1$ . **(c)** Spin echo is tested by scanning the central  $\pi$ -pulse displacement  $\tau_d$  using  $T_2^* = 23.2$  ns. Fidelity measures are explained in main text. **(d)** Operational fidelity as a function of total echo delay  $\tau_e$ . **(e)** Effect of spin-flips occurring during rotation pulses. **(f)** Effect of spin  $T_2^*$ .

experiment (without optical excitations) is simulated with the same framework and the fidelity calculated according to  $F_{echo} = |\langle 0 | \hat{\rho}_{MC} | 0 \rangle|^2$ . Both simulations yield a Gaussian  $\tau_d$  dependence according to theory (6.48). Fidelity does not reach unity at  $\tau_d = 0$  due to  $T_2^*$  induced rotation errors. Presumably, having the additional photonic qubit makes it easier to detect errors causing  $\mathcal{F}_{MC}^{op} < F_{echo}$ .

The simulation yields a perfect spin-echo as demonstrated in figure 10.3d where the entanglement fidelity is independent of the total echo duration  $\tau_e$ . A rough estimate of the real  $T_2$  contribution is made by plotting  $\frac{1}{2}(1 + e^{-\tau_e/T_2})$  for the measured  $T_2 = 448 \text{ ns}^{-1}$ .

Figure 10.3e and figure 10.3f show the effect of adding only spin-flips and  $T_2^*$ , respectively, on the fidelity of  $\pi$ -pulses, spin echo and full two-qubit entanglement.  $\pi$ -pulses and spin echo are simulated using the MC framework but omitting the optical excitations. It becomes clear that the entanglement experiment is more sensitive to errors than the bare echo experiment. Although the entanglement protocol is in principle  $T_2^*$ -insensitive, our  $T_2^* = 23.2 \text{ ns}$  limits  $\mathcal{F}_{MC}^{op}$  to  $\approx 96.7\%$  through errors induced on the slow Raman pulses.

By applying the estimated  $T_2^* = 23.2 \text{ ns}$  and  $\kappa = 0.021 \text{ ns}^{-1}$  (estimated from figure 6.7), we also reproduce the measured  $F_\pi = 88.5\%$  (section 6.3.2) and confirm consistency with the previous master equation description of spin rotations.

#### 10.4.2 EXCITATION ERRORS

Figure 10.4a shows the key  $\Phi$ -coefficients (defined in section 10.3.3) estimated by simulating optical excitation. The pulse duration  $T_{opt}$  is varied and  $\Omega_0$  is adjusted to always fulfill the  $\pi$ -pulse condition (10.38). Increasing  $T_{opt}$  has the following important effects:

1.  $|\Phi_{21}|^2$ , the probably of exciting  $|1\rangle \rightarrow |2\rangle$  without decay, slightly decreases, as pulse-photons become more probable.
2.  $|\Phi_{30}|^2$ , the probably of exciting the detuned  $|0\rangle \rightarrow |3\rangle$  transition without decay, rapidly decreases with longer  $T_{opt}$  and exhibits detuned Rabi oscillations.
3.  $|\Phi_{11}^p|^2$  and  $|\Phi_{21}^p|^2$ , the probabilities to emit a pulse-photon while driving  $|1\rangle \rightarrow |2\rangle$ , monotonously increase for longer  $T_{opt}$ .

This  $T_{opt}$  dependence leads to a global maximum in the entanglement fidelity as shown in figure 10.4b. However, the fidelity depends on the type of filtering. In the *distinguishable* case, pulse-photons are distinguishable from the spontaneously emitted photons. This corresponds to not performing the transformation in (10.56), and all trajectories containing a pulse-photon have zero fidelity. However, in the actual experiment, we don't precisely resolve the detection time. In the *indistinguishable* case, we cannot distinguish the different photons and apply the (10.56) transformation. The fidelity is additionally improved by using filtering to prevent the detection of pulse-photons. *Full filtering* uses  $\eta_p = 0$  while *Partial filtering* uses  $\eta_p = 0.247\eta$  estimated from the etalon transmission and the excitation pulse bandwidth.  $\eta_p = 0$ , i.e. perfect rejection of pulse-photons, give rise to a near-constant fidelity for long  $T_{opt}$  as the bad trajectories which pass postselection are exclusively due to two-photon emission. Given the simulation in figure 10.4b, our choice of  $T_{opt} = 35.6 \text{ ps}$  seems appropriate.

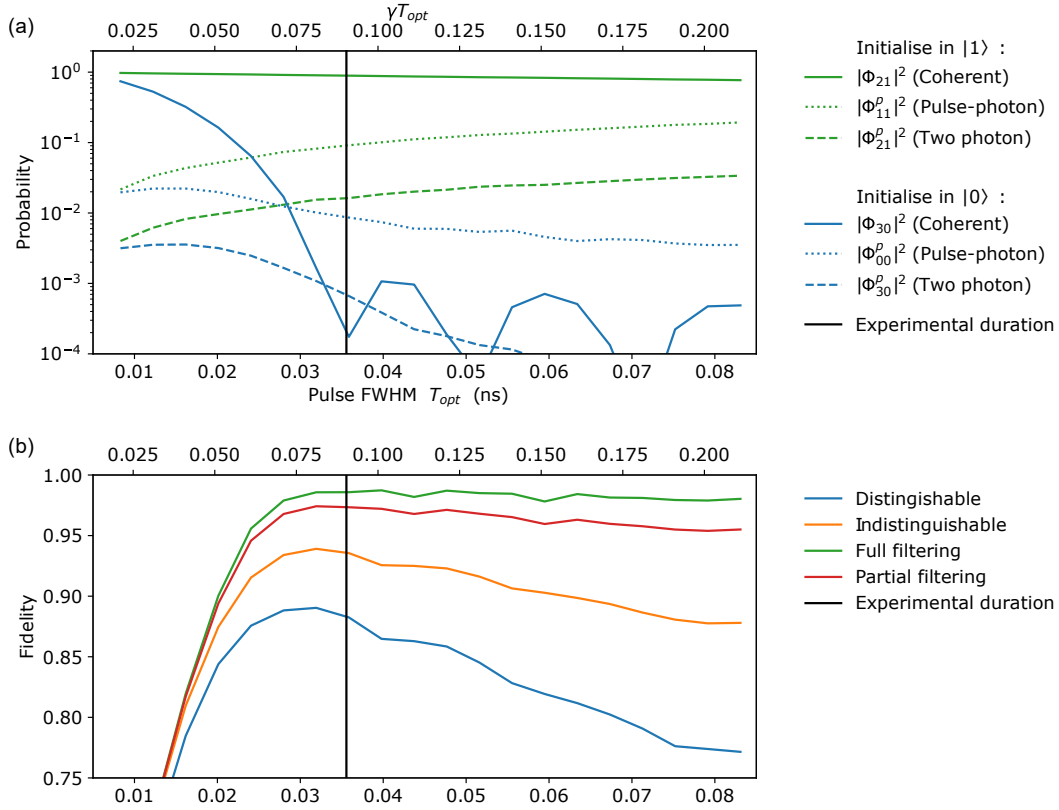


**Figure 10.4:** (a) Estimation of probability amplitudes describing optical excitation.  $\Phi$ -values are estimated by simulating  $10^5$  trajectories for the  $|0\rangle$  and  $|1\rangle$  initial spin states. The top x-axis shows pulse width in units of radiative lifetime. (b) Entanglement fidelity resulting from excitation errors alone as a function of pulse duration. The different fidelity measures are explained in the main text.

We can also apply this simulation to estimate the intensity autocorrelation  $\mathcal{G} = g^{(2)}(0)$ . We now consider a  $g^{(2)}$  experiment where the spin is prepared in  $|1\rangle$  and excited once as in section 9.6. We approximate the emitted photon state as a mixture of 0,1 and 2 photon components

$$\hat{\rho}_{ph} = (\eta|\Phi_{21}|^2 + \eta_p|\Phi_{11}^p|^2) |1\rangle\langle 1| + \eta\eta_p|\Phi_{21}^p|^2 |2\rangle\langle 2| + A|0\rangle\langle 0|, \quad (10.61)$$

where  $|0\rangle$ ,  $|1\rangle$  and  $|2\rangle$  denote the photon number and  $A$  is chosen to ensure  $\text{tr}\{\hat{\rho}_{ph}\} = 1$ . The  $|2\rangle\langle 2|$  term in (10.61) represents the detection of both photons from multiphoton emission. We have neglected terms where only one photon from multiphoton emission is detected. Using the definition in (9.29),  $\mathcal{G}$  is directly evaluated using

$$\mathcal{G}_{MC} = \frac{\text{tr}\{\hat{\rho}_{ph}\hat{a}^{\dagger 2}\hat{a}^2\}}{\text{tr}\{\hat{\rho}_{ph}\hat{a}^\dagger\hat{a}\}^2} = \frac{2\frac{\eta_p}{\eta}|\Phi_{21}^p|^2}{(|\Phi_{21}|^2 + \frac{\eta_p}{\eta}|\Phi_{11}^p|^2 + 2\eta_p|\Phi_{21}^p|^2)^2} \quad (10.62)$$

For the experimental  $T_{opt} = 35.6$  ps, the excitation simulation yields  $|\Phi_{21}|^2 = 89.1\%$ ,  $|\Phi_{11}^p|^2 = 9.2\%$  and  $|\Phi_{21}^p|^2 = 1.6\%$ . Using (10.62) then gives

$$\mathcal{G}_{MC}^{NoFilter} = 3.37\%, \quad (10.63)$$

$$\mathcal{G}_{MC}^{Filter} = 0.96\%. \quad (10.64)$$

$\mathcal{G}_{MC}^{NoFilter}$  assumed no filtering and  $\eta = \eta_p = 0.3\%$ . This number is in reasonable agreement with the values calculated in Ref. [133] and actually fits well with the experimentally measured  $\mathcal{G} \approx 3.3\%$  when the laser impurity has been subtracted (table 9.4). However, our experiment does apply filtering, and we should instead consider the  $\mathcal{G}_{MC}^{Filter} = 0.96\%$  estimate which assumed a pulse-photon detection efficiency of  $\eta_p = 0.247\eta$ . This is considerably below the measured  $\mathcal{G} \approx 3.3\%$ , hence, we cannot completely explain the observed  $\mathcal{G}$  from multi-photon emission. There is likely some aspect of the optical excitation and filtering which is not fully captured by our model. Alternatively, we could have underestimated the pulse duration  $T_{opt}$ . Measuring  $T_{opt}$  with an intensity autocorrelator would be an improvement over the current spectrometer based method.

### 10.4.3 BELL STATE SIMULATION

Figure 10.5 shows the GHZ-method simulated for a variety of errors. We simulate the exact same pulse sequence as in the actual experiment. The Z-measurements are constructed by simulating both the  $|\uparrow\rangle$  and  $|\downarrow\rangle$  readout sequences while the X-measurement is constructed by simulating the  $|+\rangle$  readout and applying the interferometer transform. Only a single rotated basis is simulated as nothing in the simulating creates a preference for X or Y Pauli errors. Hence, the simulated fidelity is calculated by

$$\mathcal{F}_{GHZ,MC}^{N=1} = \frac{\langle \hat{P}_z \rangle - \langle \hat{\mathcal{M}}_1 \rangle}{2}. \quad (10.65)$$

In the absence of errors, the MC simulation is seen to perfectly reproduce the ideal detection pattern. Adding the cyclicity and spin rotation errors ( $T_2^*$  and  $\kappa$ ) results in Z-coincidences in very close agreement with experiment and the late/early ratio discussed in section 10.2. Adding the remaining errors (excitation, phonon dephasing, readout and initialisation) yields the estimates

$$\langle \hat{P}_z \rangle_{MC} = 86.7\%, \quad (10.66)$$

$$\langle \hat{\chi} \rangle_{MC} = -\langle \hat{\mathcal{M}}_1 \rangle_{MC} = 52.2\%, \quad (10.67)$$

$$\mathcal{F}_{GHZ,MC}^{N=1} = 69.4\%. \quad (10.68)$$

Here  $\langle \hat{P}_z \rangle_{MC}$  falls below the experimental value. This most likely implies that  $F_r$  or  $F_\pi$  have been slightly underestimated. We also observe that the simulated  $\langle \hat{\chi} \rangle_{MC}$  remains higher than the measured value. This is less surprising, as more errors occur for X-measurements. It seems likely that the spin coherence time and

hence non-perfect spin echo is the main effect missing from the simulations. This error could be included in the MC by varying  $\Delta_{OH}$  during a trajectory evolution using a semi-classical noise model. This however requires a firmer grasp of the nuclear noise spectrum and should ideally reproduce the echo visibility dips observed in figure 6.12. Given the discrepancies between the measured and simulated  $g^{(2)}$ , radiative-decays during excitation might be more prevalent than expected. The additional dephasing from this mechanism would also serve to reduce  $\langle \hat{\chi} \rangle_{MC}$ .

Table 10.1 summarises all infidelity mechanisms and emphasizes the greater vulnerability of X-measurements. Additionally, the minor errors from TBI visibility and laser scatter, which were not simulated, should result in an additional  $\approx 1\%$  decrease in  $\mathcal{F}_{GHZ,MC}$ . This would bring our simulation within 1.8% of the measured fidelity.

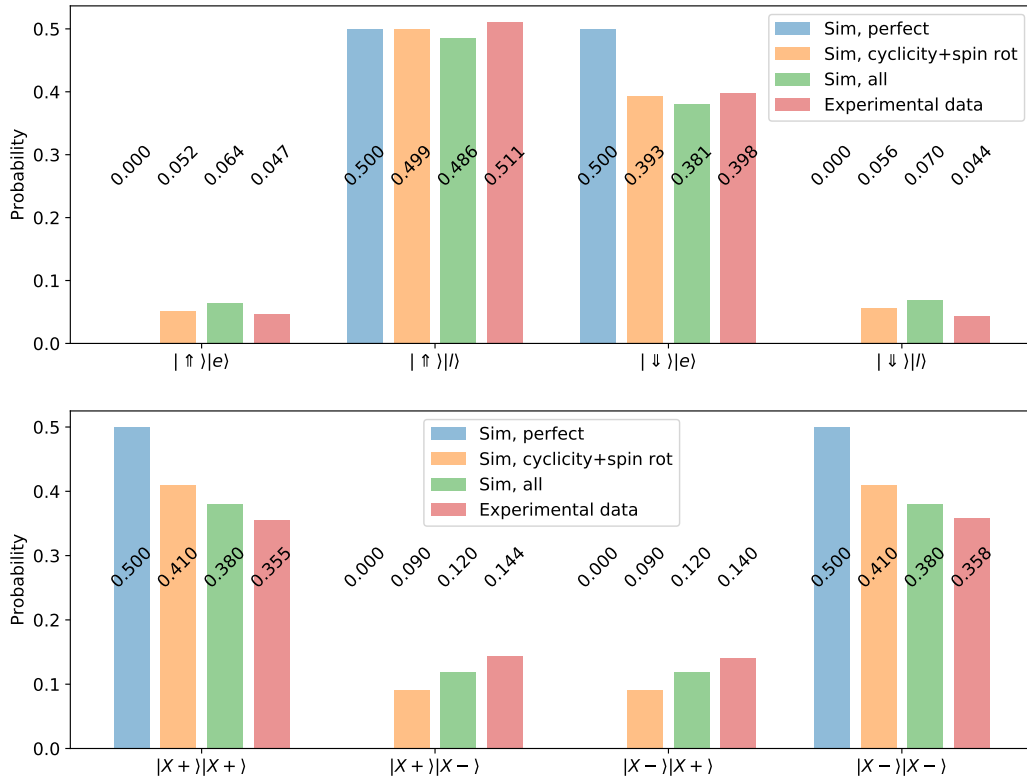


**Figure 10.5:** Simulation of two-qubit GHZ-measurement for various levels of error. Three spin readout sequences were simulated with each sequence consisting of  $n = 10^6$  simulated trajectories.

Error	$\hat{P}_z$	$\hat{\chi}$	Parameter value	Infidelity
Cyclicity	Yes (for $N > 1$ )	Yes	$C = 14.7$ $\eta = 1\%$	1.62% (simulated)
Phonon dephasing	No	Yes	$I = 95.7\%$	2.34% (simulated)
Excitation	No (for $c \gg 1$ )	Yes	$\gamma = 2.54 \text{ ns}^{-1}$ , $\Delta_0 = 17 \times 2\pi$ , $T_{opt} = 35.6 \text{ ps}$ .	2.66% (simulated)
Spin control ( $\kappa$ & $T_2^*$ )	Yes	Yes	$T_2^* = 23.2 \text{ ns}$ , $\kappa = 0.021 \text{ ns}^{-1}$	22.8% (simulated)
Spin readout	Yes	Yes	$F_r = 96.6\%$	5.1% (simulated)
Spin initialisation	No	Yes	$F_i = 98\%$	2.0% (simulated)
Laser background, uncorrelated counts	Yes	Yes	$\xi = 0.544\%$	0.8% (using (10.8))
Interferometer	No	Yes	$\mathcal{V}_{TBI} = 99.6\%$	0.2% (using (10.9))
Spin coherence ( $T_2$ )	No	Yes	$T_2 = 448 \text{ ns}^{-1}$ .	Not estimated
Excitation induced dephasing	No	Yes	Not estimated	Not estimated
Cross excitation	Yes	Yes	Not estimated	Not estimated

**Table 10.1:** Summary of all error mechanism, their key parameter values, and their impact on Bell state fidelity (in absence of other errors) according to MC simulations (using  $10^6$  trajectories) and calculations. The  $\hat{P}_z$  and  $\hat{\chi}$  columns indicate whether an error reduces visibility of Z and XY-basis measurements, respectively.

## 10.5 DISCUSSION

The MC simulations have proven successful in replicating the previously studied intrinsic errors and incorporating additional errors. By simulating the GHZ-method, we arrive at a simulated fidelity with minor deviations from the measured value. Adding more error mechanisms conveniently equates to modifying the individual blocks in figure 10.1. The simulation can be readily extended to more protocol rounds, either by expanding the Hilbert space or, perhaps more conveniently, immediately measuring the generated photon after each round and noting the result.

Unsurprisingly, the simulations emphasize the importance of high fidelity spin control as  $T_2^*$  and  $\kappa$  currently result in a significant 22.8% error.  $\kappa = 0$  would reduce this to the 3.3% error given by  $T_2^*$ . Increasing spin readout and initialisation fidelities would result in the second largest improvement. However, these errors are independent of the number of qubits and thus less important for scalability.

# 11 | Conclusion and Outlook

Charged quantum dots embedded in photonic nanostructures offer an efficient and coherent coupling between photons and a single spin qubit. Generating spin-mediated multi-photon entanglement has several important applications in quantum information processing. However, scalable entanglement generation requires excellent experimental control and a protocol playing to the strengths of the system.

In this work, we have mainly focused on manipulating the meta-stable hole spin, which can be optically induced and is sufficiently long-lived. A key limitation of QDs is the incompatibility of optical cycling transitions with coherent spin control. We have overcome this limitation through a novel application of photonic crystal waveguides, where the linear Voigt dipoles are selectively enhanced by the waveguide mode. Numerical simulations predict near-unity  $\beta$ -factors and cyclicity enhancements above 100 for a well-positioned QD and realistic group indices. In contrast to cavities, which can also induce cyclicity, our waveguide approach is broadband, compatible with low magnetic fields, and allows easier application of detuned rotation pulses. By employing optical pumping, we measured a cyclicity of  $14.7 \pm 0.2$ . The coherent nature of the spin-waveguide interface was additionally highlighted by the spin-perturbed waveguide transmission, which in itself may facilitate spin-photon gates. Transmission measurements also revealed the QD dipole orientation to be independent of the magnetic field, suggesting the hole Zeeman splitting to be dominated by hole-mixing.

Another important aspect of this work has been achieving optical control of the hole spin. By selectively driving the y-dipoles, as facilitated by the PCW geometry, we demonstrated a  $\approx 98\%$  hole spin initialisation fidelity. This was combined with a Raman scheme allowing full phase control of the spin and electronically defined rotation pulses. Using spin echo techniques, we demonstrated a  $T_2^* = (23.2 \pm 1.3)$  ns dephasing time, which exceeds most experiments employing comparable nanostructures, and a  $T_2 = (448 \pm 37)$  ns coherence time. Unfortunately, the spin rotation fidelity was limited to  $F_\pi = (88.5 \pm 0.3)\%$  as evident from the dampening of spin Rabi oscillations. This dampening could only be attributed to laser-induced spin flips, which could be a consequence of unwanted photocreations.

Our unprecedented combination of cyclicity and spin control in a QD system has paved the way for implementing a time-bin entanglement protocol, potentially capable of generating entangled photons at a 100 MHz rate. This protocol offers  $T_2^*$ -insensitivity and is compatible with high magnetic fields and PCWs as opposed to the Lindner-Rudolph protocol. We analysed this protocol in great detail and

highlighted the PCW's role in optimising the fidelity. Assuming realistic parameters, we predict intrinsic errors to result in a 2.1% error per photon, which is close to the bound for fault-tolerant quantum computing.

The time-bin protocol was experimentally demonstrated on a QD using a custom double-pass interferometer with 99.6% visibility. The interferometer's self-stabilising design, in conjunction with the spin phase control, enabled efficient fidelity estimation of N-qubit GHZ states using only N+1 measurement settings. Using this method, we measured a spin-photon Bell state with  $(66.6 \pm 0.5)\%$  fidelity and 124 Hz detection rate. Extending to three qubits was experimentally simple and yielded  $(42.3 \pm 1.2)\%$  fidelity with clear indications of coherence. Additionally, using the same interferometer, we measured an  $X^+$  single-photon  $g^{(2)}(0) = (3.8 \pm 0.6)\%$ , raw HOM visibility of  $(88.8 \pm 0.6)\%$  and a corrected HOM visibility of  $(96.9 \pm 0.7)\%$  in reasonable agreement with comparable PCW-embedded QDs. The HOM visibility is especially encouraging, as it greatly exceeds that of dark excitons [105], which were previously used to demonstrate the Lindner-Rudolph protocol [20].

Finally, by constructing an exhaustive Monte Carlo simulation, we were able to incorporate almost all experimentally relevant errors. The simulations nearly reproduce the experimentally measured infidelities and definitively emphasize spin rotation errors as the dominant error mechanism. The comprehensive understanding of the error mechanisms provides a useful tool for improving the experiment.

## 11.1 OUTLOOK

Let us consider the outlook on multi-photon entanglement with solid-state emitters. For the specific experiment presented here, a few improvements will enable states with more photons and greater fidelity. First and foremost, the rotation pulse fidelity must be improved. Further investigations into the origins of laser-induced spin-flips and hole photocreation can hopefully guide heterostructure design to better protect the hole spin. Alternatively, the electron spin can be used, either by adopting the nuclear spin narrowing techniques of Refs. [39, 41] or switching to ultra-fast rotation pulses, which should work equally well according to theory. Increasing the magnetic field will likely also be beneficial by increasing  $T_2$ ,  $T_2^*$  and the total Zeeman splitting  $\Delta_0$ . Additionally, adopting an arbitrary waveform generator can enable more flexible spin control and greater tunability of the entanglement protocol.

Motivated by the challenges of photonicly inducing cyclicity, it is natural to explore systems with intrinsic cycling transitions. Indeed, the Faraday geometry results in excellent cyclicity for InAs QDs [30], but the lack of spin control prevents its use. GaAs QDs may offer an interesting platform [134], in part by reducing the quadrupolar interactions which limit nuclear spin cooling in InAs QDs [41]. Given a cleaner nuclear environment, microwave control of the electron spin could perhaps be achieved, permitting time-bin entanglement using the intrinsic Faraday cyclicity. Less strained QDs might also allow magnetic field control over the optical Voigt dipoles offering new degrees of tuneability.

Silicon vacancy centres in diamond have significantly stronger zero-phonon-line emission than NV-centres, possess intrinsic cyclicity, and have recently demonstrated impressive levels of spin control, cavity integration and spin-photon entanglement [65]. Provided that good single-photon properties can be achieved, Silicon vacancy centres may also offer an attractive platform for time-bin entanglement generation.

Coming back to QDs, the time-bin protocol is not necessarily the ultimate approach. The Lindner-Rudolph protocol could see renewed life upon the discovery of a spin qubit with simultaneously high indistinguishability and good coherence at very low magnetic fields, although the experimental challenges of laser background rejection would persist. Based on the previously demonstrated spin-frequency entanglement [89,93], one could also imagine a generalisation to multiple frequency entangled photons, although it is currently unclear how such a protocol would depend on  $T_2^*$  and how to measure the frequency qubits. Of course, the spin-spin or photon-photon gates needed to create two-dimensional cluster states may also favour a certain qubit encoding and thus entanglement protocol.

A final aspect of entanglement generation, which has not been the focus of this work, is the need for a high source efficiency, e.g. more than 50% for one-way quantum computing [135] and more than 95% in the photonic repeater scheme in Ref. [11]. High efficiency will require the adoption of a one-sided PCW to remove the 50% directionality loss currently suffered and should be combined with deterministic QD positioning. The efficiency of our waveguide platform is discussed in greater detail in Ref. [18], where an  $> 84\%$  on-chip efficiency is demonstrated. Additionally, quantum repeater schemes would likely require conversion to the 1550 nm telecom wavelength. In this regard, time-bin photons from a waveguide embedded QD are attractive, as the conversion can take place on-chip [67].

As a final summary, this work has demonstrated a novel approach to a solid-state spin-photon interface, which may enable deterministic spin-multi-photon entanglement. Many challenges lie ahead in scaling up the entanglement source, and it will be exciting to follow what the future brings.



## A | FPGA Architecture

A field-programmable gate array (FPGA) is used to synchronise the optical modulators, MW switches and time tagger with the Mira laser. Specifically, we use a Terasic De-10 Nano development board containing an Intel Cyclone V FPGA.

FPGAs are incredibly powerful but difficult<sup>1</sup> to program. The FPGA architecture was developed completely from scratch and will now be described in moderate detail, as it solves very common synchronisation problems in quantum optics experiments. The FPGA used here costs \$130 but drives 8 outputs and can be expanded to a far greater number.

The main architecture is summarised in figure A.1. The FPGA is interfaced with a PC, which may reconfigure FPGA registers to change the functionality. The influence of registers is denoted by red text and "Data" in figure A.1. Two different clock

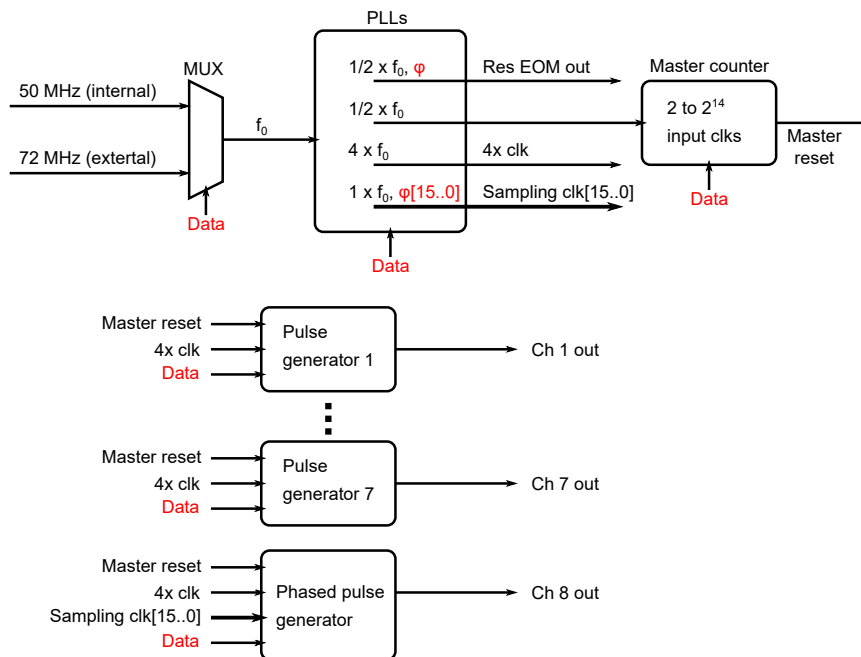


**Figure A.1:** Simplified FPGA architecture block diagram excluding modules for PC communication. Abbreviations: Multiplexer (MUX), Phase locked loop (PLL).

<sup>1</sup>Horrible

signals can be used as the base clock  $f_0$ : An internal 50 MHz clock or an external clock signal which in our case is the 72 MHz Mira pulse train. The base clock then drives several phase-locked loops (PLLs). PLLs are one of the main attractions of FPGA for experimental synchronisation as they can derive new clock signals with multiplied frequencies and well-defined phases. Two clocks at frequency  $f_0/2$  are derived from the base clock. The first clock has a variable phase and can be used to drive the resonant EOM in the TBI (section 8.5). The second clock drives the master counter. The master counter determines the duration of the pulse sequence by counting the number of  $f_0/2$  clocks. Once the max count is reached (as defined by a register), the master counter sends out a reset pulse. This ensures that all pulse generators are reset. In addition, the PLLs create a  $4 \times f_0$  clock and 16 independent  $f_0$  clocks with individually programmable phases, which are used for pulse generation.

### A.0.1 PULSE GENERATORS

The design contains 7 pulse generators, which are described in figure A.2. Each generator is capable of producing 8 square pulses within a pulse sequence by using a counting architecture. A counter is incremented by the  $4x$  clock and reset by the master reset. The value of the 16 bit counter  $c$  is distributed to each of the 8 pulse nodes where it is compared against the  $a$  and  $b$  registers on the rising edge of the  $4x$  clock.  $a$  and  $b$  are 16 bit registers indicating the counts at which a node goes high and low (see waveforms in figure A.2). The outputs of all the nodes are combined by an OR gate, allowing a single pulse generator to output 8 square pulses. The timing resolution is limited to  $1/(4f_0)$  and the maximum pulse sequence duration is  $(2^{16} - 1)/(4f_0)$ . For  $f_0 = 72$  MHz, this equates a 3.47 ns resolution and 228  $\mu$ s maximum duration. This approach does not use a lot of logic and is scalable.

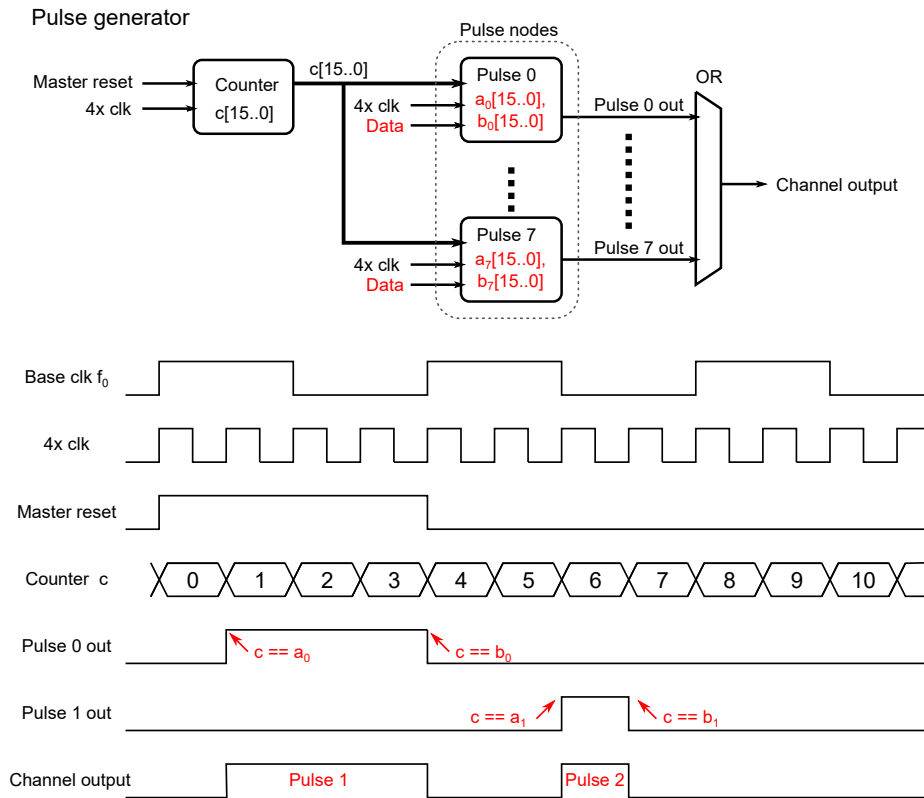


**Figure A.2:** Architecture of a pulse generator. A counter feeds a count bus to 8 pulse nodes, which set their outputs high and low at certain count values defined by registers. The waveform show an example for creating an output with two pulses.

### A.0.2 PHASED PULSE GENERATORS

The phased pulse generator builds upon the principle of the normal pulse generator but uses resampling to improve temporal resolution. First, a pulse node creates a square pulse (second line in (figure A.2)). Initially, the output is zero. On a rising edge of the sampling  $\text{clk}[0]$ , the value of the pulse node is sampled (blue lines in figure A.2). If high, the output is set high, and the sampling  $\text{clk}[1]$  is given the role of sampling. Once the pulse node is found to be low at a rising edge of sampling  $\text{clk}[1]$ , the output is set low and sampling  $\text{clk}[0]$  returns to the role of sampling the pulse node. Hence, we are using two clock signals to resample the output of a slow pulse. This allows the generation of long pulses with a temporal resolution set by the sampling clocks. This resolution is set by the internal PLL clock, which runs at  $12 \times f_0$  and can lock to 8 phase values. Hence, a resolution of  $1/(12 \times 8 \times f_0) = 145 \text{ ps}$  is achieved for  $f_0 = 72 \text{ MHz}$ . The PLL phase is highly repeatable and allows very linear stepping of the duration of the final pulses. The big disadvantage is the need to calibrate the PLL phases to achieve a specific pulse duration. This is in part due to random propagation delays between the PLL and the resampling logic created from synthesizing the design.

Similar to the normal pulse generator, 8 pulses are combined with an OR gate. However, the number of pulses is limited by the FPGA's PLL resources (5 PLLs with 9 outputs each), as each pulse requires 2 clocks.

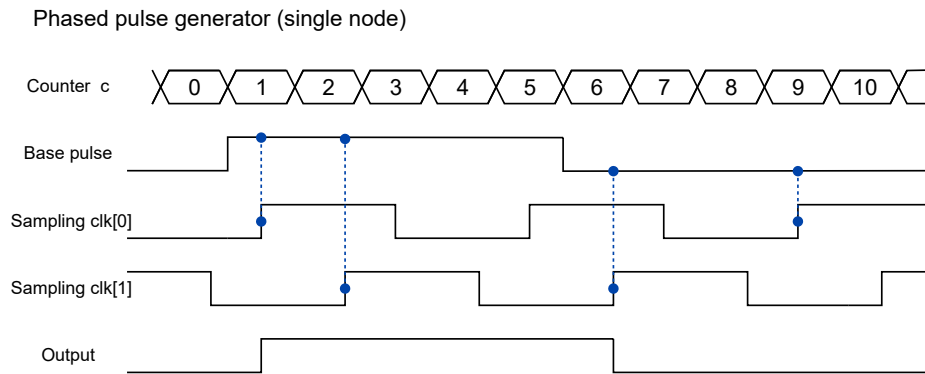


**Figure A.3:** Waveform explanation of the phased pulse generator. Pulse 0 corresponds to Pulse 0 in figure A.2. This pulse is sampled (blue lines) by two phase shiftable sampling clocks, creating a new output with higher temporal resolution.

### A.0.3 PERFORMANCE METRICS

The FPGA produces a 3.3 V output with 0.7 ns rise time, presumably limited by the electrical properties of the header pins used on the board. The timing jitter between two pulse generators is 20 ps RMS, while the jitter between the phased pulse generator and a normal pulse generator is 40 ps RMS.

## B | MW Phase Calibration

The phase shift induced by the variable phase shifter in the MW setup (figure 6.4) is calibrated by switching Switch 1 from input 2 to input 1 and measuring the MW signal directly on a fast oscilloscope. Figure B.1 shows the MW signal measured with a 20 GS/s, 4 GHz bandwidth oscilloscope. The MW signal decreases in amplitude during switching and re-emerges with a new phase dependent on the programmable phase shifter. The MW signal is fit with a sinusoid before and after the switch activation to estimate the phase change. The phase shifter contains a variable attenuator, which has been adjusted to keep the MW amplitude constant.

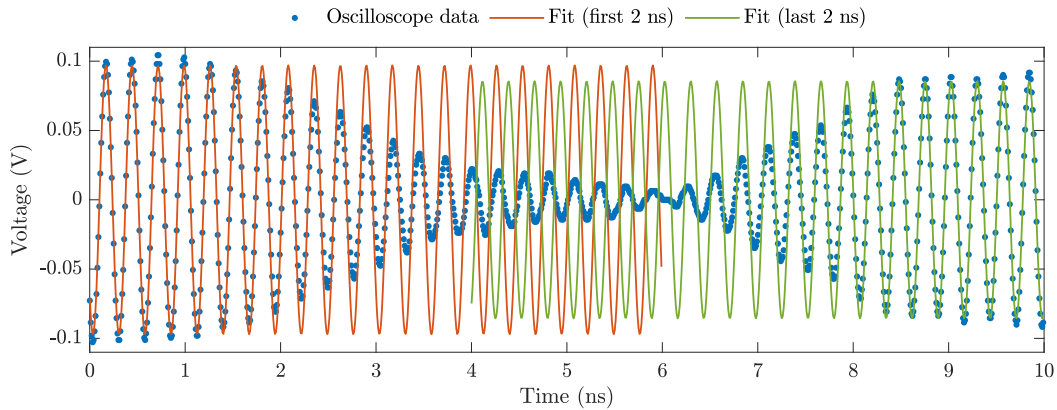


**Figure B.1:** MW signal from Switch 1 measured on an oscilloscope. The fits use data in the first and last 2 ns of the trace.

This calibration measurement is repeated for different values of the device phase, see figure B.2a. Due to dispersion in the MW transmission lines, the phase shift becomes frequency-dependent. This dependence is measured in figure B.2b. These two calibrations allow determining the device phase needed to achieve a target phase for a given frequency.

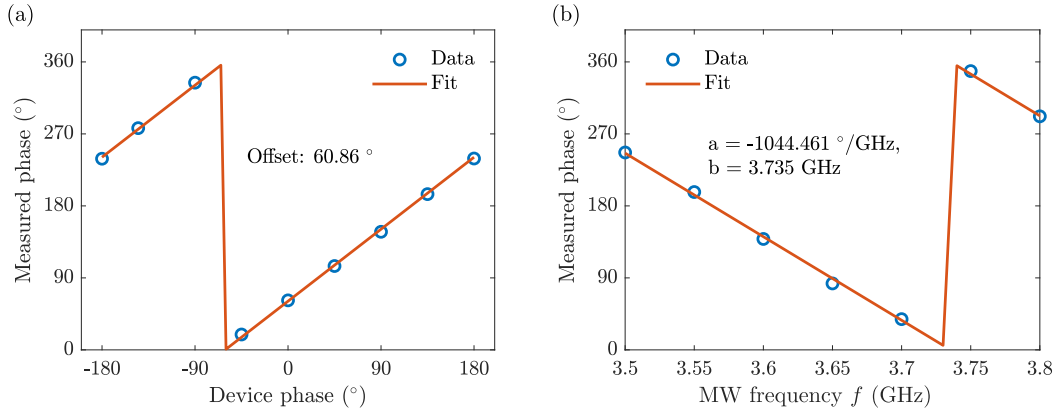


**Figure B.2:** (a) Measured phase shift as a function of device phase. Fit model:  $\phi_{meas} = (\phi_{device} + \phi_0) \bmod 360^{\circ}$ . (b) Measured phase shift as a function of MW frequency  $f$ . Fit model:  $\phi_{meas} = a \cdot (f - b) \bmod 360^{\circ}$ .

## C | Single Shot Readout

The derivation of single-shot readout already published in Ref. [32] is now repeated. This follows the approach in Ref. [136]. Consider the level structure in figure C.1

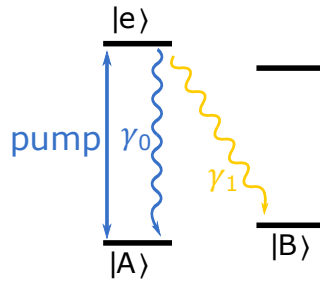


**Figure C.1:** Ideal level diagram for single shot readout with a resonance fluorescence measurement. If the QD spin state is  $|A\rangle$ , fluorescence is generated by driving  $|A\rangle \leftrightarrow |e\rangle$  until the QD decays to  $|B\rangle$  after which no additional photons are emitted.

The readout is performed by pumping  $|A\rangle \leftrightarrow |e\rangle$  and counting the number of detected photons  $N_d$ . If  $N_d > k$  we conclude  $|\psi\rangle = |A\rangle$  where  $k$  is an integer threshold. If we detect  $N_d \leq k$  we conclude  $|\psi\rangle = |B\rangle$ . The single shot readout fidelity is then

$$F_{ss} = P(N_d > k|A)P(A) + P(N_d \leq k|B)P(B), \quad (\text{C.1})$$

where  $P(\cdot|\cdot)$  denotes conditional probability and  $P(A)$  and  $P(B)$  are the initial occupation probabilities of  $|A\rangle$  and  $|B\rangle$ , respectively. Assuming no prior information of the spin state,  $P(A) = P(B) = 1/2$ , and zero fluorescence emitted given  $|\psi\rangle = |B\rangle$ , the best performing threshold is trivially  $k = 0$  and the fidelity reduces to

$$F_{ss} = \frac{1}{2} + \frac{1}{2}P(N_d > 0|A) = 1 - \frac{1}{2}P(N_d = 0|A). \quad (\text{C.2})$$

$P(N_d = 0|A)$  can be computed by first calculating the probability mass function of the number of emitted photons,  $P(N_e)$ . When the excited state emits a photon the population returns to  $|A\rangle$  with probability  $P_r = \frac{\gamma_y}{\gamma_0} = \frac{C}{1+C}$  where  $C$  is the cyclicity. We assume that the photon emitted on  $|e\rangle \leftrightarrow |B\rangle$  is always lost, which is the case of an ideally coupled QD,  $\beta_{\perp} = 0$ . The probability to emit  $N_e$  photons is then equal to the probability of decaying  $N_e$  consecutive times to  $|A\rangle$  times the probability of

decaying to  $|B\rangle$ :

$$P(N_e) = (1 - P_r)(P_r)^{N_e}. \quad (\text{C.3})$$

The probability mass function for the number of detected photons  $P(N_d)$  is given by

$$P(N_d) = \sum_{N_e \geq N_d}^{\infty} B(N_d; \eta, N_e) P(N_e), \quad (\text{C.4})$$

where

$$B(N_d; \eta, N_e) = \eta^{N_d} (1 - \eta)^{N_e - N_d} \binom{N_e}{N_d} \quad (\text{C.5})$$

is the binomial probability of detecting  $N_d$  photons given  $N_e$  emissions and total detection efficiency  $\eta$ . For  $N_d = 0$  the expression becomes

$$P(N_d = 0) = \sum_{N_e=0}^{\infty} (1 - P_r) P_r^{N_e} (1 - \eta)^{N_e} = \frac{1 - P_r}{1 - P_r(1 - \eta)} = \frac{1}{1 + C\eta}. \quad (\text{C.6})$$

Substituting into (C.2) gives the final fidelity

$$F_{ss} = 1 - \frac{1}{2} \left( \frac{1}{1 + C\eta} \right). \quad (\text{C.7})$$

The fidelity is fundamentally limited by the chance of not detecting a photon given  $|A\rangle$ . Even if  $\eta = 1$  the QD may decay via the undetected  $|e\rangle \rightarrow |B\rangle$  transition.

## D | Adiabatic Elimination

We will now explain the adiabatic approximation used to derive the effective Raman dynamics. The derivation closely follows the supplementary material of Ref. [77]. We follow the level scheme in figure D.1 where a laser detuned by  $\Delta_r$  drives both optical  $\Lambda$ -systems. Optical spin control generally operates in the regime  $\Delta_r \gg \omega_g, \omega_t, \gamma$  where both  $\Lambda$ -systems contribute equally to the coherent evolution.

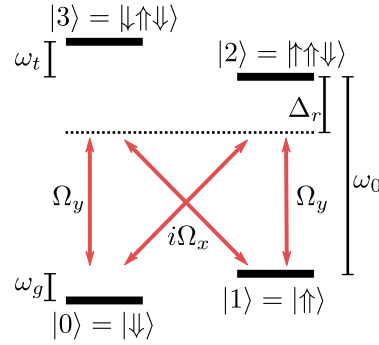


**Figure D.1:** Level scheme of a positively charged QD in Voigt geometry. A detuned laser drives both  $\Lambda$ -systems, thereby coupling the spin ground states.

The Hamiltonian is given by

$$\hat{H} = \hat{H}_0 + \hat{H}_l \quad (\text{D.1})$$

$$\begin{aligned} &= -\omega_g |0\rangle\langle 0| + \omega_0 |2\rangle\langle 2| + (\omega_0 + \omega_t) |3\rangle\langle 3| \\ &+ \frac{\Omega_y(t)}{2} e^{i\omega_l t} (|3\rangle\langle 0| + |2\rangle\langle 1|) + h.c. \\ &+ \frac{-i\Omega_x(t)}{2} e^{i\omega_l t} (|2\rangle\langle 0| + |3\rangle\langle 1|) + h.c. \end{aligned} \quad (\text{D.2})$$

where  $\omega_0$  is the trion energy,  $\omega_l$  is the laser optical frequency and  $\Omega_x(\Omega_y)$  is the Rabi frequency of the x(y) polarised transitions. We have chosen the  $|1\rangle$  state to have zero energy. The time dependence of (D.2) can be removed by switching to the rotation frame defined by the unitary

$$\hat{U} = |0\rangle\langle 0| + |1\rangle\langle 1| + e^{-i\omega_l t} |2\rangle\langle 2| + e^{-i\omega_l t} |3\rangle\langle 3| \quad (\text{D.3})$$

giving the transformed hamiltonian

$$\tilde{H} = \hat{U}^\dagger \hat{H} \hat{U} + i \frac{d\hat{U}^\dagger}{dt} \hat{U} \quad (\text{D.4})$$

$$\begin{aligned} &= -\omega_g |0\rangle\langle 0| + \Delta_r |2\rangle\langle 2| + (\omega_t + \Delta_r) |3\rangle\langle 3| \\ &\quad + \frac{\Omega_y(t)}{2} (|0\rangle\langle 3| + |1\rangle\langle 2|) + h.c. \\ &\quad + \frac{-i\Omega_x(t)}{2} (|0\rangle\langle 2| + |1\rangle\langle 3|) + h.c. \end{aligned} \quad (\text{D.5})$$

where  $\Delta_r = \omega_0 - \omega_l$ . We can write the system wavefunction as

$$|\psi\rangle = c_0 |0\rangle + c_1 |1\rangle + c_2 |2\rangle + c_3 |3\rangle, \quad (\text{D.6})$$

where the amplitudes' time dependence has been omitted for brevity. The trion evolution can be found by solving the Schrödinger equation

$$i\dot{c}_2 = \langle 2 | \tilde{H} | \psi \rangle \quad (\text{D.7})$$

$$\Rightarrow \dot{c}_2 = -i\Delta_r c_2 - i\frac{\Omega_y^*}{2} c_1 + \frac{\Omega_x^*}{2} c_0. \quad (\text{D.8})$$

$$i\dot{c}_3 = \langle 3 | \tilde{H} | \psi \rangle \quad (\text{D.9})$$

$$\Rightarrow \dot{c}_3 = -i(\Delta_r + \omega_t) c_3 + \frac{\Omega_x^*}{2} c_1 - i\frac{\Omega_y^*}{2} c_0. \quad (\text{D.10})$$

What follows is an adiabatic elimination of the trion states by setting  $\dot{c}_2 = \dot{c}_3 = 0$ . This is justified in the limit  $\Delta_r \gg \Omega_x, \Omega_y, \Omega_x^*, \Omega_y^*$  [77]. Equations (D.8) and (D.10) can then be solved for  $c_2$  and  $c_3$  yielding

$$c_2 = \frac{-\Omega_y^* c_1 - i\Omega_x^* c_0}{2\Delta_r}, \quad (\text{D.11})$$

$$c_3 = \frac{-i\Omega_y^* c_1 - \Omega_x^* c_0}{2(\Delta_r + \omega_t)}. \quad (\text{D.12})$$

The ground states can now be solved following using the same method as in (D.8) and (D.10):

$$\dot{c}_0 = -\omega_g c_0 - i\frac{\Omega_x}{2} c_2 - i\frac{\Omega_y}{2} c_3, \quad (\text{D.13})$$

$$\dot{c}_1 = -i\frac{\Omega_y}{2} c_2 - i\frac{\Omega_x}{2} c_3. \quad (\text{D.14})$$

Inserting the steady state amplitudes from (D.11) and (D.12) into  $\dot{c}_0$  and  $\dot{c}_1$  yields the final equations of motion

$$\dot{c}_0 = i \left( \frac{|\Omega_x|^2}{4\Delta_r} + \frac{|\Omega_y|^2}{4(\Delta_r + \omega_t)} + \omega_g \right) c_0 + \left( \frac{\Omega_x \Omega_y^*}{4\Delta_r} - \frac{\Omega_x^* \Omega_y}{4(\Delta_r + \omega_t)} \right) c_1 \quad (\text{D.15})$$

$$\dot{c}_1 = i \left( \frac{|\Omega_x|^2}{4(\Delta_r + \omega_t)} + \frac{|\Omega_y|^2}{4\Delta_r} \right) c_1 + \left( -\frac{\Omega_x^* \Omega_y}{4\Delta_r} + \frac{\Omega_x \Omega_y^*}{4(\Delta_r + \omega_t)} \right) c_0 \quad (\text{D.16})$$

This equations of motion correspond to the effective Hamiltonian

$$\hat{H}_{eff} = \begin{bmatrix} -\frac{|\Omega_x|^2}{4\Delta_r} - \frac{|\Omega_y|^2}{4(\Delta_r + \omega_t)} - \omega_g & i\frac{\Omega_x\Omega_y^*}{4\Delta_r} - i\frac{\Omega_x^*\Omega_y}{4(\Delta_r + \omega_t)} \\ -i\frac{\Omega_x^*\Omega_y}{4\Delta_r} + i\frac{\Omega_x\Omega_y^*}{4(\Delta_r + \omega_t)} & -\frac{|\Omega_y|^2}{4\Delta_r} - \frac{|\Omega_x|^2}{4(\Delta_r + \omega_t)} \end{bmatrix} \quad (D.17)$$

By adding  $\frac{|\Omega_y|^2}{4\Delta_r} + \frac{|\Omega_x|^2}{4(\Delta_r + \omega_t)}$  to the diagonal we achieve the effective Hamiltonian

$$\hat{H}_{eff2} = \begin{bmatrix} \omega_{AC} - \omega_g & \frac{\Omega_{eff}}{2} \\ \frac{\Omega_{eff}^*}{2} & 0 \end{bmatrix} \quad (D.18)$$

where the effective ground state coupling  $\Omega_{eff}$  and AC-stark shift are given by

$$\Omega_{eff} = \frac{i}{2} \left( \frac{\Omega_x\Omega_y^*}{\Delta_r} - \frac{\Omega_x^*\Omega_y}{(\Delta_r + \omega_t)} \right) \Delta_r \underset{\approx}{\approx} \omega_t i \frac{\text{Im}\{\Omega_x\Omega_y^*\}}{\Delta_r}, \quad (D.19)$$

$$\omega_{AC} = \frac{\omega_t}{4\Delta_r(\Delta_r + \omega_t)} (|\Omega_y|^2 - |\Omega_x|^2). \quad (D.20)$$



## E | Jones Matrices

Below are the Jones matrices for a quarter-wave plate (QWP), half-wave plate (HWP) and linear polariser (pol).  $\theta$  is angle of the fast axis wrt. horizontal.  $M_{ARB}$  represents a birefringent material with phase retardation  $\eta$ .

$$M_{qwp}(\theta) = e^{-i\pi/4} \begin{bmatrix} \cos^2(\theta) + i \sin^2(\theta) & (1 - i) \sin(\theta) \cos(\theta) \\ (1 - i) \sin(\theta) \cos(\theta) & i \cos^2(\theta) + \sin^2(\theta) \end{bmatrix} \quad (\text{E.1})$$

$$M_{hwp}(\theta) = e^{-i\pi/2} \begin{bmatrix} \cos^2(\theta) - \sin^2(\theta) & 2 \sin(\theta) \cos(\theta) \\ 2 \sin(\theta) \cos(\theta) & \sin^2(\theta) - \cos^2(\theta) \end{bmatrix} \quad (\text{E.2})$$

$$M_{pol}(\theta) = \begin{bmatrix} \cos^2(\theta) & \sin(\theta) \cos(\theta) \\ \sin(\theta) \cos(\theta) & \sin^2(\theta) \end{bmatrix} \quad (\text{E.3})$$

$$M_{ARB}(\theta, \eta) = e^{-i\eta/2} \begin{bmatrix} \cos^2(\theta) + e^{i\eta} \sin^2(\theta) & (1 - e^{i\eta}) \sin(\theta) \cos(\theta) \\ (1 - e^{i\eta}) \sin(\theta) \cos(\theta) & e^{i\eta} \cos^2(\theta) + \sin^2(\theta) \end{bmatrix} \quad (\text{E.4})$$



## F | EOM Pulse Sequence Alignment

This appendix details the rotation pulse sequences for the entanglement experiment and the considerations behind their construction. Figure F.1 shows histograms of the four first pulse sequences in table 9.1. These pulse sequences have been manually optimised in order to meet the following requirements:

1. The middle pulse  $R_2$  must be placed in-between the early and late optical excitation.
2. The inter-pulse delays for reading the spin in  $|+\rangle$  must be symmetric to ensure spin echo.
3. Rotation pulses must have the correct pulse area.

Requirement 3 relates to ensuring the correct energy in each pulse. The energy is related to the mean optical rotation power  $\langle P_{rot} \rangle$  as measured by a power meter through

$$U_i = \langle P_{rot} \rangle T_{rep} D_i, \quad (\text{F.1})$$

where  $U_i$  is the energy in the  $i$ -th rotation pulse,  $T_{rep}$  is the repetition rate and  $D_i$  is the dutycycle of the  $i$ -th pulse. As  $\langle P_{rot} \rangle$  and  $T_{rep}$  are kept fixed,  $U_i$  is tuned through the duty cycle.  $D_i$  is measured by

$$D_i = \frac{\text{Counts in } R_i}{\text{Total histogram counts}}, \quad (\text{F.2})$$

using a histogram measurement of the pulse sequence. The rotation pulses and buffer pulse are then optimised to ensure the correct values of  $D_1, D_2$  and  $D_3$ . The final duty cycles are shown in figure F.2 with the worst pulse deviating 3% from its ideal value. Note that the bars do not sum to unity as EOM leakage ( $\approx 1/1000$ ) contributes about 2% of the total counts in the full histogram. This leakage must be included as it contributes to the measured  $\langle P_{rot} \rangle$ .

Perfect optimisation of pulse areas is challenging, as our MW setup only allows variation of the pulse durations in 144 ps increments. Furthermore, the MW switch used for intensity modulation is imperfect, leading to pulse shape distortion when pulses follow in rapid succession. This is evident from the difference between the  $R_1$  and  $R_3$  pulse shapes in the  $|+\rangle$  sequence. The final pulse widths as quantified by a FWHM are 6.89 ns for  $R_2$  and 3.75 ns for a  $R_1 \pi/2$  pulse. The pulse delays for the  $|+\rangle$  sequence are given in figure F.1 and only differ by 0.19 ns which is negligible compared to  $T_2^*$ .

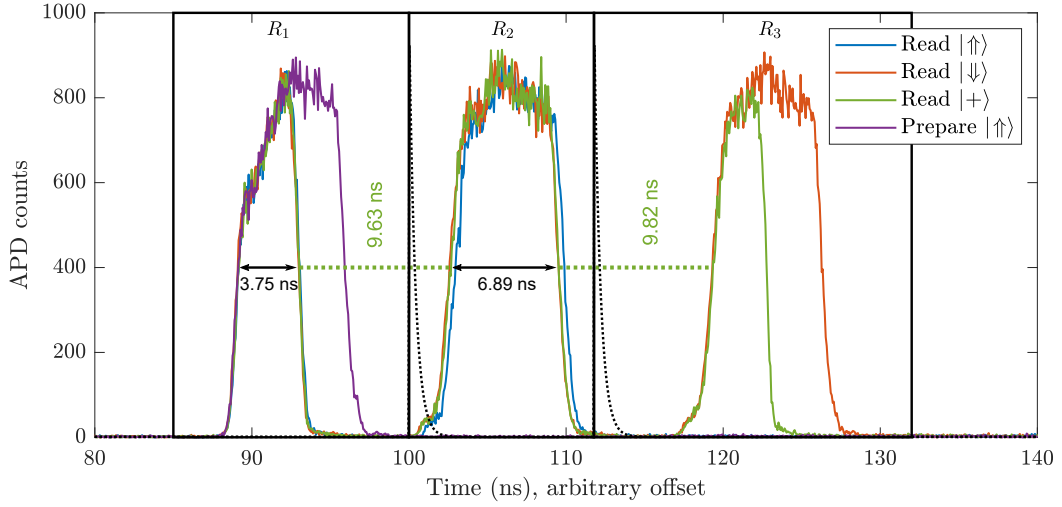


**Figure F.1:** Histograms of rotation pulse sequences recorded by connecting the EOM output to an APD. The time axis is shifted with respect to entanglement measurements due to the different detection setup. The black boxes indicate the detection windows used for pulse area estimation. The dotted lines indicate the  $e^{-\gamma_0 t}$  photon envelope. Buffer pulses beginning at 420 ns are not shown.

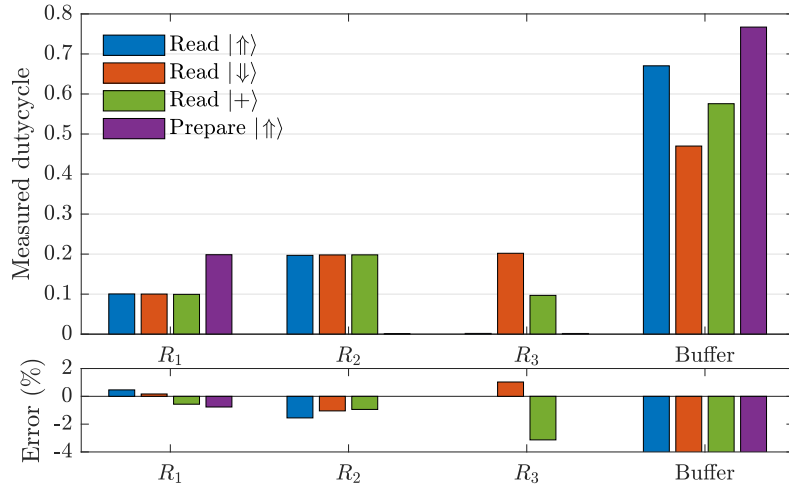


**Figure F.2:** Pulse areas normalised to total rotation power. The pulses have been optimised to reach 10% and 20% of the total power for a  $\pi/2$  and  $\pi$  pulse, respectively. Bottom plot shows the relative deviation from ideal dutycycle.

## G | Optical Loss Budget

Table G.1 shows an estimated loss budget for the entanglement experiment and predicts a total loss of 20.65 dB. In contrast, we estimated a 0.282% (25.5 dB) single photon detection efficiency in section 9.3.4, and thus have 5 dB of unaccounted loss. This may be related to the shallow etch grating couplers, which were not fully characterised on our sample. Imperfect fabrication of the grating couplers or imperfect mode matching to the collection fibre could likely be responsible for additional losses. The main sources of loss relate to the two-sided nature of the PCW and the 50/50 BS<sub>1</sub> in figure 3.4a. Additionally, the grating couplers may be improved with the use of a DBR mirror below the grating as discussed in Ref. [18].

Loss source	Efficiency (%)	Loss (dB)	Source/comment
<b>Sample</b>			
XP efficiency	75	1.25	Figure 4.8
Zero phonon line	90	0.46	Educated guess
PCW $\beta_{\parallel}$	88	0.56	(5.27)
Two-sided PCW	50	3.01	Equal left/right coupling
Nanobeam interfaces	96	0.18	[18]
Grating coupler	60	2.22	[18]
Pi-pulse efficiency	90	0.46	Educated guess
Sum		<b>8.13</b>	
<b>Cryostat optics</b>			
Optical insert	75	1.25	Measured
50/50 BS1	49	3.10	Measured
Polarisation optics	85	0.71	Measured
Collection fiber coupler	60	2.22	[18]
Sum		<b>7.27</b>	
<b>Interferometer</b>			
Two fibre matings	76	1.19	Measured
Etalon filtering	73	1.37	Measured
Interferometer optics	80	0.97	Measured
Average fibre coupling	84	0.76	Measured
SNSPD detectors	80	0.97	Assuming unpolarised input
Sum		<b>5.25</b>	
Total loss		<b>20.65</b>	

**Table G.1:** Predicted loss budget of the entanglement experiment.

## Bibliography

- [1] J. S. Bell, “On the Einstein Podolsky Rosen Paradox,” *Physics Physique Fizika*, vol. 1, pp. 195–200, 1964.
- [2] B. Hensen, H. Bernien, A. E. Dreaú, A. Reiserer, N. Kalb, M. S. Blok, J. Ruitenberg, R. F. Vermeulen, R. N. Schouten, C. Abellán, W. Amaya, V. Pruneri, M. W. Mitchell, M. Markham, D. J. Twitchen, D. Elkouss, S. Wehner, T. H. Taminiau, and R. Hanson, “Loophole-free Bell inequality violation using electron spins separated by 1.3 kilometres,” *Nature*, vol. 526, no. 7575, pp. 682–686, 2015.
- [3] D. Deutsch and R. Jozsa, “Rapid solution of problems by quantum computation,” *Proc. R. Soc. Lond. A*, vol. 439, pp. 553–558, 1992.
- [4] L. K. Grover, “A fast quantum mechanical algorithm for database search,” *Proceedings of the Twenty-Eighth Annual ACM Symposium on Theory of Computing*, pp. 212–219, 1996.
- [5] P. Shor, “Algorithms for quantum computation: discrete logarithms and factoring,” *Proceedings 35th Annual Symposium on Foundations of Computer Science*, pp. 124–134, 1994.
- [6] R. L. Rivest, A. Shamir, and L. Adleman, “A Method for Obtaining Digital Signatures and Public- Key Cryptosystems,” *Commun. ACM*, vol. 21, no. 2, pp. 120–126, 1978.
- [7] C. H. Bennett and G. Brassard, “Quantum cryptography: Public key distribution and coin tossing,” *Theor. Comput. Sci.*, vol. 560, pp. 7–11, 2014.
- [8] H. J. Kimble, “The quantum internet,” *Nature*, vol. 453, no. 7198, pp. 1023–1030, 2008.
- [9] L. M. Duan, M. D. Lukin, J. I. Cirac, and P. Zoller, “Long-distance quantum communication with atomic ensembles and linear optics,” *Nature*, vol. 414, no. 6862, pp. 413–418, 2001.
- [10] K. Azuma, K. Tamaki, and H.-K. Lo, “All-photonic quantum repeaters,” *Nat. Commun.*, vol. 6, no. 1, p. 6787, 2015.
- [11] J. Borregaard, H. Pichler, T. Schröder, M. D. Lukin, P. Lodahl, and A. S. Sørensen, “One-way quantum repeater based on near-deterministic photon-emitter interfaces,” *Phys. Rev. X*, vol. 10, no. 2, p. 021071, 2019.

- [12] R. Raussendorf and H. J. Briegel, “A One-Way Quantum Computer,” *Phys. Rev. Lett.*, vol. 86, no. 22, pp. 5188–5191, 2001.
- [13] H. S. Zhong, Y. Li, W. Li, L. C. Peng, Z. E. Su, Y. Hu, Y. M. He, X. Ding, W. Zhang, H. Li, L. Zhang, Z. Wang, L. You, X. L. Wang, X. Jiang, L. Li, Y. A. Chen, N. L. Liu, C. Y. Lu, and J. W. Pan, “12-Photon Entanglement and Scalable Scattershot Boson Sampling with Optimal Entangled-Photon Pairs from Parametric Down-Conversion,” *Phys. Rev. Lett.*, vol. 121, no. 25, p. 250505, 2018.
- [14] D. Leibfried, R. Blatt, C. Monroe, and D. Wineland, “Quantum dynamics of single trapped ions,” *Rev. Mod. Phys.*, vol. 75, no. 1, pp. 281–324, 2003.
- [15] M. W. Doherty, N. B. Manson, P. Delaney, F. Jelezko, J. Wrachtrup, and L. C. Hollenberg, “The nitrogen-vacancy colour centre in diamond,” *Phys. Rep.*, vol. 528, no. 1, pp. 1–45, 2013.
- [16] P. Lodahl, S. Mahmoodian, and S. Stobbe, “Interfacing single photons and single quantum dots with photonic nanostructures,” *Rev. Mod. Phys.*, vol. 87, no. 2, pp. 347–400, 2015.
- [17] H. Thyrestrup, G. Kiršanske, H. Le Jeannic, T. Pregnolato, L. Zhai, L. Raahauge, L. Midolo, N. Rotenberg, A. Javadi, R. Schott, A. D. Wieck, A. Ludwig, M. C. Löbl, I. Söllner, R. J. Warburton, and P. Lodahl, “Quantum Optics with Near-Lifetime-Limited Quantum-Dot Transitions in a Nanophotonic Waveguide,” *Nano Lett.*, vol. 18, no. 3, pp. 1801–1806, 2018.
- [18] R. Uppu, F. T. Pedersen, Y. Wang, C. T. Olesen, C. Papon, X. Zhou, L. Midolo, S. Scholz, A. D. Wieck, A. Ludwig, and P. Lodahl, “Scalable integrated single-photon source,” *Sci. Adv.*, vol. 6, p. eabc8268, 2020.
- [19] N. H. Lindner and T. Rudolph, “Proposal for pulsed On-demand sources of photonic cluster state strings,” *Phys. Rev. Lett.*, vol. 103, no. 11, p. 113602, 2009.
- [20] I. Schwartz, D. Cogan, E. R. Schmidgall, Y. Don, L. Gantz, O. Kenneth, N. H. Lindner, and D. Gershoni, “Deterministic generation of a cluster state of entangled photons,” *Science*, vol. 49, no. 7285, pp. 1804–1807, 2016.
- [21] R. J. Warburton, “Single spins in self-assembled quantum dots,” *Nat. Mater.*, vol. 12, no. 6, pp. 483–493, 2013.
- [22] G. A. Narvaez, G. Bester, and A. Zunger, “Carrier relaxation mechanisms in self-assembled (In,Ga) As GaAs quantum dots: Efficient P→S Auger relaxation of electrons,” *Phys. Rev. B - Condens. Matter Mater. Phys.*, vol. 74, no. 7, p. 075403, 2006.
- [23] M. C. Löbl, S. Scholz, I. Söllner, J. Ritzmann, T. Denneulin, A. Kovács, B. E. Kardynał, A. D. Wieck, A. Ludwig, and R. J. Warburton, “Excitons in InGaAs quantum dots without electron wetting layer states,” *Commun. Phys.*, vol. 2, no. 1, p. 93, 2019.

- [24] J. H. Prechtel, A. V. Kuhlmann, J. Houel, A. Ludwig, S. R. Valentin, A. D. Wieck, and R. J. Warburton, “Decoupling a hole spin qubit from the nuclear spins,” *Nat. Mater.*, vol. 15, no. 9, pp. 981–986, 2016.
- [25] P. Michler, *Quantum Dots for Quantum Information Technologies*. Springer International Publishing, 2017.
- [26] M. Bayer, G. Ortner, O. Stern, A. Kuther, A. A. Gorbunov, A. Forchel, P. Hawrylak, S. Fafard, K. Hinzer, T. L. Reinecke, S. N. Walck, J. P. Reithmaier, F. Klopff, and F. Schäfer, “Fine structure of neutral and charged excitons in self-assembled In(Ga)As/(Al)GaAs quantum dots,” *Phys. Rev. B*, vol. 65, no. 19, p. 195315, 2002.
- [27] D. Huber, M. Reindl, S. F. Covre Da Silva, C. Schimpf, J. Martín-Sánchez, H. Huang, G. Piredda, J. Edlinger, A. Rastelli, and R. Trotta, “Strain-Tunable GaAs Quantum Dot: A Nearly Dephasing-Free Source of Entangled Photon Pairs on Demand,” *Phys. Rev. Lett.*, vol. 121, no. 3, p. 33902, 2018.
- [28] A. V. Koudinov, I. A. Akimov, Y. G. Kusrayev, and F. Henneberger, “Optical and magnetic anisotropies of the hole states in Stranski-Krastanov quantum dots,” *Phys. Rev. B*, vol. 70, p. 241305(R), 2004.
- [29] J. H. Prechtel, F. Maier, J. Houel, A. V. Kuhlmann, A. Ludwig, A. D. Wieck, D. Loss, and R. J. Warburton, “Electrically tunable hole g factor of an optically active quantum dot for fast spin rotations,” *Phys. Rev. B - Condens. Matter Mater. Phys.*, vol. 91, no. 16, p. 165304, 2015.
- [30] J. Dreiser, M. Atatüre, C. Galland, T. Müller, A. Badolato, and A. Imamoglu, “Optical investigations of quantum dot spin dynamics as a function of external electric and magnetic fields,” *Phys. Rev. B*, vol. 77, no. 7, p. 075317, 2008.
- [31] D. A. Steck, “Quantum and Atom Optics.” <http://steck.us/teaching>, 2017.
- [32] M. H. Appel, A. Tiranov, A. Javadi, M. C. Löbl, Y. Wang, S. Scholz, A. D. Wieck, A. Ludwig, R. J. Warburton, and P. Lodahl, “Coherent Spin-Photon Interface with Waveguide Induced Cycling Transitions,” *Phys. Rev. Lett.*, vol. 126, no. 1, p. 013602, 2021.
- [33] P. Tighineanu, C. L. Dreeßen, C. Flindt, P. Lodahl, and A. S. Sørensen, “Phonon Decoherence of Quantum Dots in Photonic Structures: Broadening of the Zero-Phonon Line and the Role of Dimensionality,” *Phys. Rev. Lett.*, vol. 120, no. 25, p. 257401, 2018.
- [34] A. V. Kuhlmann, J. Houel, A. Ludwig, L. Greuter, D. Reuter, A. D. Wieck, M. Poggio, and R. J. Warburton, “Charge noise and spin noise in a semiconductor quantum device,” *Nat. Phys.*, vol. 9, no. 9, pp. 570–575, 2013.
- [35] T. O. T. H. E. Voigt and B. Review, “Empirical fits to the Voigt line width: A brief review,” *J. Quant. Spectrosc. Radiat. Transf.*, vol. 17, pp. 233–236, 1977.

- [36] J. Sakurai and J. J. Napolitano, *Modern Quantum Mechanics*. Pearson, 2nd ed., 2013.
- [37] B. Urbaszek, X. Marie, T. Amand, O. Krebs, P. Voisin, P. Maletinsky, A. Högele, and A. Imamoglu, “Nuclear spin physics in quantum dots: An optical investigation,” *Rev. Mod. Phys.*, vol. 85, no. 1, pp. 79–133, 2013.
- [38] A. Bechtold, D. Rauch, F. Li, T. Simmet, P.-L. Ardel, A. Regler, K. Müller, N. A. Sinitsyn, and J. J. Finley, “Three-stage decoherence dynamics of an electron spin qubit in an optically active quantum dot,” *Nat. Phys.*, vol. 11, pp. 1005–1009, 2015.
- [39] G. Éthier-Majcher, D. Gangloff, R. Stockill, E. Clarke, M. Hugues, C. Le Gall, and M. Atatüre, “Improving a Solid-State Qubit through an Engineered Mesoscopic Environment,” *Phys. Rev. Lett.*, vol. 119, no. 13, p. 130503, 2017.
- [40] R. Stockill, C. Le Gall, C. Matthiesen, L. Huthmacher, E. Clarke, M. Hugues, and M. Atatüre, “Quantum dot spin coherence governed by a strained nuclear environment,” *Nat. Commun.*, vol. 7, pp. 1–7, 2016.
- [41] D. A. Gangloff, G. Éthier-Majcher, C. Lang, E. V. Denning, J. H. Bodey, D. M. Jackson, E. Clarke, M. Hugues, C. Le Gall, and M. Atatüre, “Quantum interface of an electron and a nuclear ensemble,” *Science*, vol. 364, no. 6435, pp. 62–66, 2019.
- [42] L. Huthmacher, R. Stockill, E. Clarke, M. Hugues, C. LeGall, and M. Atatüre, “Coherence of a dynamically decoupled quantum-dot hole spin,” *Phys. Rev. B*, vol. 97, p. 241413(R), 2018.
- [43] S. Hughes, L. Ramunno, J. F. Young, and J. E. Sipe, “Extrinsic optical scattering loss in photonic crystal waveguides: Role of fabrication disorder and photon group velocity,” *Phys. Rev. Lett.*, vol. 94, no. 3, p. 033903, 2005.
- [44] M. Arcari, I. Söllner, A. Javadi, S. Lindskov Hansen, S. Mahmoodian, J. Liu, H. Thyrrestrup, E. H. Lee, J. D. Song, S. Stobbe, and P. Lodahl, “Near-Unity Coupling Efficiency of a Quantum Emitter to a Photonic Crystal Waveguide,” *Phys. Rev. Lett.*, vol. 113, no. 9, p. 093603, 2014.
- [45] P. Türschmann, H. Le Jeannic, S. F. Simonsen, H. R. Haakh, S. Götzinger, V. Sandoghdar, P. Lodahl, and N. Rotenberg, “Coherent nonlinear optics of quantum emitters in nanophotonic waveguides,” *Nanophotonics*, vol. 8, no. 10, pp. 1641–1657, 2019.
- [46] L. Midolo, T. Pregolato, G. Kiršanske, and S. Stobbe, “Soft-mask fabrication of gallium arsenide nanomembranes for integrated quantum photonics,” *Nanotechnology*, vol. 26, p. 484002, 2015.
- [47] X. Zhou, I. Kulkova, T. Lund-Hansen, S. L. Hansen, P. Lodahl, and L. Midolo, “High-efficiency shallow-etched grating on GaAs membranes for quantum photonic applications,” *Appl. Phys. Lett.*, vol. 113, no. 25, p. 251103, 2018.

- [48] H. Le Jeannic, T. Ramos, S. F. Simonsen, T. Pregnolato, Z. Liu, R. Schott, A. D. Wieck, A. Ludwig, N. Rotenberg, J. J. García-Ripoll, and P. Lodahl, “Experimental Reconstruction of the Few-Photon Nonlinear Scattering Matrix from a Single Quantum Dot in a Nanophotonic Waveguide,” *Phys. Rev. Lett.*, vol. 126, no. 2, p. 023603, 2021.
- [49] A. Delteil, Z. Sun, W.-b. Gao, E. Togan, S. Faelt, and A. Imamoglu, “Generation of heralded entanglement between distant hole spins,” *Nat. Phys.*, vol. 12, pp. 218–223, mar 2016.
- [50] A. Kurzmann, A. Ludwig, A. D. Wieck, A. Lorke, and M. Geller, “Auger Recombination in Self-Assembled Quantum Dots: Quenching and Broadening of the Charged Exciton Transition,” *Nano Lett.*, vol. 16, no. 5, pp. 3367–3372, 2016.
- [51] A. Högele, M. Kroner, C. Latta, M. Claassen, I. Carusotto, C. Bulutay, and A. Imamoglu, “Dynamic nuclear spin polarization in the resonant laser excitation of an InGaAs quantum dot,” *Phys. Rev. Lett.*, vol. 108, no. 19, p. 197403, 2012.
- [52] A. Javadi, S. Mahmoodian, I. Söllner, and P. Lodahl, “Numerical modeling of the coupling efficiency of single quantum emitters in photonic-crystal waveguides,” *J. Opt. Soc. Am. B*, vol. 35, no. 3, p. 514, 2018.
- [53] T. Pregnolato, X. L. Chu, T. Schröder, R. Schott, A. D. Wieck, A. Ludwig, P. Lodahl, and N. Rotenberg, “Deterministic positioning of nanophotonic waveguides around single self-assembled quantum dots,” *APL Photonics*, vol. 5, no. 8, p. 086101, 2020.
- [54] J. P. Lee, B. Villa, A. J. Bennett, R. M. Stevenson, D. J. P. Ellis, I. Farrer, D. A. Ritchie, and A. J. Shields, “A quantum dot as a source of time-bin entangled multi-photon states,” *Quantum Sci. Technol*, vol. 4, p. 025011, 2019.
- [55] S. Sun, H. Kim, G. S. Solomon, and E. Waks, “A quantum phase switch between a single solid-state spin and a photon,” *Nat. Nanotechnol.*, vol. 11, no. February, p. 46, 2015.
- [56] S. S. G. Carter, T. M. T. Sweeney, M. Kim, C. C. S. Kim, D. Solenov, S. E. Economou, T. L. Reinecke, L. Yang, A. S. Bracker, and D. Gammon, “Quantum control of a spin qubit coupled to a photonic crystal cavity,” *Nat. Photonics*, vol. 7, no. 4, pp. 329–334, 2013.
- [57] P. W. Milonni and J. H. Eberly, *Laser Physics*. Wiley, 1st ed., 2010.
- [58] R. J. Young, R. M. Stevenson, A. J. Shields, P. Atkinson, K. Cooper, D. A. Ritchie, K. M. Groom, A. I. Tartakovskii, and M. S. Skolnick, “Inversion of exciton level splitting in quantum dots,” *Phys. Rev. B - Condens. Matter Mater. Phys.*, vol. 72, no. 11, p. 113305, 2005.

- [59] M. H. Appel, A. Tiranov, K. Tiurev, A. Javadi, Y. Wang, L. Milodo, S. Scholz, A. D. Wieck, A. Ludwig, R. J. Warburton, and P. Lodahl, “Towards spin-multiphoton entanglement using quantum dots with asymmetric waveguide coupling,” *Conf. Lasers Electro-Optics, OSA Tech. Dig. (Optical Soc. Am. 2020), Pap. FW3C.1*, 2020.
- [60] L. Duan and H. J. Kimble, “Scalable Photonic Quantum Computation through Cavity-Assisted Interactions,” *Phys. Rev. Lett.*, vol. 92, p. 127902, 2004.
- [61] A. Delteil, W. B. Gao, P. Fallahi, J. Miguel-Sanchez, and A. Imamoglu, “Observation of quantum jumps of a single quantum dot spin using submicrosecond single-shot optical readout,” *Phys. Rev. Lett.*, vol. 112, no. 11, p. 116802, 2014.
- [62] Q. Zhang, Y. Guo, W. Ji, M. Wang, J. Yin, F. Kong, Y. Lin, C. Yin, F. Shi, Y. Wang, and J. Du, “High-fidelity single-shot readout of single electron spin in diamond with spin-to-charge conversion,” *Nat. Commun.*, vol. 12, no. 1, p. 1529, 2021.
- [63] M. Raha, S. Chen, C. M. Phenicie, S. Ourari, A. M. Dibos, and J. D. Thompson, “Optical quantum nondemolition measurement of a single rare earth ion qubit,” *Nat. Commun.*, vol. 11, no. 1, p. 1605, 2020.
- [64] A. N. Vamivakas, C. Y. Lu, C. Matthiesen, Y. Zhao, S. Fält, A. Badolato, and M. Atatüre, “Observation of spin-dependent quantum jumps via quantum dot resonance fluorescence,” *Nature*, vol. 467, no. 7313, pp. 297–300, 2010.
- [65] M. K. Bhaskar, R. Riedinger, B. Machielse, D. S. Levonian, C. T. Nguyen, E. N. Knall, H. Park, D. Englund, M. Lončar, D. D. Sukachev, and M. D. Lukin, “Experimental demonstration of memory-enhanced quantum communication,” *Nature*, vol. 580, no. 7801, pp. 60–64, 2020.
- [66] C. Papon, X. Zhou, H. Thyrestrup, Z. Liu, S. Stobbe, R. Schott, A. D. Wieck, A. Ludwig, P. Lodahl, and L. Midolo, “Nanomechanical single-photon routing,” *Optica*, vol. 6, no. 4, pp. 524–530, 2019.
- [67] A. Singh, Q. Li, J. Liu, X. Lu, C. Schneider, and K. Srinivasan, “Frequency Conversion of a Quantum Dot Single-Photon Source on a Nanophotonic Chip,” *2018 Conf. Lasers Electro-Optics, CLEO 2018 - Proc.*, vol. 6, no. 5, 2018.
- [68] G. Reithmaier, M. Kaniber, F. Flassig, S. Lichtmannecker, K. Müller, A. Andrejew, J. Vučković, R. Gross, and J. J. Finley, “On-Chip Generation, Routing, and Detection of Resonance Fluorescence,” *Nano Lett.*, vol. 15, no. 8, pp. 5208–5213, 2015.
- [69] D. Witthaut and A. S. Sorensen, “Photon scattering by a three-level emitter in a one-dimensional waveguide,” *New J. Phys.*, vol. 12, p. 043052, 2010.

- [70] D. E. Chang, A. S. Sørensen, E. A. Demler, and M. D. Lukin, “A single-photon transistor using nanoscale surface plasmons,” *Nat. Phys.*, vol. 3, no. 11, pp. 807–812, 2007.
- [71] S. Sun, H. Kim, Z. Luo, G. S. Solomon, and E. Waks, “A single-photon switch and transistor enabled by a solid-state quantum memory,” *Science*, vol. 361, no. 6397, pp. 57–60, 2018.
- [72] D. Witthaut, M. D. Lukin, and A. S. Sørensen, “Photon sorters and QND detectors using single photon emitters,” *Epl*, vol. 97, no. 5, p. 50007, 2012.
- [73] S. Rosenblum, A. Borne, and B. Dayan, “Analysis of deterministic swapping of photonic and atomic states through single-photon Raman interaction,” *Phys. Rev. A*, vol. 95, no. 3, p. 033814, 2017.
- [74] H. Wang, Y. M. He, T. H. Chung, H. Hu, Y. Yu, S. Chen, X. Ding, M. C. Chen, J. Qin, X. Yang, R. Z. Liu, Z. C. Duan, J. P. Li, S. Gerhardt, K. Winkler, J. Jurkat, L. J. Wang, N. Gregersen, Y. H. Huo, Q. Dai, S. Yu, S. Höfling, C. Y. Lu, and J. W. Pan, “Towards optimal single-photon sources from polarized microcavities,” *Nat. Photonics*, vol. 13, no. 11, pp. 770–775, 2019.
- [75] D. D. Awschalom, R. Hanson, J. Wrachtrup, and B. B. Zhou, “Quantum technologies with optically interfaced solid-state spins,” *Nat. Photonics*, vol. 12, no. 9, pp. 516–527, 2018.
- [76] M. Kroner, K. M. Weiss, B. Biedermann, S. Seidl, S. Manus, A. W. Holleitner, A. Badolato, P. M. Petroff, B. D. Gerardot, R. J. Warburton, and K. Karrai, “Optical detection of single-electron spin resonance in a quantum dot,” *Phys. Rev. Lett.*, vol. 100, no. 15, p. 156803, 2008.
- [77] D. Press, T. D. Ladd, B. Zhang, and Y. Yamamoto, “Complete quantum control of a single quantum dot spin using ultrafast optical pulses,” *Nature*, vol. 456, no. 7219, pp. 218–221, 2008.
- [78] J. H. Bodey, R. Stockill, E. V. Denning, D. A. Gangloff, G. Éthier-Majcher, D. M. Jackson, E. Clarke, M. Hugues, C. L. Gall, and M. Atatüre, “Optical spin locking of a solid-state qubit,” *npj Quantum Inf.*, vol. 5, no. 1, p. 95, 2019.
- [79] D. Press, K. De Greve, P. L. McMahon, T. D. Ladd, B. Friess, C. Schneider, M. Kamp, S. Hofling, A. Forchel, and Y. Yamamoto, “Ultrafast optical spin echo in a single quantum dot,” *Nat. Photonics*, vol. 4, no. 6, pp. 367–370, 2010.
- [80] D. Ding, M. H. Appel, A. Javadi, X. Zhou, M. C. Löbl, I. Söllner, R. Schott, C. Papon, T. Pregolato, L. Midolo, A. D. Wieck, A. Ludwig, R. J. Warburton, T. Schröder, and P. Lodahl, “Coherent optical control of a quantum-dot spin-qubit in a waveguide-based spin-photon interface,” *Phys. Rev. Appl.*, vol. 11, no. 3, p. 031002, 2019.

- [81] S. M. Barnett, *Quantum Information*. Oxford University Press, first ed., 2009.
- [82] G. Wolfowicz and J. J. Morton, “Pulse techniques for quantum information processing,” *eMagRes*, vol. 5, no. 4, pp. 1515–1528, 2016.
- [83] A. Kurzmann, A. Ludwig, A. D. Wieck, A. Lorke, and M. Geller, “Photoelectron generation and capture in the resonance fluorescence of a quantum dot,” *Appl. Phys. Lett.*, vol. 108, no. 26, p. 263108, 2016.
- [84] Z. Sun, A. Delteil, S. Faelt, and A. Imamoglu, “Measurement of spin coherence using Raman scattering,” *Phys. Rev. B*, vol. 93, p. 241302, 2016.
- [85] A. Greilich, S. G. Carter, D. Kim, A. S. Bracker, and D. Gammon, “Optical control of one and two hole spins in interacting quantum dots,” *Nat. Photonics*, vol. 5, no. 11, pp. 702–708, 2011.
- [86] T. M. Godden, J. H. Quilter, A. J. Ramsay, Y. Wu, P. Brereton, S. J. Boyle, I. J. Luxmoore, J. Puebla-Nunez, A. M. Fox, and M. S. Skolnick, “Coherent optical control of the spin of a single hole in an InAs/GaAs quantum dot,” *Phys. Rev. Lett.*, vol. 108, no. 1, p. 017402, 2012.
- [87] S. G. Carter, S. C. Badescu, A. S. Bracker, M. K. Yakes, K. X. Tran, J. Q. Grim, and D. Gammon, “Coherent Population Trapping Combined with Cycling Transitions for Quantum Dot Hole Spins Using Triplet Trion States,” *Phys. Rev. Lett.*, vol. 126, no. 10, p. 107401, 2021.
- [88] J. Mizrahi, B. Neyenhuis, K. G. Johnson, W. C. Campbell, C. Senko, D. Hayes, and C. Monroe, “Quantum control of qubits and atomic motion using ultrafast laser pulses,” *Appl. Phys. B Lasers Opt.*, vol. 114, no. 1-2, pp. 45–61, 2014.
- [89] W. B. Gao, P. Fallahi, E. Togan, J. Miguel-Sanchez, and A. Imamoglu, “Observation of entanglement between a quantum dot spin and a single photon,” *Nature*, vol. 491, no. 7424, pp. 426–430, 2012.
- [90] A. J. Ramsay, A. V. Gopal, E. M. Gauger, A. Nazir, B. W. Lovett, A. M. Fox, and M. S. Skolnick, “Damping of exciton rabi rotations by acoustic phonons in optically excited InGaAs/GaAs quantum dots,” *Phys. Rev. Lett.*, vol. 104, no. 1, pp. 20–23, 2010.
- [91] P. G. Kwiat, K. Mattle, H. Weinfurter, A. Zeilinger, A. V. Sergienko, and Y. Shih, “New high-intensity source of polarization-entangled photon pairs,” *Phys. Rev. Lett.*, vol. 75, no. 24, pp. 4337–4341, 1995.
- [92] D. Huber, M. Reindl, Y. Huo, H. Huang, J. S. Wildmann, O. G. Schmidt, A. Rastelli, and R. Trotta, “Highly indistinguishable and strongly entangled photons from symmetric GaAs quantum dots,” *Nat. Commun.*, vol. 8, p. 15506, 2017.

- [93] K. De Greve, L. Yu, P. L. McMahon, J. S. Pelc, C. M. Natarajan, N. Y. Kim, E. Abe, S. Maier, C. Schneider, M. Kamp, S. Höfling, R. H. Hadfield, A. Forchel, M. M. Fejer, and Y. Yamamoto, “Quantum-dot spin–photon entanglement via frequency downconversion to telecom wavelength,” *Nature*, vol. 491, pp. 421–425, 2012.
- [94] R. Stockill, M. J. Stanley, L. Huthmacher, E. Clarke, M. Hugues, A. J. Miller, C. Matthiesen, C. Le Gall, and M. Atatüre, “Phase-Tuned Entangled State Generation between Distant Spin Qubits,” *Phys. Rev. Lett.*, vol. 119, p. 010503, 2017.
- [95] J. W. Pan, D. Bouwmeester, M. Daniell, H. Weinfurter, and A. Zeilinger, “Experimental test of quantum nonlocality in three-photon Greenberger-Horne-Zeilinger entanglement,” *Nature*, vol. 403, no. 6769, pp. 515–519, 2000.
- [96] M. Gimeno-Segovia, P. Shadbolt, D. E. Browne, and T. Rudolph, “From Three-Photon Greenberger-Horne-Zeilinger States to Ballistic Universal Quantum Computation,” *Phys. Rev. Lett.*, vol. 115, no. 2, p. 020502, 2015.
- [97] H. A. Zaidi, C. Dawson, P. Van Loock, and T. Rudolph, “Near-deterministic creation of universal cluster states with probabilistic Bell measurements and three-qubit resource states,” *Phys. Rev. A - At. Mol. Opt. Phys.*, vol. 91, no. 4, p. 042301, 2015.
- [98] S. E. Economou, N. Lindner, and T. Rudolph, “Optically generated 2-dimensional photonic cluster state from coupled quantum dots,” *Phys. Rev. Lett.*, vol. 105, no. 9, p. 093601, 2010.
- [99] T. Rudolph, “Why i am optimistic about the silicon-photonic route to quantum computing,” *APL Photonics*, vol. 2, no. 3, p. 030901, 2017.
- [100] G. Kiršanske, H. Thyrrstrup, R. S. Daveau, C. L. Dreeßen, T. Pregolato, L. Midolo, P. Tighineanu, A. Javadi, S. Stobbe, R. Schott, A. Ludwig, A. D. Wieck, S. I. Park, J. D. Song, A. V. Kuhlmann, I. Söllner, M. C. Löbl, R. J. Warburton, and P. Lodahl, “Indistinguishable and efficient single photons from a quantum dot in a planar nanobeam waveguide,” *Phys. Rev. B*, vol. 96, no. 16, p. 165306, 2017.
- [101] R. J. Coles, D. M. Price, J. E. Dixon, B. Royall, E. Clarke, P. Kok, M. S. Skolnick, A. M. Fox, and M. N. Makhonin, “Chirality of nanophotonic waveguide with embedded quantum emitter for unidirectional spin transfer,” *Nat. commun.*, vol. 7, no. 2015, p. 11183, 2016.
- [102] P. Lodahl, S. Mahmoodian, S. Stobbe, A. Rauschenbeutel, P. Schneeweiss, J. Volz, H. Pichler, and P. Zoller, “Chiral quantum optics,” *Nature*, vol. 541, no. 7638, pp. 473–480, 2017.
- [103] F. Van Laere, W. Bogaerts, P. Dumon, G. Roelkens, D. Van Thourhout, and R. Baets, “Focusing polarization diversity grating couplers in silicon-on-insulator,” *J. Light. Technol.*, vol. 27, no. 5, pp. 612–618, 2009.

- [104] I. Schwartz, E. R. Schmidgall, L. Gantz, D. Cogan, E. Bordo, Y. Don, M. Zielinski, and D. Gershoni, “Deterministic writing and control of the dark exciton spin using single short optical pulses,” *Phys. Rev. X*, vol. 5, no. 1, p. 011009, 2015.
- [105] L. Gantz, D. Cogan, I. Schwartz, E. Schmidgall, G. Bahir, and D. Gershoni, “A new study of on-demand emission of indistinguishable single photons from single quantum dots,” *2017 Conf. Lasers Electro-Optics, CLEO 2017 - Proc.*, p. JTu5A.16, 2017.
- [106] K. Tiurev, P. L. Mirambell, M. B. Lauritzen, M. H. Appel, A. Tiranov, P. Lodahl, and A. S. Sørensen, “Fidelity of time-bin entangled multi-photon states from a quantum emitter,” *arXiv:2007.09298*, 2020.
- [107] H. Ollivier, S. E. Thomas, S. C. Wein, I. Maillette de Buy Wenniger, N. Coste, J. C. Loredó, N. Somaschi, A. Harouri, A. Lemaitre, I. Sagnes, L. Lanco, C. Simon, C. Anton, O. Krebs, and P. Senellart, “Hong-Ou-Mandel Interference with Imperfect Single Photon Sources,” *Phys. Rev. Lett.*, vol. 126, no. 6, p. 063602, 2021.
- [108] K. Tiurev, M. H. Appel, P. L. Mirambell, M. B. Lauritzen, A. Tiranov, P. Lodahl, and A. S. Sørensen, “High-fidelity multi-photon-entangled cluster state with solid-state quantum emitters in photonic nanostructures,” *arXiv:2007.09295*, 2021.
- [109] K. De Greve, P. L. McMahon, D. Press, T. D. Ladd, D. Bisping, C. Schneider, M. Kamp, L. Worschech, S. Höfling, A. Forchel, and Y. Yamamoto, “Ultrafast coherent control and suppressed nuclear feedback of a single quantum dot hole qubit,” *Nat. Phys.*, vol. 7, no. 11, pp. 872–878, 2011.
- [110] R. Raussendorf, J. Harrington, and K. Goyal, “A fault-tolerant one-way quantum computer,” *Ann. Phys. (N. Y.)*, vol. 321, no. 9, pp. 2242–2270, 2006.
- [111] D. F. V. James, P. G. Kwiat, W. J. Munro, and A. G. White, “Measurement of qubits,” *Phys. Rev. A*, vol. 64, p. 052312, 2001.
- [112] O. Gühne, C. Y. Lu, W. B. Gao, and J. W. Pan, “Toolbox for entanglement detection and fidelity estimation,” *Phys. Rev. A - At. Mol. Opt. Phys.*, vol. 76, no. 3, p. 030305(R), 2007.
- [113] B. B. Blinov, D. L. Moehring, L.-M. Duan, and C. Monroe, “Observation of entanglement between a single trapped atom and a single photon,” *Nature*, vol. 428, no. 6979, pp. 153–157, 2004.
- [114] F. Vedovato, C. Agnesi, M. Tomasin, M. Avesani, J. Å. Larsson, G. Vallone, and P. Villoresi, “Postselection-Loophole-Free Bell Violation with Genuine Time-Bin Entanglement,” *Phys. Rev. Lett.*, vol. 121, no. 19, p. 190401, 2018.
- [115] R. Munroe, “XKCD What if 13,” <https://what-if.xkcd.com/13/>, 2017.

- [116] R. Uppu, T. A. W. Wolterink, T. B. H. Tentrup, and P. W. H. Pinkse, “Quantum optics of lossy asymmetric beam splitters,” *Opt. Express*, vol. 24, no. 15, pp. 16440–16449, 2016.
- [117] E. Optics, “Eksma: Optics Pockels cells,” <https://eksmaoptics.com/electro-optics/pockels-cells/ktp-pockels-cells/>, 2021.
- [118] EOSpace, “EOSpace: Dual-Output Modulators,” <https://www.eospace.com/1x2-and-2x2-dual-output-modulator>.
- [119] Qubig, “Qubig: Resonant EOM,” <https://www.qubig.com/products/electro-optic-modulators-230/amplitude-modulators/am8-nir.html>.
- [120] Thorlabs, “Thorlabs note on free space electro optical modulators,” [https://www.thorlabs.com/newgrouppage9.cfm?objectgroup\\_id=2729](https://www.thorlabs.com/newgrouppage9.cfm?objectgroup_id=2729).
- [121] O. Gühne and G. Tóth, “Entanglement detection,” *Phys. Rep.*, vol. 474, pp. 1–75, 2009.
- [122] R. Vasconcelos, S. Reisenbauer, C. Salter, G. Wachter, D. Wirtitsch, J. Schmiedmayer, P. Walther, and M. Trupke, “Scalable spin–photon entanglement by time-to-polarization conversion,” *npj Quantum Inf.*, vol. 6, no. 1, p. 9, 2020.
- [123] C. Gerry and P. Knight, *Introductory Quantum Optics*. Cambridge University Press, first ed., 2005.
- [124] C. Santori, D. Fattal, J. Vučković, G. S. Solomon, and Y. Yamamoto, “Indistinguishable photons from a single-photon device,” *Conf. Quantum Electron. Laser Sci. - Tech. Dig. Ser.*, vol. 89, pp. 8–11, 2003.
- [125] J. Johansen, B. Julsgaard, S. Stobbe, J. M. Hvam, and P. Lodahl, “Probing long-lived dark excitons in self-assembled quantum dots,” *Phys. Rev. B - Condens. Matter Mater. Phys.*, vol. 81, no. 8, p. 081304(R), 2010.
- [126] S. Kako, C. Santori, K. Hoshino, S. Götzinger, Y. Yamamoto, and Y. Arakawa, “A gallium nitride single-photon source operating at 200K,” *Nat. Mater.*, vol. 5, no. 11, pp. 887–892, 2006.
- [127] C. K. Hong, Z. Y. Ou, and L. Mandel, “Measurements of Subpicosecond Time Intervals between Two Photons by Interference,” *Phys. Rev. Lett.*, vol. 59, no. 18, pp. 2044–2046, 1987.
- [128] X. Ding, Y. He, Z. C. Duan, N. Gregersen, M. C. Chen, S. Unsleber, S. Maier, C. Schneider, M. Kamp, S. Höfling, C. Y. Lu, and J. W. Pan, “On-Demand Single Photons with High Extraction Efficiency and Near-Unity Indistinguishability from a Resonantly Driven Quantum Dot in a Micropillar,” *Phys. Rev. Lett.*, vol. 116, no. 2, p. 020401, 2016.
- [129] L. Monniello, C. Tonin, R. Hostein, A. Lemaitre, A. Martinez, V. Voliotis, and R. Grousson, “Excitation-induced dephasing in a resonantly driven InAs/GaAs quantum dot,” *Phys. Rev. Lett.*, vol. 111, no. 2, p. 026403, 2013.

- [130] K. Mølmer, Y. Castin, and J. Dalibard, “Monte Carlo wave-function method in quantum optics,” *J. Opt. Soc. Am. B*, vol. 10, no. 3, p. 524, 1993.
- [131] QuTip, “QuTip note on Monte Carlo Simulation,”  
<http://qutip.org/docs/latest/guide/dynamics/dynamics-monte.html>.
- [132] L. Zhai, *Characterisation of Single-Photon sources: from Pulse-Width and Power Dependence of Single-Photon Purity to Effect of Spectral Filtering*. PhD thesis, University of Copenhagen, 2017.
- [133] L. Hanschke, K. A. Fischer, S. Appel, D. Lukin, J. Wierzbowski, S. Sun, R. Trivedi, J. Vu, J. J. Finley, and K. Müller, “Quantum dot single-photon sources with ultra-low multi-photon probability,” *npj Quantum Inf.*, vol. 4, no. August, p. 43, 2018.
- [134] L. Zhai, M. C. Löbl, G. N. Nguyen, J. Ritzmann, A. Javadi, C. Spinnler, A. D. Wieck, A. Ludwig, and R. J. Warburton, “Low-noise GaAs quantum dots for quantum photonics,” *Nat. Commun.*, vol. 11, no. 1, p. 4745, 2020.
- [135] M. Varnava, D. E. Browne, and T. Rudolph, “Loss tolerance in one-way quantum computation via counterfactual error correction,” *Phys. Rev. Lett.*, vol. 97, no. 12, p. 120501, 2006.
- [136] J. M. Kindem, A. Ruskuc, J. G. Bartholomew, J. Rochman, Y. Q. Huan, and A. Faraon, “[Supplementary] Control and single-shot readout of an ion embedded in a nanophotonic cavity,” *Nature*, vol. 580, no. 7802, pp. 201–204, 2020.